Understanding Polymer-Lipid Bilayer Interactions

A DISSERTATION SUBMITTED TO THE FACULTY OF UNIVERSITY OF MINNESOTA BY

Joseph Hassler

IN PARITAL FULFILLMENT OF THE REQUIREMENTS

FOR THE DEGREE OF

DOCTOR OF PHILOSOPHY

Advisors: Benjamin J. Hackel, Frank S. Bates, and Timothy P. Lodge

Acknowledgements

First, I want to thank my advisors: Ben Hackel, Frank Bates, and Tim Lodge. You gave me a tremendous amount of freedom and trust from day one and showed patience when progress was slow. You prioritized my development over my progress and were extremely supportive through hard times. Your advice, feedback, and mentorship have made me a confident, independent scientist, and I am excited for my next steps. I am grateful to have had advisors who can simultaneously light a fire under my feet and make me laugh.

I want to thank the NIH for providing funding for my projects and the University of Minnesota, particularly CEMS and Chemistry, for providing access to the necessary facilities. I also want to thank the polymer-sarcolemma team: Dr. Joseph Metzger, Dr. Samira Azarin, Dr. Marc Hillmyer, Dr. Dongwoo Han, Joey Quick, and Taylor Kuebler.

I want to thank my mentors, Dr. Mihee Kim and Dr. Michael Sims. You taught me so much about research and chemistry, and without you I would have been lost in my first years of grad school. I also want to thank Dr. Wenjia Zhang for laying a very solid foundation of work on which mine could be built. I also want to thank Dr. Adelyn Crabtree, Dr. Nick van Zee, Dr. Lucy Liberman, and Pranati Mondkar for our years of collaboration and discussions. You all expanded my work beyond what I could have achieved on my own.

Thank you to Gonzalo Garcia, Erika Cerna Arroyo, and Megan Lawson. I am fortunate to have had the opportunity to work with you all, and I am very proud of what we accomplished together.

Thank you to all the people who trained me on various instruments and methods: Dr. Julia Early and Dr. Aaron Lindsay (Anionic polymerization), Dr. Wenjia Zhang (DLS and liposome prep), Dr. Nick van Zee (PFG-NMR and liposome prep), Dr. Adelyn Crabtree and Dr. Mihee Kim (cell culture), Dr. Monica Ohnsorg (ROMP), and Dr. Michael Sims (RAFT + chemistry consultation). Also, thank you to Dr. Thomas Smith, your expertise and advice was instrumental to my work.

Thank you to all past and present Bates, Lodge, and Hackel group members I have overlapped with. Your questions, feedback, and answers to my questions have made me a better speaker and scientist. Your enthusiasm and collegiality have made the office and lab a fun place to come to work for the past 5 years. I am sad to be leaving this environment, and I am looking forward to all your progress in the future.

Finally, thank you to all my friends and family who have been a part of me making it through this program and the past 5 years. There are too many to name but specifically thank you to Saurabh Usgaonkar and Matt Hausladen for helping me through the long hours of homework and exams. Thank you to Joe Vallin for being a great climbing partner. Thank you to the 316-office cohort and coffee crew, particularly Zach Gdowski, Joanna White, Josh Goetze, Michael Sims, and Bo Zhang for answering my many questions, reviewing manuscripts, and chatting about data, sports, pets, and random things. Thank you to Brandon McCollam for being an amazing roommate and pushing me in many unique ways. Thank you to my mom, dad, Claire, and Liza for all your unconditional love, support, and food. Finally, thank you to my beautiful girlfriend, Carron. Thank you for listening on my good and bad science days and for supporting me through life.

Dedication

To my family, especially Liza. I miss you, and you continue to inspire me.

Abstract

Cell membrane instability is a common feature to Duchenne Muscular Dystrophy, heart attacks, strokes, and traumatic brain injury, which together affect over a million people in the United States every year and currently have no clinical treatment. In 1992, it was discovered that poloxamers, a class of biocompatible block polymer amphiphile stabilized cell membranes under stress, thereby having therapeutic potential. Unfortunately, the stabilization mechanism is not fully understood, hindering the engineering of more effective treatments.

Bottlebrush polymers have a wide parameter space and known relationships between architectural parameters and polymer properties, enabling their use as a tool for mechanistic investigations of polymer−lipid bilayer interactions. In this thesis, I report a synthetic strategy for making grafted block polymers with poly(propylene oxide) and poly(ethylene oxide) side chains, "bottlebrush poloxamers (BBPs)." Combined anionic and sequential ring-opening metathesis polymerization yielded low dispersity polymers, at full conversion of the macromonomers, with control over graft length, graft end-groups, and overall molecular weight. Dynamic light scattering and transmission electron microscopy were used to characterize micelle formation in aqueous buffer. The critical micelle concentration scales exponentially with overall molecular weight for both linear and bottlebrush poloxamers; however, the scaling coefficient is two orders of magnitude smaller in the bottlebrush architecture compared to the linear architecture, suggesting that micellization of BBPs is less sensitive to molecular weight.

I then employed this synthetic platform to create a set of BBPs over a range of molecular weight, with two PEO block side chain lengths, and with block and statistical architectures. Then, this set of molecules was used to interrogate the effects of bottlebrush architectural parameters on binding to, and protection of, phospholipid bilayers using pulsed-field-gradient NMR and an *in vitro* osmotic stress assay, respectively. I found that the binding affinity of a bottlebrush poloxamer (BBP) (*B*-$E_{10}^{43}P_{5}^{15}$, M_n = 26 kDa) is about 3 times higher than a linear poloxamer with a similar composition and number of PPO units (*L*-$E_{93}P_{54}E_{93}$, M_n = 11 kDa). Furthermore, BBP binding is

sensitive to overall molecular weight, side-chain length, and architecture (statistical versus block). Finally, all tested BBPs exhibit a protective effect on cell membranes under stress at sub-μM concentrations. As the factors controlling membrane affinity and protection efficacy of bottlebrush poloxamers are not understood, these results provide important insight into how they adhere to and stabilize a lipid bilayer surface.

The final two chapters of this thesis return to commercially available, linear poloxamers and seek to understand the effect of temperature and the role of lipid phase coexistence on poloxamer-liposome interactions. Hydrogen bonding between water and oxygen atoms in PEO and PPO units results in thermoresponsive behavior because the bound water shell around both blocks dehydrates as temperature increases. This motivates an investigation of poloxamer-lipid bilayer interactions as a function of temperature and thermal history. Pulsed-field gradient NMR spectroscopy measurements revealed that the fraction of chains bound to 1-palmitoyl-2-oleoyl-glycero-3-phosphocholine (POPC) liposomes increased by 11 (± 3)× at 37 °C relative to 27 °C. Moreover, following incubation at 37 °C, it takes weeks for the system to re-equilibrate at 25 °C. Such slow desorption kinetics suggests that at elevated temperatures polymer chains can pass through the bilayer and access the interior of the liposomes, a mechanism that is inaccessible at lower temperatures. We propose a molecular mechanism to explain this effect, which could have important ramifications on the cellular distribution of ABPs and could be exploited to modulate mechanical and surface properties of liposomes and cell membranes.

The lipid raft and picket fence models assert that the cell membrane contains liquid ordered domains (L_o) among a matrix of liquid disordered domains (L_d). These domains have different structural and physical properties, affecting protein conformation, cell signaling, and cellular processes. Therefore, I employed a liposome model consisting of a saturated lipid, an unsaturated lipid, and cholesterol that has a well-documented phase space to explore how lipid phase behavior affects polymer binding. I found that polymer binding is maximized in a window of the phase space coinciding with coexistence of the two liquid domains. This is likely because the borders

between the L_o and L_d domains are attractive binding sites. The proximity between bound polymer and lipid rafts could provide a non-specific mechanism by which flexible, non-polar amphiphilic block polymers affect cell signaling.

Table of Contents

Chapter 1: Introduction

1.1 Motivation

All known biological cells are bordered by a cell membrane. This critical organelle helps the cell maintain homeostasis by regulating transport of nutrients and waste, by preserving a transmembrane ion gradient, and by serving as a scaffold for proteins which play innumerable roles in cell-cell communication and in responding to environmental stimuli.[1–3] Numerous types of stresses such as oxidative stress,[4] mechanical trauma,[5] osmotic stress,[6] and genetic mutations[1,7] can disrupt the cell membrane, preventing it from acting as an effective barrier which can lead to cell death. These stresses affect different cell types to varying degrees and tissue in the brain, heart, and skeletal muscle are particularly affected during ischemic stroke, myocardial infarct (heart attack) and Duchenne's Muscular Dystrophy (DMD), respectively. These three diseases share an underlying cause (cell membrane instability), have no clinical treatment, and together affect over a million people per year in the United States alone.[8] Developing medicines to protect cells from these stresses and restore cell membrane stability is an active area of research.

In 1992, it was discovered that F68 (also known as P188), a member of a specific class of biocompatible block polymer amphiphiles known as pluronics (poloxamers), attenuated the increase in cell membrane permeability of skeletal muscle cells upon electropermeabilization and reduced the inflammatory response of mice exposed to electrical shock.[9] This result was hypothesized to be due to interactions between the amphiphilic polymer and amphiphilic phospholipids, the basic building block of the cell membrane, resulting in stabilization of the stressed membrane. Over the three decades since this discovery, research has focused on understanding the mechanism(s) by which poloxamers confer their protective effect. By improving understanding about how these polymers interact with the cell membrane, we may be able to engineer more effective therapeutics for heart attack victims, stroke victims, and DMD patients.

This thesis has gained mechanistic insights into polymer-lipid bilayer interactions by developing a novel poloxamer architecture, by elucidating the effect of temperature on polymer-

liposome binding events, and by exploring the role of lipid rafts in polymer-lipid bilayer interactions. Before detailing my specific contributions, I will first outline the current understanding of the constituent molecules and contemporary models of the cell membrane, describe the chemistry and properties of poloxamers, and summarize the mechanistic studies that have been performed over the past 30 years on this subject.

1.2 Cell membrane composition and current models

1.2.1 Constituent molecules of the cell membrane

The cell membrane is made up of four basic building blocks: phospholipids, cholesterol, proteins, and carbohydrates. The ratio of these four components varies tremendously by cell type, from cell to cell, and it changes in response to stimuli.[1,10,11] Approximately 50% of the membrane mass is phospholipids, 20-50% is proteins, and the balance is cholesterol and carbohydrates.[3,12,13] Before one can understand the roles of each of these molecules, it is useful to understand the chemical structures. Therefore, the general structure and a few important phospholipids and cholesterol are highlighted in Figure 1.1 below.

Phospholipids consist of a polar (hydrophilic) headgroup and a non-polar (hydrophobic) tail group. Due to this amphiphilicity, when phospholipids are placed in water it is thermodynamically favorable for them to self-assemble into structures that isolate the hydrophobic tails from the water-rich environment while leaving the hydrophilic headgroups exposed.[14] One such structure is the phospholipid bilayer shown in Figure 1.1a, which is the basic structure of the cell membrane. The lipid bilayer is ~50 Å thick and is highly dynamic.[15,16,17] Individual lipid molecules translate past one another,[18,19] rotate about the z-axis (normal to the bilayer plane),[20] and flip-flop between the interior and exterior leaflets.[21,22] These dynamic properties impact cellular processes and are influenced by headgroup and tailgroup identity. As shown by Figure 1.1b, there is a plethora of distinct headgroups and tailgroups which leads to diverse bilayer properties. Some important phospholipid molecules are shown in Figure 1.1b, which are grouped into three classes based on headgroup identity: zwitterions which have a positive and negative charge, Hydrogen-bond

donors, and glycolipids which have a sugar moiety covalently tethered to the headgroup. Representative molecules of each class were chosen to highlight trends between various structural parameters and physical properties.

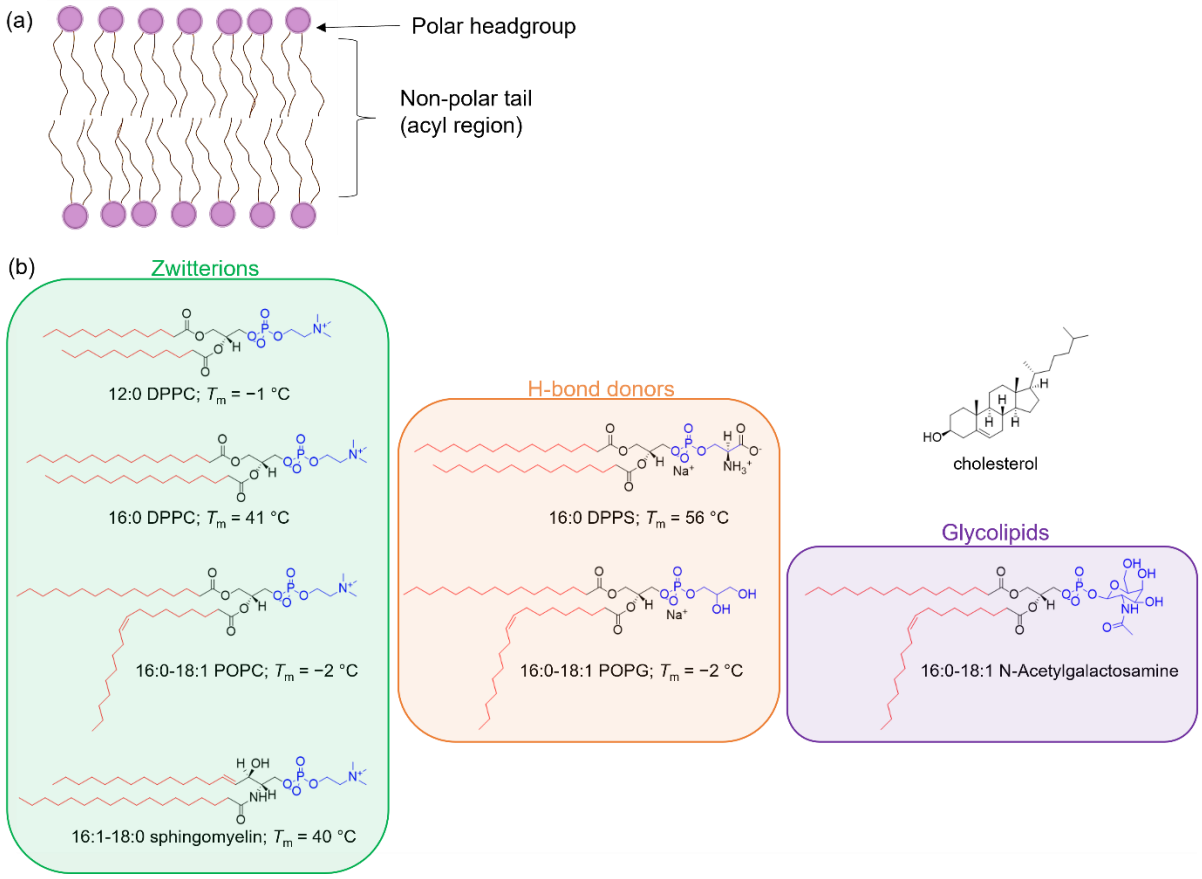

Figure 1.1: Phospholipid bilayer and important constituent molecules. (a) Simplified schematic of the phospholipid bilayer self-assembly. (b) Selected phospholipid molecules to illustrate diversity in tail group length and saturation and head group identities. The nomenclature of phospholipids, for example 16:0-18:1 POPC refers to the number of carbon atoms and the number of double bonds in each tail group.

One important property of phospholipids is the melting temperature (T_m) where a gel (butter-like) to liquid (oil-like) transition in the bulk occurs. Upon traversing the melting transition, neighboring lipid molecules become less oriented and diffuse more rapidly in the bilayer plane. This impacts protein clustering, therefore influencing cell signaling and behaviors such as cell

adhesion and growth.[23] The tail group primarily dictates T_m via its length, degree of unsaturation, and location of the unsaturation. The numbers in the nomenclature of a phospholipid describe the tail group and the letters identify the headgroup. For example, 16:0-18:1 POPC indicates that one tail has 16 C atoms with no carbon-carbon double bonds (desaturations) and the other tail has 18 C atoms and 1 desaturation. By comparing 12:0 and 16:0 DPPC, where the tail length increases from 12 to 16 carbon atoms, T_m increases from −1 °C to 41 °C. This general trend holds for other phospholipids; as the tailgroup is shortened, van der Waals forces are weaker and less able to hold neighboring lipids near one another, therefore less thermal energy is needed for the molecules to flow. Additionally, longer lipid tails lead to thicker bilayers.[24] A second factor influencing T_m is carbon-carbon double bonds, or desaturations, in the tail region. The rotational rigidity of the double bond forces the tail to kink, preventing the lipids from packing efficiently and depressing T_m. The location of the desaturation plays an important role. This can be seen by comparing the T_m of 16:0-18:1 POPC to 16:1-18:0 Sphingomyelin (PSM). For POPC, the desaturation occurs in the middle of the acyl tail, leading to a significant disruption of lipid-lipid packing and a relatively low T_m of −2 °C. On the other hand, the desaturation in PSM is at the headgroup-tailgroup interface, so the tails are much straighter and can pack more efficiently, leading to a relatively high T_m of 40 °C.

The headgroup also influences the bilayer properties, which have critical biological implications. As shown by Figure 1.1b, the chemical moieties that exist in the headgroup region are much more diverse than the tailgroup. There are zwitterionic species, species that can participate in hydrogen bonding pairs, and species that are modified with sugar molecules. These variations lead to differences in the bilayer dipole potential,[25] the area per lipid,[26] and the spatial proximity and alignment of neighboring lipids of different types.[27] Furthermore, the headgroup is in direct contact with the aqueous environment and therefore the first part of the bilayer to come into contact with extracellular proteins, drug molecules, and other cells. Lipid headgroups with hydrogen bond donors and acceptors have been shown to significantly slow lipid motion and the

dynamics of the bound water layer at the headgroup-water interface, which influences protein folding and therefore function.[28,29] Finally, one powerful example of the impact of covalently attached sugar molecules to the headgroup of phospholipids is its role in blood typing. Red blood cells are enriched in phospholipids modified with certain carbohydrates; type A is modified with N-Acetylgalactosamine as shown in Figure 1.1b while type B is modified with galactose, and these chemical differences lead to distinct cellular recognition events.[30]

Cholesterol has a very small hydrophilic moiety, a single alcohol group, followed by a four-ring structure, which makes it rigid, and then a hydrophobic hydrocarbon tail (Figure 1.1b). Because its hydrophilic domain is so small, it sits relatively deep in the lipid bilayer where a single molecule crosses the bilayer midplane.[31] This leads to an increase in interleaflet friction, hindering the independent diffusion of species in the inner and outer leaflets.[32] The conical shape of cholesterol gives it a preferred curvature, and this leads to an asymmetric distribution of cholesterol across the two leaflets with roughly 65 mol% of cholesterol typically residing in the outer leaflet.[31,33,34] Cholesterol also impacts the mechanical properties of lipid bilayers in interesting ways depending on the surrounding lipid type. In disordered bilayers, consisting of low T_m lipids, cholesterol reduces the free volume available, leading to an increase in order and packing density, a decrease in lipid lateral mobility, and an increase in the bending modulus (stiffening effect).[18,35] On the other hand, if the lipids are saturated (high T_m, ordered) introducing a molecule with a dramatically different shape disrupts packing order and has a fluidizing effect. Because of its ability to manipulate bilayer mechanical properties, cholesterol plays a role in viral entry to cells, cell membrane healing processes and cell motility.[36,37]

Proteins are biological polymers derived from the 20 naturally occurring amino acid monomers. They are assembled based on a genetic code via messenger RNA and therefore the sequence of amino acids is precisely controlled. The biggest difference between proteins and synthetic polymers is that the precise sequence control leads proteins to have specific secondary and tertiary structures governed by intramolecular interactions between different amino acid

residues.[38] This enables proteins to interact via a lock-and-key mechanism where a particular spot of one folded protein fits specifically within a binding pocket of another. These binding interactions, which are extremely sensitive to the protein conformation, are the basis for events such as cell signaling, enzymatic catalysis, and immune cell recognition/ activation. There are many important proteins that are embedded within the cell membrane and play important roles. Importantly, there is a feedback loop between proteins and the lipid bilayer as the mechanical properties of the lipid bilayer can impact protein conformation while proteins can regulate the mechanical properties of the bilayer.[39]

1.2.2 Lipid phase coexistence in abiotic and physiological membranes

Since biological cell membranes consist of thousands of different types of lipids, cholesterol, and membrane bound proteins, it is important to consider the interplay between these molecules. In simplified, abiotic membrane models consisting of a low T_m lipid, a high T_m lipid, and cholesterol, differences in packing densities and interaction energies of the different lipid components leads to phase separation into a liquid-ordered phase and a liquid-disordered phase. The liquid-ordered phase is enriched in cholesterol and the high T_m lipid and has a higher bending and stretching moduli, lower translational diffusion coefficient, reduced area per lipid, and an increased thickness.[2,15,40–42,43] Unsurprisingly, these differences lead to different interactions with proteins and have been shown to impact protein conformation and therefore protein function.[1,44]

The phase space as a function of lipid composition and temperature has been well-mapped for a number of 3-component systems by Veatch and co-workers.[14,41,45–47] Figure 1.2a demonstrates the effect of temperature and cholesterol content on the phase coexistence of 1:1 DOPC/DPPC + 25 mol% cholesterol. Phase coexistence was observed using fluorescence microscopy by doping a small amount of Texas red DPPE, which is a fluorescent probe covalently tethered to a saturated lipid; therefore the bright phases are the liquid-ordered domains.[48] In pathway 1-2, phase separation occurs as the vesicle is cooled and the miscibility temperature is traversed. In pathway

1'-2', the vesicles were treated with methyl-β cyclodextrin, a polysaccharide with a ring structure that extracts cholesterol from lipid bilayers. As the cholesterol is removed, phase separation is observed. These images are snapshots of a dynamic process, and as phase separated domains collide, they coalesce to minimize surface energy, ultimately leading to a single bright domain on the timescale of minutes. However, if the system is held near a phase boundary, metastable fluctuating domains can persist that resemble spinodal decomposition, as shown in Figure 1.2b.

Lipid phase separation also occurs in biological membranes, and Figure 1.2c is a representative image of this occurring in a living macrophage.[49] Lipid phase coexistence in living systems is much more complex than in abiotic models, due to many more components and a continuously changing composition. The lipid-raft hypothesis, first proposed in 1997 by Simons and Ikonen,[50] asserts that the liquid-ordered domains form functional platforms (lipid rafts) that play a role in many cellular processes such as endocytosis,[51] membrane repair,[37] and cell signalling.[2,3] Lipid rafts exist on both leaflets and can extend through both leaflets in the same lateral location. They are only ~10−100 nm in diameter and have short lifetimes, making them difficult to observe in living systems which has led to controversy over the past several decades.[52,53] Currently, there is general agreement regarding the existence and importance of lipid rafts; however, the length and time scales of the liquid-ordered phase heterogeneities and the best techniques to observe them are subjects of debate. [49,52,54–56,57] Molecular dynamics simulations are useful due to the ability to construct bilayers computationally that would be difficult to obtain with an experimental abiotic model and their ability to probe very short timescales.[2,31] Imaging techniques such as 2-photon microscopy, fluorescence microscopy, and confocal microscopy are useful for obtaining images over an entire cell or vesicle surface, capturing lateral heterogeneities; although long acquisition times make observing transient domains and time-sensitive processes difficult.[56,58,59] Diffusion techniques such as fluorescence recovery after photobleaching[60,61] and pulsed field gradient NMR[41] have been applied to estimate molecular mobility of probes having preferential solubility in one of the lipid phases. Future improvements to the spatial and temporal resolution of all these

techniques will aid in generating additional knowledge about the roles of lipid rafts in disease and how lipid rafts can be modulated by potential therapeutics.

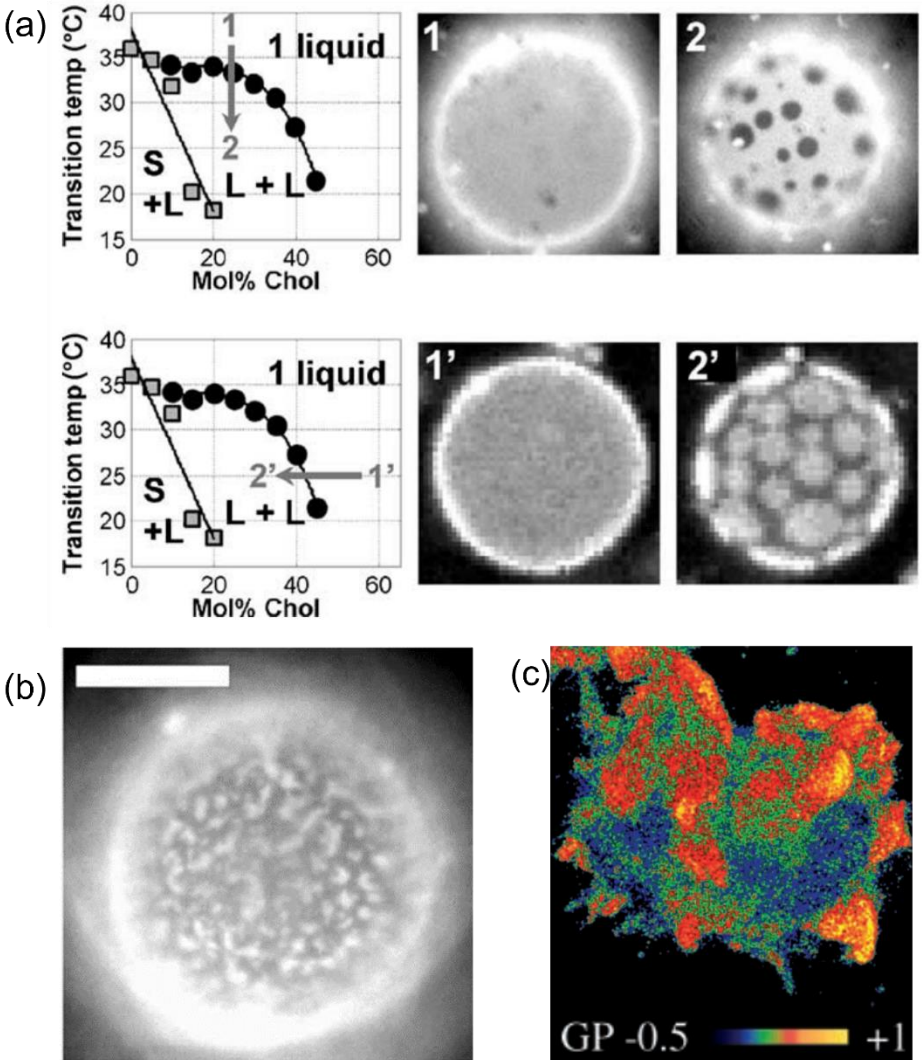

Figure 1.2: (a) Phase map and fluorescence microscopy images of vesicles corresponding to the paths shown. 1-2 shows the effect of temperature and 1'-2' the effect of cholesterol content. Vesicles are 1:1 DOPC/DPPC + 25% cholesterol and are ~30 μm in diameter. Figure adapted from Veatch and Keller, *Biochimica*, 2005.[48] (b) Giant unilamellar vesicle of 1:1 DPhyPC/DPPC + 50% cholesterol at 33 °C, close to a critical point and leading to rapid fluctuations in phase boundaries resembling spinodal decomposition. Scale bar is 20 μm. Figure adapted from Veatch and Keller, *Biochimica*, 2005. In panels (a) and (b) the bright domains are liquid-disordered. (c) Image of phase coexistence in a living macrophage via 2-photon microscopy. GP is generalized polarization and a higher value (orange) indicates more lipid order. Figure adapted from Gaus *et al. PNAS*, 2003 Copyright 2003 National Academy of Sciences.[49]

The discovery of lipid phase coexistence has changed the way the scientific community thinks about the cell membrane. Figure 1.3 shows the historical development of cell membrane models beginning with the Fluid Mosaic model proposed by Singer and Nicolson in 1972, which posited that the lipid bilayer is a disorganized, viscous fluid matrix for proteins which orient within the bilayer with specific conformations due to their amphiphilicity.[62] After evidence of lipid phase separation in abiotic membrane models emerged, this model was updated by the lipid raft hypothesis. As mentioned above, this model accounts for heterogeneities across the bilayer surface that are consistent with equilibrium thermodynamics (although a living cell membrane is certainly not at equilibrium), and it asserts that the lipid bilayer is organized and plays an active role in many aspects of membrane biology. Finally, in 2011, Kusumi and coworkers developed the picket fence model where the actin cytoskeleton and extracellular matrix impose dynamic constraints on protein/ lipid raft diffusion, leading to a three-tiered hierarchical structure.[63] They used single molecule tracking techniques to observe diffusion of fluorescently labelled proteins and saw that the proteins diffuse relatively rapidly within localized neighborhoods, imposed by the cytoskeleton, and hopping events between neighborhoods takes place on much longer timescales than lateral diffusion.[64]

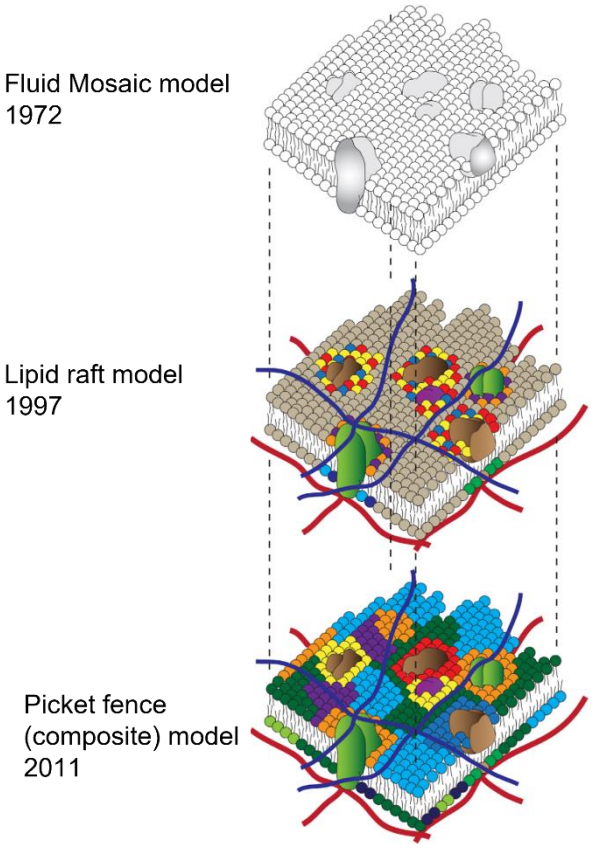

Figure 1.3: Historical development of cell membrane models. Figure adapted from Kalappurakal *et al. Protein Science.* 2020.[10]

1.2.3 Types of abiotic membrane models

Because the membranes of living cells contain thousands of distinct species and because cells perform many active processes, abiotic membrane models enable necessary simplifications to develop a fundamental understanding of membrane properties and interactions between potential drug molecules such as polymers, proteins, peptides, and surfactants on lipid membranes. Secondly, abiotic membrane models obviate the constraints of performing experiments under physiological conditions and keeping the cell alive, thereby expanding the suite of characterization techniques that can be performed. Generally, there are three classes of abiotic membrane models: lipid monolayers, supported lipid bilayers, and vesicles. All these classes are useful because they are compatible with distinct sets of characterization experiments, as shown by Figure 1.4.

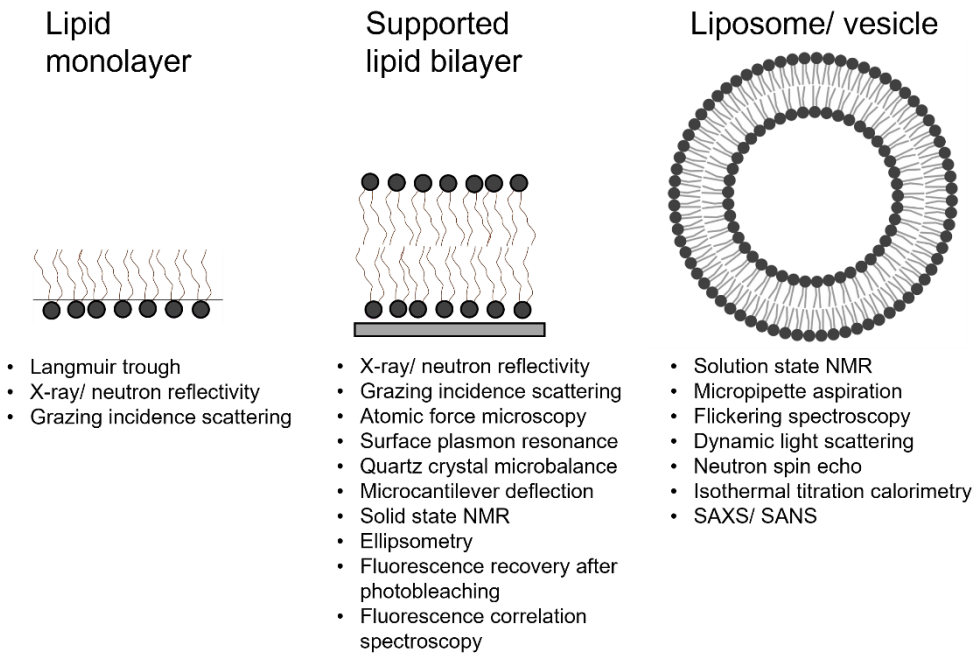

Figure 1.4: Types of abiotic membrane models and a summary of the types of experiments compatible with each membrane geometry.

Lipid monolayers are very easy to prepare, as the amphiphilic nature of lipid molecules naturally leads to a film at the air-water interface. The experimentalist typically spreads a small volume of the lipid dissolved in a good solvent for both the head and the tail (chloroform) onto the water surface and waits for the organic phase to evaporate.[65,66] Perhaps the most useful characterization technique that is compatible with lipid monolayers is the Langmuir Trough method. In this technique, the area of the interface is systematically compressed or expanded while the surface pressure is measured.[67] This allows one to detect changes in lipid phase via a sudden change in the compressibility and area per molecule. Furthermore, by injecting a polymer or protein into the aqueous subphase, one can quantify protein or polymer insertion into the lipid monolayer as an increase in the surface pressure.[65–69] Finally, this technique can be combined with fluorescence microscopy,[70,71] Brewster angle microscopy,[72] and surface characterization techniques such as grazing incidence X-ray scattering, X-ray reflectivity, to observe changes to the lipid phase and structural parameters *in situ* with monolayer compression.[65]

One criticism of using lipid monolayers as models for the cell membrane is that they only include half of the bilayer. Therefore, they are not well suited for systems where tailgroup interactions or membrane insertion depth are important. Supported lipid bilayers (SLBs) overcome this limitation; however, their preparation is more difficult. Typically, vesicles are prepared via extrusion and then introduced to the two-dimensional substrate, leading to a multi-step process involving vesicle adhesion, rupture, and bilayer spreading, the outcome of which is dependent on the surface properties of the substrate.[73,74] As shown by Figure 1.4, after successful preparation, SLBs are compatible with a wide range of characterization techniques, enabling quantification of many important biophysical membrane properties and characterization of interactions between membranes and various types of molecules. For example, atomic force microscopy can be used to map the topography, the height profile of the membrane in the x-y plane, and to quantify the force required to puncture a bilayer in the presence of various membrane modifiers.[17,75] Secondly, the insertion depth of macromolecules can be estimated via neutron reflectometry.[17] Additionally, techniques such as surface plasmon resonance, quartz crystal microbalance, and microcantilever deflection can be used to probe the membrane binding affinity and rate constants of adsorption of membrane-binding molecules.[73,76,77] The orientational order parameter, which characterizes the packing of lipid tails can be measured with solid-state NMR.[78,79] Finally, the lateral diffusion coefficient of fluorescently labelled lipids or other types of membrane-bound species can be measured with techniques such as fluorescence recovery after photobleaching (FRAP) or fluorescence correlation spectroscopy (FCS).[34,75,76,80]

Vesicles are another type of common abiotic membrane model and their distinguishing feature from lipid monolayers and SLBs is that they have a three-dimensional geometry, have an inherent curvature, and are typically freely diffusing in solution. This enables access to solution characterization techniques such as dynamic light scattering for particle sizing[81,82] and solution-state NMR to characterize the dynamics of membrane bound water molecules,[83] the relative proximity between lipid components and membrane-inserted polymers,[84] and the membrane

affinity of macromolecules.[85–88] Another technique commonly employed to measure the membrane-affinity of a given molecule towards lipid vesicles is isothermal titration calorimetry.[89,90] Furthermore, vesicles are commonly used to assess the bending and stretching moduli of lipid bilayers which are important mechanical properties governing cell membrane deformation. This is typically done with techniques such as flickering spectroscopy[91,92] or micropipette aspiration.[24,93,94] Liposomes, which are the cell membrane model employed in this thesis, are a subclass of vesicles with diameters ~50−500 nm.

While these abiotic membrane models are tremendous abstractions from a living membrane, they enable access to information that would be unattainable with *in vitro* experiments because of the broad variety of characterization techniques that can be used with these models. Furthermore, the ability to incorporate only a few specific lipid, protein, or cholesterol molecules allows the experimentalist to ask targeted questions that would be impossible to answer with the confounding effects of active cellular processes and the extremely complex mixture of lipids that constitute a living cell's membrane. Therefore, abiotic membrane models have a very important place in fundamental biophysical studies; however, the molecules used in each membrane model must be carefully chosen to ensure as much relevancy to the corresponding cellular application as possible.

1.3 Poloxamers are thermoresponsive and therapeutically useful molecules

1.3.1 Poloxamer background and thermoresponsive character

Poloxamers are A-B-A triblock polymers, where the A block is poly(ethylene oxide) (PEO) and the B block is poly(propylene oxide) (PPO). Poloxamers are commercially produced by BASF under the trade name Pluronics® and have widespread utility because of their aqueous solubility, amphiphilic nature, and biocompatibility. Their chemical structure is shown in Figure 1.5a, and they are available over a wide range of compositions and molecular weights as shown by Figure 1.5b. Throughout this thesis, blue will represent PEO and red will represent PPO. The naming convention used in Figure 1.5b was developed by BASF to communicate the physical appearance of the formulation and details of the architecture. The letter indicates if the bulk formulation is a

liquid (“L”), paste (“P”), or flake (“F”). The final digit can be multiplied by 10 to give the wt% PEO and the preceding digit(s) can be multiplied by 300 to give the molecular weight of the PPO block. This nomenclature is opaque to all except those very familiar with poloxamer formulations, so I will use it sparingly and instead favor the nomenclature $E_xP_yE_x$ where E indicates PEO, P indicates PPO, and x and y are the number averaged degree of polymerization of the corresponding block.

The structures of the PEO and PPO repeat units give poloxamers interesting, and useful, properties in aqueous solution. The oxygen atoms in both units can form hydrogen bonds with water, leading to a bound water shell.[95,96] The methyl group of PPO makes it harder for water molecules to interact with the oxygen atoms, leading to fewer H-bonds per oxygen and a longer H-bond distance in PPO relative to PEO.[96] This makes PPO less hydrophilic than PEO, giving poloxamers amphiphilic character and surfactant-like properties, making them useful for applications such as detergents, foams, and emulsifiers.[97,98] Furthermore, because H-bonding is an entropically driven phenomenon, it is sensitive to temperature. Thus, the H-bonded water shell dehydrates as temperature is increased, going from 6 H-bonds/ O atom in PEO at 25 °C to only 1 H-bond/ O atom at 70 °C.[96] This mechanism makes aqueous poloxamer systems thermoresponsive, with lower critical solution temperature behavior, meaning that chains dissolve in solution at low temperatures and then form aggregates and phase separate into polymer-rich and polymer-poor domains at elevated temperatures. This phase separation leads to clouding, and the temperature at which it occurs is called the cloud-point temperature, T_{cp}. The solvent quality of water for PEO/PPO chains can also be modified by adding salt to the solution as the electrolyte disrupts the water shell, thus depressing T_{cp}.[99]

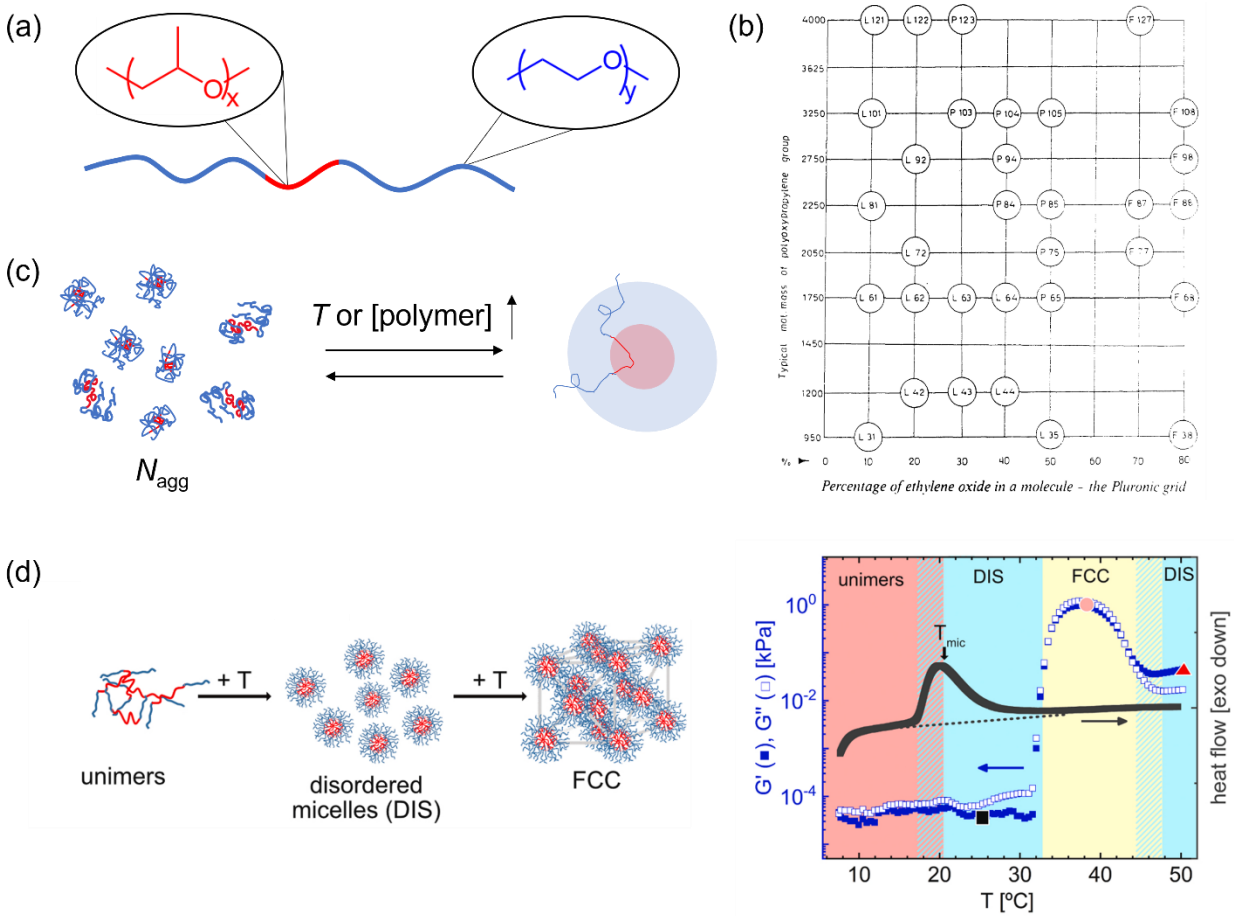

Figure 1.5: (a) Structure of a poloxamer. (b) Commercially available poloxamer formulations, figure adapted from Alexandridis *et al.*[100] (c) Sketch of many poloxamer chains aggregating into a micelle – a particle with a distinct core-corona structure which occurs at sufficiently high temperatures and/ or concentrations. (d) Sketch of a solution to gel transition of a concentrated poloxamer solution and corresponding DSC and rheology data corresponding to the two transitions. Figure 1.5d was adapted from White *et al.* and used with permission.[101]

1.3.2 Micellization thermodynamics and importance

One consequence of the thermoresponsive nature of poloxamer solutions is micellization, which is illustrated by Figure 1.5c and is defined as the aggregation of many chains into a structure with a well-defined solvophobic core and solvophilic corona. Micelles can be exploited for applications such as viscosity modification, as excipients to stabilize hydrophobic drugs, and as drug-delivery vehicles.[97] Key parameters of micellization are the critical micellization concentration (CMC), the concentration at which micelles first appear in solution, the critical

micellization temperature (CMT), the temperature at which micelles first appear in solution, the aggregation number (N_{agg}), the number of chains that occupy a micelle, and the hydrodynamic radius (R_h), which characterizes the rate of diffusion if the micelle were a hard sphere. There are several equilibrium theories that have been used to develop scaling relationships between polymer parameters such as molecular weight (M_n), composition (fraction of the solvophobic block), the interaction energies between each of the two blocks and the solvent ($\chi_{A\text{-}S}$, and $\chi_{B\text{-}S}$), and the interfacial energy at the core/corona interface (γ) to the CMC/ CMT, micelle radius of gyration (R_g), and N_{agg}.[102,103] These models consider the entropic cost of localizing many chains together, an elastic chain stretching penalty (also an entropic contribution), and the enthalpic interfacial energy at the core-corona interface.[103]

Model predictions are consistent with experimental results in some contexts; however, it should be noted that there are significant energetic barriers to micelle formation and it is a multi-molecular process, so it is easy for micellar systems to be out of equilibrium, and this is true for poloxamer systems.[104,105,106] Furthermore, due to composition dispersity, micellization of polymer solutions is not a strict phase transition, but rather it occurs over a range of temperatures and concentrations, is sensitive to sample preparation, and different measurement techniques often lead to different estimates for the CMC or CMT.[97] Common techniques used to detect micelles are dye solubilization,[97] differential scanning calorimetry (DSC),[101] surface tension measurements,[107,108] and dynamic light scattering (DLS).[87,109,110,111,112] Alexandridis *et al.* performed a systematic study of poloxamer micellization using a dye solubilization technique and found that the CMC and CMT decrease exponentially with increasing PPO block length. Furthermore, when the PPO block length was fixed, CMC marginally increases with increasing PEO block length. Therefore, although increased PEO content delays the onset of micellization with increasing temperature or concentration, the hydrophobic block length is a far more critical parameter.[97] The hydrophobic block was also found to dominate the micellization of PEO-PBO diblocks and triblocks.[112] As can be seen by the DSC data in Figure 1.5c, micellization of a poloxamer solution is endothermic.

Therefore, it must be an entropically dominated phenomenon which might seem counterintuitive as one might expect aggregation of many individual polymer chains into a single micelle to have an entropic penalty. However, as poloxamer chains aggregate, the PPO blocks are dehydrated and the increase in the translational entropy of the water molecules is much larger than the entropic penalty of the chains aggregating.

Measuring the CMC is of practical importance for two reasons: first, it is important to understand the distribution of chains between the unimer and micellar states, as these states can have different functions in any given application. Second, an estimate for the CMC can be used to calculate the free energy change of micellization via Equation 1:

$$\Delta G^0 = RT \times \ln(\chi_{CMC}) \quad \text{(Eq. 1)}$$

where R is the universal gas constant, T is the temperature in Kelvin, χ_{CMC} is the CMC in mass fraction units, and ΔG^0 is the free energy difference between micelles and free chains at atmospheric pressure and temperature. ΔG^0 can then be used as a proxy for hydrophobicity when comparing molecular designs.

A second interesting consequence of poloxamer thermoresponsivness is gelation behavior. If a micellar poloxamer solution is at a sufficiently high concentration (>15 wt%), it will undergo a reversible solution-to-gel transition as temperature is increased. Gelation leads to an increase in the storage modulus by several orders of magnitude and is illustrated in Figure 1.5d.[101] This transition is caused by ordering of the micelles onto a lattice and it is sensitive to polymer architecture, molecular weight and composition. Careful tuning of these properties has been used to develop a drug delivery platform for antimicrobials across the tympanic membrane as a treatment method for ear infections with high patient compliance.[101]

1.4 Poloxamers as cell membrane stabilizers

1.4.1 Cell membrane stabilization via poloxamers in cellular and animal models

In addition to applications as gels and micelles for drug delivery, individual poloxamer chains interact with phospholipid bilayers. In the early 1990s, Thomas *et al.* and Papoutsakis *et al.* independently discovered that adding F68 ($E_{75}P_{30}E_{75}$) to bioreactors stabilized mammalian cells against shear stresses.[113,114] Initially, this was thought to be because the surfactant properties of F68 stabilized the surface foams, therefore minimizing bubble bursting events which are known to stress nearby cells. However, Thomas and co-workers showed via micropipette aspiration that F68 increases the bending modulus and lysis tension of the cell membranes, suggesting that the polymer chains directly interact with the cell membrane and manipulate its mechanical properties.[114] Since poloxamers are amphiphilic molecules, it is not surprising that they interact with amphiphilic phospholipid bilayers.

In 1992, Lee and co-workers were the first to document the membrane stabilizing effect of F68 both *in vitro* and *in vivo*.[9] They showed that F68 reduced the release of an intracellular fluorophore after exposure to an electrical shock *in vitro* and simultaneously increased the electrical resistance of muscle tissue and reduced the inflammatory response after electrical injury in a mouse model.[9] Since that discovery, F68 and similar poloxamers have demonstrated efficacy in reducing damage against a very wide range of stresses that cause cell membrane instability. For example, F68 treatment has been shown to reduce release of macromolecules from neurons that experience shear stress[115] or mechanical trauma.[116] Therefore poloxamers show potential as a treatment for traumatic brain injury (TBI), as a hallmark of TBI is shear stress which reduces the ability of the cell membrane to regulate transport of macromolecules.[115–117] Furthermore, several research groups have demonstrated that poloxamers protect neuronal cells,[69,118,119] testicular cells,[120] and cardiomyocytes[121,122,123] from oxygen/ glucose deprivation (OGD), therefore holding potential as therapeutics for stroke and heart attack victims. The beneficial effects of poloxamers have also been observed *in vivo* as Bartos and co-workers demonstrated that intracoronary treatment of F68 reduces heart damage after a myocardial infarct (heart attack) in a pig model.[124] Additionally,

several poloxamers, and another commercially available PEO-PPO copolymer architecture called poloxamines, have demonstrated an ability to protect cells from oxidative damage, which is caused by radical species produced by nutrient deprivation or ionizing radiation. Oxidative damage leads to a loss of membrane barrier properties, a reduction in membrane thickness, and reduced lateral lipid diffusion coefficients. [81, 125–129] Finally, in 2005, Metzger and co-workers were the first to demonstrate that the membrane sealing effects of poloxamers have beneficial implications for patients with muscular dystrophy.[7] In muscular dystrophy patients, skeletal and heart muscle cells under express dystrophin, a protein that connects the cell membrane to the actin cytoskeletal network and acts as a molecular force-dampener as the muscle cells contract.[13] Without dystrophin, the membranes of muscle cells develop rips or pores, leading to free diffusion of proteins and ions such as Ca^{2+} across the membrane. This causes mitochondrial damage, metabolic exhaustion, and an inability to control muscle cell contraction, ultimately leading to a loss of the force a muscle tissue can exert over time.[13,130,131] Call and co-workers and Houang and co-workers used distinct animal models to show that poloxamer treatment reduced the loss of force over repeated lengthening-contraction cycles in ankle and quadriceps tissues of dystrophic mouse models, respectively.[130,131]

The ability of poloxamers to improve barrier properties of many different cell types across a diverse range of stresses highlights their therapeutic promise as treatments for heart attacks, strokes, radiation damage, and muscular dystrophy. To fully realize the potential of poloxamers, we must understand the molecular mechanism, or more likely *mechanisms*, behind their protective effects. Mechanistic investigations have been ongoing since the original discovery by Lee and co-workers in 1992, and while significant progress has been made, there are still many open questions and competing stabilization mechanisms that have been proposed. In the next sections, I will highlight a few open questions and then summarize recent advances in our understanding of the stabilization mechanism(s).

1.4.2 Summary of open questions

One open question in the field is: to what extent are active cellular processes and cell signaling events involved in the protective effect of poloxamers? Because PEO-PPO block polymers are flexible macromolecules with no specific conformation, they will not have any specific interactions with proteins. Thus, one might expect that poloxamer presence would have little effect on cell signaling since these events necessitate protein-protein interactions in a lock-and-key mechanism. However, there is a tremendous amount of experimental evidence that PEO-PPO block polymers affect many cell signaling pathways that govern a range of cell behavior. For example, F68 presence during oxidative stress limited changes in gene expression of pathways involved in reorganization of the cytoskeleton such as cofilin 2, thymosin beta 4, and profilin 1.[128] Additionally, PEO homopolymer and poloxamers inhibited caspase 3 and cytochrome c production in response to hypoxia/ reoxygenation insult; thereby interfering with the apoptosis cascade.[118,121] Recently, Crabtree *et al.* performed RNA sequencing on C2C12 myoblasts subjected to osmotic stress in the presence of either F68 or a PEO homopolymer to get a complete picture of changes to mRNA expression in various treatments.[132] They found that both polymers induce changes in gene expression; although there was little difference between these polymers. Additionally, osmotic stress significantly alters gene expression and polymer presence does not return it to unstressed levels, despite the well documented protective effects.[132]

One plausible mechanism for how polymers could alter gene expression is by modulating lipid rafts. As discussed in Section 1.2.1, lipid rafts impact protein conformation, which affects cell signaling and therefore gene expression. Osmotic stress changes the area per lipid, and oxidative stress breaks carbon-carbon double bonds in the tail region. Both of these effects alter the line tension in the membrane which has been identified as a key determinant of lipid phase separation.[133,125,134] By inserting into the cell membrane, polymers exert a lateral pressure and reduce membrane tension[135–137] which could impact the equilibrium between liquid-ordered and liquid-disordered domains. There has been one study to date which demonstrated that a PEO homopolymer with M_n ~15-20 kDa prevented the coalescence of lipid rafts upon exposure to

ionizing radiation.[125] Another possible mechanism for polymer impacting cell signaling under stress is that by stabilizing the membrane, the polymer limits the cell's active responses to membrane stress. For example if polymer binding limits free diffusion of ions across the membrane, it could inhibit the apoptosis cascade.[13]

Another significant debate in the field is whether poloxamers act by preventing damage from occurring (protective effect), or by facilitating innate membrane repair processes (facilitated healing). Work by Togo *et al.* developed an *in vitro* assay where fibroblasts were damaged with a microneedle and the release of a fluorophore was observed by continuously recording fluorescence intensity in the supernatant over time.[137] The time at which the supernatant fluorescence stabilizes was taken as the membrane resealing time. They found that F68 presence decreased the membrane resealing time in the presence and non-presence of endocytosis inhibitors, suggesting that F68 facilitates pore closure via a passive process. In a second paper from the same group, they correlated the reduced membrane resealing time with a reduction in the membrane tension.[137,138] Kwiatkowski *et al.* tracked the release of an intracellular fluorophore following a laser ablation insult and similarly found that F68, and other poloxamers, reduced the resealing time.[139] It should be noted that in both of these studies, the poloxamer was present prior to the injury, and because membrane resealing occurs on the order of 100s of seconds, it is impractical to add polymer after the injury. Therefore, although poloxamer presence accelerated pore closure, it is still possible that the poloxamer had a protective effect by limiting the extent of the injury in addition to facilitating repair after injury. Additionally, Shelat *et al.* performed an *in vitro* OGD deprivation assay where F68 was introduced at several timepoints pre/post damage. They found that as long as F68 was introduced within 12 hours after damage, there was no difference in the percent viability of the neuronal culture 24 hours after the stress was imposed.[118] They argued that F68 interfered with the apoptosis cascade thereby preventing cell death even if it was not present when the damage occurred. On the contrary, in a multi-step myocardial infarct porcine model, Bartos *et al.* observed that the efficacy of F68 is markedly higher when it is present prior to damage as compared to only

after damage occurs, suggesting that in this scenario the protective effect is far stronger than the facilitated healing effect.[124] There are a number of animal studies that have documented both the timing and delivery route of poloxamers can lead to differing protective efficacy.[13,131] Ultimately, both the protective and rescue effects are consistent with molecular mechanisms and there is experimental evidence for both contributions. Which effect dominates is likely dependent on the cell type and the dynamics of the stress imposed.

Finally, the molecular details of the membrane stabilization mechanism remain elusive, hindering the engineering of better therapeutics. Understanding what parameters of the block polymer (end groups, composition, molecular weight, architecture) affect interactions with cell membranes is key to engineering the next generation of membrane therapeutics. Additionally, understanding what biological molecules in the cell membrane are involved in polymer-membrane interactions and what cell membrane features play a role could inform molecular design choices. To answer these questions, many studies have been performed using molecular dynamics simulations, simplified abiotic membrane models, cellular assays, and *in vivo* experiments to gain fundamental insights into the mechanism(s) of action.

1.4.3 Summary of current mechanistic understanding

Pulsed field gradient NMR,[85,87] isothermal titration calorimetry,[81] and microcantilever deflection[80] experiments have demonstrated that increasing the hydrophobicity of the molecule, which is dictated by the ratio of PEO to PPO units, increases the association of polymer with liposomes. Poloxamers with 80 wt% PEO or higher have low to undetectable binding with phospholipid bilayers; however, as mentioned above F68 (80 wt% PEO) is one of the most widely used and efficacious membrane stabilizers.[6,85] This suggests that binding to liposomes does not necessarily inform protection efficacy and that polymers with weak bilayer association can still have a therapeutic effect. Additionally, hydrophobic poloxamers having < 30 wt% PEO accelerate lipid flip-flop and destabilize cell membranes, which has applications for enhancing delivery of

chemotherapeutics to tumor cells.[140–142] Clearly, the composition of the polymer matters as hydrophobic and hydrophilic poloxamers have very different effects on the cell membrane. Increasing the molecular weight, at the same composition, also increases the membrane affinity; however this effect is less pronounced than the effect of composition.[85] It is important to note that membrane binding is not unique to commercially available triblock poloxamers, as diblock PEO-PPO and PEO-PBO copolymers have also shown the ability to bind to liposomes.[85,87] In the diblock architecture, the end-group on the hydrophobic block impacts binding and protection efficacy with the relatively bulky, hydrophobic tert-butyl group leading to the highest affinity and best protection.[6,85,143] Molecular dynamics simulations have shown that increasing the hydrophobicity of the PPO block end-group leads to a deeper insertion depth.[143] These results are summarized by Figure 1.6a and can be described by the anchor-and-chain hypothesis which asserts that binding is driven by the PPO block due to entropically dominated hydrophobic forces. The PPO block inserts into the acyl region of the bilayer while the PEO blocks persist near the extra-cellular leaflet and interact with the lipid headgroups and bound water layer.

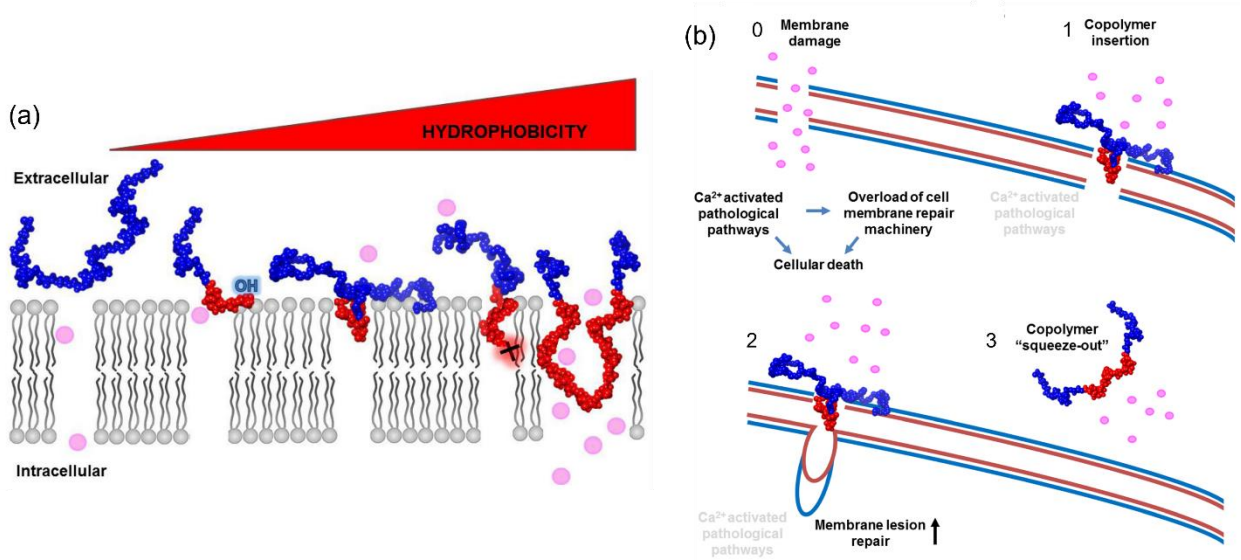

Figure 1.6: (a) Sketch of the anchor-and-chain interaction hypothesis. PEO homopolymers and PEO-PPO block copolymers with high wt% PEO may weakly adsorb to exterior leaflet while increasing the PPO block content or end-group hydrophobicity leads to higher membrane affinity and deeper insertion. (b) Time course of an injury resulting in membrane damage without polymer (0) and in the presence of poloxamer (1-3). Both figures were adapted from Houang *et al.* and used with permission.[13]

The anchor-and-chain hypothesis is also consistent with Langmuir trough experiments performed by Lee and co-workers that showed that F68 preferentially inserts into lipid monolayers at low surface pressures (high area per lipid), which are analogous to damaged regions of the bilayer.[65,66,71] This result was also corroborated with MD simulations that showed hydrophilic polymers only insert into bilayers when there is an applied strain.[144] Upon insertion into a DPPC monolayer, the F68 chain exerts a lateral pressure, reducing the area available and inducing ordering of the lipid tails at a higher area per lipid than in a neat monolayer. Furthermore, the lattice parameters of the crystalline phase are unchanged by polymer presence.[65] This result suggests that the PPO block is inserted into the acyl region rather than the polymer being exclusively adsorbed to the exterior leaflet. Furthermore, since polymer presence does not change the crystal structure of ordered domains, the polymer must be excluded from the crystalline domains.[66] Additionally, if surface pressure in the trough is increased after the polymer is inserted, eventually the pressure-area isotherms of neat lipid monolayer and lipid monolayer + polymer overlap, indicating that the

polymer is squeezed out. The implication is that the polymer can adsorb at regions of high area per lipid, disordered or damaged regions of the cell membrane, then as the cell's innate healing processes repair the membrane, the polymer is squeezed out.

In addition to constraining the area of nearby lipids, polymer insertion changes the dynamics and mechanical properties of the bilayer. Recent results using ^{1}H Overhauser dynamic nuclear polarization enhanced NMR experiments showed poloxamer binding slowed the rate of diffusion of water in the layer just above the lipid headgroups.[83,145] By slowing diffusion in this region, membrane-bound polymers could act as a diffusive shield, slowing the diffusion of radical or ionic species across the membrane. Van Zee *et al.* used micropipette aspiration to measure the bending and stretching moduli of POPC vesicles in the presence of poloxamers over a range of molecular weights and compositions. They found that poloxamer binding does not significantly change the bending modulus; however low molecular weight poloxamers reduced the stretching modulus, the amount of energy required to create new membrane area by pulling neighboring lipids apart, by ~10% and high molecular weight poloxamers reduced it by ~30%.[94] These results are consistent with the studies by Togo *et al.* that found that poloxamer treatment reduced line tension of the cell membrane in living cells.[137,138]

Finally, work by Zhang *et al.* explored poloxamer-lipid bilayer interactions by building liposome models with mixed compositions.[82,86,146] First, the membrane constituent with the most significant impact is cholesterol, as increasing cholesterol content dramatically reduced polymer binding independently of polymer composition and molecular weight.[86] At a cholesterol content > 20 mol%, no polymer binding was observed via PFG-NMR. As mentioned in section 1.2.1 cholesterol changes the mechanical and structural properties of lipid bilayers. Specifically, micropipette aspiration and ^{2}H NMR spectroscopy experiments on mixed POPC/ sterol vesicles showed that increasing sterol content led to an increase in the stretching and bending moduli and an increase in packing order.[147] Combining these results suggests that polymer insertion is more difficult as the membrane becomes stiffer and more ordered. Therefore, one might hypothesize that in a living cell membrane, the polymer will preferentially insert into liquid-disordered domains.

As the lipid headgroup region is the first part of the bilayer that the polymer contacts, it is not surprising that it has a significant effect on polymer-lipid bilayer interactions. In POPC/POPG mixed bilayers (see Figure 1.1b for structures), as POPG content increases, the binding of F127 increases, which was attributed to hydrogen bonding between the POPG headgroup and the ether groups of the PEO/PPO units.[146] Additionally, if both lipid tails have a desaturation or if multiple desaturations are added, F127 binds more readily.[82] Most surprisingly, in mixed POPC (one unsaturation, $T_m = -2$ °C)/ DPPC (saturated, $T_m = 41$ °C) bilayers, the fraction of F127 chains bound has a non-monotonic relationship with DPPC fraction.[82] At low DPPC content, increasing the saturated component decreased binding until ~30 mol% DPPC at which point there is a significant increase with added DPPC content.[82] This could coincide with the onset of gel/fluid coexistence in the mixed bilayers.

1.5 Contributions of this thesis

In this thesis, I expanded the set of block polymer amphiphiles available as membrane stabilizers by developing a synthetic scheme for the preparation of bottlebrush PEO-PPO diblock polymers, which will be referred to as "bottlebrush poloxamers" (BBPs) in the rest of this thesis. Bottlebrush polymers consist of polymer side chains grafted onto a central backbone as shown by Figure 1.7. Bottlebrush polymers have an extensive parameter space, including the length of the side chains (N_{sc}), the length of the backbone (N_{bb}), and the spacing between side chains (N_g). Importantly, there are relationships between these parameters and properties of the molecule such as side chain flexibility,[148,149] persistence length,[150] shape,[151,152] and the ability to share space with other macromolecules.[153,154] Unfortunately, propylene oxide is vulnerable to side reactions during radical[155] and anionic polymerizations,[156,157] making the synthesis of BBPs non-trivial. Chapter 3 describes a scalable synthetic strategy that provides control over all the parameters mentioned above. Additionally, the micellization behavior of BBPs is compared to that of linear poloxamers in an aqueous environment.

As described in sections 1.3.3 and 1.3.4, the linear poloxamer parameter space has been extensively explored for improved membrane stabilizers. While significant mechanistic insights have been gained, little improvement over the efficacy of F68, the first-in-class molecule, has been obtained. Furthermore, due to its low molecular weight, F68 is cleared by the kidneys relatively quickly $t_{1/2} \sim 24$ h,[158,159] necessitating frequent injections to patients with muscular dystrophy. I hypothesized that the relationships between bottlebrush architectural parameters and polymer properties could be exploited to simultaneously gain mechanistic understanding of polymer-lipid bilayer interactions and realize more efficacious molecules. Chapter 4 presents a systematic study where the effects of BBP architectural parameters on polymer binding to POPC liposomes and cellular protection efficacy against osmotic stress were explored. This work culminated in understanding a likely membrane-bound BBP conformation, polymers with enhanced membrane affinity, and BBPs that outperform the first-in-class control in a cellular level *in vitro* osmotic stress assay and in a tissue level lengthening-contraction assay.

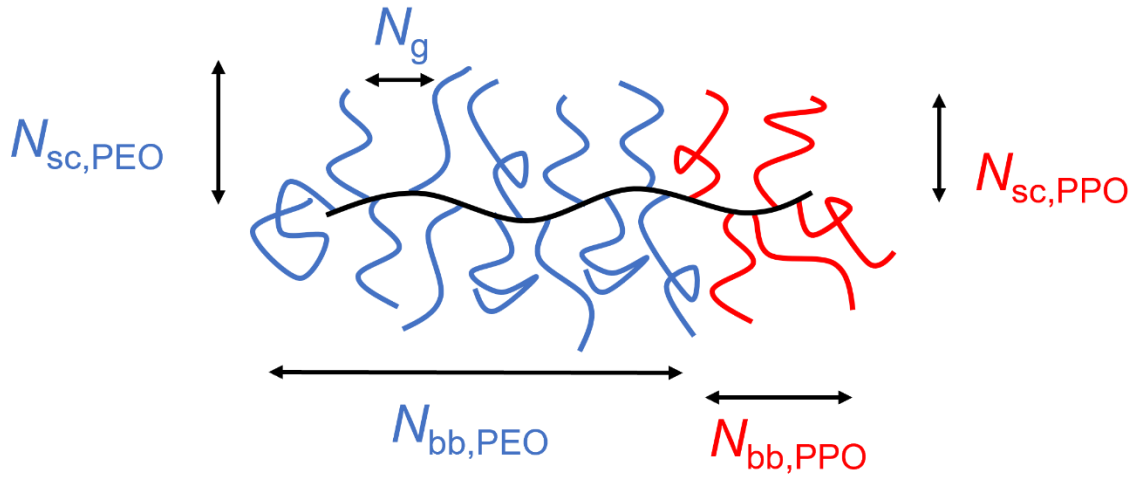

Figure 1.7: Sketch of bottlebrush poloxamer architecture and its architectural parameters.

The second major thrust of this thesis was to explore the effects of two potentially important differences between abiotic liposome models and the physiological condition: temperature and lipid phase coexistence. Due to the thermoresponsive character of poloxamers and the importance of the hydrophobic effect in

polymer-membrane binding events, temperature could have a significant impact on polymer-lipid bilayer interactions. Previous studies by our group and others have probed the stabilization and binding mechanisms of amphiphilic block polymers and lipid monolayers, bilayers, and liposomes; however, most of these studies have been done at a single temperature, often room temperature. While the findings of these studies are relevant and impactful, understanding the impact of temperature is important to accurately compare prior results done at different temperatures and to put mechanistic insights into context with the physiological temperature. I employed an established PFG-NMR binding assay to study the effect of temperature on polymer-lipid bilayer interactions over a range of polymer compositions and molecular architectures. I found that over a relatively narrow range of temperature, 27 °C (temperature of prior experiments by our group) and 37 °C (physiological temperature), the fraction of F127 chains bound to a POPC membrane increases by roughly an order of magnitude. Furthermore, the system exhibits a surprising time-temperature dependence, which is interpreted based on transport across the lipid bilayer.

Finally, as discussed in Section 1.2.2, lipid rafts play many important roles in cell membrane biology including regulating protein conformation and therefore cell signaling. Prior work by our group has explored the impacts of cholesterol, the lipid headgroup, and the lipid tailgroup exclusively in two-component liposome systems. While these systems co-exist as solid ordered (gel) and liquid disordered (fluid),[160] they are not the ideal model for lipid rafts. Instead, a model liposome that exhibits liquid-ordered/ liquid-disordered phase coexistence would more accurately represent the fluid nature of lipid rafts. This can be achieved using three-component models with cholesterol, a saturated lipid, and an unsaturated lipid. In Chapter 6, I constructed three-component liposomes of POPC/PSM/Chol (see Figure 1.1 for structures) over a range of compositions. This system was chosen because these components are abundant in mammalian cell membranes and it has a well characterized phase space.[47] I found a non-monotonic relationship between polymer binding and the mole fraction of the saturated lipid. Interestingly, binding is maximized over a window of the phase space where there is liquid-ordered/liquid-disordered co-existence, perhaps suggesting that the borders between these two phases present attractive binding sites. If this

suggestion is true, one might expect the polymer to play a role in regulating lipid rafts in cell membranes, possibly explaining how polymers impact such a diverse range of cell signaling pathways.

Chapter 2: Important experimental methods

2.1 Liposome extrusion

Liposomes of a controlled size and composition were prepared via extrusion through a polycarbonate filter with a defined pore size using a mini-extruder (Figure 2.1 - Avanti polar lipids). There are three steps to producing liposomes: form a lipid film with a desired mixture of lipids and cholesterol, hydrate this film in the desired aqueous solution, and then extrude this polydisperse solution of vesicles through a filter with the desired pore size.

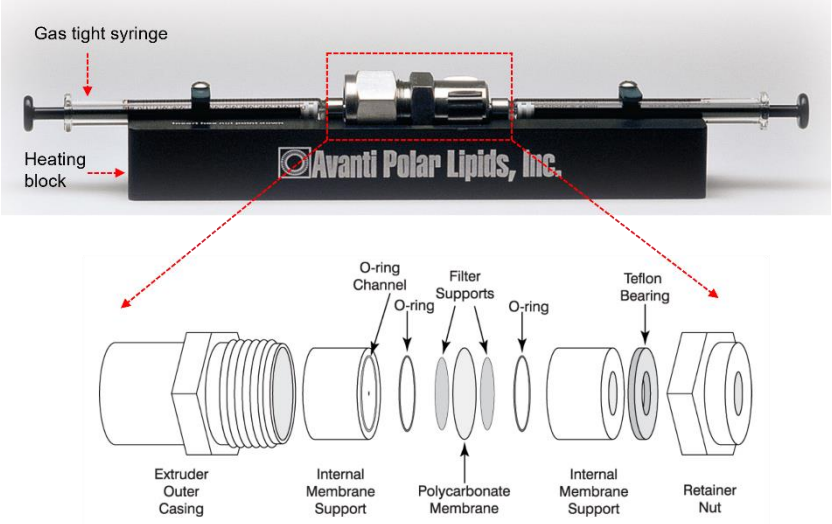

Figure 2.1: (Upper) Fully assembled Avanti mini-extruder setup used to prepare liposomes throughout this thesis. (Lower) Sketch of the mini-extruder setup with each part labelled. This figure was adapted from the Avanti website (https://tinyurl.com/t4n7nuss).

Chloroform solutions of 1-palmitoyl-2-oleoyl-glycero-3-phosphocholine (POPC), sphingomyelin (PSM), and cholesterol at known concentrations were mixed to control the composition of the liposomes. The lipids are dissolved as single molecules because chloroform is a good solvent for the tailgroup and headgroup. Then, the chloroform is slowly removed by flowing a filtered stream of N_2 over the solution as the vial is rotated. It is critical to remove all the chloroform to ensure the liposomes are stable, so the vial is then placed under high vacuum for

≥1 h. If chloroform is not removed, the bilayer is disrupted, and the liposomes destroyed within hours.

The second step in the protocol is hydrating the lipid film. This was done in H_2O, D_2O, aqueous buffers,[82] or sugar solutions,[94] depending on the experimental requirements. It is critical that hydration is done above the highest T_m in the lipid mixture, to ensure uniform hydration of all components and therefore a nearly uniform lipid composition across all vesicles in the solution. For POPC liposomes with and without cholesterol ($T_m = -2$ °C), this was done at room temperature on a vortex plate for at least one hour. If a higher T_m lipid such as DPPC ($T_m = 40$ °C) or PSM ($T_m = 41$ °C) was included in the formulation, then rapid cycles between a water bath at 50 °C and the vortex plate (30 s at each step) were performed (although a sonication bath with a controllable temperature would be a preferred method).

After hydration, the lipids exist as multi-lamellar vesicles with a very broad size distribution and variable numbers of lipid bilayers in each structure. The final step of the liposome protocol is to extrude this solution through a filter with a known pore diameter, which is 50 nm, 100 nm or 200 nm for experiments in this thesis. The mini-extruder is assembled from the components shown in Figure 2.1, and the manufacturers protocol were found online with the following link: https://tinyurl.com/t4n7nuss. First, a drop of the desired solvent is placed on the internal membrane supports, then a filter support is placed on top of this drop. One of the membrane + filter supports assemblies is placed into the extruder outer casing and the filter support is re-adjusted to be in the center of the membrane support and not overlapping with the O-ring. Then, a polycarbonate membrane of the desired pore diameter is gently placed on top of the filter support within the metal casing. Finally, the second filter support assembly is gently slid into the metal casing and the retainer nut + Teflon bearing are screwed onto the metal casing. It is best practice to run the desired aqueous solution through the extruder 4-6× to ensure there are no leaks in the system prior to extruding the vesicle solution. The volume of the mini-extruder is ~0.2 mL, so the first pass will appear to have a volume loss even when there is no leak. After hydration, the polydisperse vesicle

solution will have an opaque, milky appearance and during extrusion the solution becomes translucent with a slight blue tint due to the change in the size of the vesicles from ~1 μm to ~50−200 nm liposomes.

The quality of all liposome preparations was validated by dynamic light scattering (DLS). Section 2.2 will discuss the theory of DLS measurements, describe practical considerations and the methodology for liposomes, and present a representative dataset for high quality liposomes.

2.2 Dynamic Light Scattering

2.2.1 Dynamic light scattering fundamentals

Dynamic light scattering is a solution characterization technique that is commonly employed to measure the size distribution of suspended particles such as polymer micelles and liposomes.[35,85,87,109,161,162] A laser is shone through the sample and the intensity is recorded as a function of time, as shown in Figure 2.2. Within what looks like noise is encoded a characteristic timescale due to concentration fluctuations as individual particles diffuse in and out of the laser path.[163] If the relaxation mode is diffusive, a requirement for accurate particle sizing which were validated with a multi-angle measurement, the characteristic timescale $\tau_{diff} \sim (q^2 D_m)^{-1}$. Here, D_m is the mutual diffusion coefficient and q is the scattering vector which were calculated according to Equation 2.1:

$$q = \frac{4\pi n}{\lambda} \sin\left(\frac{\theta}{2}\right) \qquad \text{(Eq 2.1)}$$

where n is the refractive index of the solvent, λ is the wavelength of the laser, and θ is the angle between the incident laser and the detector. The mutual diffusion coefficient were estimated by calculating the correlation function $g_2(\tau)$ as a function of a differential time step (τ) from the data shown in Figure 2.2a via Equation 2.2 below:

$$g_2(\tau) = \frac{\langle I(t)I(t+\tau)\rangle}{\langle I(t)\rangle^2} \qquad \text{(Eq 2.2)}$$

where $I(t)$ is the measured scattering intensity at the given time. A sketch of the correlation function is shown in Figure 2.2b. At small values of τ relative to τ_{diff}, the particles have hardly moved so g_2

~ 1. This were visualized by the black and orange circles in Figure 2.2 which both reside on the same peak and hence are highly correlated. At large values of τ relative to τ_{diff}, the particle has diffused a large distance, randomizing its position, and the scattering intensity at $t + dt$ is equally likely to be above average as it is below average. Therefore, the numerator of Eq. 2.2 approaches zero, which is illustrated by the black and green circles in Figure 2.2.

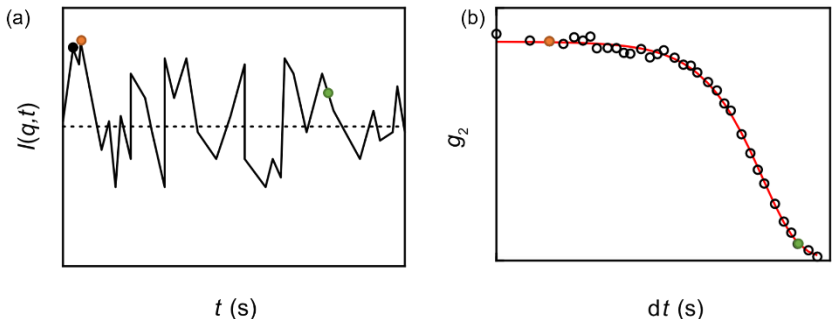

Figure 2.2: (a) Raw data of a DLS measurement is the scattering intensity as a function of time. (b) Illustration of the correlation function which is calculated from the data in Figure 2.2a. The short (black vs orange) and long (black vs green) time limits relative to the timescale of diffusion are illustrated to highlight how the correlation function is calculated. Figure adapted and used with permission from Andreas Mueller.

The important regime of g_2 is where it decays from the plateau at early differential times to zero. This decay is exponential in time, just like the solution to Fick's law describing the time decay of concentration fluctuations.[163] Therefore, by fitting g_2 to a function with an exponential form, one can estimate D_m. The most common fitting function for sizing particles with a uni-modal size distribution is the second cumulant model:

$$g_2(\tau)-1=B\exp[-\Gamma\tau+2k_2\tau^2] \qquad \text{(Eq. 2.3)}$$

where B is a fitting parameter controlling the height of the plateau and is of little consequence, Γ is a fitting parameter known as the 1st cumulant and is related to the mutual diffusion coefficient ($\Gamma = D_m$), and k_2 is fitting parameter known as the 2nd cumulant and is related to the breadth of the size distribution. In the dilute limit, the mutual diffusion coefficient is equal to the translational

diffusion coefficient, so Γ were related to the hydrodynamic radius (R_h) via the Stokes-Einstein equation:

$$R_h = \frac{k_B T}{6\pi\eta_s \Gamma} \quad \text{(Eq. 2.4)}$$

where k_B is Boltmann's constant, T is absolute temperature, and η_s is the solvent viscosity. Furthermore, the polydispersity of the particle size distribution were calculated from the ratio of the 1st and 2nd cumulants via Equation 2.5:

$$Đ = 1 + k_2/\Gamma^2. \quad \text{(Eq. 2.5)}$$

Another useful fitting function is the biexponential model which is often employed for particle size distributions that are expected to be bimodal such as micelles undergoing fragmentation[162] or coexisting micelles and unimers.[109] This model is given by Equation 2.6 below:

$$g_2(\tau) - 1 = B_1 \exp[-\Gamma_1 \tau] + B_2 \exp[-\Gamma_2 \tau] \quad \text{(Eq. 2.6)}$$

where B_i and Γ_i are the coefficient and 1st cumulant corresponding to the i^{th} population. To reduce the number of fitting parameters, the 2nd cumulant is often neglected in both exponents, therefore this function fits the decay to two delta functions, meaning the dispersity of both populations is neglected.

2.2.2 Practical considerations for DLS measurements

Since DLS measures the scattering intensity, dust contamination is a significant issue. If dust is present, there will be sudden spikes in the observed intensity and the calculation of the correlation function will be inaccurate rending it impossible to accurately fit g_2 to the models described above. Therefore, DLS samples must be filtered using a compatible filter with a pore diameter of 0.2−0.4 μm and placed into a clean, scratch-free tube; the outside of the tube should be wiped thoroughly prior to placing in the instrument.

Secondly, the sample must be dilute for two reasons: first, the rate of decay of g_2 is related to the *mutual* diffusion coefficient which can only be related to R_h if the solution is in the dilute limit

where $D_m = D_t$. Second, if the sample is too concentrated, then non-diffusive relaxation modes can contribute to g_2. For polymeric samples, one must always perform the experiment at ~10% of the critical overlap concentration. For liposomes or spherical particles, an upper bound of concentration is not straightforward to calculate and instead one should perform the experiment over a range of concentrations and see if R_h changes. Although R_h was estimated from a single DLS measurement, it is best practice to perform multiple measurements at different angles. Then, a plot of Γ vs q^2 were constructed which will be linear and have a y-intercept of zero if and only if the relaxation mode being observed is diffusive. The slope of this curve gives D_t.

When performing a DLS experiment on a new sample, it is informative to estimate the τ range that will encompass the relaxation rate of the particles. The timescale of the experiment depends on q and Dt. Since most light scattering instruments have a single incident wavelength, the scattering vector, q, is only a function of the angle range of the instrument and is typically limited from 0.005−0.05 nm^{-1}. After calculating the q range, one can estimate the particle size to determine a good starting point for the minimum and maximum τ values used in the experiment. A sample calculation is outlined in Example 9.5 of *Polymer Chemistry 3rd Edition.*[163] Practically, since a DLS measurement only takes minutes to acquire data at a given angle, one can hone in on an optimal q-range via trial and error until a plateau region is observed at small τ and at long τ, as were seen by the data presented in Figure 2.3a.

2.2.3 DLS method and representative data for POPC liposomes

After every preparation of liposomes, a DLS measurement was performed to confirm a narrow size distribution of the desired size.[88] The extruded liposome stock solution was diluted to 1.5 mg/mL POPC, filtered with a 0.2 μm wwPTFE filter into a clean, glass DLS tube (200 mm × 7 mm with an inner diameter of 5 mm). The outside of the DLS tube was wiped with acetone and dried with a stream of air prior to submerging into the refractive index matching bath (decalin). All liposome quality check experiments were performed at room temperature on a Brookhaven

BI-200SM instrument with a 637 nm laser. Autocorrelation functions (g_2) were collected at 60, 75, 90, 105, and 120° with a τ range of 1−100,000 μs.

A representative dataset and analysis for POPC liposomes extruded through a 50 nm diameter pore in D_2O is shown in Figure 2.3. Figure 2.3a shows the autocorrelation function data which were fit to the second cumulant model (Eq. 2.3). The residuals (data – model) for both fits are shown in Figure 2.3b to quantitatively compare the fit quality and choose the more suitable model. Small residuals and random the scattering about y=0 indicate a superior fit; however, it is important to note that adding terms to a model can lead to a "better" fit while simultaneously being less meaningful. In the absence of a demonstrably smaller or more random residual, one should always choose the simpler model – the one with fewer fitting parameters. As were seen in Figure 2.3b, the residuals of both fits are comparable in order of magnitude and randomness, therefore the 2nd cumulant model (gray circles) is more likely to represent the physical process being observed. Therefore, the size distribution of the liposomes is unimodal, and we can estimate the size and the polydispersity using Eq. 2.4 and Eq. 2.5, respectively. For the 90° measurement, the R_h = 44 nm and $Đ$ = 1.01. Thus, the size distribution is relatively narrow and is roughly consistent with the pore size used during extrusion. Since the lipid bilayer is malleable, it deforms as it passes through the pore, enabling it to be slightly larger than the pore dimensions. Finally, the linearity and y-intercept of the Γ vs q^2 relationship in Figure 2.3c demonstrates that the relaxation is diffusive, and the slope gives a more reliable estimate of the R_h = 44 ± 2 nm.

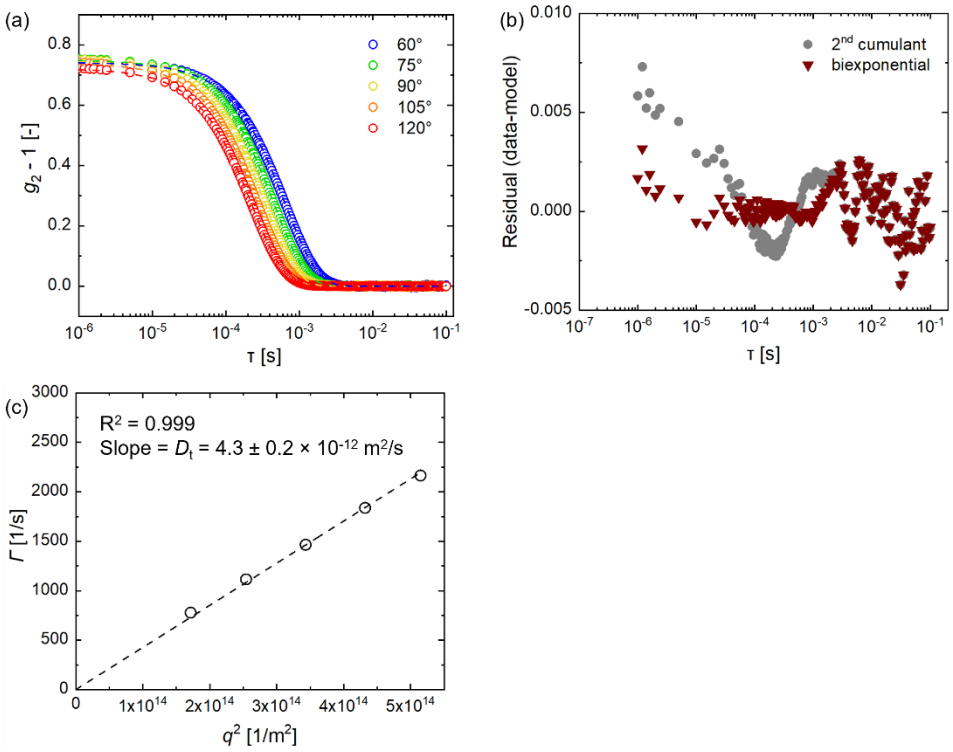

Figure 2.3: (a) Autocorrelation functions at 5 different detector angles, fit to the 2nd cumulant model. (b) Comparison of the residuals for the 2nd cumulant and biexponential models. (c) Relationship between Γ and q^2 to validate that a diffusive process is being observed.

2.3 Pulsed field gradient NMR (PFG-NMR) binding assay

2.3.1 PFG-NMR background

PFG-NMR is a 2-dimensional NMR spectroscopy technique where a gradient in the magnetic field strength is imposed along one axis of the sample to encode spatial information into the excited nuclear spins. A common pulse sequence is displayed in Figure 2.4a. The radio frequency channel "RF" is responsible for exciting the ^{1}H nuclei. The first 90° pulse is the same excitation that occurs in a standard ^{1}H NMR spectroscopy experiment, where the radio frequency pulse perturbs the spins from the ground state (nuclear spins aligned with the z-axis) to an excited state (in the x-y plane). This is followed by relaxation back to the ground state, which in a magnetic field, occurs at a characteristic frequency that is dependent on the chemical environment. As the spins relax, they lose their coherence in the x-y plane and the second pulse 180° helps to rephase them prior to signal acquisition to limit peak broadening. This type of pulse sequence is called a spin echo.[164]

The magnetic field channel "G" is responsible for encoding spatial information into the excited spins. During the first pulse of strength g and duration δ, the phases of spins are aligned according to their spatial location within the magnetic field gradient. Next, during the time between magnetic field pulses, Δ, the molecules diffuse freely in solution hence Δ is referred to as the diffusion time. Then, the second pulse in the magnetic field channel rephases the spins in the x-y plane prior to data acquisition. During the diffusion time, any motion parallel to the magnetic field gradient (typically the z-axis of the NMR tube) de-phases the excited nuclear spins, thereby preventing total rephasing and resulting in a loss of signal intensity. The signal intensity decay scales exponentially with pulse sequence parameters and the translational diffusion coefficient according to Equation 2.7:

$$\frac{I}{I_0}=\exp[-\gamma^2\delta^2 g^2\left(\Delta-\frac{\delta}{3}\right)D_t] \qquad \text{(Eq. 2.7)}$$

where I and I_0 are the observed intensity at the given magnetic field gradient strength and a strength of 0, γ is the gyromagnetic ratio of the nucleus (42.6 MHz/T for a ^{1}H), and g, δ, and Δ are the pulse sequence parameters described above.[85,87,88,165] Thus, by observing the rate at which a given NMR signal decays we can determine the rate of translational diffusion of the molecule(s) contributing to the given signal. PFG-NMR has been used to quantify drug solubilization into surfactant micelles,[166] to estimate drug entrapment into polymer nanoparticles,[167] and to quantify the lateral diffusion coefficient of several lipid components via solid-state NMR measurements.[168]

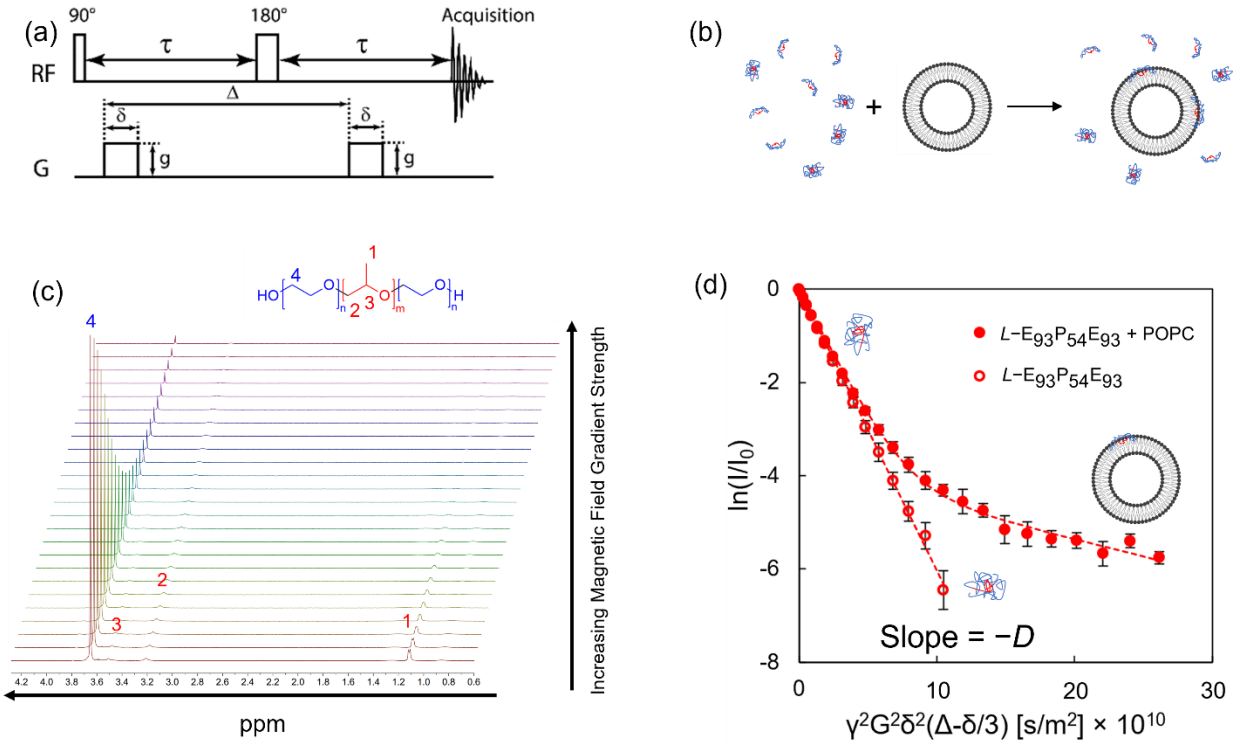

Figure 2.4: (a) An example PFG-NMR pulse sequence. Figure taken from Pages *et al.*[165] (b) Illustration of the polymer + liposome model system employed to estimate the membrane association of a polymer of interest. (c) 2-dimensional NMR dataset illustrating signal decay according to Equation 2.7. (d) Analysis of an example PFG-NMR data set corresponding to a mixture of 14 μM F127 + 875 μM POPC. The liposomes extruded through a 200 nm diameter pore. Figure 2.4d was adapted from Hassler *et al.*[88] and used with permission.

2.3.2 Example PFG-NMR dataset: F127 + POPC liposomes

PFG-NMR were used to quantify the fraction of polymer chains that adsorb to a liposome. Figure 2.4b shows a schematic of the system. A polymer of interest is mixed with liposomes and incubated for at least 2 hours, at which point a steady state is reached[85] where some fraction of chains are bound to the liposomes and some remain free in solution. Since the free linear polymer chains are roughly Gaussian coils, the R_h of the free state were estimated from the chain length. For poloxamers ranging from 5-20 kDa $R_{h,\ free\ chains}$ ranges from 2−4 nm. As discussed in Sections 2.1 and 2.2, the smallest liposomes used were extruded through 50 nm diameter pores and had $R_{h,\ liposome} = 44 \pm 2$ nm via a DLS measurement. Since the length scales of the bound polymer and free

polymer differ by an order of magnitude, we can detect two rates of diffusion by analyzing the decay of the signal intensity of an NMR peak corresponding to the polymer.

An example dataset is shown in Figure 2.4c. At low magnetic field gradient strengths, all signals are quite strong and then as the magnetic field gradient strength is increased, the signal decays until it is barely detectable. To quantify this data, only the PEO peak at ~3.7 ppm is integrated because it has the highest signal to noise ratio. The natural logarithm of the ratio of the integrals $\ln(I/I_0)$ is plotted as a function of $\gamma^2 g^2 \delta^2 (\Delta - \delta/3)$ as shown in Figure 2.4d. By examining Equation 2.7, when the data are plotted in this format, the slope of the relationship gives D_t. For the polymer-only control dataset (open symbols in Figure 2.4d), the data exhibit a linear relationship. This indicates that there is only one rate of signal decay and therefore one species in the solution, and the $R_h = 3.1 \pm 0.5$ nm, which is consistent with the estimate of F127 (L-$E_{93}P_{54}E_{93}$) if it were a Gaussian coil. For the polymer + liposome dataset (filled symbols in Figure 2.4d), there is clearly curvature which indicates that multiple species are present with distinct rates of diffusion. We can apply a sum of exponentials model described by Equation 2.8 to quantify the mol fraction of polymer chains in each state and the size of each state:

$$\ln\left(\frac{I}{I_0}\right) = \ln\left(\sum_i f_i \exp\left(-\gamma^2 \delta^2 G\left(\Delta - \frac{\delta}{3}\right) D_i\right)\right) \qquad \text{(Eq. 2.8)}$$

where all variables and parameters are the same as described in Eq. 2.7 except now f_i is the mol fraction of chains in state i and D_i is the corresponding translational diffusion coefficient. The F127 + POPC dataset shown in Figure 2.4d, was fit to a 2-term expansion of Eq. 2.8 "biexponential model" and $f_{bound} = 2.3 \pm 0.9$ mol% with an $R_{h,\ liposome} = 26 \pm 6$ nm.[88] Thus, F127 has a relatively low, but reliably quantifiable, membrane affinity under these conditions.

It is important to note that the R_h estimates from PFG-NMR and DLS are not in agreement. For the POPC liposomes used in the experiment reported in Figure 2.4d, the DLS validation suggested that $R_{h,\ liposomes} = 97$ nm with $Đ = 1.03$. There are two reasons for this apparent discrepancy. First, light scattering intensity scales with the radius of the scatterer to the 6th power; thus, the larger species in the size distribution scatter light much more intensely than the small

species, leading DLS to overestimate liposome size. Secondly, in an NMR measurement, the constrained motion of polymer adsorbed to the lipid bilayer surface increases the longitudinal relaxation time, causing broadening of the signal from polymer bound to larger species in the distribution.[20] Thus, the true liposome radius is intermediate to the estimates given by PFG-NMR and DLS and this was confirmed using cryo-TEM which will be discussed in Chapter 4.

2.3.3 PFG-NMR binding assay protocol and practical considerations

All PFG-NMR experiments were performed on a Bruker Avance III 500 MHz spectrometer with a 5 mm TBP triple-resonance PFG probe. The ledbpg2s pulse sequence was applied for all experiments. This pulse sequence minimizes eddy currents that were induced by the magnetic field gradient pulses, therefore minimizing the effects of inhomogeneities.[169] For all PFG-NMR experiments in this thesis, 25 spectra were collected over a range of gradient field strengths varying linearly from 2−95%, each with 32 scans, an acquisition time and delay time of 1 s, a gradient pulse duration (δ) of 5 ms, and a diffusion time (Δ) of 700 ms. The total experiment time for this sequence is ~37 minutes. Polymer and liposomes were incubated for a minimum of 2 hours prior to PFG-NMR data acquisition to ensure a steady state was reached.

It is important to choose these parameters carefully as they are sensitive to the system of interest. The number of scans is chosen to by trial and error until a sufficiently high signal to noise ratio is achieved to give reliable integration of the NMR signal. As polymer concentration is reduced, the number of scans required should be increased to compensate if necessary. It is important to note that signal to noise scales with the square root of the number of scans, so increasing the number of scans can only yield so much benefit before it becomes prohibitively time consuming. The acquisition time (AQ) and relaxation delay (D1) parameters follow the same guidelines as for a standard NMR experiment: $AQ + D1 > 3T_1$ where T_1 is the transverse relaxation time which is dependent on the signal being observed and were measured via an inversion recovery experiment.[164] The linear ramp of the magnetic field gradient strength from 2−95% is general and

should work for any sample. Perhaps the most important parameters to optimize to collect good PFG-NMR data are δ and Δ which depend on the sizes of the species in the sample. For an accurate fit to the sum of exponentials model, it is critical that there is at least ~90% signal attenuation between the 2% and 95% gradient strength spectra. Therefore, prior to running the ledbpg2s sequence with a given set of δ and Δ, it is imperative to perform a ledbpg2s1d (same pulse sequence but only 1 of the FIDs is collected at the specified value of g) experiment at g = 2% and g = 95%. Then overlay the 2% and 95% spectra and if there is less than ~90% signal attenuation, increase δ and/ or Δ. An SOP, written by Letitia Yao who was the former director of the NMR lab at the UMN, describing this parameter optimization were found in Appendix A.

Finally, when performing PFG-NMR experiments on mixtures of components that interact, such as polymers and liposomes, it is important to perform control experiments on the individual components. In the polymer + liposome systems this is important for two reasons. First, the polymers can form micelles when above the CMC or CMT. This introduces another rate of diffusion, complicating the sum of exponentials model. If two populations differ in Rh by a factor of ~2, they were resolved as distinct populations. Therefore, it is possible to fit the PFG-NMR data to a 3-term expansion of Eq. 2.8; to account for free chains, micelles, and polymer bound to liposomes. In this case, the polymer-only control is valuable because it informs the model choice and were used to constrain the diffusion coefficients, thereby reducing the number of free parameters from 5 to 3, greatly improving the accuracy of the fitting protocol. More details on this fitting procedure will be given in Chapter 4.

2.4 *in vitro* osmotic stress protection assay

2.4.1 Motivation

High-throughput screening techniques have been instrumental in understanding cell-material interactions across a range of different materials including proteins and polymers. High-throughput is ambiguous, as the magnitude of the number of distinct molecules that were screened varies from hundreds to beyond billions depending on the type of molecule being screened and the type of

experimental technique employed. For example, a library of millions of distinct proteins were expressed on the surface of yeast cells or inside a bacterial host cell, introduced to a target or substrate of interest, and then techniques such as flow cytometry,[170,171] fluorescence assays,[171] or depletion assays[172,173] were used to evaluate relationships between protein sequence and binding affinity, protein stability, or antimicrobial potency respectively. Since synthetic polymers cannot be encoded using DNA, instead requiring each variant to be independently synthesized, libraries are much smaller. However synthetic polymers do still have an extensive parameter space as molecular weight, composition, concentration, end-group, and architecture can influence behavior in biological systems. Thus, techniques to rapidly span a given parameter space and then probe the desired metric of cell-material interactions are of great value.[174,175,176,177]

To screen poloxamers and their architectural variants, Kim and co-workers developed an osmotic stress assay that can screen ~100 conditions in a single day.[6] A schematic of the assay is shown in Figure 2.5, and the specific protocol is described in Section 2.4.2. C2C12 myoblast cells, which are mouse muscle stem cells, were chosen because they are a fair proxy for human skeletal muscle cells at a pre-clinical stage, and they are relatively easy to culture. These cells adhere to the surface of the well, enabling the supernatant to be extracted and replaced. The cells are subjected to a cycle of buffers with varying salt content to impose an osmotic stress across the cell membrane. During the hypotonic step, the cell expands as water rushes into the cytoplasm to equilibrate the osmotic pressure. This stretches the cell membrane, imposing stress. If the membrane is damaged during this step, intra-cellular macromolecules such as enzymes and proteins leak out into the supernatant. To quantify the membrane permeability, the concentration of lactate dehydrogenase (LDH), an enzyme necessary for metabolism, in the supernatant is quantified by enzymatic colorimetry. Although the damage to the membrane occurs during the hypotonic step, maximal LDH release is observed during the isotonic recovery step because in this step the net flow of solution is out of the cell. Therefore, the isotonic recovery step has the highest signal-to-noise ratio and is used in all analysis in this thesis.

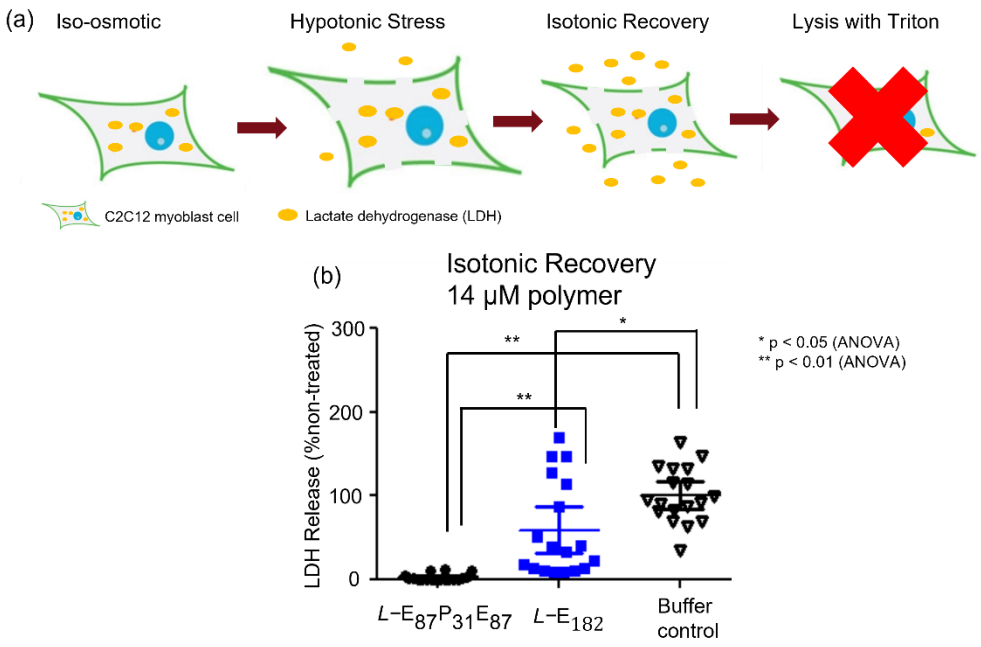

Figure 2.5: (a) Schematic of the *in vitro* osmotic stress screening assay for the ability of a polymer treatment to prevent an increase in membrane permeability. (b) Example dataset for the first-in-class control, F68 (*L*-$E_{87}P_{31}E_{87}$) and a PEO homopolymer with a similar molecular weight (*L*-E_{182}). Statistical comparisons were made using a one-way ANOVA with Tukey's post hoc test.

2.4.2 Protocol and an example dataset

C2C12 myoblast cells were seeded into a 96-well plate and cultured in growth media (79% Dulbecco's modified Eagle's medium, 20% fetal bovine serum, 1% penicillin-streptomycin) to ~70% confluency. Cell morphology was checked via optical microscopy prior to all experiments to ensure cells remained independent, spherical myoblasts. Myoblast to myotube (tubular morphology with poorly resolved cell boundaries) differentiation can occur at high confluency and would fundamentally change the cellular system under study. Then, the growth media was removed and replaced with 100 μL of an isotonic buffer solution that was pH adjusted to pH = 7.2 (330 mOsm; 140 mM NaCl, 5 mM KCl, 2.5 mM $CaCl_2$, 2 mM $MgCl_2$, and 10 mM HEPES). After 30 minutes at this initial iso-osmotic condition, the supernatant was collected, stored, and replaced with an equal volume of a hypotonic buffer solution (pH = 7.2; 75 mOsm; 20 mM NaCl, 5 mM KCl, 2.5 mM $CaCl_2$, 2 mM $MgCl_2$, 10 mM HEPES). The hypotonic step lasts for 50 minutes and

then supernatant is collected, stored, and replaced with the same isotonic buffer solution as the first step. This isotonic recovery step lasts for 30 minutes, then the supernatant is collected, stored, and replaced with a 1% solution of Triton X-100. Cells are treated with the Triton solution for 50 minutes to ensure complete lysis and therefore total LDH release, prior to collection of the supernatant. Since all the LDH is released in every well, we can normalize the LDH release of each step to the total LDH release, to account for slight differences in cell number well-to-well. After each solution exchange, the cells were returned to a cell culture incubator at 37 °C and 5% CO_2. During this assay, the polymer is dissolved in both the isotonic and hypotonic buffer solutions. Thus, the polymer is present in the first three steps of the assay and notably is introduced 30 minutes prior to the hypotonic stress.

The concentration of LDH in each of the four supernatant solutions (initial isosmotic, hypotonic, isotonic recover, and Triton X-100) was then quantified using an LDH assay kit (Pointe Scientific Inc.). The kit contains solutions of nicotinamide adenine dinucleotide NAD^+ and L-lactate which are combined with a small volume of the supernatant solution. The LDH in the supernatant catalyzes the reduction of NAD^+ to NADH, which absorbs light at 340 nm. A spectrophotometer was used to measure the absorbance over time for 120 minutes. The concentration of LDH in the supernatant can then be calculated from the slope of the absorbance vs time data.

An example dataset is shown in Figure 2.5b. Here, the three conditions are 14 μM F68 (*L*-$E_{87}P_{31}E_{87}$; M_n = 9400 g/mol $Đ$ = 1.19) the first-in-class control and most ubiquitous polymer in the membrane stabilizing field, 14 μM of a PEO homopolymer with a similar molecular weight (*L*-E_{182}; M_n = 8000 g/mol $Đ$ = 1.06), and a positive control that receives the same cycle of buffers except no polymer is present. The y-axis is normalized to the average of all replicates of the positive control, so the positive control is 100% LDH release by definition. Because of this normalization, if any well has more LDH released than the average of all the buffer controls, it will have > 100% LDH release. If a polymer has a protective effect, the LDH release will be

significantly lower than the positive control. Based on the data in Figure 2.5b, both F68 and *L*-E_{182} have a substantial protective effect at 14 μM. Furthermore, F68 is significantly more protective than *L*-E_{182}, suggesting that the PPO block leads to improved protection efficacy. This experiment were repeated over a series of polymer concentrations to determine the concentration at which the polymer treatment no longer leads to significantly less LDH release than the positive control.[6,88,178]

Chapter 3: Synthesis and characterization of bottlebrush poloxamers

This chapter was adapted from Hassler, J.F.; Van Zee, N.J.; Crabtree, A.A.; Bates, F.S.; Hackel, B.J.; Lodge, T.P. "Synthesis and Micellization of Bottlebrush Poloxamers." *ACS Macro Letters.* 2022, 11, 460-467.[109]

3.1 Motivation for developing bottlebrush poloxamers (BBPs)

Block polymer amphiphiles in aqueous environments assemble into diverse micelle and vesicle morphologies,[179,180] with applications in numerous fields including pharmaceutical delivery[181,182] and as nanoreactors.[183] Additionally, single chains or unimers interact with phospholipid bilayers in therapeutically relevant ways, ranging from membrane solubilization to stabilization.[6,85,143,184–187]

Poloxamers are a specific class of linear block polymer amphiphiles containing poly(ethylene oxide) (PEO) and poly(propylene oxide) (PPO) blocks that are commercially available (e.g., Pluronics®), biocompatible, and have demonstrated efficacy as cell membrane stabilizing agents against many types of stresses.[6,9,69,126,188] A range of prior studies have focused on the mechanisms of poloxamer-lipid interactions; however, a complete picture of the stabilization mechanism is still lacking.[13,17,146,189–191,66,70,73,80,81,83,86,137] Amphiphilic bottlebrush polymers have potential as a tool to yield additional mechanistic insights, through architectural variation. As shown by Figure 1.7, bottlebrush polymers have multiple parameters to tune (e.g., backbone length N_{bb}, side chain length N_{sc}, and spacing between side chains N_g) and aspects of the relationships among these parameters and molecular properties such as segmental dynamics,[148,192,193] molecular shape,[152] and ability to share space,[149,194–196] are understood. Thus, a synthetic platform that enables bottlebrush block polymers with PEO and PPO side chains, "bottlebrush poloxamers (BBPs)," with control over molecular parameters could enable pursuit of many structure-function hypotheses across a variety of fields.

Synthesis of BBPs is challenging due to side reactions that can occur due to the PPO units. Controlled radical polymerization can produce grafted PPO polymers; however, these methods require low monomer conversion or low grafting density to maintain modest dispersities.[182,197–201] In this chapter, I will disclose a novel synthetic route to PPO-containing BBPs that circumvents these challenges and gives more control over parameters such as graft length and graft density. I will then examine the micellization behavior of a set of BBPs to understand the relationship between the critical micellization concentration (CMC) and the total molecular weight. The resulting scaling relationship provides a comparison of the thermodynamic drive towards micellization between the bottlebrush and the chemically analogous linear architecture. Finally, I will assess how the bottlebrush architecture affects the glass transition and crystallization of the PEO block as a function of the side chain length.

3.2 BBP synthesis scheme and validation

The synthetic route to BBPs is shown in Figure 3.1. Living anionic polymerization followed by chain end modification was used to make norbornene (NB)-functionalized macromonomers (MMs), which were then polymerized sequentially via ring opening metathesis polymerization (ROMP). ROMP has successfully been combined with living polymerization strategies such as anionic, RAFT, and ATRP and is compatible with PEO.[202–205] This strategy has several advantages. First, anionic polymerization can yield low dispersity PEO and PPO polymers of a targeted molecular weight with well-defined α-chain ends.[6,206,207] Second, ROMP of NB macromonomers reaches >99% conversion within min. Third, ROMP avoids chain transfer/coupling side reactions that are often observed during radical polymerization, to which PPO macromonomers are vulnerable due to the abstractable proton on the tertiary carbon site of every repeat unit.[155] Together, these advantages enable high-throughput synthesis of high molecular weight, high grafting density, low dispersity BBPs, with control over graft length and graft end-group. The nomenclature adopted for the BBPs is $B\text{-E}^{N_{sc}}_{N_{bb}}\text{P}^{N_{sc}}_{N_{bb}}$ where B indicates the

bottlebrush architecture, E the PEO block, P the PPO block, and N_{sc} and N_{bb} are the side chain and backbone number average degrees of polymerization, respectively.

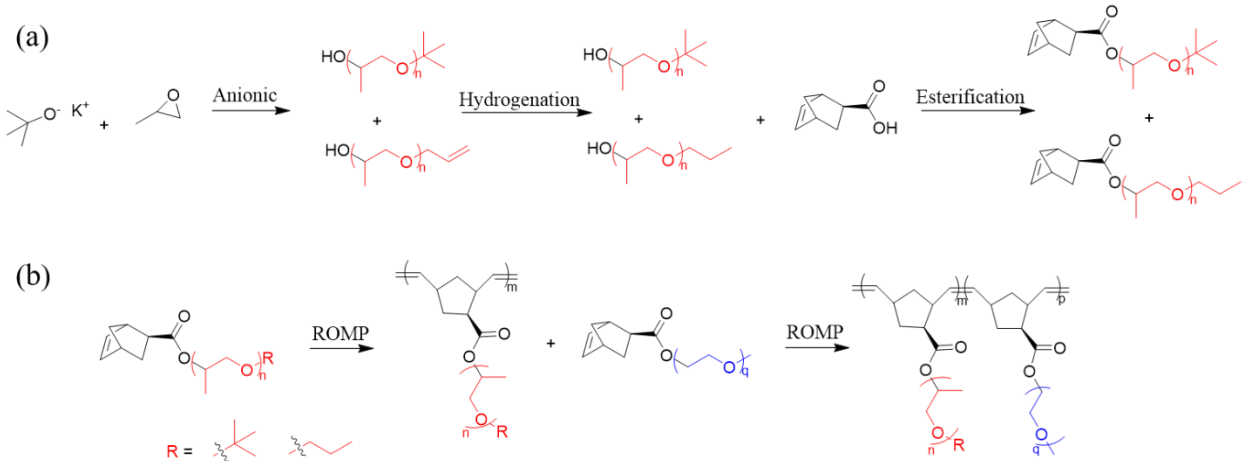

Figure 3.1: Reaction scheme to synthesize bottlebrush poloxamers. (a) Anionic polymerization was initiated with potassium *tert*-butoxide and ran to full conversion at 25 °C in the presence of 18-crown-6 ether. Hydrogenation was achieved over palladium on carbon. Esterification used a 50% molar excess of norbornene-carboxylic acid and was facilitated by DIC and DMAP. (b) Sequential ROMP was performed using Grubbs 3rd generation catalyst.

The black trace in the bottom-half of Figure 3.2a shows matrix-assisted laser desorption/ ionization mass spectrometry (MALDI) spectra of the PPO product from anionic polymerization. Notably, there are two populations with peak spacings of 58 g/mol, indicating that both are PPO. The more intense family of peaks is the desired product, with a *tert*-butyl α-chain end and an alcohol ω-chain end (*t*-PPO-OH). The family labelled with blue squares is an impurity with an alkene α-chain end, arising from chain transfer to monomer or polymer side reactions due to the acidity of the PPO methyl groups.[156] This assessment is confirmed by ^{1}H nuclear magnetic resonance (NMR) spectroscopy, as shown by the red spectrum in Figure 3.2b. We employed established methods to limit this side reaction using 18-crown-6 and a relatively low temperature (25 °C),[156,207] but from NMR roughly 7 mol% of the chains have this impurity. We hypothesized

that this alkene impurity would be susceptible to cross-metathesis during ROMP, leading to high dispersity polymers with limited control over molecular weight.[208] Thus, we performed a post-polymerization hydrogenation to eliminate this alkene impurity. The MALDI spectra in Figure 3.2a show a 2 g/mol increase in molecular weight for each of the peaks identified in the alkene chain end population, blue squares to green circles, which indicates that 2 hydrogen atoms were added across the double bond, hence this chain end modification was successful without changing the molecular weight distribution. Furthermore, in the ^{1}H NMR spectrum presented in Figure 3.2b, the alkene chain end peaks labeled a, b, and c in the pre-hydrogenation polymer disappear after hydrogenation.

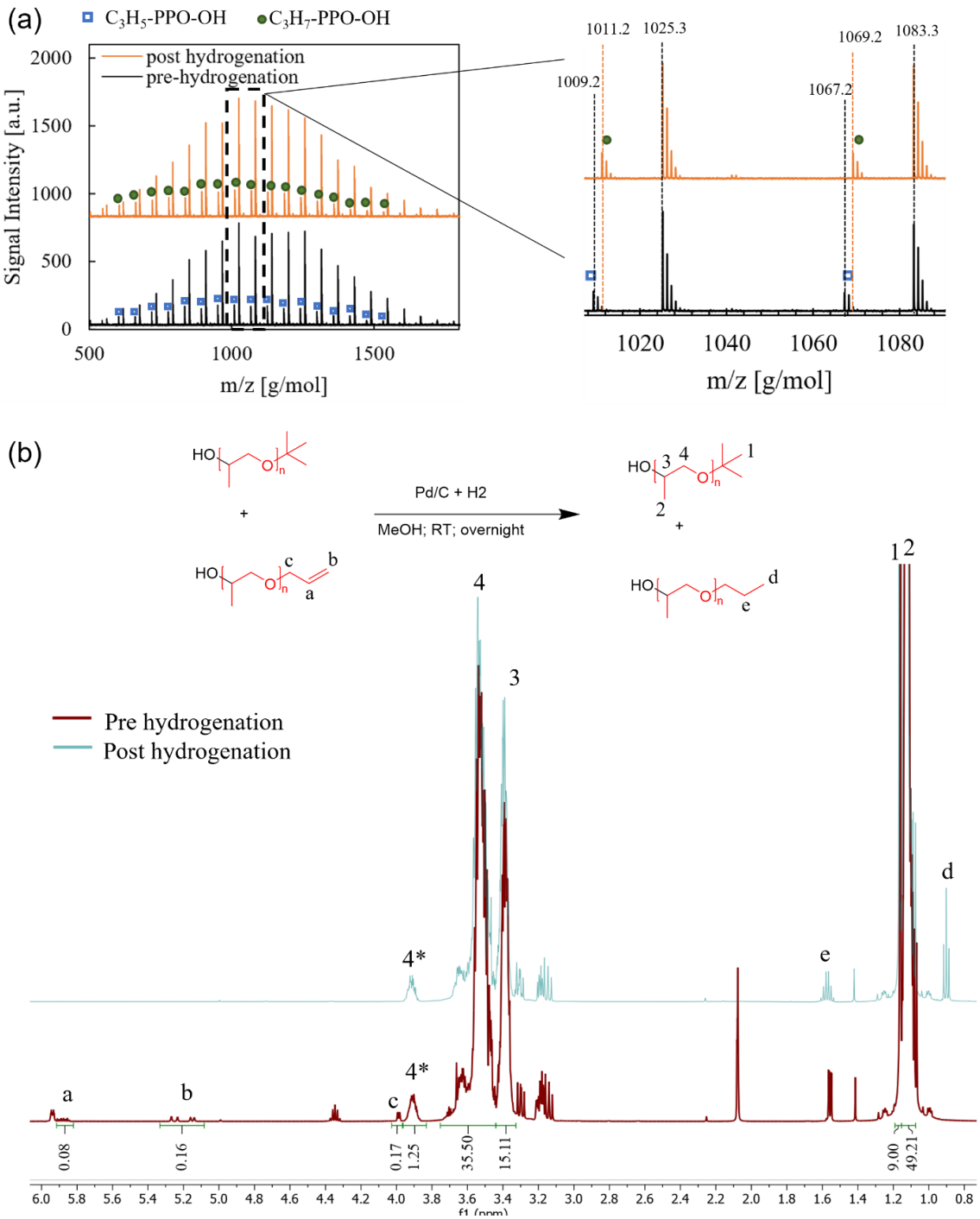

Figure 3.2: (a) MALDI-ToF data of PPO polymer as synthesized via anionic polymerization (black) and post hydrogenation (orange). M_w = 1220 g/mol and $Đ$ = 1.12 for both polymers. The most intense family of peaks in both samples is *tert*-butyl-PPO-OH (*t*-PPO-OH) and is unchanged during hydrogenation. Alkene and alkane α-chain end impurities are labelled accordingly. (b) ^{1}H NMR of PPO polymer pre (red) and post (teal) hydrogenation. The alkene chain end peaks a, b, and c disappear after hydrogenation.

The final step of MM preparation was to convert the ω-alcohol to an NB-ester by modifying an existing esterification protocol[181,209] for the PPO chemistry. Figure 3.3a shows a close-up of the MALDI spectrum to highlight the peak shifting after chain end modification; the full spectrum can be found in Fig. 3.8. The blue triangle population, present as the majority in the starting material (black spectrum) and a minority in the product (blue spectrum), is *t*-PPO-OH. After esterification, this population shifts by +4 g/mol in *m/z* (yellow stars). Adjacent peaks do not have the same degree of polymerization, thus the expected peak shift after an end-group modification is the difference in molecular weight of the end-groups minus an integer multiple of the repeat unit molecular weight. For the NB-ester replacing an alcohol endgroup of a PPO polymer, a +4 g/mol shift in *m/z* confirms successful conjugation with the NB functional group. A similar shift, +6 g/mol, occurs between the blue square and yellow circle populations, which correspond to the alkene-PPO-OH and alkane-PPO-NB, respectively. Note the black trace is from the material prior to hydrogenation while the blue trace is post-hydrogenation and esterification. Fig. 3.8c shows size exclusion chromatography (SEC) traces of the *t*PPO-OH starting material and the functionalized MM, and the molecular weight distributions are identical. ^{1}H NMR spectroscopy was used to assess the purity of the resulting polymer and to corroborate successful chain end modification. The peak shape and integration of the alkene multiplet at 6.09-6.24 ppm (Figure 3.3b) suggests that 95 mol% of the NB is on a polymer chain end.[210] Excess NB-carboxylic acid was needed to achieve high conversion and was removed by vacuum drying at 50 °C for 7 days. The NB-carboxylic acid could not be removed using chromatography, precipitation, or dialysis due to similar solvent/ stationary phase interactions as PPO and the small molecular weight of the PPO. We deemed this level of purity to be acceptable, but there will be some incorporation of NB-carboxylic acid in the polymer backbone. When accounting for the small molecule (~5 mol%) and the alkane ω-end-group (~7 mol%) impurities in the analysis of the integral values of the NB peaks (6, 7, 8), which were referenced to the *t*-butyl peak (1), we conclude that quantitative conversion of alcohol to NB at the ω-end-groups was achieved. A similar protocol was used to synthesize a

NB-functionalized MM from a commercial methyl ether PEO (M_n = 1970 g/mol, $Đ$ = 1.04). MALDI and ^{1}H NMR characterization are shown in Fig. 3.9.

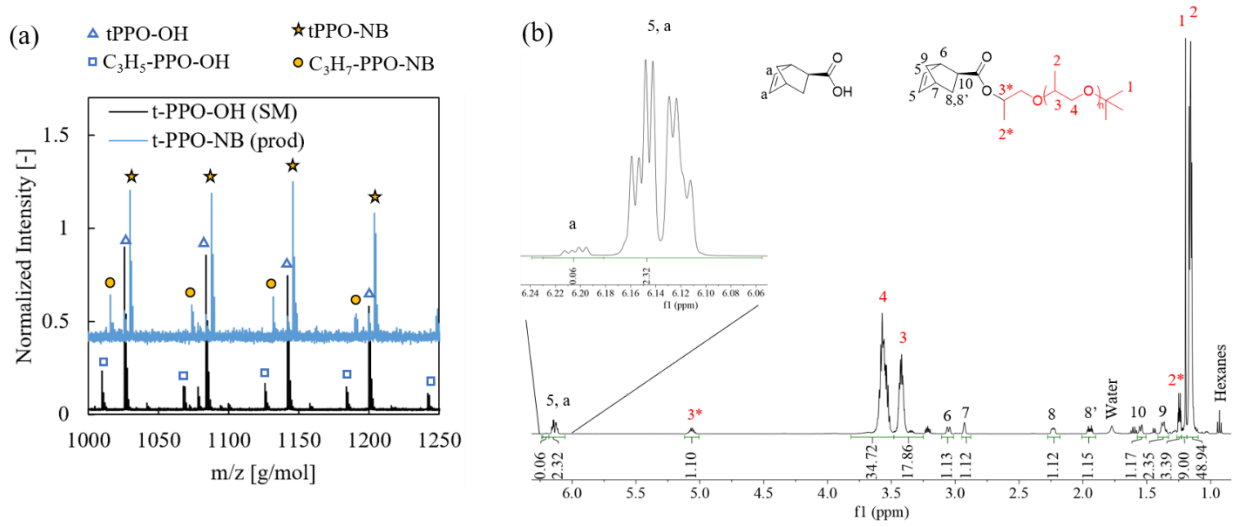

Figure 3.3: (a) MALDI of *t*-PPO-OH and the NB functionalized macromonomer, *t*-PPO-NB, following the hydrogenation and esterification reactions. M_w = 1210 g/mol and $Đ$ = 1.12 for the SM and M_w = 1330 g/mol and $Đ$ = 1.14 for the product. (b) ^{1}H NMR spectrum of the *t*-PPO-NB macromonomer.

After synthesis of the MMs, sequential ROMP afforded a grafted polynorbornene diblock polymer, where one block has PEO side chains and the other PPO sidechains. To our knowledge, this is the first report of a bottlebrush PEO-*b*-PPO polymer. The representative SEC traces in Figure 3.4a show that both the PPO block and the diblock have low dispersities, achieve the target molecular weight, and shift systematically to shorter retention times for higher M_n. The ^{1}H NMR spectrum in Fig. 3.11b shows complete conversion of the monomeric NB alkene peaks to backbone alkene peaks, confirming that the reaction achieved full conversion of monomer. To our knowledge, this is the first report of a grafted PPO polymer where the macromonomer was fully consumed, making synthesis of multi-blocks possible. SEC traces and ^{1}H NMR spectra for all polymers discussed in this chapter are shown in Figs. 3.10-3.12.

Finally, the importance of the hydrogenation step of the PPO macromonomer is highlighted by Figure 3.4b. As stated above, we hypothesized that the alkene α-chain end impurity would lead to cross-metathesis and a poorly controlled polymerization. To test this hypothesis, we reserved a small amount of the *t*-PPO-NB macromonomer and attempted a ROMP reaction. By skipping the hydrogenation step, the ~7 mol% alkene chain end impurity was present during the ROMP reaction. Figure 3.4b shows an SEC trace of the resulting bottlebrush PPO polymer which has a $Đ$ = 2.62 and overshot the targeted molecular weight, confirming that without the hydrogenation step the ROMP reaction is not well controlled.

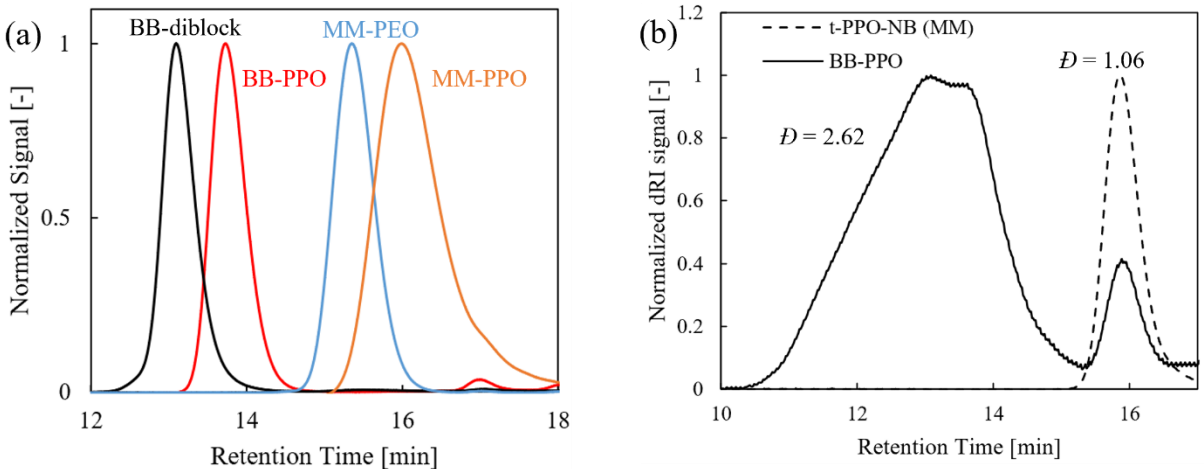

Figure 3.4: (a) SEC traces with differential refractive index detection of a representative sequential ROMP polymer *B*-$E_{21}^{43}P_{11}^{15}$. The macromonomer traces are included for reference. From the multi-angle light scattering detector, the BB-PPO aliquot has a M_w = 11,600 g/mol and $Đ$ = 1.20 and the BB-diblock has a M_w = 55,300 g/mol and Đ = 1.10, both were within error of the targeted molecular weight. The small peak at ~17 min in the BB-PPO chromatogram is likely a small molecule impurity in the PPO macromonomer, possibly 18-crown-6, that does not impact the subsequent polymerization. (b) SEC trace of the tPPO-NB macromonomer without the hydrogenation step and the resulting BB-PPO product from ROMP.

3.3 Effect of bottlebrush architecture on micellization in water

To understand the effect of the bottlebrush architecture on micellization behavior, we synthesized three BBPs with constant side chain lengths and similar compositions (70-80 wt%

PEO), with total molecular weights ranging from 26 kDa to 394 kDa. All materials had narrow molecular weight distributions ($Đ$ < 1.15), and the characterization data are summarized in Table 1. Micelle solutions were prepared via direct dissolution in aqueous buffer and were equilibrated at 37 °C for at least 24 h. The CMC_a and hydrodynamic radius (R_h) were determined via dynamic light scattering (DLS). DLS measures the diffusive relaxation of concentration fluctuations in dilute solution, which yields the particle size distribution by analyzing the correlation function via cumulant analysis or inverse Laplace techniques such as regularized positive exponential sum.[162,211–213]

Table 3.1: Materials characterization and micelle data summary

Polymer	M_n[a] [kDa]	$Đ$[a]	wt% PEO[a]	wt% NB[a]	CMC [mg/mL][b]	R_h [nm][c]	R_{core} [nm][d] (calc)	R_{core} [nm][e] (expt)
L-E_{455}	20.0	1.10	100	0	N/A	-	-	-
L-$E_{76}P_{29}E_{76}$ (F68)[f]	8.4[f]		80[f]	0	70 ± 10[f]			
L-$E_{103}P_{39}E_{103}$ (F88)[f]	11.4[f]		80[f]	0	6 ± 0.9[f]			
L-$E_{132}P_{50}E_{132}$ (F108)[f]	14.6[f]		80[f]	0	0.4 ± 0.1[f]			
B-$E_{10}^{43}P_{5}^{15}$	26.2	1.07	72	8	8 ± 3	17 ± 4	5	6 ± 1
B-$E_{21}^{43}P_{11}^{15}$	55.3	1.10	74	8	2 ± 0.5	25	8	
B-$E_{168}^{43}P_{43}^{15}$	394	1.15	80	7	0.4 ± 0.1	150	30	15 ±8
B-$E_{54}^{10}P_{8}^{15}$	40.9	1.09	62	20	1 ± 0.4	18	6	

[a]SEC with multiangle light scattering detection. [b]Determined by DLS. [c]DLS data reported for 10 mg/mL solution using the second cumulant model. The error is the standard deviation of three independent replicates. [d]Model described in Figure 3.21: sum of core forming block backbone contour length and twice the radius of gyration of its side chains. [e]cryo-TEM. [f]Data from Alexandridis *et al*. measured via the fluorescent dye method.[97]

To estimate the CMC_a, we analyzed the excess scattering intensity ($I_{ex} = I - I_{solvent}$) as a function of polymer concentration.[112,214] Because I_{ex} scales with the product of the concentration of scatterers (c) and the size of the scatters (M), the concentration at which I_{ex} increases relative to the control (linear PEO homopolymer with M_n = 20 kDa which cannot form micelles) indicates aggregation (Figure 3.5a). To ensure that the aggregates were micelles, we performed cryo-transmission electron microscopy (TEM) on the smallest and largest BBPs. A representative micrograph of the largest polymer is shown in Figure 3.5b, which clearly demonstrates a core-

corona structure. Micrographs of the smallest polymer clearly show a core, although the corona block is too short to be observed. Additional micrographs are shown in Figs. 3.13 and 3.14.

On qualitative inspection of Figure 3.5a, as M_n increases, the CMC_a decreases. Quantitative analysis is challenging because micellization is not a phase transition; therefore, a precise CMC_a is difficult to extract and is sensitive to the method employed.[100, 215] A representative CMC_a was taken as the intersection of two logarithmic fits: one at low polymer concentrations, and one at high polymer concentrations, representing the free chain and micelle regimes, respectively. The error is estimated as the difference in the CMC_a when the number of data points in the micelle regime is increased by 1. To ensure these CMC_a estimates are representative, we also fit the DLS data to a closed association model,[100,216] which includes the CMC_a as a fitting parameter (Fig. 3.15). Consistent trends were observed with both methods.

The relationship between M_n and CMC_a for 80 wt% PEO linear poloxamers[97] and 72-80 wt% PEO BBPs are shown in Figure 3.5c. The free energy of a micelle is the sum of the core-corona interfacial energy, the energy of chain deformation, and the entropy of mixing between solvent and corona units. The closed association model asserts that above the CMC_a there is an equilibrium between unimers ([unimers] = CMC_a) and micelles of a constant size. Minimization of the total free energy of the system (micelles, unimers, and solvent) yields an exponential scaling between the CMC_a and M_n.[100,112,217,218] Therefore, the data are fit to an exponential form as shown in Eq. 3.3.1.

$$CMC_a = A \times e^{-\alpha M_n} \qquad \text{(Eq 3.3.1)}$$

Strikingly, the coefficient in the exponent of the fit (slope in Fig. 3.5c) is two orders of magnitude smaller in the bottlebrush case than in the linear case. Because $\alpha \sim \chi$, the Flory-Huggins interaction parameter, the reduced scaling coefficient suggests a decreased degree of solvent-core incompatibility, and therefore reduced thermodynamic driving force for micellization, in BBPs compared to linear poloxamers. One explanation for this is that the PPO units near the hydrophobic NB backbone are relatively dehydrated in the unimer state. Thus, some of the entropic gain in the

solvent upon dehydrating PPO in going from unimer to micelle is lost. Additionally, a BBP with $M_n \sim 400$ kDa has a comparable CMC_a to a linear poloxamer with $M_n \sim 14$ kDa, which is consistent with a recent molecular dynamics result.[219] This finding is of practical significance because in BBPs the CMC_a is less sensitive to molecular weight, enabling synthesis of vastly higher M_n materials that will exist as unimers in aqueous solutions.

This reduction of α for BBPs compared to linear poloxamers cannot be explained by the hydrophobic backbone. If the added hydrophobicity of the backbone were a significant contributor to micellization, we would observe the opposite effect, namely the BBPs would form micelles at lower concentrations compared to linear poloxamers due to the added hydrophobicity. Rather, we speculate that the backbone is significantly shielded from the aqueous environment by the side chains, which reduces the enthalpic contribution of water-backbone interactions. Similarly, the 5 mol% carboxylic acid impurity along the backbone is presumably not fully exposed to the aqueous environment and likely does not impact the CMC_a. Also, the effect of the alkane α-chain end impurity on micellization is assumed to be negligible because it represents less than 0.3 wt% of the hydrophobic block and has a minimal difference in hydrophobicity compared to either the *tert*-butyl end-group or the PPO repeat unit.

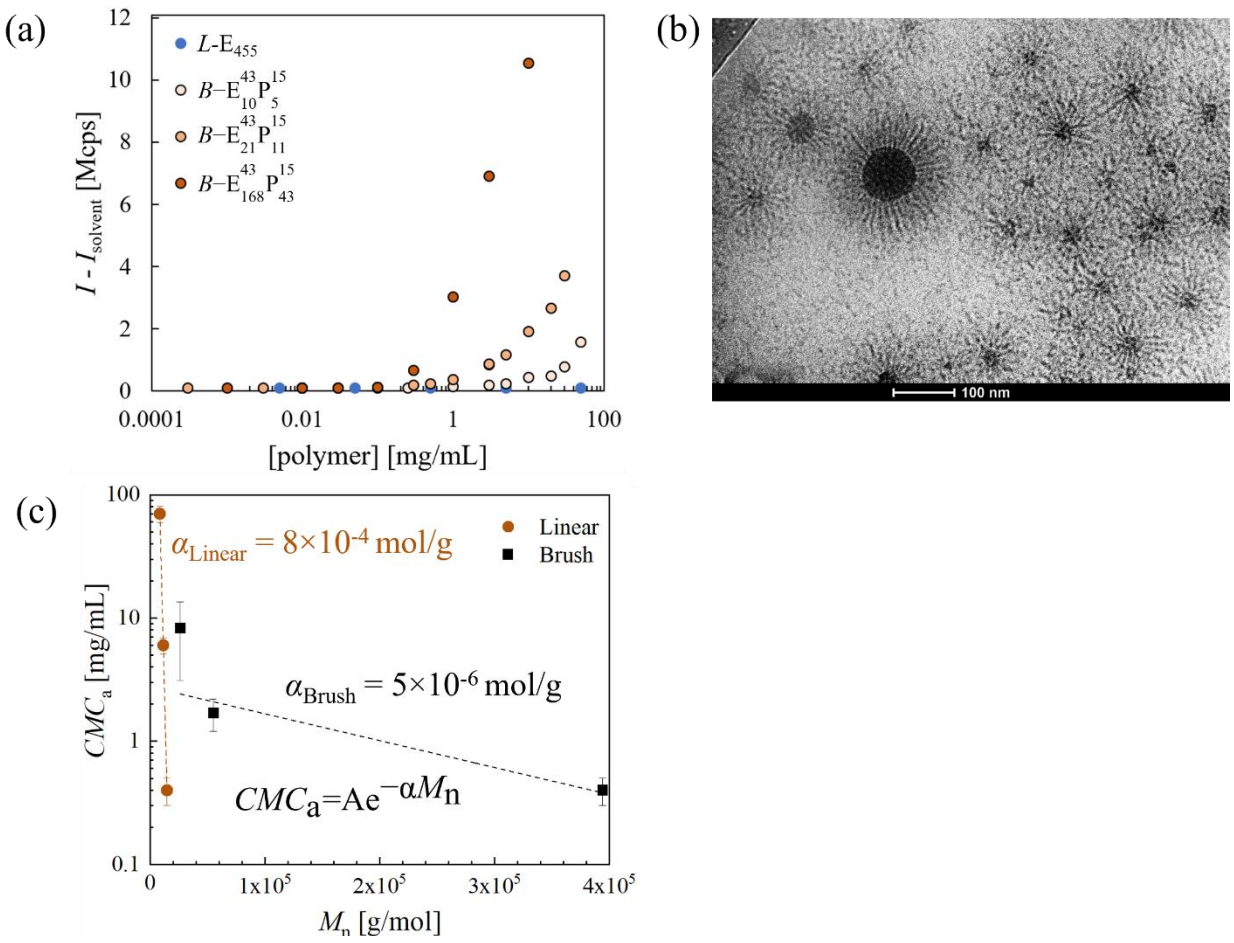

Figure 3.5: (a) Excess scattering intensity at 37 °C, as a function of polymer concentration. Linear PEO with an M_n = 20 kDa is a negative control for micellization. (b) cryo-TEM micrograph of B-$E_{168}^{43}P_{43}^{15}$ at a concentration of 10 mg/mL in aqueous buffer with 40,000x magnification. (c) Trend between CMC_a and M_n for linear and bottlebrush poloxamers of similar wt% PEO. Data for linear poloxamers (40 °C) are taken from Alexandridis *et al.*[97] Data are fit to the exponential function shown on the graph and the correlation coefficients are 0.99 and 0.58 for linear and brush, respectively.

Analysis of the correlation functions via the second cumulant model (Eq. 3.5.1) shows that R_h increases approximately linearly with molecular weight, suggesting that the chains adopt an extended conformation in the micelles. Additionally, for every micellar BBP solution a biexponential model (Eq. 3.5.2), accounting for two relaxation rates, yields a superior fit than a single exponential model (Figs. 3.16-3.18). Multi-angle DLS on a 3 mg/mL solution of the highest

M_n polymer confirmed that both relaxation modes are diffusive, and both have R_h values larger than expected for a unimer, suggesting existence of a bimodal micelle size distribution (Fig. 3.19). The TEM micrograph in Figure 3.5b also hints at a bimodal population of spherical micelles. This could be due to the direct dissolution method not allowing the micelle size distribution to fully equilibrate; however, the micelle size distribution does not change when annealed at 37 °C for 35 days (Fig. 3.20), suggesting that the micelles have reached a steady state. Recent theoretical and experimental work has shown that the side chain length asymmetry of the two blocks can impact micelle morphology, aggregation number, and surface roughness due to packing frustration at the core-corona interface.[151,220,221,108] We hypothesize that the additional free energy contribution of side chain crowding near the core-corona interface creates at least two local minima in free energy-micelle size space that are separated by a significant energy barrier; thus leading to a bimodal micelle size distribution.

To test this hypothesis, we synthesized *B*-$E_{54}^{10}P_8^{15}$. For this polymer, since the PEO corona block has shorter side chains than the core block, there is minimal overlap of adjacent PEO brush blocks at the core-corona interface. Figure 3.6 compares the autocorrelation functions corresponding to 10 mg/mL solutions of *B*-$E_{54}^{10}P_8^{15}$ and *B*-$E_{21}^{43}P_{11}^{15}$, two BBPs with comparable M_n and core blocks, but with PEO side chain lengths differing by a factor of 4×. Both autocorrelation functions were fit to the second cumulant and biexponential models and the residuals are compared in Figure 3.6b and 3.6d. When the PEO side chains are longer than the PPO side chains, the biexponential model is a significantly better fit as shown by Figure 3.6b, indicating coexistence of two populations. However, when the PEO side chains are shorter than the PPO side chains, the two models are equivalent, suggesting that a single micelle population exists. Therefore, minimizing steric overlap between neighboring PEO corona blocks at the core-corona interface led to a single, stable micelle size, which is consistent with our hypothesis.

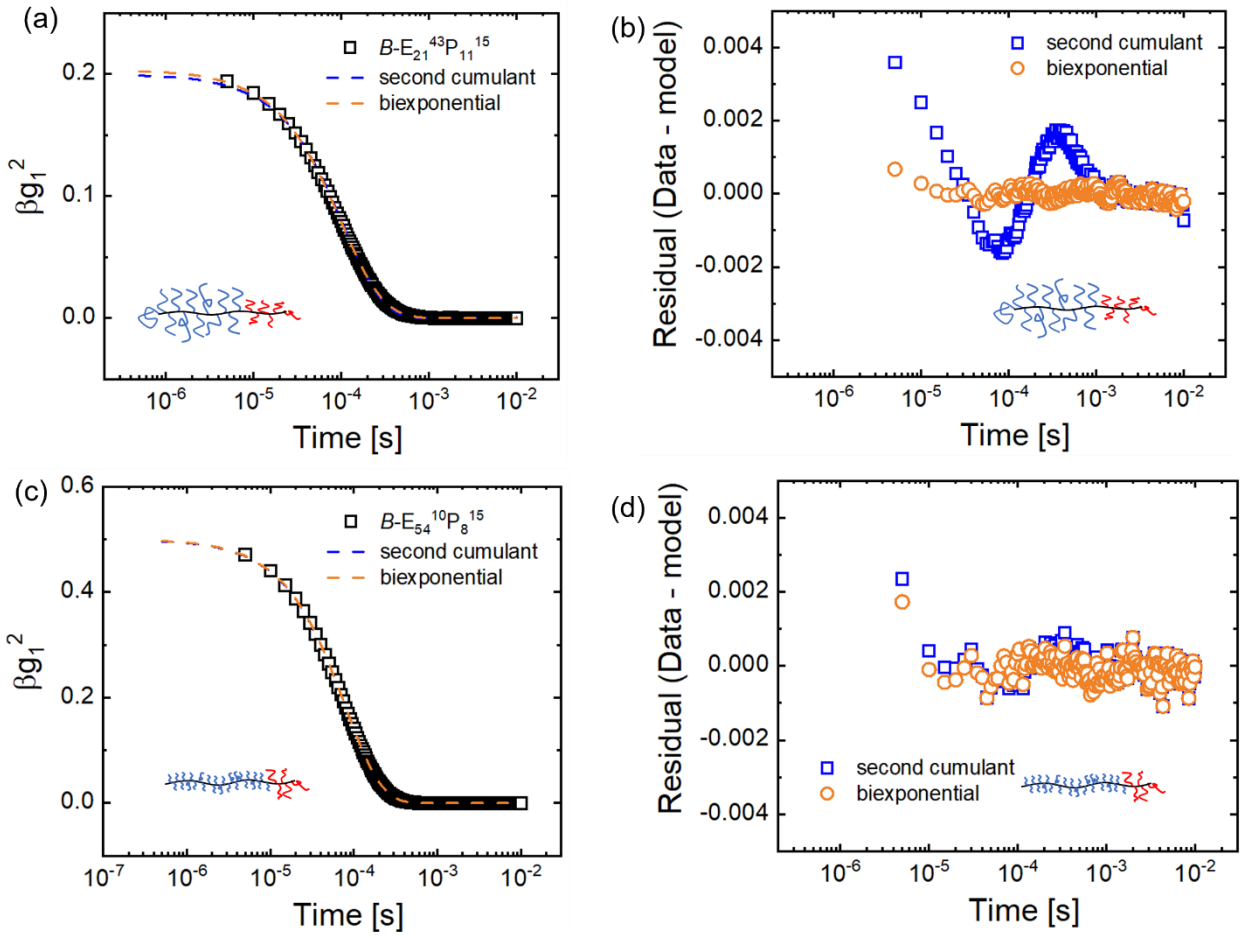

Figure 3.6: Effect of PEO side chain length on the number of micelle populations detected via DLS at 10 mg/mL and 37 °C. (a) Autocorrelation function corresponding to *B*-$E_{21}^{43}P_{11}^{15}$. (b) Residuals resulting from the second cumulant and biexponential model fits to the data in panel (a). (c) Autocorrelation function corresponding to *B*-$E_{54}^{10}P_{8}^{15}$. (d) Residuals resulting from the second cumulant and biexponential model fits to the data in panel (c).

To estimate the micelle core radius (R_{core}), we modelled the core-forming block as a cylinder plus a hemisphere, where the cylinder length equals the contour length of the backbone and the hemisphere radius is twice the radius of gyration of a PPO side chain, Fig. 3.21. This simplified model assumes that the backbone is a rigid rod, the side chains are Gaussian coils, and that there is no chain overlap. Comparison of the calculated and experimental R_{core} values in Table 3.1 shows

that this model agrees reasonably well with TEM data at short core block lengths ($N_{c,bb} \sim 5$), but is an overestimate for longer chains ($N_{c,bb} \sim 40$). This behavior resembles that of the Kratky-Porod wormlike chain model, and it suggests that in the micelle core a sufficiently long bottlebrush PPO can adopt a flexible conformation despite the high grafting density.[222,223] Finally, for polynorbornene grafted with 1 kDa PPO side chains, a persistence length estimate of ~10 nm is consistent with a transition from rod-like to coil-like behavior occurring within the interval $5 < N_{c,bb} < 40$. This estimate is markedly higher than the 0.7 nm persistence length of a linear polynorbornene polymer,[224] as expected for a densely grafted bottlebrush.[150,192] Finally, based on the average R_{core} determined from cryo-TEM and the density of PPO (1.00 g/cm^3),[163] the average aggregation number of the micelles is 70 ± 40 and 110 ± 50 for *B*-$E_{10}^{43}P_5^{15}$ and *B*-$E_{160}^{43}P_{43}^{15}$, respectively.

In conclusion, we report an efficient, high-throughput synthetic strategy to create bottlebrush poloxamers for the first time. The combination of living anionic and ROMP polymerization affords control over graft length and graft end-group and enables quantitative conversion of macromonomer. A series of bottlebrush poloxamers with 72−80 wt% PEO was synthesized over a range of molecular weights and the micellization behavior was compared to linear poloxamers. Bottlebrush poloxamers exhibited a remarkably reduced driving force for micellization compared to linear poloxamers as evidenced by a two order of magnitude smaller scaling exponent between M_n and CMC_a.

3.4 Effect of bottlebrush architecture on T_g, T_m, and percent crystallinity

Thermal transitions of polymers in the melt are important to understand because they impact polymer mechanical properties and processability. The glass transition occurs for all polymers and strongly influences chain mobility. Below the glass transition temperature (T_g), the system is non-equilibrium and molecular motion is very slow because there is very little free volume between chains. The mechanical properties of a glassy polymer are those of a solid; however, the molecular

packing is disordered and resembles a liquid.[163] T_g can be measured empirically by performing a temperature sweep with dynamic mechanical analysis. At the T_g, the loss modulus (G") is maximized.[163] Differential scanning calorimetry (DSC) is another common method because the heat capacity changes as T_g is traversed. Since the glass transition is not a phase transition in practice, the measurement of T_g is sensitive to the thermal path. Because molecular motion is so slow below T_g, high T_g polymers can be used to eliminate dynamic effects to simplify experimental systems. For example, if micelles are prepared with a high T_g core block, below T_g the aggregation number of micelles cannot change, essentially freezing-out chain exchange.[225,226]

Crystallization is another important phenomenon in polymer science that impacts many material properties. Because the crystalline state has a lower free energy than the amorphous state below the melting temperature (T_m), crystal formation is exothermic and can be readily observed via DSC. Two temperatures define crystallization for a given polymer: the temperature of crystallization, T_c, is the temperature at which crystals form upon cooling from a melt state, and the melting temperature, T_m, is the temperature at which crystals melt upon heating. If a bulk polymer is held between T_g and T_m, the chains have a relatively high degree of rotational and translational mobility, enabling a crystal to nucleate and then grow into a well-defined lattice. The parameters of the unit cell and lamellar spacing can be assessed via x-ray scattering experiments, and are well characterized for many polymers.[163] Because crystal formation requires regular packing of many different chains onto a lattice, irregularities along the backbone suppress crystal formation. These irregularities can be branching sites as in low density polyethylene, chain ends, or irregular patterns of stereoisomers and regioisomers along the backbone. Thus, most atactic (no pattern to the stereochemistry of repeat units along the backbone) polymers cannot form crystals, but isotactic (all repeat units have identical stereochemistry) and syndiotactic (alternating stereochemistry) polymers do readily form crystals because the stereoregularity enables efficient packing.

Linear PEO forms monoclinic crystals with well characterized unit cell parameters and a typical T_m value of 66 °C.[163] PPO, on the other hand, does not form crystals because the methyl group creates a stereocenter in every repeat unit. Since the PPO throughout this thesis was synthesized from a racemic mixture of propylene oxide stereoisomers in a non-stereo-specific reaction mechanism, it is exclusively atactic. Since the bottlebrush architecture places significant configurational constraints on the PEO units, it could affect T_g and change crystal structure and crystal growth kinetics. Crystallization of bottlebrush PEO has been studied in densely grafted bottlebrush polymers with exclusively PEO side chains,[195,227] random copolymers with an amorphous diluent,[228] and in bottlebrush molecules with diblock sidechains (core-shell structures).[229,230] Sun *et al.* found that the configurational constraints of tethering many PEO chains to a common backbone slows crystal growth and reduces spherulite size. They also used wide angle x-ray scattering and found that the unit cell of bottlebrush PEO is identical to linear PEO.[195] The PEO units distal from the backbone have the flexibility needed to orient into a crystal lattice while steric constraints near the backbone creates an amorphous region. This results in spherulites where the backbone orients along the radial direction of the spherulite, while PEO sidechains form the stems of the lamellae and are, on average, aligned tangentially to the spherulite.[195,227,229] Kripotou *et al.* studied PEO crystallization in bottlebrush polymers with PEO-PPO diblock sidechains resulting in a core-shell structure. Surprisingly, they found that when the PEO block was closer to the backbone, the T_m and percent crystallinity were higher than when the PEO block was further from the backbone, suggesting that the steric constraints near the backbone facilitate packing into a crystalline lattice. In this thesis, we studied the effect of PEO side chain length ranging from very short (N_{sc} = 10 units) to moderate (N_{sc} = 43 units), to elucidate which portion of the side chains occupies the crystalline phase. Furthermore, we explored the effect of molecular shape (approximately spherical vs cylindrical) on T_m and percent crystallinity. We used the ROMP polymerization scheme described in Section 3.2 to synthesize a set of bottlebrush PEO polymers over a range of backbone and side chain lengths and then applied DSC to study thermal transitions

in the bulk. Molecular and thermal characterization data for the molecules discussed in this section are summarized in Table 3.2.

Table 3.2: Molecular and thermal characterization data summary

Name	M_n [kDa]	$Đ$	N_{sc}	N_{bb}	T_g [°C]	T_m [°C]	%xtal
L-E_{455}	20.0	1.02	-	-	−53	57	82
L-E_{43}	2.0	1.04	-	-		53	87
L-E_{43}-NB	2.1	1.03	-	-	−41	51	72
L-E_{10}	0.5	1.07	-	-	−76	−20	58
L-E_{10}-NB	0.6	1.07	-	-	−76	−35	33
B-E_{12}^{43}	25.0	1.16	43	12	−35	49	61
B-E_{126}^{43}	260	1.08	43	120	−38	49	63
B-E_{50}^{10}	30.8	1.09	10	50	−64	-	0

First, a positive control experiment was performed using linear PEO with M_n = 20 kDa and two alcohol chain ends (*L*-E_{455}), and the DSC thermogram upon cooling and second heating is shown in Figure 3.7a. Upon cooling from the melt (blue), there is a sharp, exothermic crystallization peak at T_c = 45 °C. All quantitative estimates in this section are reported from second heating (red) with a ramp rate of 10 °C/min unless otherwise noted. The glass transition is observed as a change in slope due to a change in the heat capacity of the material. As can be seen in the inset of Figure 3.7a, this transition occurs over a range of temperatures (−65 to −40 °C). A single value is determined by finding the midpoint of two extrapolated lines from the data before and after the transition. For PEO-20k this yields a T_g = −52 °C, which is comparable to literature values for PEO.[163] As the material is heated, the crystalline domains melt at T_m = 57 °C.

Furthermore, the area under the curve gives the total enthalpy change during crystal melting, which can be compared to the theoretical enthalpy of a 100% crystalline PEO phase (ΔH_m = 197 J/g) to calculate the crystalline fraction as 82 wt% for linear PEO-20k.[230]

Figure 3.7b shows the DSC thermogram for *L*-E$_{43}$-NB, a linear PEO homopolymer with M_n = 2.1 kDa (PEO-2k), one methyl chain end, and one norbornene chain end. Since this is the macromonomer used to synthesize the bottlebrush PEO polymers in Figures 3.7c and 3.7d, it is an important control. *L*-E$_{43}$-NB has a T_m = 51 °C and 72 wt% of the PEO were in crystalline domains. The depressed T_m and crystal fraction of *L*-E$_{43}$-NB relative to *L*-E$_{455}$ is due to both the lower molecular weight and the norbornene end-group. The bulky norbornene end-group will presumably be excluded from the crystal and at a lower molecular weight the concentration of chain ends is higher; both factors lead to thinner lamellae and therefore a lower T_m.

The inset in Figure 3.7b suggests that $T_g \approx -40$ °C; however, the poorly defined slope on the high temperature side of the glass transition makes the midpoint method of T_g estimation questionable. Another method is to find the inflection point in the data which can be seen by a local maximum in a plot of the derivative of heat flow with respect to temperature. Figure 3.8 demonstrates this analysis and $T_g \approx -41$ °C for *L*-E$_{43}$-NB, which is consistent with the midpoint method. The inflection point method will be applied throughout the rest of this analysis.

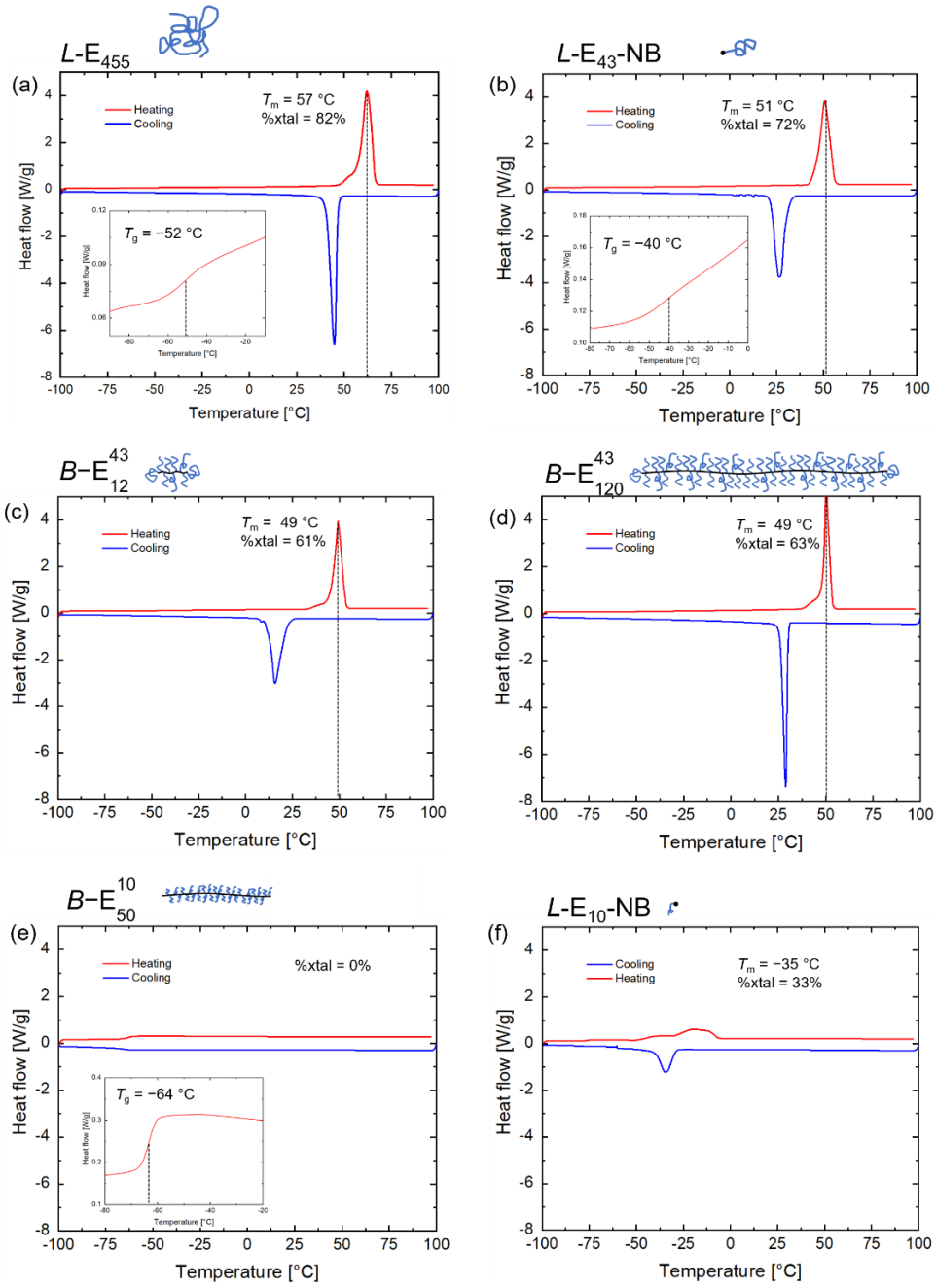

Figure 3.7: DSC thermograms of linear and bottlebrush PEO polymers. (a) *L*-E$_{455}$ with two alcohol end-groups (M_n = 20 kDa). (b) *L*-E$_{43}$-NB with one methyl and one norbornene end-group (M_n = 2.1 kDa). (c) Bottlebrush PEO with a short backbone and 2.1 kDa side chains resulting in a spherical "star-like" conformation. (d) Bottlebrush PEO with a long backbone and 2.1 kDa side chains resulting in a cylindrical "rod-like" conformation. (e) Bottlebrush PEO with a long backbone and 0.4 kDa side chains resulting in a cylindrical "rod-like" conformation. (f) Linear PEO with one methyl and one alcohol end-group (M_n = 0.4 kDa). Endothermic transitions are defined as positive.

Figure 3.7c and 3.7d present DSC thermograms of two bottlebrush PEO polymers with the same side chain length (N_{sc} = 43) but a factor of 10× difference in backbone length (N_{bb} = 12 vs N_{bb} = 126). The ratio of side chain to backbone lengths (N_{sc}/N_{bb}) determines the molecular shape. When the side chains are long relative to the backbone the molecule is approximately spherical, and as the backbone length is increased the shape becomes more cylindrical.[152] On cooling, B-E_{126}^{43} shows a very sharp crystallization peak at T_c = 26 °C whereas the crystallization peak for B-E_{12}^{43} is slightly broader and occurs at T_c = 15 °C. This suggests that the cylindrical shape leads to faster crystallization kinetics despite having a 10× larger M_n. Possibly, when two cylindrical bottlebrushes align with their backbones parallel to each other, many PEO units are brought into proximity, facilitating packing. In contrast, for a rotationally symmetrical spherical bottlebrush, when two molecules approach, a smaller fraction of the PEO chains can align before the backbone must bend. On heating, the melting endotherms of B-E_{12}^{43} and B-E_{126}^{43} both occur at T_m = 49 °C and have nearly identical areas. Therefore, the fraction of PEO chains that occupy crystals and the stability of the crystalline phase are independent of the molecular shape.

The inflection point analysis of the DSC data shown in Figure 3.8 shows that the T_g of B-E_{12}^{43} and B-E_{126}^{43} are −35 °C and −38 °C, respectively. Since the corresponding macromonomer (L-E_{43}-NB; T_g = −41 °C) had a very similar T_g, for bottlebrush PEO with relatively long side chains (M_n = 2.1 kDa) the bottlebrush architecture and the shape of the molecule (sphere vs cylinder) has very little impact on the glass transition, as expected.

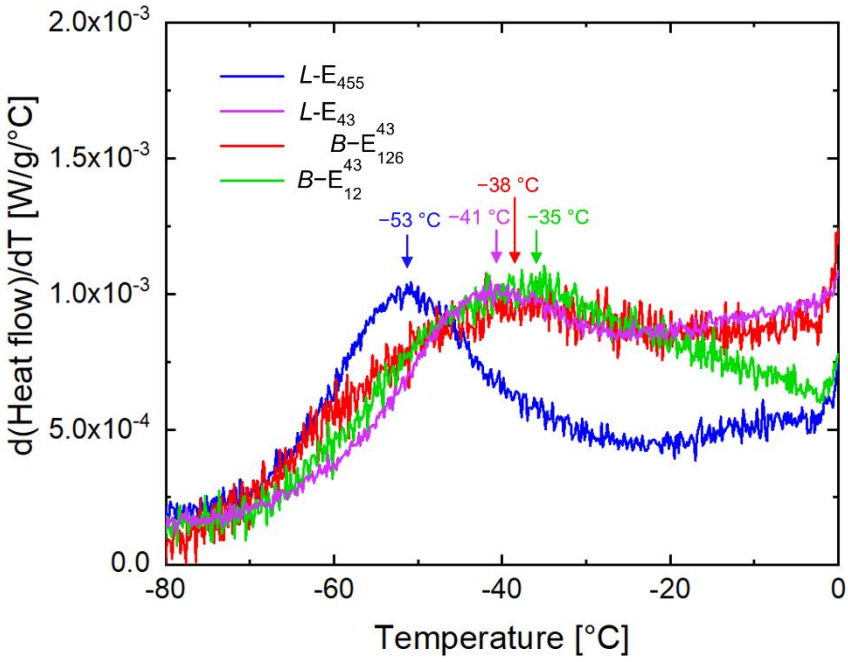

Figure 3.8: Inflection point analysis to more accurately determine T_g.

To assess the impact of N_{sc}, we synthesized a cylindrical bottlebrush with very short side chains: B-E_{50}^{10}, where N_{sc} is only 10 PEO units. Figure 3.7e clearly demonstrates that this molecule does not form a crystalline phase. To verify that this is a consequence of the steric constraints of the backbone, a DSC thermogram of the macromonomer L-E_{10}-NB is shown in Figure 3.7f, which clearly shows crystal formation. Roughly 33 wt% of the PEO units in the macromonomer occupy crystals that melt at roughly −35 °C. Melting occurs over a broad temperature range with two peaks, possibly suggesting different lamellar thicknesses. Two crystallization peaks were also observed in L-E_{10}, a linear PEO homopolymer with the same molecular weight and an alcohol end-group in place of the norbornene, so it is likely attributable to the low molecular weight and not the norbornene end-group. This experiment was repeated with a cooling/ heating rate of 1 °C/ min and multiple crystallization peaks were also observed. The two crystallization peaks are likely a kinetic effect resulting from formation of lamellae with two thicknesses.

Furthermore, the T_g of B-E_{50}^{10} was −64 °C, which is significantly lower than the T_g of the bottlebrushes with longer side chains likely due to the increased concentration of chain ends. In

this case, the glass transition was readily apparent as shown by the inset in Figure 3.7e, so the midpoint method was used. Finally, the T_g of B-E_{50}^{10} is about 10 °C higher than that of the corresponding macromonomer (L-E_{10}-NB; $T_g = -76$ °C). Thus, for bottlebrush PEO with short side chains, the bottlebrush architecture slightly increases T_g compared to a linear homopolymer with a molecular weight equal to the side chain molecular weight. This is consistent with the trend observed by López-Barrón *et al.* for atactic poly(propylene) bottlebrush polymers although to a significantly reduced extent.[194]

To conclude this study, shortening the PEO side chains from 43 units to 10 completely suppressed crystal formation in bottlebrush PEO homopolymers; however, the corresponding macromonomer, linear PEO homopolymer, does have a significant crystalline fraction, 33%. Therefore, we conclude that the configurational constraints created by tethering the side chains to the backbone suppress crystallization in the short side chain limit. Therefore, the crystalline domains observed when N_{sc} = 43 must be the segments of the side chain furthest from the backbone. Additionally, for both sets of side chain lengths, T_m and the crystalline fraction decrease when the linear PEO chain is functionalized with norbornene and then decrease further when the macromonomer is polymerized into a bottlebrush ($T_{m,\ L\text{-E43}} > T_{m,\ L\text{-E43-NB}} > T_{m,\ B\text{-}E_x^{43}}$). This trend was also observed by Sun *et al.*[195] Finally, spherical (star-like) and cylindrical (bottlebrush-like) molecules have similar T_m and reach comparable crystalline fractions, but the cylindrical shape has a significantly higher Tc and a sharper crystallization peak, suggesting that molecular shape impacts crystallization kinetics.

3.5 Materials and methods for Chapter 3

Materials:

All materials were used as received. The following materials were purchased from Sigma: propylene oxide, (>99.0%), butyl-magnesium chloride, potassium tert-butoxide, 18-crown-6 ether, palladium (10% on activated charcoal), 4-dimethylaminopyridine (>99%), N,N’

diisopropylcarbodiimide (99%), exo-5-norbornene-2-carboxylic acid (97%), methyl ether poly(ethylene glycol) (M_n = 2000 g/mol), poly(ethylene oxide) (M_n = 20,000 g/mol), tetrahydrofuran (ACS reagent, 97%, stabilized with 250 ppm BHT), pyridine (>99%), ethyl vinyl ether (stabilized with 0.1% KOH, 99%), benzene (ACS reagent, 99%), sodium chloride (99.5%), potassium chloride (>99%), calcium chloride (anhydrous, 96%), magnesium chloride (97%), HEPES buffer (99.5%), tetrahydrofuran (anhydrous, 99.9%), second generation Grubbs catalyst® M204, α-cyano-4-hydroxycinnamic acid, and sodium trifluoroacetic acid (98%). The following materials were purchased from Fisher Scientific: methanol (HPLC grade), diatomaceous earth (Celite), dichloromethane (ACS reagent, anhydrous, 99.8%), diethyl ether (anhydrous), and sodium sulfate (anhydrous). SiliaMetS DMT was purchased from Silicycle. Deuterated chloroform (99.8% d) was purchased from Cambridge Isotope Laboratories. Hydrogen gas was purchased from Airgas.

Methods:

Anionic polymerization of propylene oxide:

Synthesis of tert-butyl-poly(propylene oxide) (*t*-PPO-OH) was carried out though anionic polymerization. Details of the synthetic procedure can be found in previous publications.[206,231] Briefly, anionic polymerization was carried out in a water- and air-free environment under argon. Tetrahydrofuran was dried using an alumina column and used as the solvent. 18-crown-6-ether was used in a 2:1 molar ratio relative to potassium ions to reduce unwanted side reactions and increase conversion of PPO.[207,232] Propylene oxide was purified over butyl-magnesium chloride and added to the reactor. Potassium *t*-butoxide was added to initiate the reaction at 25 ºC and the reaction was stirred for 72 h. The polymerization was terminated with acidic methanol. The resulting product was then subjected to repeated filtering and rotary evaporation followed by two hexane/water liquid-liquid extractions in a separatory funnel to remove crown ether and salts from the product. The volume ratio of hexane:water was roughly 1:2 and the hexane phase was collected, dried over anhydrous sodium sulfate, and the solvent was removed with a rotary evaporator.

Hydrogenation of poly(propylene oxide):

An example hydrogenation protocol is as follows. Poly(propylene oxide) (PPO) polymer, faint yellow gel (1.19 g, 1.1 mmol) was put in a round bottom flask with palladium on carbon catalyst (0.27 g) at a 5:1 PPO: Pd/C by mass. The flask was gently rotated to coat the polymer with the catalyst. 10 mL of methanol was added, and the solution was stirred and bubbled with argon for 30 min. Hydrogen gas was collected using a balloon and syringe technique and added to the flask via a needle. A 25 gauge needle was used to displace argon with hydrogen for 1 min. The reaction was stirred at room temperature overnight. The reaction effluent was diluted with methanol and filtered with Celite until the filtrate was clear. Solvent was evaporated using a rotary evaporator to yield a faint yellow gel (72% yield).

Esterification of PPO-OH:

An example esterification protocol is as follows. Hydrogenated PPO (0.83 g, 0.76 mmol) was dried using a vacuum line in a 20 mL scintillation vial. Then, 4-dimethylaminopyridine (DMAP) (0.019 g, 0.16 mmol) and exo-5-norbornene-2-carboxylic acid (0.16 g, 1.15 mmol) were added to the scintillation vial and dissolved in 4.5 mL anhydrous dichloromethane. Meanwhile, N,N' diisopropylcarbodiimide (DIC) (0.14 g, 1.14 mmol) was mixed with 1 mL of anhydrous dichloromethane. The DIC solution was then added dropwise to the reaction vial over 3 min while stirring. White precipitate formed within 30 min and the reaction was stirred at room temperature for 7 days. The reaction solution was filtered with a fine filter to remove the precipitate, and the effluent was diluted with hexanes and washed three times with a 0.1 M NaOH solution with addition of a small volume ~3 mL of saturated NaCl brine. The organic phase was dried over sodium sulfate, concentrated with a rotary evaporator to yield a faint yellow gel with crystals due to excess exo-5-norbornene-2-carboxylic acid. This mixture was then dried in a vacuum oven at 50 ℃ for 7 days where the crystals slowly sublimed to leave a yellow gel (90% yield).

Esterification of PEO-OH:

The same reaction protocol as for PPO esterification was performed, except the reaction was run for 48 h. The reaction solution was filtered with a fine filter to remove the precipitate and dried

on a rotary evaporator. The product was dissolved in tetrahydrofuran and the polymer was purified from the excess exo-5-norbornene-2-carboxylic acid by two precipitations in cold diethyl ether to yield a white powder (64% yield).

Grubbs catalyst preparation:

Second generation Grubbs catalyst (G2) [(H2IMes)(PCy3)Cl2Ru=CHPh] was purchased from Millipore sigma and converted to Grubbs third generation catalyst (G3) using an established procedure.[233] G2 (1.01 g, 1.2 mmol) was mixed with pyridine (3.0 g, 36 mmol) in a 50 mL round bottom flask and stirred in air for 10 min. An immediate color change from dark red to dark green was observed. 20 mL of pentane was layered on top and the flask was placed in a -20 °C freezer overnight. The product, green powder, was recovered via vacuum filtration and washed with excess pentane (98% yield).

Sequential Ring Opening Metathesis Polymerization (ROMP):

All ROMP reactions were done in a glovebox with an argon atmosphere ([O_2] < 10 ppm; [H_2O] < 10 ppm) with a monomer concentration of approximately 0.05 M in anhydrous dichloromethane and were stirred at room temperature for 10 min. Fresh G3 stock solution (dark green) and monomer stock solutions were prepared with precisely known molar concentrations. To initiate polymerization, a precise volume of G3 stock solution was added to the first monomer solution via a gas tight syringe such that the molar ratio of monomer to catalyst was equal to the target degree of polymerization. The solution quickly fades from dark green to rust brown upon initiation. The reaction was stirred for 10 min, then a minimal volume of the reaction was taken as an aliquot and quenched with a 1:1 (vol) mixture of ethyl vinyl ether: dichloromethane. The second monomer solution was added to the reaction vessel, again such that the molar ratio of monomer to catalyst was equal to the target degree of polymerization. The reaction was taken out of the glovebox and quenched by stirring with an equal volume of the ethyl vinyl ether: dichloromethane mixture for 10 min. G3 catalyst was removed by diluting the reaction with ~50 mL dichloromethane and stirring with several scoops of SiliaMetS-DMT (silicycle) for ~2 h until the supernatant is clear. The silicycle with bound G3 was removed by filtering though a column of Celite. The effluent was

dried with a rotary evaporator, dissolved in benzene and freeze dried to recover the polymer as a white powder. Typical yields are ~80%.

Polymer characterization:

^{1}H NMR: All NMR samples were prepared in deuterated chloroform at a sample concentration between 10 – 20 mg/mL. All spectra were collected using a Bruker Avance III HD-500 MHz spectrometer with a 5mm Prodigy TCl cryoprobe. Chemical shifts are reported in parts per million and were referenced to the residual chloroform peak at 7.26 ppm. ^{1}H NMR spectroscopy was used to quantify conversion, assess purity, and confirm polymer composition.

Size Exclusion Chomatography (SEC): All SEC samples were prepared in tetrahydrofuran at a concentration of 5 mg/mL and filtered with a 0.2 um PTFE filter. An instrument equipped with 2 phenogel columns and a Wyatt Dawn Heleos II multi-angle light scattering detector was used to obtain molecular weights and dispersities. The reported refractive index increment (dn/dc) of PEO and PPO in THF are 0.068 mL/g and 0.087 mL/g, respectively.[85] The dn/dc of all diblocks was taken as the weighted average of these components based on the targeted composition.[7]

MALDI-ToF: To prepare MALDI samples, a 30 mg/mL solution of α-cyano-4-hydroxycinnamic acid (CHCA), a 3 mg/mL polymer solution, and a 1 mg/mL sodium trifluoroacetic acid (NaTFA) solution, were all prepared in THF. The CHCA and polymer solutions were mixed in a volume ratio of 2:1 and a drop of the NaTFA solution was added. An AB SCIEX TOF/TOF 5800 instrument was used in reflector mode. For every MALDI-ToF spectrum collected, the laser power of the first shot was deliberately set too low to transfer the polymers into the gas phase. The laser power was then ramped in small steps until a clear spectrum was observed. Thus, all spectra reported were taken near the minimal laser power required, minimizing likelihood of sample degradation.

Micelle solution preparation:

Aqueous buffer was prepared according to an established recipe.[6] The buffer solution is 140 mM NaCl, 5 mM KCl, 2.5 mM $CaCl_2$, 2 mM $MgCl_2$, and 10 mM HEPES, which was prepared in milliQ water (18 Ω) and pH adjusted to pH = 7.2 with NaOH. Micelle stock solutions were

prepared via direct dissolution, and a vortexer was used to facilitate dissolution. To ensure complete dissolution, solutions were held at 4 ℃ for 1 hour. Each series of micelle solutions was then prepared via serial dilution and annealed at 37 ℃ overnight prior to measurements.

Dynamic Light Scattering (DLS):

DLS experiments were performed with a Brookhaven BI-200SM instrument equipped with a 637 nm laser and an adjustable goniometer. All measurements were done at 37 ℃ in a refractive index matching bath. All solutions were filtered with a 0.2 um GHP filter into clean glass test tubes (200 mm x 7 mm with 5 mm inner diameter) and sealed with parafilm. All excess scattering intensity measurements were performed at a detector angle of 90°, a laser power of 5 mW, and an aperture setting of 400 nm. Intensity autocorrelation functions, $g_2(t)$ were recorded for a minimum of 5 min.

The Siegert relation was applied to convert $g_2(t)$ to the electric field autocorrelation function, $g_1(t)$. $g_1(t)$ was then fit to a second-order cumulant model (Eq. 3.5.1) and a biexponential model (Eq. 3.5.2) and the residuals were compared (Figs. S11-S13).

$$g_1(t) = B\exp(-2\Gamma t + k_2 t^2) \quad \text{(Eq. 3.5.1)}$$

$$g_1(t) = f_1 \exp(-2\Gamma_1 t) + f_2 \exp(-2\Gamma_2 t) \quad \text{(Eq. 3.5.2)}$$

The mutual diffusion coefficient, D_m, of a species can be obtained by dividing the decay coefficient (Γ in the equations above) by the scattering vector q given by $q = (4\pi n/\lambda)\sin(\theta/2)$ where n is the refractive index of the medium, λ is the wavelength of the laser, and θ is the angle of detection. For dilute solutions, the mutual diffusion coefficient (D_m) and the tracer diffusion coefficient (D_t) are almost equivalent. D_t can then be related to the hydrodynamic radius via the Stokes-Einstein equation.

Cryo-TEM:

For sample vitrification, 200 mesh lacey carbon copper grids (Ted Pella) were exposed to glow discharge to increase their surface energy. They were then transferred to an environmentally controlled chamber (FEI Vitrobot Mark III), which was held at 25 °C and 100% humidity. 5 μL of a 10 mg/mL polymer solution was then deposited onto the grid and blotted for 7 s. It was then

allowed to anneal for 1 s before being plunged into a vat of liquid ethane ($T = -89$ °C). The samples were stored in liquid nitrogen prior to imaging using an FEI Technai Spirit Bio-Twin TEM at an accelerating voltage of 120 keV. Samples were kept at −176 ± 1 °C during imaging. Images were captured using a magnification of 40000× and an under-focus of approximately −20. Image analysis was performed using ImageJ software, and the built-in enhance local contrast filter was applied to all images. A minimum of 10 objects were measured in each image, and at least two grid locations were included in every analysis.

Differential Scanning Calorimetry:

Roughly 5-10 mg of polymer sample was loaded into Tzero aluminum pans and sealed. DSC experiments were performed on a TA Instruments Q1000 DSC instrument. Pans were placed into the instrument and equilibrated at 40 °C for 10 min, then the pan was heated to 100 °C and held for 10 min. This first heating was performed to eliminate the effects of the thermal history of the sample. Then, a cooling scan was performed from 100 °C to −100 °C at 10 °C/min followed by a second heating cycle between −100 °C to 100 °C at 10 °C/min. All thermal transitions were reported based on the second heating scan.

3.6 Supporting Information for Chapter 3

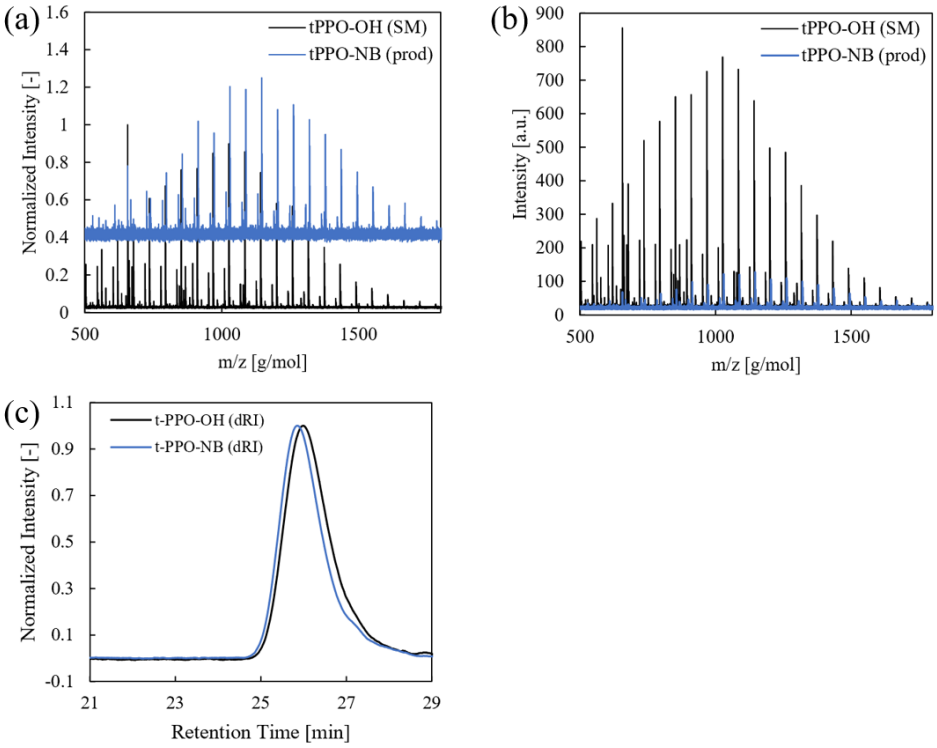

Figure 3.8. (a) Full, normalized MALDI spectra of the *t*-PPO$_{15}$-R materials shown in Fig. 2. Black is the starting material prior to hydrogenation and blue is the product of the esterification step (vertically shifted). (b) Comparison of the absolute intensity of the MALDI spectra as a function of the ω-end-group. The alcohol (black) and NB (blue) appear to impact the ability of the polymer to ionize and/or fly, as the preparation protocol and laser intensity were identical. (c) Comparison of the SEC(dRI) traces of the *t*-PPO-OH prior to hydrogenation and the functionalized *t*-PPO-NB macromonomer post hydrogenation and esterification. The overlap of these chromatograms suggests that these reactions did not cause chain coupling or degradation.

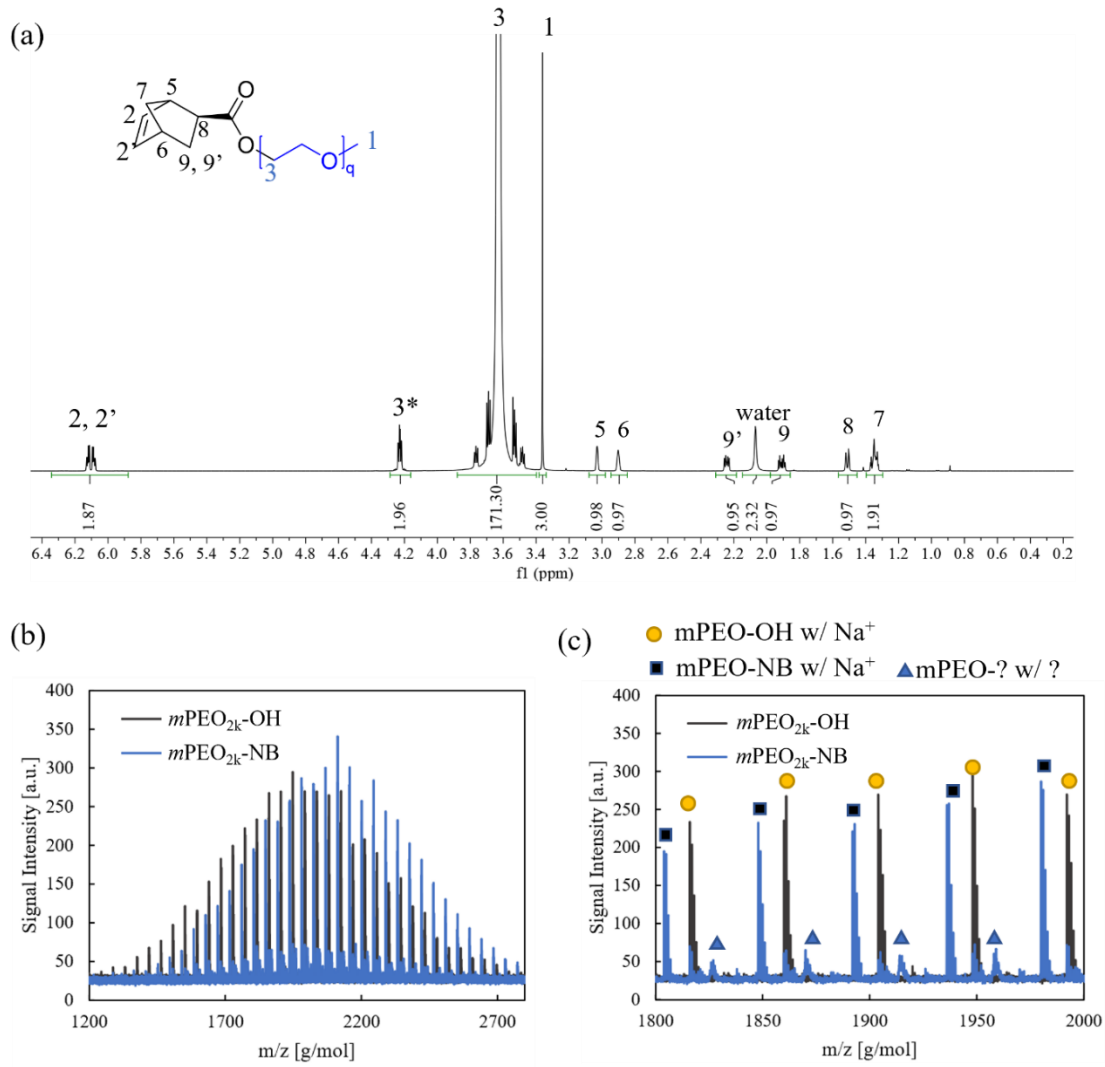

Figure 3.9: characterization of PEO2k-NB macromonomer (*L*-E$_{43}$-NB) and starting material (*L*-E$_{43}$-OH). (a) ^{1}H NMR spectrum of the purified methyl terminated PEO2k-NB macromonomer. The peak shape of peak 2, 2' indicates that all excess norbornene small molecule was removed via the precipitations. The ratio of the norbornene end-group to the methyl end-group suggests the conversion of alcohol to norbornene was 94%. (b) MALDI of the starting material (mPEO-OH (*L*-E$_{43}$-OH): M_n = 1970 g/mol, $Đ$ = 1.04) and the product (mPEO-NB (*L*-E$_{43}$-NB) - M_n = 2049 g/mol, $Đ$ = 1.03). The shift to higher molecular weight suggests successful addition of a norbornene end-group; however, the shift in Mn is less than the molecular weight difference between norbornene and alcohol because a fraction of the chains (~6%) do not react and the ionizability of these two populations are not the same. Extending the mass range recorded in the MALDI to 5500 g/mol indicated that no chain coupling occurred (data not shown). (c) Zoom in on the MALDI spectra from 1800-2000 g/mol. Gold circle corresponds to unreacted alcohol endgroups (mPEO-OH), black square corresponds to the desired mPEO-NB, and blue triangles is a methyl terminated PEO with an undetermined ω chain end that does not interfere with ROMP and is a small fraction of the sample.

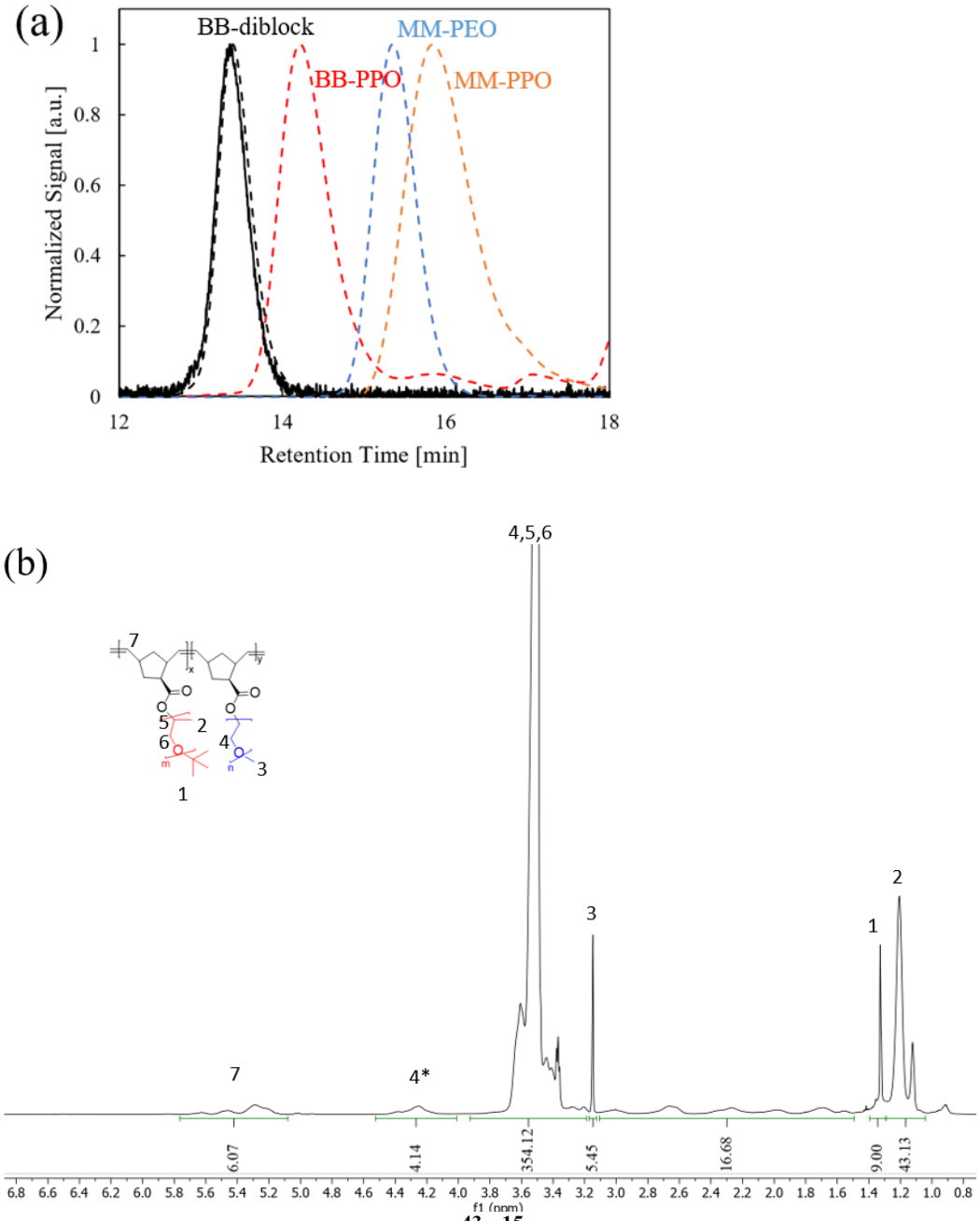

Figure 3.10: Characterization of *B*-$E_{10}^{43}P_{5}^{15}$. (a) SEC chromatograms for both monomers, the BB-PPO block aliquot and the BB-PEO-b-BB-PPO diblock with the refractive index (dashed) and light scattering (solid) traces shown. From Zimm analysis M_n = 6,000 g/mol and $Đ$ = 1.31 for the BB-PPO aliquot and M_n = 26,200 g/mol and $Đ$ = 1.07 for the diblock. The resulting composition is 72 wt% PEO. (b) ^{1}H NMR spectrum for the diblock. The ratio of the methyl graft chain ends (3) to the backbone alkene peaks (7) gives an estimate of the composition of the polymer of 77 wt% PEO, confirming the SEC result. The absence of the monomeric NB peak at 6.0-6.2 ppm indicates full conversion of macromonomer.

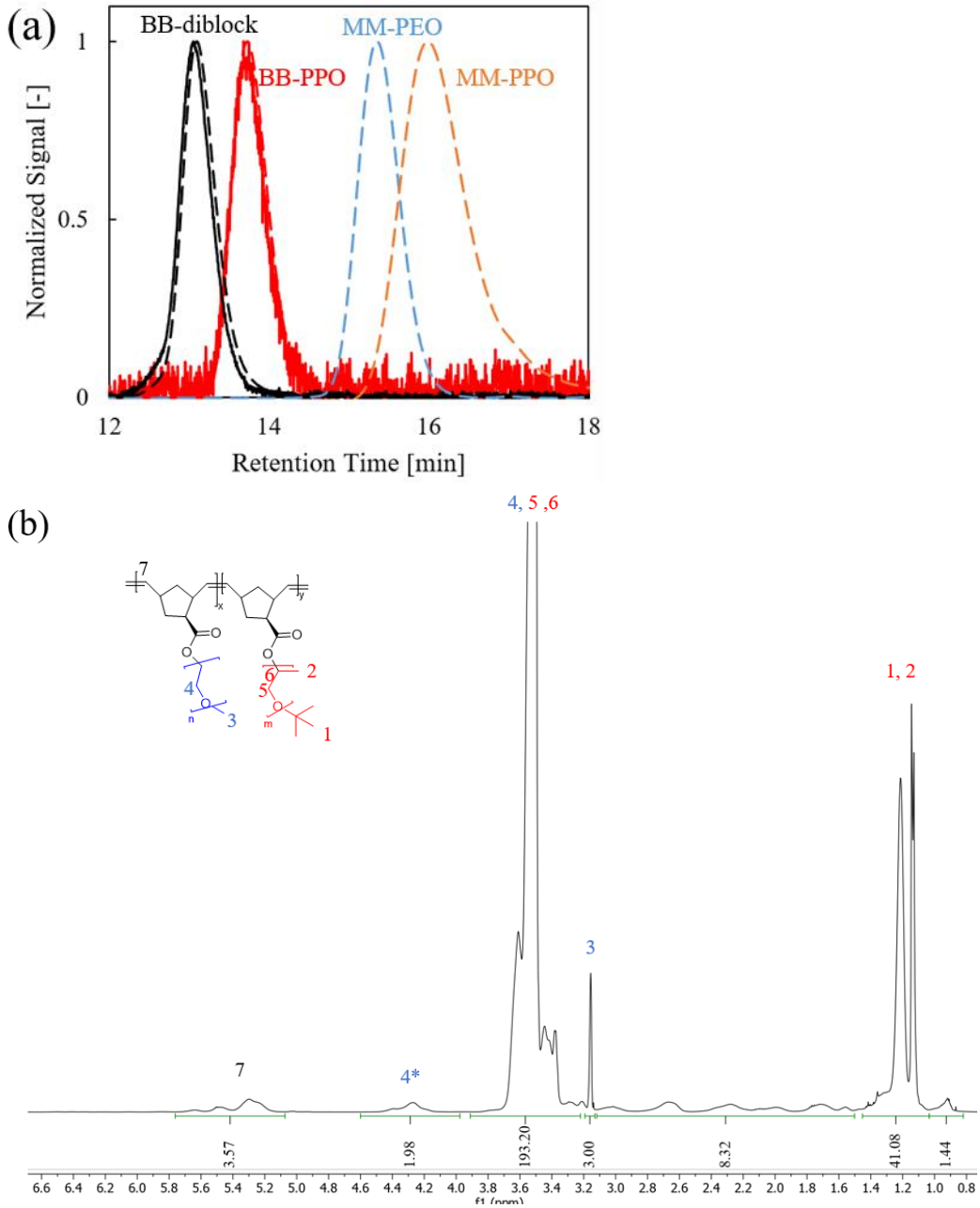

Figure 3.11: Characterization of *B*-$E_{21}^{43}P_{11}^{15}$. (a) SEC chromatograms for both monomers, the BB-PPO block aliquot and the BB-PEO-b-BB-PPO diblock with the refractive index (dashed) and light scattering (solid) traces shown. From Zimm analysis M_n = 11,600 g/mol and $Đ$ = 1.20 for the BB-PPO aliquot and M_n = 55,300 g/mol and $Đ$ = 1.10 for the diblock. The resulting composition is 74 wt% PEO. (b) ^{1}H NMR spectrum for the diblock. The ratio of the methyl graft chain ends (3) to the backbone alkene peaks (7) gives an estimate of the composition of the polymer of 72 wt% PEO, confirming the SEC result. The absence of the monomeric NB peak at 6.0-6.2 ppm indicates full conversion of macromonomer.

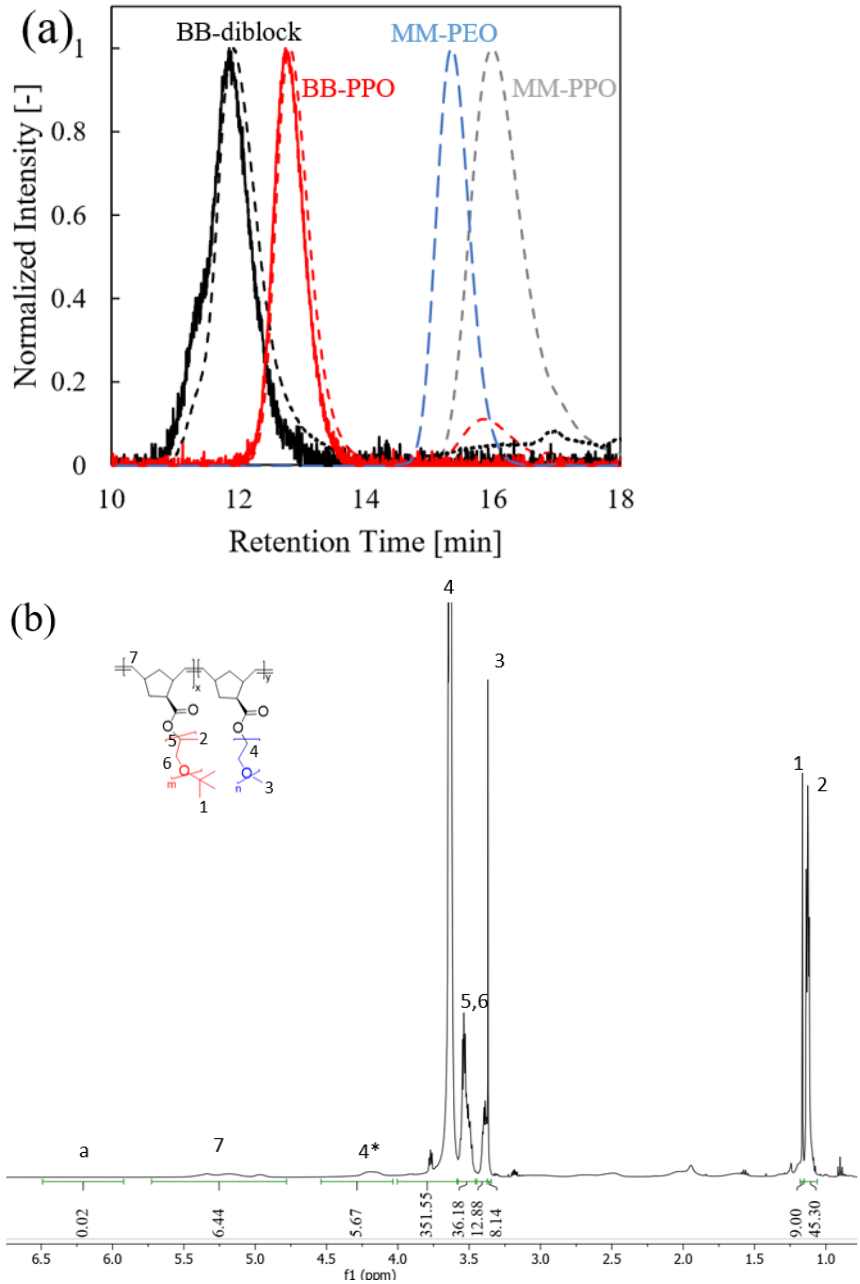

Figure 3.12: Characterization of *B*-$E_{160}^{43}P_{43}^{15}$. (a) SEC chromatograms for both monomers, the BB-PPO block aliquot and the BB-PEO-b-BB-PPO diblock with the refractive index (dashed) and light scattering (solid) traces shown. From Zimm analysis M_n = 46,800 g/mol and $Đ$ = 1.09 for the BB-PPO aliquot and M_n = 394,000 g/mol and $Đ$ = 1.15 for the diblock. The resulting composition is 82 wt% PEO. (b) ^{1}H NMR spectrum for the diblock. The ratio of the methyl graft chain ends (3) to the backbone alkene peaks (7) gives an estimate of the composition of the polymer of 80 wt% PEO, confirming the SEC result. The small monomeric NB peak at 6.0-6.2 ppm (a) indicates ~99% conversion of macromonomer.

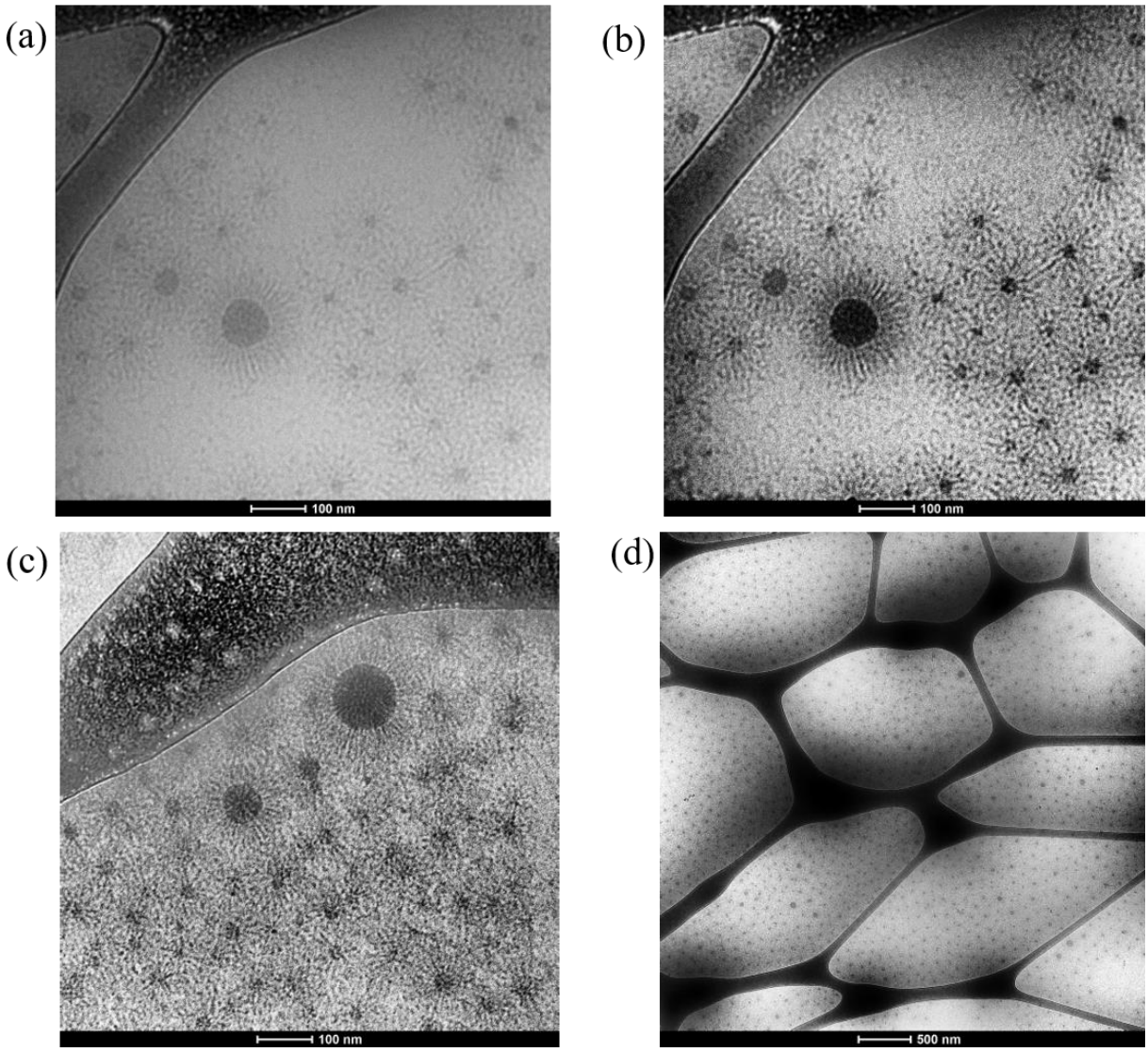

Figure 3.13: additional cryo-TEM micrographs of micelles of *B*-$E_{160}^{43}P_{43}^{15}$. (a) Magnification of 40,000x and the same spot on the grid as Figure 4b in the main text but with reduced exposure time. No beam damage is observable on the grid. (b) Same image as in panel (a) after the enhance local contrast filter has been applied. (c) 40,000x magnification on an additional spot on the grid. (d) 8,000x magnification of an additional spot on the grid.

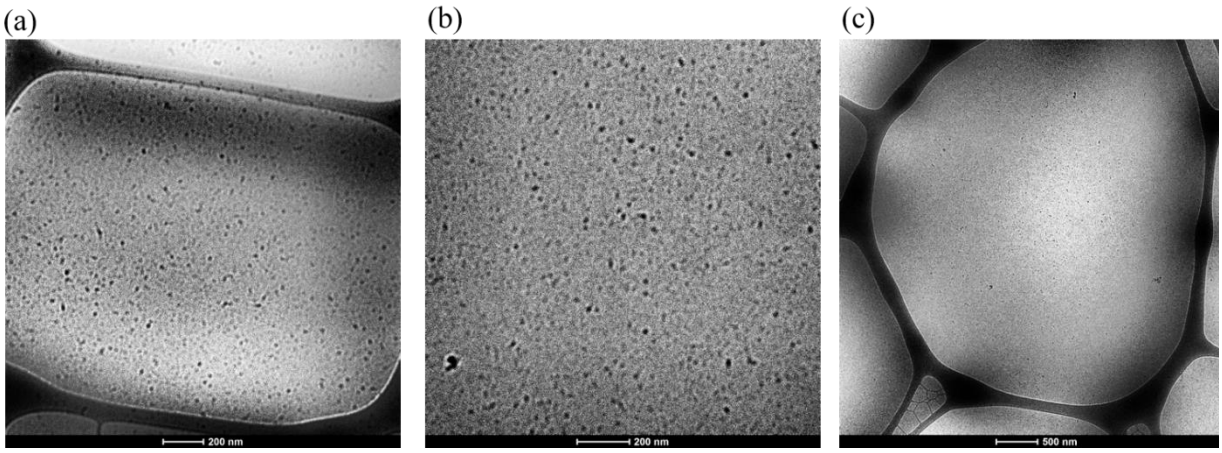

Figure 3.14: cryo-TEM micrographs of micelles of *B*-$E_{10}^{43}P_5^{15}$. (a) Magnification of 20,000x and the same spot on the grid as Figure 4b in the main text but with reduced exposure time. No beam damage is observable on the grid. (b) 20,000x magnification on an additional spot on the grid. (c) 8,000x magnification of an additional spot on the grid.

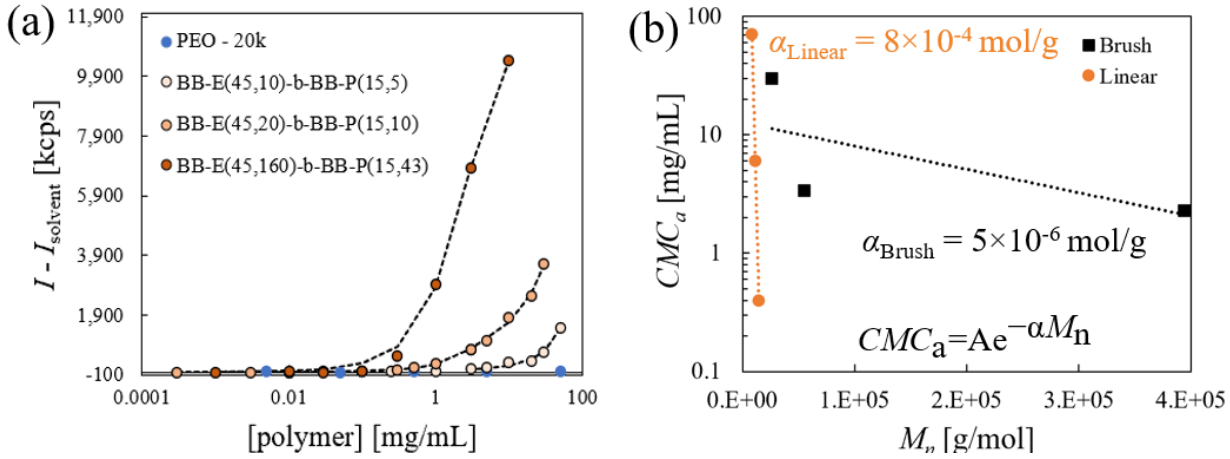

Figure 3.15: Closed association modelling as an alternative method to assess *CMC*$_a$. (a) Excess scattering intensity of each polymer fit to the closed association model described below. (b) The relationship between M_n and *CMC*$_a$ where the *CMC*a has been defined based on the model results. The same trend and scaling exponent as shown in Figure 4c are apparent.

The purpose of this analysis is to apply a model to define the apparent critical micellization concentration *CMC*$_a$; thus, removing all human decision making in the cut-off between the free-chain and micelle regimes. The details of the model used are shown below.

From light scattering theory, the excess scattering intensity depends on the product of the size and number of scatterers. Thus, for a mixture of unimers and micelles, the excess scattering intensity is given by Equation S3 below.[163]

$$I_{ex}=A[\text{unimers}]+B[\text{micelles}] \quad \text{(S3)}$$

The closed association model asserts that for a solution at a concentration above the *CMC*$_a$, an equilibrium between unimers at a concentration equal to the *CMC*$_a$ and micelles of a constant number of chains, N_{agg}. This is expressed by the expressions shown below

$$N_{agg}\ \text{unimers} \leftrightarrow \text{micelle} \quad \text{(S4)}$$

$$[\text{unimers}]=\begin{cases}[\text{polymer}], & [\text{polymer}] < CMC_a \\ CMC_a, & [\text{polymer}] \geq CMC_a\end{cases} \quad \text{(S5)}$$

From a mol balance on the system, we can express the concentration of micelles as a function of the total concentration of polymer, chosen by the experimenter, the concentration of unimers and the aggregation number:

$$[\text{micelles}]=\frac{[\text{polymer}]-[\text{unimer}]}{N_{agg}} \tag{S6}$$

Now, we can express equation S3 using with a conditional expressing using only experimental quantities, [polymer], and model parameters: CMC_a, N_{agg}, A, and B:

$$I_{ex}=\begin{cases} A[\text{polymer}], & [\text{polymer}]<CMC_a \\ A\times CMC_a + B\times \frac{[\text{polymer}]-CMC_a}{N_{agg}}, & [\text{polymer}]\geq CMC_a \end{cases} \tag{S7}$$

When this model was applied to the DLS data to evaluate the CMC, the same trend between M_n and CMC was observed as for the analysis method reported in the main text.

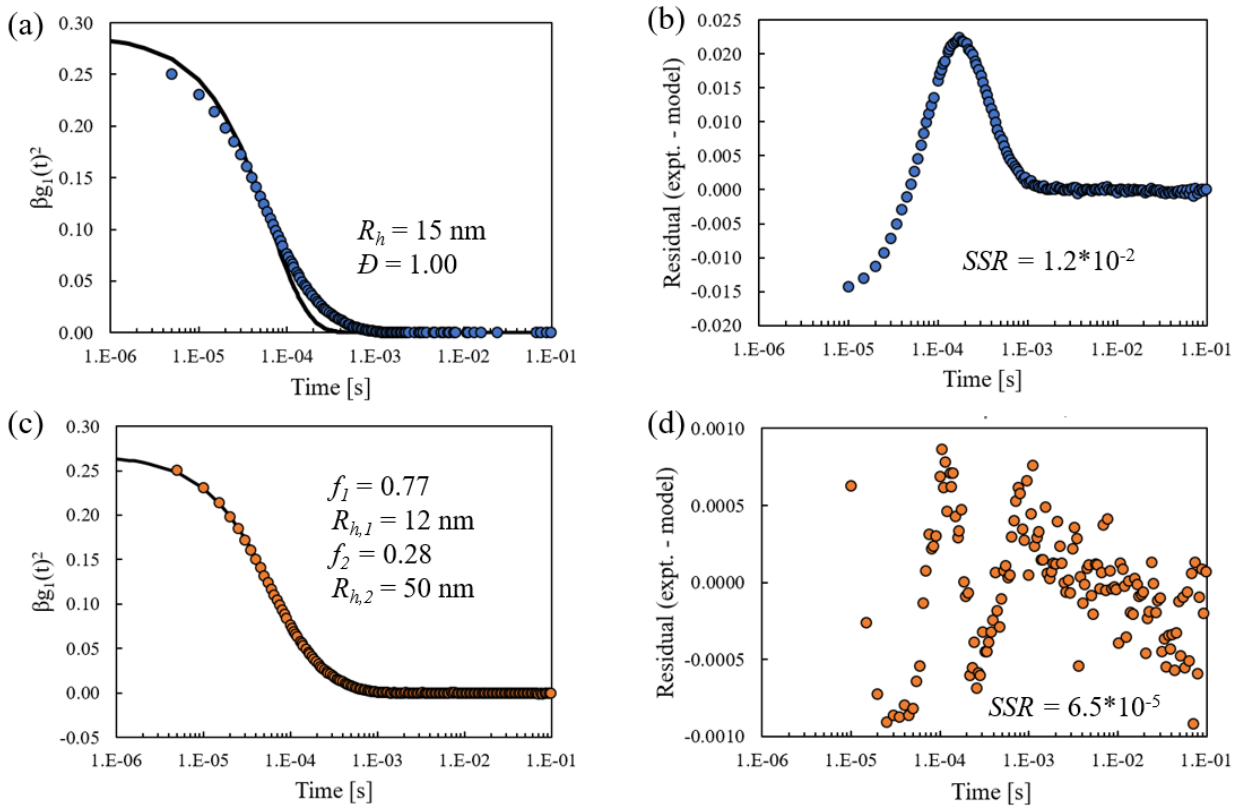

Figure 3.16: DLS correlation function fitting for micelle solution of *B*-$E_{10}^{43}P_5^{15}$ at 10 mg/mL and 37 °C. (a) Fitting of the electric field autocorrelation function to the second cumulant model (Eq. S1). (b) Residuals between the data and the fit for the second cumulant model. (c) Fitting of the electric field autocorrelation function to a biexponential model (Eq. S2). (d) Residuals between the data and the fit for the biexponential model.

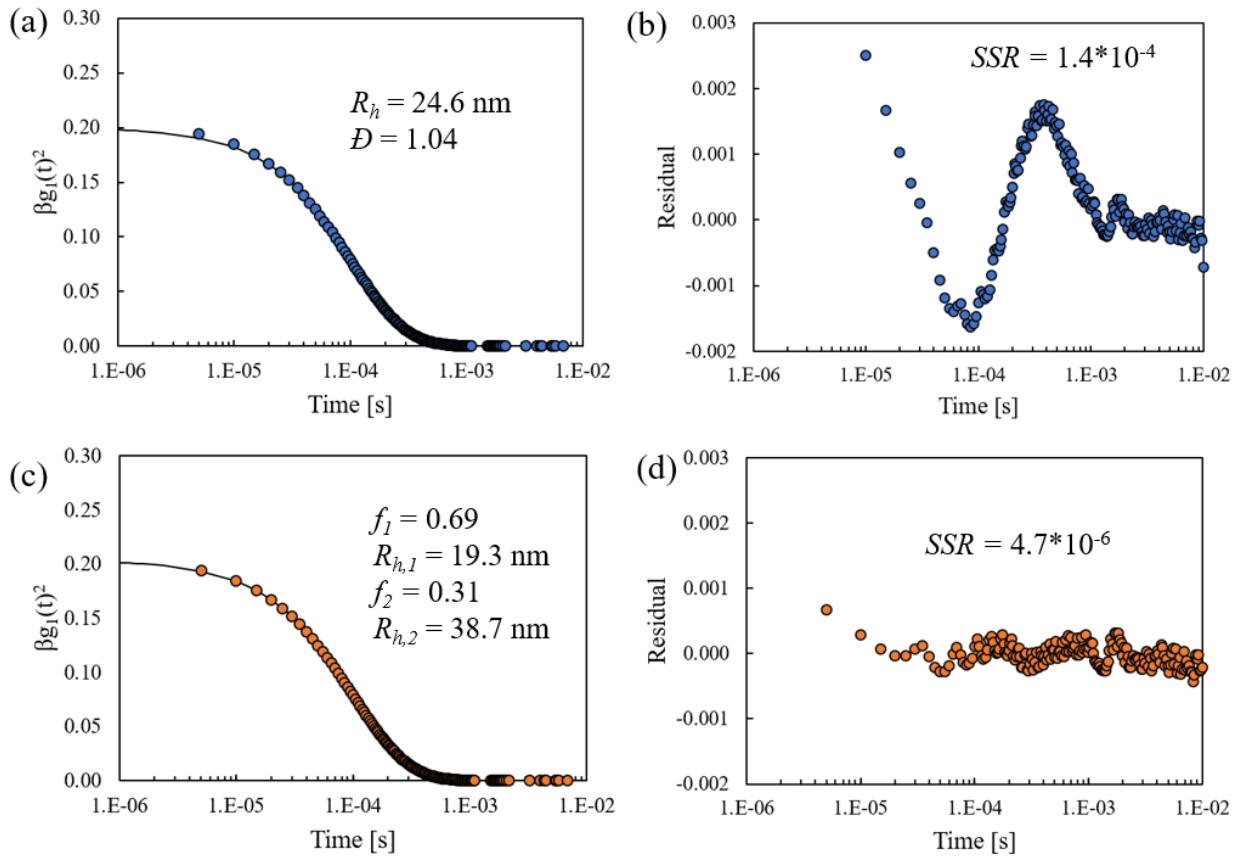

Figure 3.17: DLS correlation function fitting for micelle solution of *B*-$E_{21}^{43}P_{11}^{15}$ at 10 mg/mL and 37 °C. (a) Fitting of the electric field autocorrelation function to the second cumulant model (Eq. S1). (b) Residuals between the data and the fit for the second cumulant model. (c) Fitting of the electric field autocorrelation function to a biexponential model (Eq. S2). (d) Residuals between the data and the fit for the biexponential model.

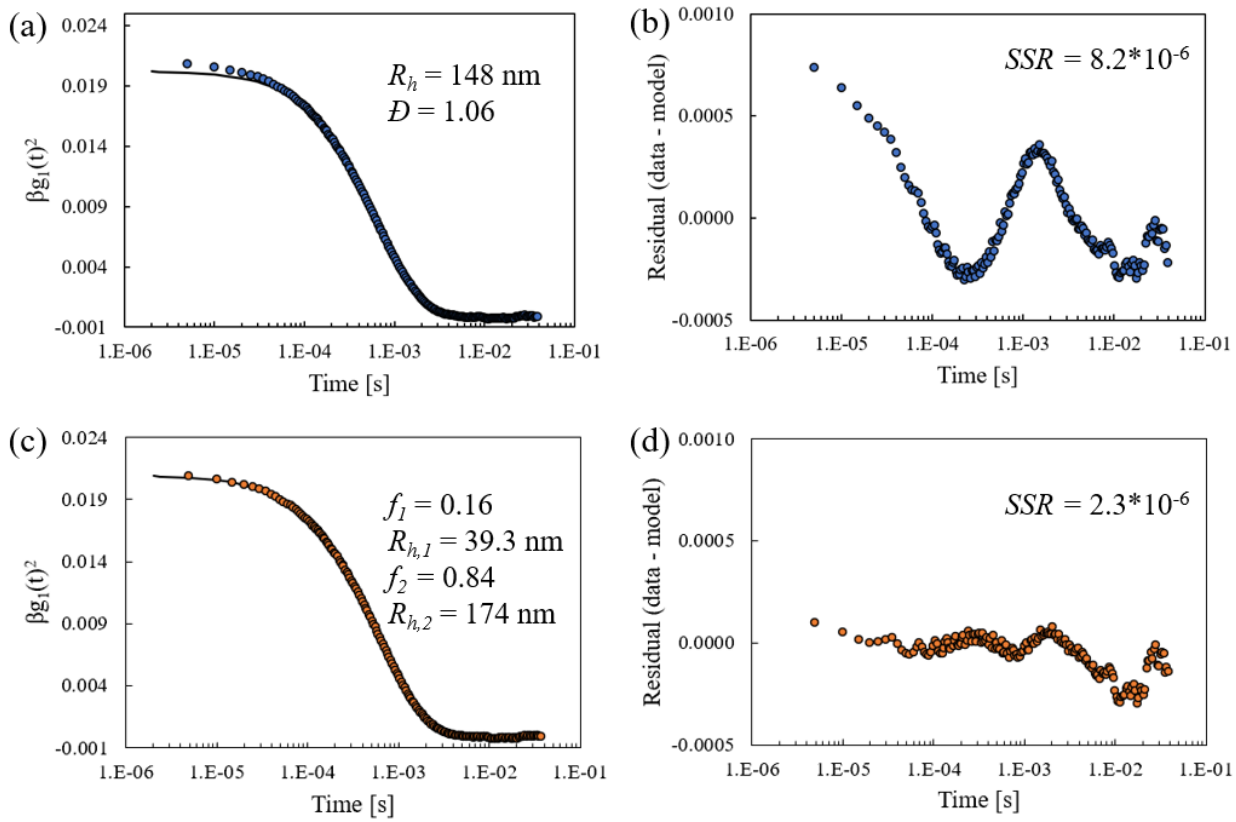

Figure 3.18: DLS correlation function fitting for micelle solution of *B*-$E^{43}_{160}P^{15}_{43}$ at 10 mg/mL and 37 °C. (a) Fitting of the electric field autocorrelation function to the second cumulant model (Eq. S1). (b) Residuals between the data and the fit for the second cumulant model. (c) Fitting of the electric field autocorrelation function to a biexponential model (Eq. S2). (d) Residuals between the data and the fit for the biexponential model.

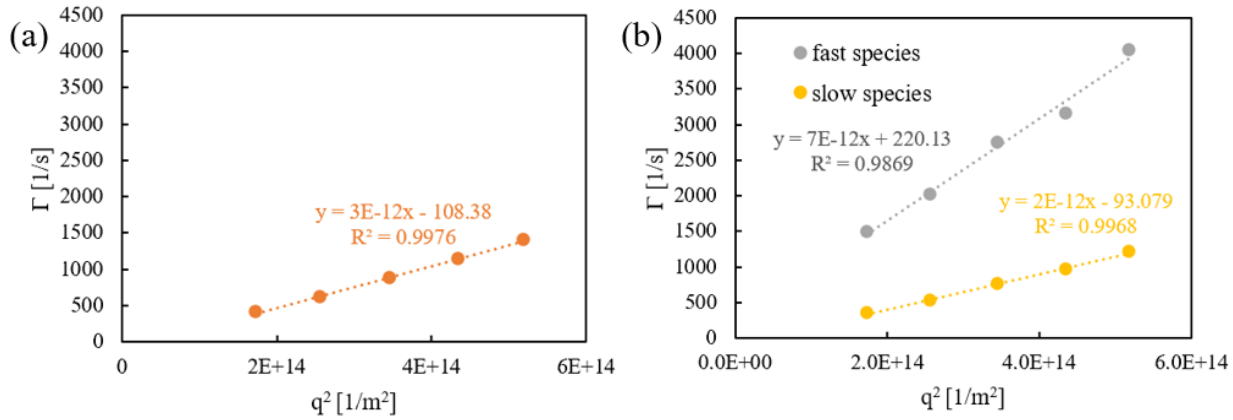

Figure 3.19: Multi-angle DLS data for micelle solution of *B*-$E^{43}_{160}P^{15}_{43}$ at 3 mg/mL and 37 °C. (a) Γ found from the second cumulant model (Eq. S1). The slope gives a diffusion coefficient of 3×10^{-12} m^2/s. Based on the Stokes-Einstein equation this corresponds to a hydrodynamic radius of R_h = 110 nm. The near zero intercept and the high R^2 value suggests the relaxation process is diffusive. (b) Γ_1 and Γ_2 found from the biexponential model (Eq. S2). Similarly to the description of part (a), the slopes in this figure correspond to species with hydrodynamic radii of $R_{h,1}$ = 47 nm and $R_{h,2}$ = 160 nm. The linearity and high R^2 values suggest that both relaxation processes are diffusive.

Table 3.3: summary of biexponential model fitting of DLS data for 10 mg/mL micelle solutions.

Polymer	M_n [g/mol]	$Đ$	wt% PEO	wt% NB	$R_{h,\,small}$ [nm]	$R_{h,\,large}$ [nm]	f_{large}
B-$E^{43}_{10}P^{15}_{5}$	26200	1.07	72	8	12 ± 0.2[a]	53 ± 2[a]	0.32 ± 0.04[a]
B-$E^{43}_{21}P^{15}_{11}$	55000	1.10	74	8	19	39	0.31
B-$E^{43}_{160}P^{15}_{43}$	394000	1.15	80	7	39	170	0.84

[a]Error is the standard deviation of three independent replicates.

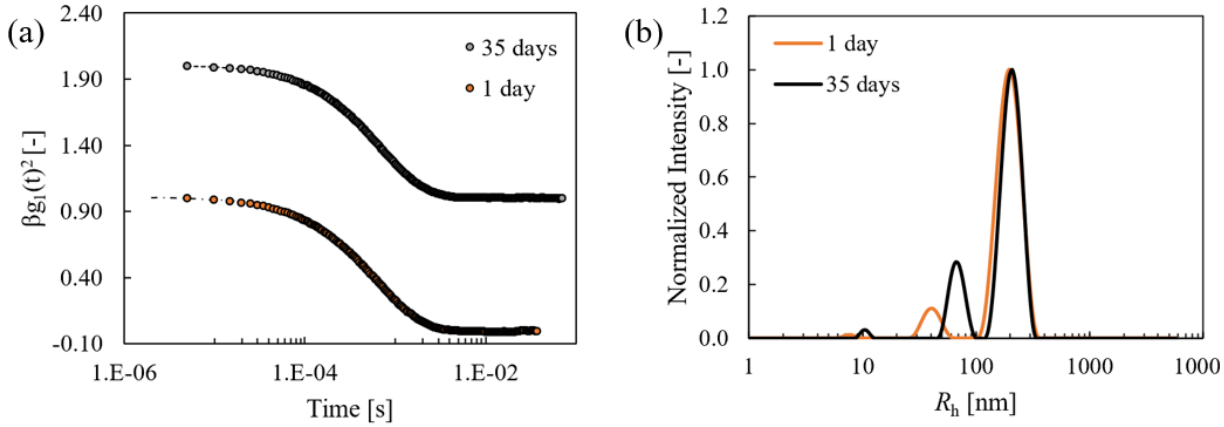

Figure 3.20: stability of micelle size distribution over a 35 day anneal at 37 °C. After the day 1 measurement was performed, the sample was recovered and placed in a sealed scintillation vial on a hotplate for 35 days. (a) Correlation function and analysis of a micellar solution of *B*-$E_{160}^{43}P_{43}^{15}$ at 10 mg/mL. The data is fit to the biexponential model and the data is summarized in Table S2, below. (b) REPES analysis of the same correlation functions shown in panel (a). Both size distributions show a bimodal population and the sizes of both populations are within error.

Table 3.4: effect of anneal time on biexponential model fitting parameters

Time of anneal	$R_{h,\,small}$ [nm][c]	$R_{h,\,large}$ [nm][c]	f_{large}
1 day	39	170	0.84
35 days	64	200	0.89

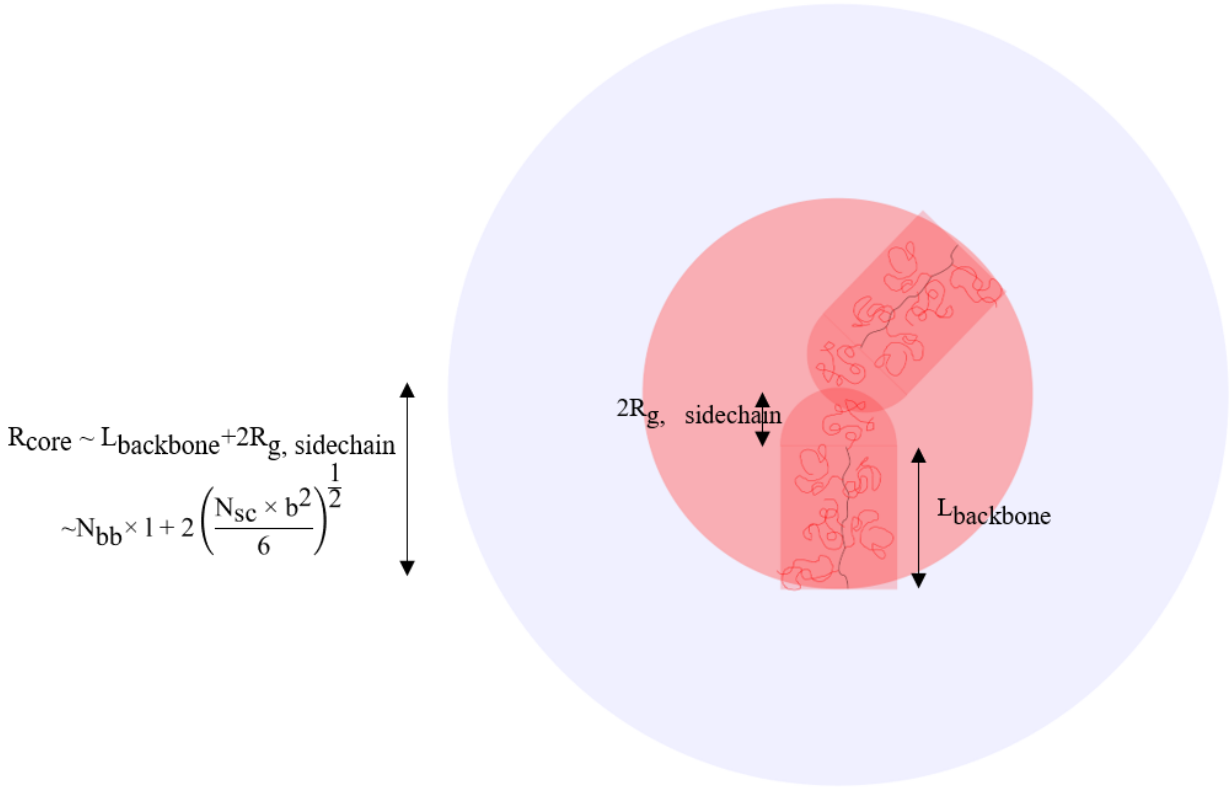

Figure 3.21: model of micelle core dimensions. This sketch illustrates the model used to estimate the micelle core dimensions from the polymer backbone and side chain degrees of polymerization. The model assumes that the backbone is a rigid rod, the side chains are gaussian coils, and there is no chain overlap; thus, this model serves as an upper bound of micelle core dimensions. Note this is a two-dimensional projection, so the side chain crowding is exaggerated because in three dimensions, side chains will have more space to avoid one another.

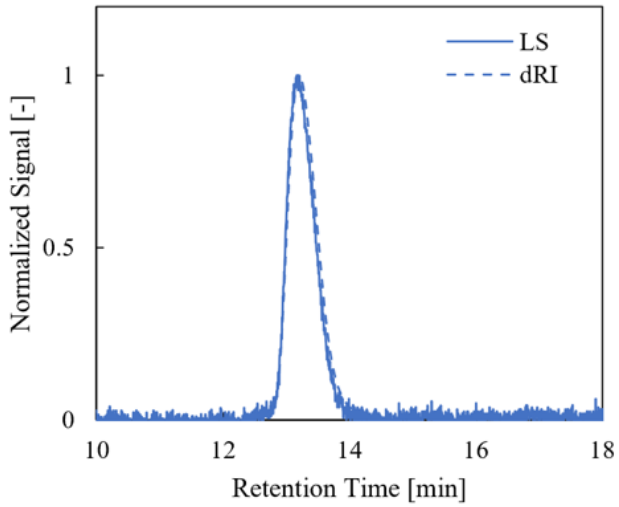

Figure 3.22: SEC characterization of linear PEO20k (*L*-E$_{455}$). The refractive index (dashed) and light scattering (solid) traces overlap and show a single peak with narrow distribution. From Zimm analysis of the light scattering data, the M_n = 20,000 g/mol and $Đ$ = 1.10.

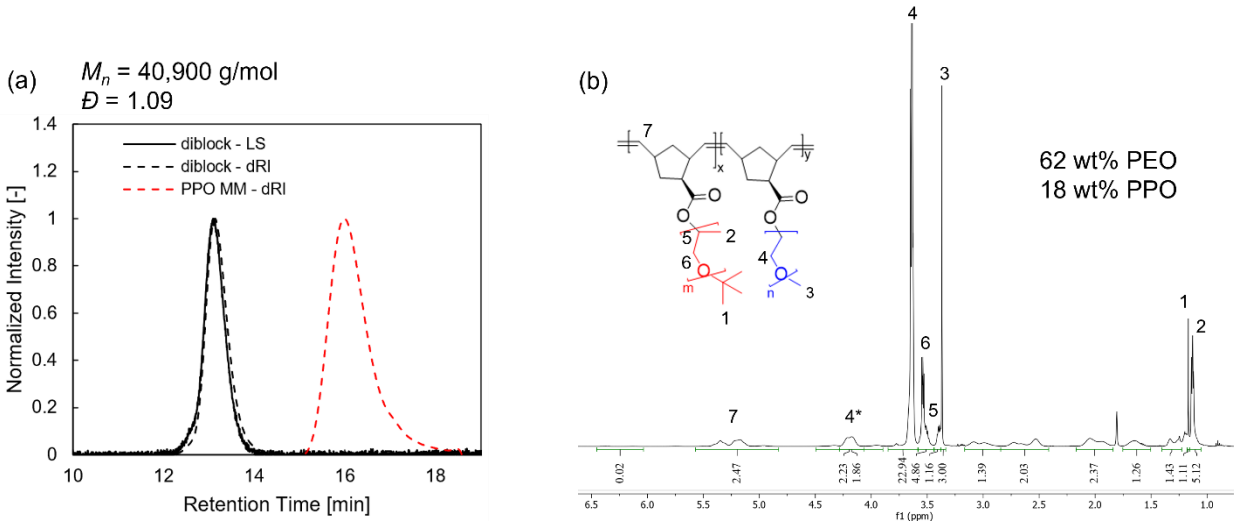

Figure 3.23: Characterization data for ***B*-E$_{54}^{10}$-P$_8^{15}$**. (a) SEC traces of the PPO macromonomer and the resulting diblock copolymer. Dashed lines are traces from the differential refractive index detector and the solid line is the light scattering detector. (b) ^{1}H NMR spectrum of the purified final product. Peaks 1 and 4* were used to estimate the composition of the diblock, where * denotes the side chain unit adjacent to the ester.

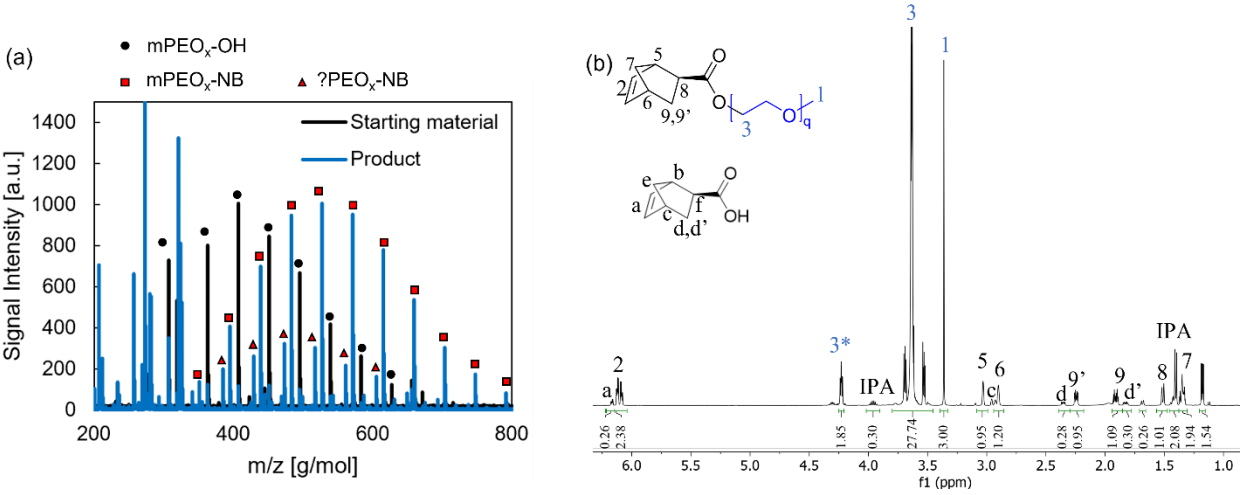

Figure 3.24: Characterization data for ***L*-E$_{10}$-OH and *L*-E$_{10}$-NB**. (a) MALDI ToF characterization of the starting material (black) and the purified product (blue). For the product, M_n = 604.9 g/mol ($N_{sc} \approx 10$) and $Đ$ = 1.07. The family of peaks labelled with red squares is the desired product and constitutes 69 mol% of the sample. (b) ^{1}H NMR spectrum of purified product. The integration and shape of the peaks at 6.0-6.2 ppm indicate that there is residual NB-COOH in the sample. This impurity is difficult to remove and makes up < 20% of the total norbornene present so was deemed acceptable.

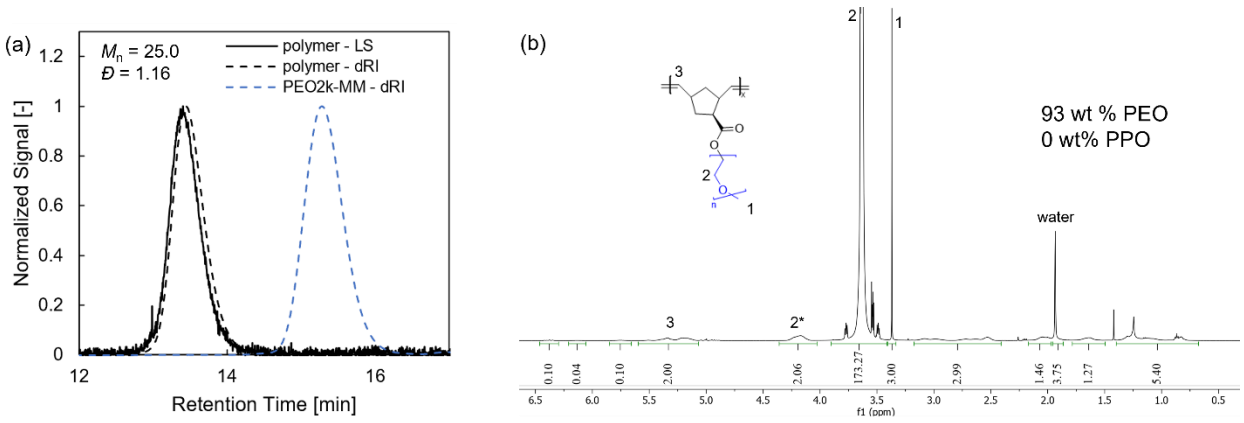

Figure 3.25: Characterization data for ***B*-E$_{12}$^{43}**. (a) SEC traces of the PEO macromonomer and the resulting bottlebrush PEO. Dashed lines are traces from the differential refractive index detector and the solid line is the light scattering detector. (b) ^{1}H NMR spectrum of the purified final product.

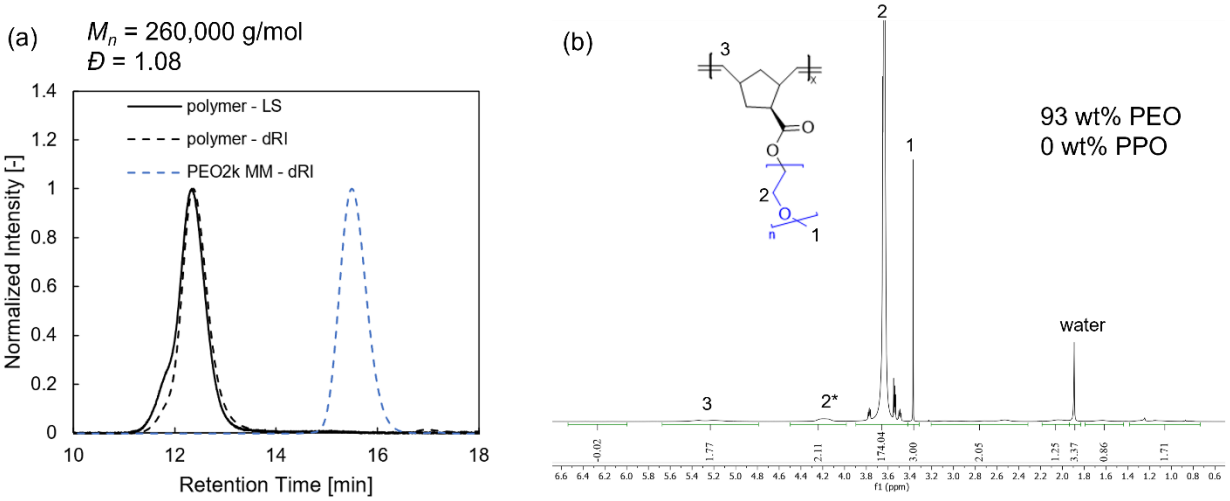

Figure 3.26: Characterization data for ***B*-E$_{126}$^{43}**. (a) SEC traces of the PEO macromonomer and the resulting bottlebrush PEO. Dashed lines are traces from the differential refractive index detector and the solid line is the light scattering detector. (b) ^{1}H NMR spectrum of the purified final product. The composition of PEO matches the composition of the PEO in the macromonomer since this is a brush "homo-polymer."

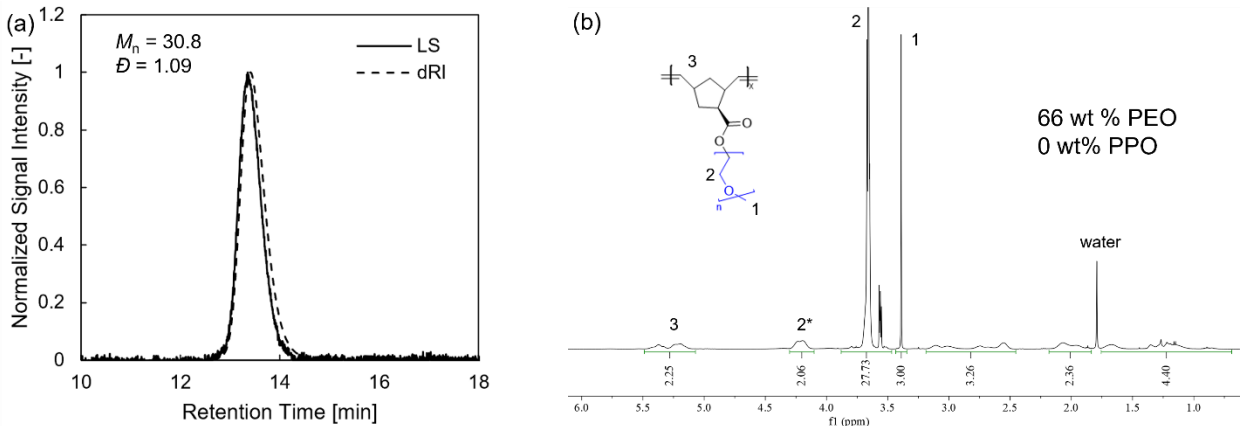

Figure 3.27: Characterization data for ***B*-E$_{50}$^{10}**. (a) SEC trace of the bottlebrush PEO. Dashed line is dRI and solid line is light scattering detectors, respectively. (b) ^{1}H NMR spectrum of the purified bottlebrush PEO.

Chapter 4: Effect of bottlebrush poloxamer architecture on binding to liposomes and protection of cells against osmotic stress

This chapter was adapted from Hassler, J.F.; Crabtree, A.A.; Liberman, L.; Bates, F.S.; Hackel, B.J.; Lodge, T.P. *Biomacromolecules.* 2023, 1, 449-461.

4.1 Motivation

Many pathologies are linked to cell membrane damage such as radiation exposure, electric shock, ischemia/ reperfusion injuries occurring after heart attacks and strokes, and Duchenne's muscular dystrophy.[9,13,123,126,127] This damage prevents the cell from regulating transport of nutrients and waste and from maintaining a transmembrane ion gradient, resulting in cell and tissue death.[12] Poloxamers, a family of commercially available block polymer amphiphiles consisting of poly(ethylene oxide) (PEO) and poly(propylene oxide) (PPO) blocks, have demonstrated *in vitro* efficacy in protecting cardiomyocyte and neuronal cells from oxidative stress,[69,119,122] reduced permeability of damaged blood brain barriers,[235] proven *in vivo* efficacy in mouse and pig ischemia/ reperfusion models,[120,124] and enabled heart and skeletal muscle function of dystrophic mice to resemble that of healthy mice.[7,131]

Over the past two decades, many reports have used simplified abiotic systems consisting of lipid monolayers, bilayers, or liposomes of various lipid compositions to explore the mechanism(s) of membrane stabilization. Experiments on lipid monolayers have revealed that poloxamers preferentially insert into damaged regions due to the reduced surface pressure.[12,66,71,89] Additionally, longer PPO blocks lead to increased membrane affinity,[85] a decrease in lipid diffusivity,[80] and different bound conformations when longer than the thickness of the acyl region of the lipid bilayer.[189,190,236] The PEO block also plays an important role because polymers that are too hydrophobic accelerate lipid flip-flops[141] and disrupt lipid packing,[237] while polymers of intermediate hydrophilicity protect membranes under stress.[6,81] These results can be summarized by the anchor and chain hypothesis which asserts that the PPO block drives binding by inserting

into the acyl region of the lipid bilayer while the PEO block interacts with the lipid headgroup and bound water layer, with both components being necessary for optimal performance.[83,143,188,191] Despite this model of polymer-membrane interactions, a complete understanding of the stabilization mechanism is lacking, hindering the engineering of more effective therapeutics.

Bottlebrush polymers consist of polymeric side chains densely grafted onto a central backbone, characterized by the backbone degree of polymerization (N_{bb}), the side chain degree of polymerization (N_{sc}), and the average degree of polymerization between side chains (N_g).[238] Compared to linear polymers, the steric repulsions among adjacent side chains leads to larger persistence lengths and reduced entanglement densities.[149,192,194] Importantly, polymer properties and interactions with other macromolecules can be tuned by manipulating bottlebrush architectural parameters. For example, the segmental relaxation time (chain mobility) is a function of side chain length.[148,239,240] Longer side chains decrease steric constraints at the units far from the backbone, which enhances interdigitation between chains.[153] Therefore, by combining an efficient strategy to synthesize bottlebrush polymers with PEO and PPO side chains — denoted bottlebrush poloxamers (BBPs)[109] — with knowledge of parameter-property relationships, the bottlebrush architecture can be used as a tool to inform the stabilization mechanism(s) of block polymers.

In this study, we compared a conventional, linear poloxamer to an analogous BBP and found that the BBP has a higher membrane affinity but similar *in vitro* protection efficacy. To better understand the effect of bottlebrush architectural parameters on membrane affinity, we performed systematic molecular variations and applied a pulsed-field-gradient NMR (PFG-NMR) binding assay to elucidate the roles of the hydrophobic backbone, overall molecular weight, side chain length asymmetry, and statistical versus block architectures. To our knowledge, this is the first report of interactions between BBPs and lipid bilayers, and the results should inform engineering of more effective membrane binders and elucidate mechanisms of polymer-lipid bilayer interactions.

4.2 Experimental

Materials: The following materials were purchased from Sigma Aldrich and used without further purification: propylene oxide (>99.0%), 18-crown-6 ether, tetrahydrofuran (ACS reagent, 97%, stabilized with 250 ppm butylated hydroxytoluene), butyl-magnesium chloride, potassium tert-butoxide, poly(ethylene oxide) monomethyl ether (M_n ≈ 2000 g/mol), poly(ethylene oxide) monomethyl ether (M_n ≈ 350 g/mol), N,N′ diisopropylcarbodiimide (99%), 4-dimethylaminopyridine (>99%), exo-5-norbornene-2-carboxylic acid (97%), α-cyano-4-hydroxycinnamic acid, sodium trifluoroacetate, Grubbs second generation catalyst M204, pyridine (>99%), ethyl vinyl ether (stabilized with 0.1% KOH, 99%), benzene (ACS reagent, 99%), sodium chloride (99.5%), magnesium chloride (97%), calcium chloride (anhydrous, 96%), potassium chloride (>99%), HEPES buffer (99.5%), and Triton X-100. The following materials were purchased from Fisher Scientific and used as received: methanol (HPLC grade), dichloromethane (DCM; ACS reagent, anhydrous, 99.8%), diethyl ether (anhydrous), chloroform, and diatomaceous earth. NMR solvents deuterium oxide and chloroform-d (99.8 atom% d) were purchased from Cambridge Isotope Laboratories. 16:0-18:1 1-palmitoyl-2-oleoyl-glycero-3-phosphocholine (POPC) was purchased from Avanti Polar Lipids and used as received. A lactate dehydrogenase (LDH) assay kit was purchased from Pointe Scientific Inc. SiliaMetS DMT was obtained from Silicycle.

Synthesis and characterization of BBPs: Synthesis methods were described in detail in a previous publication.[109] Briefly, norbornene-functionalized macromonomers (MMs) were synthesized by chain-end modification of mono-alcohol functionalized poly(propylene oxide) (PPO) and poly(ethylene oxide) (PEO). The PPO polymers were prepared via anionic polymerization.[206] The PEO polymers were purchased and freeze dried from benzene. For this study, three MMs were synthesized: PPO with M_n = 1090 g/mol (PPO-1k), PEO with M_n = 2060 g/mol (PEO-2k), and PEO with M_n = 600 g/mol (PEO-0.6k). To install the norbornene functional group, a condensation reaction was performed between 1 equiv of mono-alcohol functionalized polymer and 1.5 equiv of exo-5-norbornene-2-carboxylic acid in the presence of 0.2 equiv of 4-dimethylaminopyridine

and 1.5 equiv of N,N′ diisopropylcarbodiimide at room temperature in anhydrous DCM at a polymer concentration of 0.05 M. Condensation reactions of PEO MMs were run for 48 h while the PPO MM required 7 d. Note that in the case of PPO, a hydrogenation reaction was performed prior to the condensation reaction to eliminate alkene α-chain end impurities.[109] Percent norbornene functionality was assessed via matrix-assisted laser desorption/ionization time of flight (MALDI-ToF) spectrometry and ^{1}H NMR spectroscopy and was found to be quantitative for PPO-1k,[109] 94% for PEO-2k,[109] and 92% for PEO-0.6k (Figure S4.1). PEO-2k was purified via two precipitations in cold diethyl ether and PPO-1k and PEO-0.6k were purified by vacuum drying at 40 °C for 7 d.

After macromonomer purification, two sequential ring-opening metathesis polymerization reactions were performed in a glovebox with an argon atmosphere to yield diblock BBPs. An example protocol is: 1 equiv of Grubbs third generation catalyst (prepared by methods reported by Love, et al.)[233] was added to the reaction vessel containing the PPO-1k MM dissolved in anhydrous DCM at 0.05 M. The reaction was stirred for 10 min, and then the second MM was added also at 0.05 M. After 10 min, the reaction was removed from the glovebox and was diluted by half with a 1:1 (v:v) mixture of ethyl vinyl ether:DCM to quench the reaction. This mixture was then stirred over Silicycle for a minimum of 3 h to chelate the deactivated catalyst, which was then removed by filtering through a column of Celite. The solvent was removed via rotary evaporation and the product was freeze-dried from benzene. For statistical copolymers, two macromonomers were mixed in the desired stoichiometric ratios and then the catalyst was added.

The conversion and composition of the resulting polymers were characterized by ^{1}H NMR spectroscopy on a Bruker Avance III HD-500 MHz spectrometer equipped with a 5 mm Prodigy TCI cryoprobe. The molecular weight distributions were characterized by size exclusion chromatography equipped with a Wyatt Dawn Heleos II multi-angle light scattering detector. The refractive index increment (dn/dc) of the BBPs was taken as the mass fraction weighted average

of the dn/dc values of PEO (0.068 mL/g) and PPO (0.087 mL/g) in tetrahydrofuran.[85,234,202] Characterization data for all polymers are shown in Figures S4.11-S4.26.

Liposome production: POPC powder, typically ~15 mg, was dissolved in a minimal amount of chloroform. The chloroform was then evaporated using a gentle, filtered stream of nitrogen (0.4 μm PTFE filter) to yield a thin film of lipid around the vial walls. This film was then hydrated with 1 mL of D_2O and placed on a vortex plate for 1 h. The resulting disperse mixture of vesicles was then extruded 29 times through a membrane with 200 nm diameter pores using an Avanti mini-extruder apparatus. This was done at room temperature, which was above the melting temperature of POPC ($T_m = -2$ °C).

Dynamic Light Scattering: To assess the quality of the liposome preparation, the POPC liposome stock solution was diluted to 1750 μM in D_2O, filtered with a 0.2 μm GHP filter into a glass test tube (200 mm x 7 mm with 5 mm inner diameter) and multi-angle dynamic light scattering (DLS) was performed using a Brookhaven BI-200SM instrument with a 637 nm laser and a refractive index matching bath. Autocorrelation functions were recorded for 4 min, at angles of 60°, 75°, 90°, 105°, and 120° over a delay time range of 1 μs – 100 ms. The data were then fit to the second-order cumulant expansion model and the bi-exponential model, and in all cases the second-order cumulant expansion model yielded equally random residuals with fewer fitting parameters, indicating a superior fit and therefore a single relaxation mode.[109]

Pulsed-field-gradient-NMR (PFG-NMR) binding assay: A 1750 μM POPC liposome stock solution and a 28 μM polymer stock solution were prepared in D_2O. These stock solutions were then combined in a 1:1 volume ratio to yield the PFG-NMR sample with 875 μM POPC and 14 μM polymer. The polymer and lipid samples were incubated at room temperature for a minimum of 4 h to ensure that a steady state was reached.[85] Polymer-only control samples were prepared by diluting the polymer stock with D_2O to a final concentration of 14 μM.

PFG-NMR experiments were conducted on a Bruker Avance III 500 MHz spectrometer equipped with a 5 mm TBO triple resonance PFG probe. The ledbpg2s sequence was performed

with 32 scans, an acquisition time and delay time of 1s, a diffusion time of 700 ms, a gradient pulse duration of 5 ms, and a gradient strength ranging from 2–95%. All measurements were taken at 27 ℃. The PEO methylene signal was analyzed in all cases because it has the highest signal-to-noise ratio. Complete dissolution of all BBP samples was verified by the homogeneous, clear appearance of all samples, the existence of only two populations in the polymer-only control samples (free chains and micelles), and the ability of the spectrometer to properly lock and shim on the sample which would be hindered by any insoluble particulates.

Cloud point measurements: Cloud point measurements were performed on a home-built apparatus. A 10 mW HeNe laser (633 nm) passes through a neutral density filter, the sample chamber, and then is focused by a lens onto a photodiode detector. Samples were sealed in glass ampoules and placed in the temperature-controlled sample chamber. The samples were heated from room temperature to 95 ℃ at a rate of 0.5 ℃/min, then a fan was turned on and the sample cooled by convection for another 2 h. The transmitted light was normalized by the maximum intensity during each sweep.

Osmotic stress in vitro protection assay: C2C12 murine myoblasts were cultured using growth media (20% fetal bovine serum, 1% penicillin-streptomycin, 79% Dulbecco's modified Eagle medium) in a humidified chamber at 37 ℃. Cells were plated in a 96-well plate with 5000 cells per well and grown for 48 h. Isotonic (330 mOsm; 140 mM NaCl, 5 mM KCl, 2.5 mM $CaCl_2$, 2 mM $MgCl_2$, and 10 mM HEPES) and hypotonic (75 mOsm; 20 mM NaCl, 5 mM KCl, 2.5 mM $CaCl_2$, 2 mM $MgCl_2$, and 10 mM HEPES) buffers were prepared and adjusted to pH 7.2 by the addition of sodium hydroxide. Polymer solutions in isotonic and hypotonic buffer were prepared and diluted as needed. Once grown to approximately 70% confluency, growth media was removed from the cells and 100 μL of isotonic buffer solutions, with or without polymer, was added to the cells for 30 min. Next, hypotonic buffer solutions replaced the isotonic buffer for 50 min. This was followed by an isotonic recovery period where hypotonic buffer was removed, and isotonic buffer

solutions were added for 30 min. Lastly, the isotonic buffer was removed, and cells were lysed with 0.01% Triton X-100 for 50 min to ensure total lactate dehydrogenase (LDH) release.[6]

Supernatants from each step (isotonic, hypotonic, isotonic recovery, and Triton) were retained, and the amount of LDH present was quantified using the LDH assay kit. The quantity of LDH in the supernatants is indicative of membrane integrity: if the membrane is damaged, LDH will leak out of the cell into the solution.[6] The assay utilizes the fact that LDH catalyzes the reduction of nicotinamide adenine dinucleotide (NAD) to NADH, which absorbs light at 340 nm. Thus, the rate of increase in light absorption over 120 min is related to the concentration of LDH present in the supernatant. The total amount of LDH released is calculated per well, and the percentage of total LDH for each step is then normalized to the corresponding step in the untreated control (no polymer). This normalization can result in percent LDH releases above 100%, indicating more LDH is released in the treated sample than the untreated control. In this assay, the cell membrane is stretched during the hypoosmotic step as the cell swells; however, maximal LDH release occurs during isotonic recovery due to the net flow of solution out of the cell. Therefore, data from the isotonic recovery step is presented here because it best distinguishes performance differences among the polymers. *In vitro* experiments were carried out on three unique cell passages with three technical replicates each for a total of 9 independent replicates.

Cryo-TEM: Cryo-TEM samples were prepared inside a Vitrobot system (Thermo Fisher Scientific) kept at room temperature and 100% humidity. A 3 μL drop of sample solution was placed onto a perforated carbon support film on a copper TEM grid (lacey Formvar/carbon films on 200 mesh Cu grids, Ted Pella, Inc., Redding, CA, U.S.A), held by tweezers inside the Vitrobot, followed by blotting the sample with a filter paper into a thin film, and plunging into liquid ethane for vitrification. Before sample preparation, the TEM grids were cleaned with glow-discharge air-plasma (PELCO EasiGlow, Ted Pella, Inc.) to increase the support film hydrophilicity. Imaging was performed with a FEI Tecnai G2 F30 field emission gun TEM operated with an acceleration

voltage of 300 kV, and using a Gatan 626 cryo-holder, kept at –175 °C. Images were recorded digitally using a Gatan UltraScan 4000 4k × 4k CCD camera.

4.3 Results

Polymer-lipid bilayer association of linear and bottlebrush poloxamers: Single-component POPC liposomes were used as model cell membranes to probe polymer-lipid bilayer binding. This model has been applied extensively because POPC is the most abundant lipid in the exterior membrane of mammalian cells, so this simplified model best balances the need for efficiency and physiological relevance.[85,87,241] Scheme 4.1 shows the structures of the molecules used in this report. The nomenclature adopted for the BBPs is B-$\mathrm{E}^{N_{sc}}_{N_{bb}}\mathrm{P}^{N_{sc}}_{N_{bb}}$ where B indicates the brush architecture, E the PEO block, P the PPO block, and N_{sc} and N_{bb} are the average side chain and backbone degrees of polymerization, respectively.

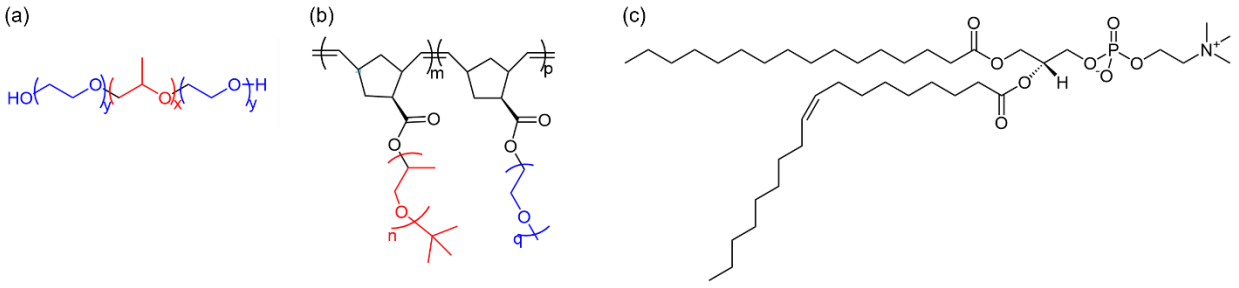

Scheme 4.1: (a) Traditional poloxamer with a linear architecture, represented by L-$\mathrm{E_yP_xE_y}$ throughout the text. (b) Bottlebrush poloxamer represented by B-$\mathrm{E}^{q}_{p}\mathrm{P}^{n}_{m}$. (c) 16:0-18:1 POPC lipid used for all liposomes in this study.

Liposome size and dispersity were assessed via multi-angle DLS. The autocorrelation function from each angle was fit to the second-order cumulant expansion model (eqn S.1) and a representative R_h and $Đ$ for the liposomes is 97 nm and 1.03, respectively, consistent with the extrusion protocol. More details of the DLS analysis can be found in Figure S4.2 of the Supporting Information. After verifying liposome quality, we incubated the liposomes with the polymer of interest for at least 4 h to allow the system to approach a steady state. We then applied PFG-NMR spectroscopy to quantify the fraction of chains bound to the liposomes. In a PFG-NMR experiment,

the intensity of all proton echo signals decays exponentially as the magnetic field gradient strength (G) increases. The rate of signal attenuation is related to the translational diffusion coefficient through eqn 1:

$$\frac{I}{I_0} = \exp\left(-\gamma^2\delta^2G^2D\left(\Delta-\frac{\delta}{3}\right)\right) \tag{4.1}$$

where I is the signal intensity at the given gradient strength, I_0 is the signal intensity with no gradient, G is the magnetic field gradient strength (2–95%), Δ is the diffusion time (700 ms), δ is the pulse duration (5 ms), γ is the gyromagnetic ration of a proton (42.6 MHz/T), and D is the translational diffusion coefficient of the species contributing to the selected ^{1}H NMR signal. Once D is determined, the Stokes-Einstein equation (eqn S.2) can be applied to calculate R_h. In our system, we are interested in resolving free polymer and liposome-bound polymer, so it is important to note that when multiple populations are present, if the length scales of the different states differ by more than a factor of ~2, they can be resolved as separate rates of decay.[165] In this case, the PFG-NMR data can be described by an expansion of exponentials shown by eqn 2:

$$\frac{I}{I_0} = \sum_{i=1}^{n} f_i \exp\left(-\gamma^2\delta^2G^2D_i\left(\Delta-\frac{\delta}{3}\right)\right) \tag{4.2}$$

where f_i and D_i are the mole fraction and diffusion coefficient of the ith species.[85,86,146,165,242]

Figure 4.1a shows the PFG-NMR results for the commercial poloxamer F127 (L-$E_{93}P_{54}E_{93}$), which a previous study found to be the linear poloxamer with the highest membrane affinity of those tested.[85] When the natural logarithm of the normalized intensity is plotted against gradient strength, the magnitude of the slope of the decay curve gives the diffusion coefficient (D). In Figure 4.1a, the decay curve for the polymer-only control (open symbols) is linear and can be described by a single exponential decay, indicating a single population with R_h = 3.1 ± 0.1 nm, which is consistent with the estimate for L-$E_{93}P_{54}E_{93}$ if it were a Gaussian coil (~2.8 nm).[163] Polymer binding to the liposomes can be seen by comparing the polymer-only control to the polymer+POPC decay curves. In the latter, polymer binding to liposomes results in the onset of a second regime with a weaker slope at high values of the x-coordinate.[85,87] Fitting the decay curve to a two-term

expansion of eqn 2 (bi-exponential model) yields an estimate of 2.3 ± 0.9 mol% of the *L*-$E_{93}P_{54}E_{93}$ chains bound to the liposomes with an R_h = 26 ± 6.1 nm.

We note that there is a significant discrepancy between the size estimates for the liposomes from PFG-NMR and DLS. This has been observed in the past and is attributed to a combination of two factors (*i*) DLS emphasizing large species because they scatter light more intensely, and (*ii*) PFG-NMR underestimating the size of liposomes because NMR signals from the larger liposomes in the distribution relax more slowly, leading to signal broadening.[20,85,87] Analysis of cryo-TEM images of liposomes extruded through a 200 nm diameter membrane yielded an estimate for the liposome radius of 63 ± 29 nm, which is intermediate to the estimates from PFG-NMR and DLS.

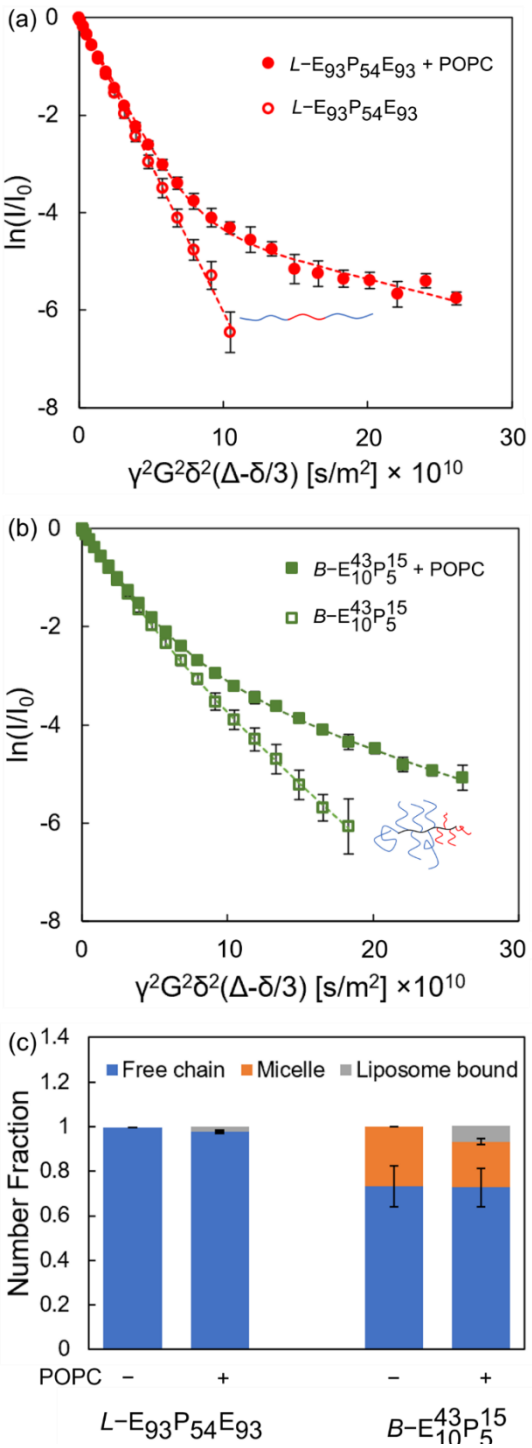

Figure 4.1: PFG-NMR binding assay reveals that a BBP binds with higher affinity than an analogous linear poloxamer. (a) Decay curves for *L*-$E_{93}P_{54}E_{93}$ polymer-only (14 μM) and polymer+POPC (14 μM polymer+875 μM POPC). (b) Decay curves for *B*-$E_{10}^{43}P_5^{15}$ polymer-only and polymer+POPC at the same conditions as panel (a). (c) Summary of the number fraction of chains in each possible state, determined by the sum of exponentials model (Equation 2). Error bars are the standard deviation of three independent measurements.

Figure 4.1b shows the PFG-NMR decay curves for *B*-$E_{10}^{43}P_5^{15}$, a BBP with a similar weight fraction of PEO and a similar number of PPO units as *L*-$E_{93}P_{54}E_{93}$. Note that a direct comparison between the linear and bottlebrush architectures where only one variable is changed is impossible, due to the backbone chemistry being unique to the bottlebrush architecture. Therefore, we chose the number of PPO units as the most appropriate variable to hold constant because the anchor and chain model of polymer-lipid interactions asserts that the PPO moiety is the primary driver of binding.[6,69,143,189] The first impact of the architectural change can be seen by comparing the two polymer-only control curves. The decay curve corresponding to *B*-$E_{10}^{43}P_5^{15}$ is non-linear, indicating the coexistence of two populations with distinct sizes. Fitting the decay curve to the bi-exponential model indicated that the sizes of the populations differ by a factor of two, which is attributed to a coexistence of free chains ($R_{h,\ free\ chains}$ = 3.9 ± 0.5 nm) and micelles ($R_{h,\ micelles}$ = 8.0 ± 1.5 nm). Because bottlebrush molecules adopt extended conformations, micelles are expected to be roughly twice as large as free chains ($R_{h,\ micelle} \sim 2R_{h,\ free\ chain}$).[109]

When liposomes are treated with *B*-$E_{10}^{43}P_5^{15}$ the decay curve shows an additional, slower decay than the polymer-only control, indicating binding to liposomes. In this case, the polymer+POPC sample contains three distinct populations: free chains, micelles, and liposome-bound polymer. To reduce the number of fitting parameters without compromising accuracy, the decay curve was fit to a constrained three-term expansion of eqn 2 (tri-exponential model). Since $R_{h,\ \text{free chains}}$ and $R_{h,\ \text{micelles}}$ are independent of liposome presence, the bi-exponential model fitting results from the polymer-only control were used to constrain the diffusion coefficients of these populations. The resulting fraction of polymer bound to liposomes is 7.3 ± 1.3 mol% and $R_{h,\ \text{liposome}}$ = 25 ± 11 nm. A Welch's T-test confirmed that the difference in bound fraction between the linear (2.3 ± 0.9 mol%) and bottlebrush (7.3 ± 1.3 mol%) poloxamers is statistically significant (p = 0.012) while there is no difference in the R_h of the liposomes (p = 0.20). The model fitting procedure described here was applied to all BBP+POPC samples. The presence of micelles in the BBP samples necessitated the use of relatively large liposomes to increase the difference in size between the micelle and bound states, particularly as the backbone degree of polymerization of the BBP is increased. Decreasing the liposome radius has been shown to increase the fraction of linear poloxamer that binds to the bilayer due to the increase in membrane curvature.[86] We expect the same trend to exist in BBPs; however, this is experimentally challenging due to the presence of micelles. As the focus of this study is to compare the binding ability of bottlebrush to linear poloxamers and to explore the bottlebrush parameter space, a single liposome size (extrusion diameter = 200 nm) was chosen.

Figure 4.1c summarizes the number fraction of chains in each state for all four decay curves. The polymer-only control for *L*-$E_{93}P_{54}E_{93}$ shows a single exponential decay, confirming no micellization at 14 μM. Adding liposomes leads to 2.3 mol% of the linear poloxamer chains binding to the bilayer vesicles. In comparison, the polymer-only control for the analogous BBP does micellize at 14 μM with 27 mol% of chains forming micelles. The fitting results for the *B*-$E_{10}^{43}P_5^{15}$+POPC sample suggest 21 mol% of chains exist in micelles and 7.3 mol% are bound to the

liposomes. A complete summary of the fitting parameters is given in Table S1 in the Supporting Information.

These results are interesting in two respects. The first is that after the introduction of liposomes, the fraction of BBP chains in the micellar state decreases while the fraction of free chains remains the same. This suggests that polymer binding to the liposome perturbs the equilibrium between free chains and micelles, at which point chain expulsion from existing micelles re-establishes equilibrium. The significant population of free chains indicates that the barrier to chain exchange is small. Furthermore, chain exchange between micelles formed by linear-*b*-brush polymers with the brush block in the core has been shown to occur relatively rapidly.[243] Secondly, the three-fold increase in the bound fraction of *B*-$E_{10}^{43}P_5^{15}$ compared to *L*-$E_{93}P_{54}E_{93}$ was surprising given the relative rigidity and steric bulk of the brush architecture. To better understand what causes this increase in membrane affinity, we systematically varied polymer composition, overall molecular weight, side chain length asymmetry, and compared statistical and block copolymers. Characterization data for all polymers are shown in Figures S4.11-S4.26 and a summary of key characteristics is given in Table 4.1. Every polymerization went to complete conversion, yielded low dispersity polymer ($Đ < 1.10$), contained no residual catalyst (absence of an NMR signal at ~20–21 ppm), and was very close to the targeted composition.

Table 4.1: Polymer Characteristics

Polymer	M_n [kDa][a]	$Đ$	wt% PEO[b]	wt% PPO[b]	N_{PEO}[c]	N_{PPO}[c]
L-$E_{87}P_{31}E_{87}$	9.4	1.19	81	19	170	31
L-$E_{93}P_{54}E_{93}$	11.3	1.14	73	27	190	54
B-$E_{10}^{43}P_{5}^{15}$	26.2	1.07	73	19	430	78
B-$E_{21}^{43}P_{11}^{15}$	55.3	1.10	72*	20*	910	160
B-$E_{168}^{43}P_{43}^{15}$	390	1.15	78	15	6900	910
B-$E_{54}^{10}P_{8}^{15}$	40.9	1.09	62	18	530	120
B-$E_{11}^{43}P_{6}^{15}$	29.4	1.06	72	20	470	94
B-E_{12}^{43}-*s*-P_{6}^{15}	32.0	1.06	75	17	530	90
B-$E_{40}^{10}P_{7}^{15}$	31.5	1.09	59	21	390	100
B-E_{40}^{10}-*s*-P_{7}^{15}	30.9	1.04	60	20	390	100
L-E_{455}	20.0	1.10	100	0	460	0
B-E_{15}^{43}	30.6	1.06	93	0	640	0
B-E_{126}^{43}	260	1.08	93	0	5400	0

[a]Determined from SEC(MALS + dRI). [b]Estimated from ^{1}H NMR spectra and knowledge of the macromonomer molecular weights after functionalization with the norbornene (MALDI-ToF) unless otherwise noted. See Figure S4.11 for a description of this calculation. *Composition reported from SEC. [c]M_n for both blocks was calculated as the product of the weight fraction of that block (including the backbone mass) and the overall molecular weight. The number of grafts in both blocks was then estimated by dividing the M_n of each block by the corresponding macromonomer molecular weight. Finally, the number of PEO/ PPO units in the chain was calculated by the product of the number of grafts and the average number of PEO/ PPO repeat units in each graft as determined via MALDI-ToF.

Effect of the hydrophobic backbone: Linear PEO homopolymers with M_n < 100 kDa do not bind to liposomes to a measurable extent, indicating that the PPO block is critical for membrane

association (Figure 4.2a). Presumably this is because PEO is too hydrophilic to drive a binding event on its own at 27 °C.[85] As shown in Scheme 1, BBPs contain a norbornene backbone, which constitutes another source of hydrophobicity that could drive binding. To evaluate this possibility, we synthesized *B*-E_{15}^{43}, which has the same total backbone degree of polymerization as the diblock discussed above (*B*-$E_{10}^{43}P_5^{15}$), but with only PEO side chains. Figure 4.2b compares the PFG-NMR data for this PEO bottlebrush homopolymer with the corresponding PEO-PPO bottlebrush diblock polymer (*B*-$E_{10}^{43}P_5^{15}$). The superposition of the polymer-only control and the polymer+POPC decay curves in the brush PEO homopolymer case is clear evidence that *B*-E_{15}^{43} does not bind to the liposomes at a detectable level. Therefore, the hydrophobicity of the backbone alone is not sufficient to drive binding, and the relatively hydrophobic PPO brush block is necessary for binding to occur. This likely reflects the steric shielding of the backbone by the PEO side chains, which could prevent the backbone from entering the acyl region of the bilayer and/or limit solvent-backbone contact.

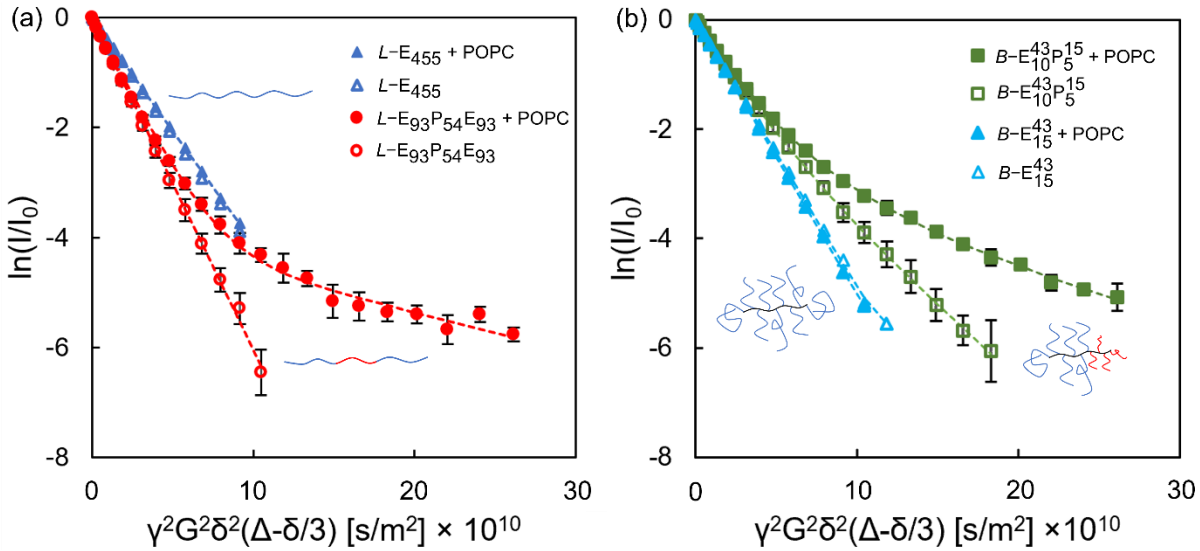

Figure 4.2: Hydrophobic backbone does not interact with lipid bilayer strongly enough to drive binding on its own. (a) Comparison of PFG-NMR decay curves for *L*-$E_{93}P_{54}E_{93}$ and a PEO homopolymer of similar size. No binding is observed for the PEO homopolymer. (b) Comparison of PFG-NMR decay curves for *B*-$E_{10}^{43}P_5^{15}$ and *B*-E_{15}^{43}, a bottlebrush PEO homopolymer with an identical backbone degree of polymerization. No binding was observed for the bottlebrush PEO homopolymer. Error bars are the standard deviation of three independent measurements.

To assess the ability of water to access the backbone we measured the cloud point of *L*-E_{455} and *B*-E_{15}^{43} to compare the hydrophilicity of these molecules. In an aqueous buffer at 3 mg/mL, neither of these solutions turn cloudy below 100 °C. We then performed cloud point measurements in a 1 M potassium fluoride solution, as this salt is known to depress the cloud point of linear PEO to a more convenient temperature range.[99,244] We observed that the bottlebrush PEO polymer had a cloud point of 48 °C and the linear PEO had a cloud point of 60 °C (Figure S4.4). This indicates that the backbone does slightly increase the hydrophobicity of the bottlebrush polymer; therefore, water must be able to access the backbone to some extent. Thus, the steric hindrance of the side chains prevents the added hydrophobicity of the backbone from affecting membrane binding, and there must be hydrophobicity on the periphery of the molecule for membrane binding to occur.

Because the backbone is unable to insert on its own, it cannot explain the increase in membrane affinity of the BBP compared to the linear poloxamer.

Molecular weight effect: The BBP discussed above (*B*-$E_{10}^{43}P_{5}^{15}$) had roughly double the molecular weight of *L*-$E_{93}P_{54}E_{93}$, the linear poloxamer control in Figure 4.1. Due to the molecular weights of the macromonomers (~1 kDa for PPO and ~2 kDa for PEO), synthesizing a diblock BBP at a molecular weight equal to *L*-$E_{93}P_{54}E_{93}$ would require degrees of polymerization of only 5 and 2 for the PEO and PPO blocks, respectively, which is impractical. Importantly, these two molecules do have similar numbers of total PPO units, 54 for *L*-$E_{93}P_{54}E_{93}$ and 78 for *B*-$E_{10}^{43}P_{5}^{15}$. Since the PPO moieties drive binding events, comparing these molecules is meaningful. However, for linear poloxamers, increasing the molecular weight increases the extent of binding,[85] so the effect of overall molecular weight must be explored in the bottlebrush architecture as well. To this end, we synthesized *B*-$E_{10}^{43}P_{5}^{15}$ and *B*-$E_{21}^{43}P_{11}^{15}$, two BBPs with identical compositions and side chain lengths but with molecular weights that differ by a factor of ~2. The PFG-NMR binding assay results for these two polymers are shown in Figure 4.3. For the higher molecular weight BBP (black), the decay curves of the polymer-only control and the polymer+POPC sample are equivalent within uncertainty. Therefore, both decay curves were fit to the bi-exponential model and the R_h of the small and large species differ by a factor of two. Thus, the large species detected in the *B*-$E_{21}^{43}P_{11}^{15}$+POPC sample is micelles. Finally, since the size of the *B*-$E_{21}^{43}P_{11}^{15}$ micelles (13 ± 1.3 nm) is significantly smaller than the R_h of the liposome-bound species detected in the *L*-$E_{93}P_{54}E_{93}$+POPC ($R_{h,\ liposome}$ = 26 ± 6.1 nm) and *B*-$E_{10}^{43}P_{5}^{15}$+POPC ($R_{h,\ liposome}$ = 25 ± 11 nm) samples, if this polymer did bind to the liposomes the PFG-NMR assay would have detected an additional mode of relaxation. We conclude that *B*-$E_{21}^{43}P_{11}^{15}$ chains do not bind to liposomes to a detectable extent. It is important to note that when the molecular weight of a BBP is increased, the size of the micelles increases. At an M_n ~ 100 kDa, the length scales of the micelles and liposomes are commensurate, and therefore the PFG-NMR binding assay cannot discriminate between them. Given the effect of

M_n between 26 kDa and 55 kDa, we expect that BBPs with M_n > 55 kDa would also have very low membrane affinity.

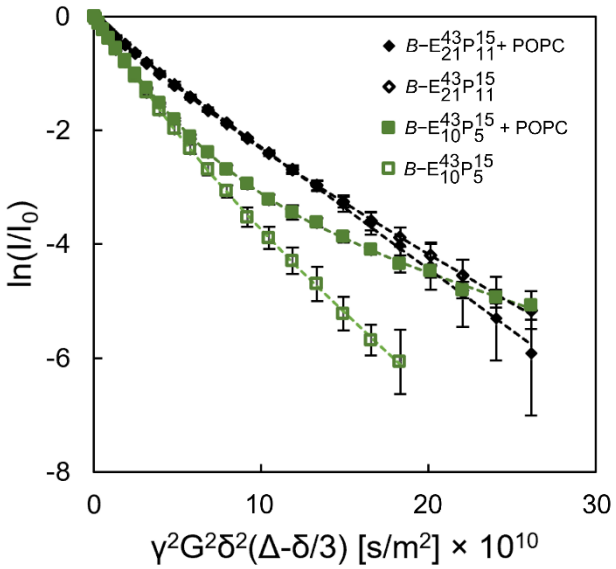

Figure 4.3: Increasing the molecular weight of a BBP leads to a complete loss of binding. PFG-NMR decay curves for *B*-$E_{10}^{43}P_5^{15}$ (M_n = 26 kDa) and *B*-$E_{21}^{43}P_{11}^{15}$ (M_n = 55 kDa). Error bars are the standard deviation of at least two replicates.

Role of PEO block side chain length: The side chain length of bottlebrush polymers impacts properties such as shape[152] and side chain flexibility,[240] which could influence polymer-membrane interactions. Thus, we evaluated the effect of the PEO block side chain length by comparing the binding ability of *B*-$E_{11}^{43}P_6^{15}$ and *B*-$E_{40}^{10}P_7^{15}$, two BBPs where the hydrophobic block is nearly identical, but the hydrophilic block side chain and backbone lengths differ by a factor of four. Notably, when $N_{sc,\,PEO}$ was reduced, $N_{bb,\,PEO}$ was increased to maintain a roughly constant number of EO units. The PFG-NMR decay curves for *B*-$E_{11}^{43}P_6^{15}$ (green points in Figure 4.4a) clearly show a shift to the upper right when liposomes are present, indicating binding. The tri-exponential fit reveals that roughly 8 ± 4 mol% of the chains bound while 29 ± 13 mol% existed as micelles; these results are consistent with those of *B*-$E_{10}^{43}P_5^{15}$ from Figure 4.1, which is a very similar molecule. The PFG-NMR data for *B*-$E_{40}^{10}P_7^{15}$ (blue points in Figure 4.4a) reveal that shortening the PEO block

side chains and lengthening the PEO backbone changes the extent of micellization and the membrane affinity of the polymer. First, fitting the polymer-only control decay curve to the bi-exponential model reveals that 80 ± 9 mol% of chains exist as micelles. This is much higher than the micelle fraction of the *B*-$E_{11}^{43}P_{6}^{15}$ polymer-only control, which is only 18 ± 12 mol%. Second, the polymer-only control and the polymer+POPC sample for *B*-$E_{40}^{10}P_{7}^{15}$ (blue points) overlap, indicating that no binding was detected despite the increased hydrophobicity of this molecule (lower wt% PEO). This result demonstrates that the PEO block does play a role in binding to liposomes. As the PEO side chain length is decreased, the units most distal from the backbone have less space and are therefore less flexible.[153,239,240] A recent study reported that bottlebrush molecules with reduced flexibility at the side chain ends formed smaller, looser aggregates due to reduced side chain interdigitation.[154] We hypothesize that a similar effect occurs in BBP interactions with lipid membranes. Specifically, the side chains of the PPO block are the first moiety of the BBP to insert into the bilayer. This brings the PEO block close to the lipid bilayer surface. If the PEO side chains are sufficiently long and flexible, they can interdigitate between lipid molecules, which disrupts the water shell around the ether units,[17] enabling the PEO block to provide an additional anchoring effect. On the other hand, short PEO side chains are too sterically constrained by their neighbors to interact with the lipid headgroups, and therefore steric repulsion between the PEO brush block and the lipids leads to rapid desorption. Figure 4.4b shows a sketch of this hypothesized mechanistic interpretation of the effect of the PEO side chain length.

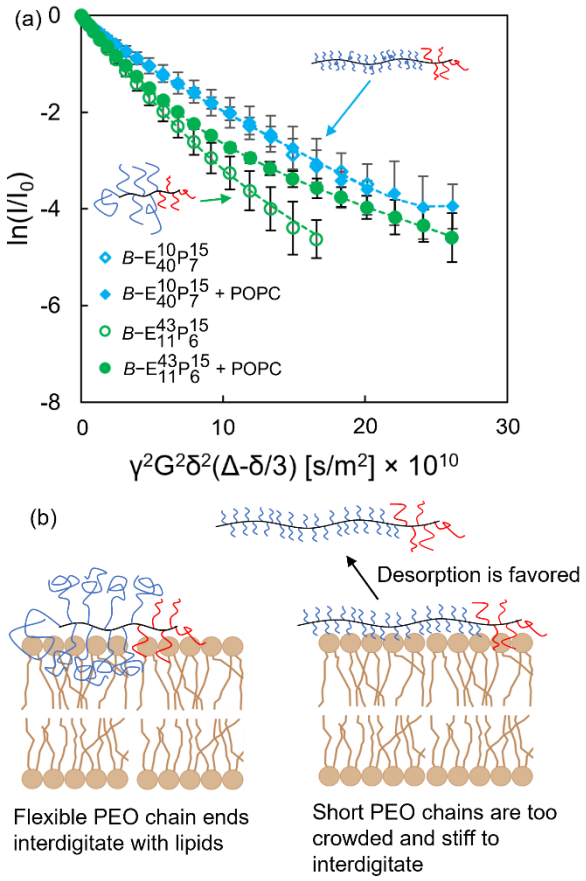

Figure 4.4: PEO block side chain length plays an important role in liposome binding. (a) PFG-NMR decay curves of two BBPs with similar molecular weights and compositions, but different PEO blocks. *B*-$E_{11}^{43}P_6^{15}$ is star-like with a short backbone and long side chains while *B*-$E_{40}^{10}P_7^{15}$ is brush-like with a long backbone and short side chains. (b) Schematic depicting a possible effect of side chain length (flexibility) on binding to lipid bilayers that is consistent with the data shown in panel (a).

Comparison of statistical vs block BBPs: Previous studies from our group have reported that the minimum PPO block length needed for significant membrane insertion of a linear poloxamer is ~14 units.[6,85,143] Since the number-average degree of polymerization of the PPO side chains in the BBPs tested meets this threshold, we hypothesized that each PPO side chain could serve as a pseudo-independent anchoring site, thereby increasing the membrane affinity. To test this hypothesis, we synthesized two pairs of molecules with different PEO side chain lengths, where

each pair contains one statistical copolymer and one block copolymer of nearly identical composition and molecular weight.

The PFG-NMR results for the statistical/block pair with long and short PEO side chains are shown in Figures 5a and 5b, respectively. The polymer-only control for the block copolymer with long PEO side chains (green open symbols in Figure 5a) shows clear curvature indicating significant micellization, and the bi-exponential fitting reveals that 18 ± 12 mol% of chains are in micelles. In contrast, the decay curve of the polymer-only control corresponding to the statistical copolymer with long PEO side chains (orange in Figure 5a) is essentially linear. In this case, the bi-exponential model estimates only 5 ± 5 mol% in micelles. The reduction of the micelle population is indirect evidence that the copolymerization of the PPO and PEO macromonomers was approximately random since the molecules are less able to organize into a core-shell structure.

Comparing the decay curves of corresponding polymer+POPC and polymer-only samples in Figure 4.5a demonstrates that only the block architecture binds to liposomes. The tri-exponential model fitting for the decay curve of *B*-$E_{11}^{43}P_{6}^{15}$+POPC indicates that roughly 8 ± 4 mol% of the chains bind to liposomes. This result suggests that when the PEO side chains are roughly three times longer than the PPO side chains, a block architecture is needed for binding to occur. At this ratio of side chain lengths, the PPO chains are essentially screened by neighboring PEO chains in the statistical architecture, but not in the block architecture. Therefore, we synthesized a statistical/block pair of copolymers with PPO side chains that are roughly twice the length of the PEO side chains to test whether removing the steric constraint allows a statistical copolymer to bind.

Figure 4.5b shows the decay curves of block and statistical copolymers with long PPO side chains relative to the PEO side chains. In this case, the statistical and block copolymers both show overlap between the polymer-only and polymer+POPC decay curves, indicating that neither architecture produced binding to liposomes. Therefore, reducing the steric hindrance of the PPO units on the periphery of the molecule did not enable the statistical copolymer to bind.

Furthermore, individual PPO side chains when statistically distributed along the entire backbone cannot act as independent anchor sites, and both a blocky architecture and a sufficiently long PEO side chain are requirements for significant binding to occur.

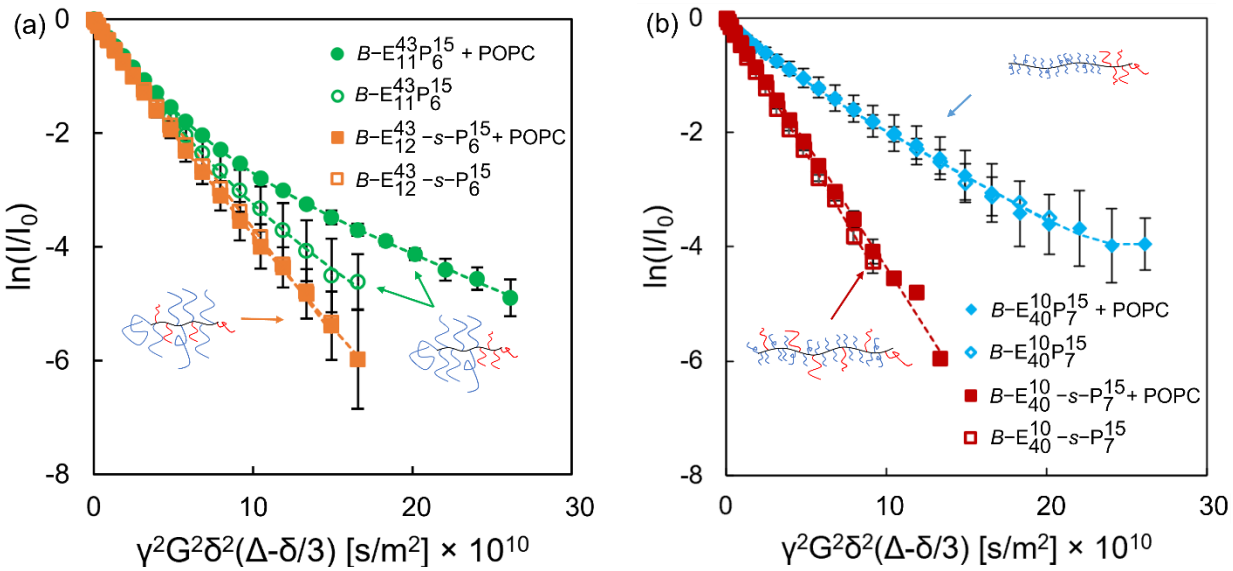

Figure 4.5: The tested statistical copolymers do not bind to liposomes, indicating that lumping hydrophobicity via the block architecture is needed for binding to occur. (a) PFG-NMR decay curves for block and statistical copolymers with longer PEO side chains ($N_{sc,\ PEO}$ = 43) than PPO side chains ($N_{sc,\ PPO}$ = 15). (b) PFG-NMR decay curves for block and statistical copolymers with shorter PEO side chains ($N_{sc,\ PEO}$ = 10) than the PPO side chains ($N_{sc,\ PPO}$ = 15).

In vitro protection efficacy against osmotic stress: Lastly, we evaluated the cellular protection efficacy of BBPs and compared them to linear analogues using an established osmotic stress assay.[6,131,143,178] Briefly, this assay subjects C2C12 myoblast cells to a hypoosmotic stress followed by isotonic recovery. If the membrane is damaged, macromolecules, such as the protein LDH, leak out of the cell and can then be detected via enzymatic colorimetry. A given polymer treatment is present throughout the assay, and a reduced LDH release relative to the non-polymer treated control indicates a protective effect.

Figure 4.6a shows a comparison of the linear and bottlebrush architectures, where *L*-$E_{87}P_{31}E_{87}$ (P188) is the most prevalent polymer used as a membrane stabilizing agent,[6,120,122,124,245] and was

included as a "first-in-class" control. *B*-$E_{10}^{43}P_5^{15}$ (green) exhibits efficacy at sub-μM concentrations, indicating that BBPs can have a protective effect. Moreover, *B*-$E_{10}^{43}P_5^{15}$ exhibits significantly greater cellular protection than the *L*-$E_{87}P_{31}E_{87}$ control ($p < 0.01$) on a molar basis. To control for the difference in PEO mass fraction between *B*-$E_{10}^{43}P_5^{15}$ and *L*-$E_{87}P_{31}E_{87}$, we also included *L*-$E_{93}P_{54}E_{93}$, a linear poloxamer with an identical mass fraction of PEO and a similar number of PPO units to *B*-$E_{10}^{43}P_5^{15}$; the protection efficacy of these two molecules is not statistically different at polymer concentrations > 0.7 μM.

A comparison of *B*-$E_{10}^{43}P_5^{15}$ and *B*-$E_{21}^{43}P_{11}^{15}$ (green and blue curves in Figure 4.6a) indicates that doubling the molecular weight of the BBP nominally decreases protection efficacy. On a per-mass basis the reduced performance of the higher M_n BBP is even more apparent (Figure S4.5). This effect was previously observed for high concentrations of linear poloxamers containing 70 and 80 wt% PEO, and was attributed to differences in the onset of micellization.[6] Micellization cannot explain the reduced protection efficacy upon increasing M_n of BBPs, because all of the BBPs tested here form micelles over part of the concentration range tested, and no coincident reduction in protection efficacy was observed. Furthermore, as BBPs adsorb to the cell membrane, micelles act as a reservoir by ejecting single chains to restore the free chain-micelle equilibrium.

A scaling theory by Hristova and Needham concerning mixtures of lipids and polymer-grafted lipids suggests that membrane mechanical properties are a function of both polymer molecular weight and concentration in the bilayer.[135] Furthermore, their theory suggests that as the molecular weight of the chain is increased, the maximum possible membrane incorporation decreases. Therefore, a possible explanation for peak protection efficacy occurring at intermediate molecular weights (M_n ~10-30 kDa) is that as M_n is increased there are competing effects: less polymer binds, but each binding event adds more polymer mass to the membrane, leading to a larger effect on mechanical properties per binding event.

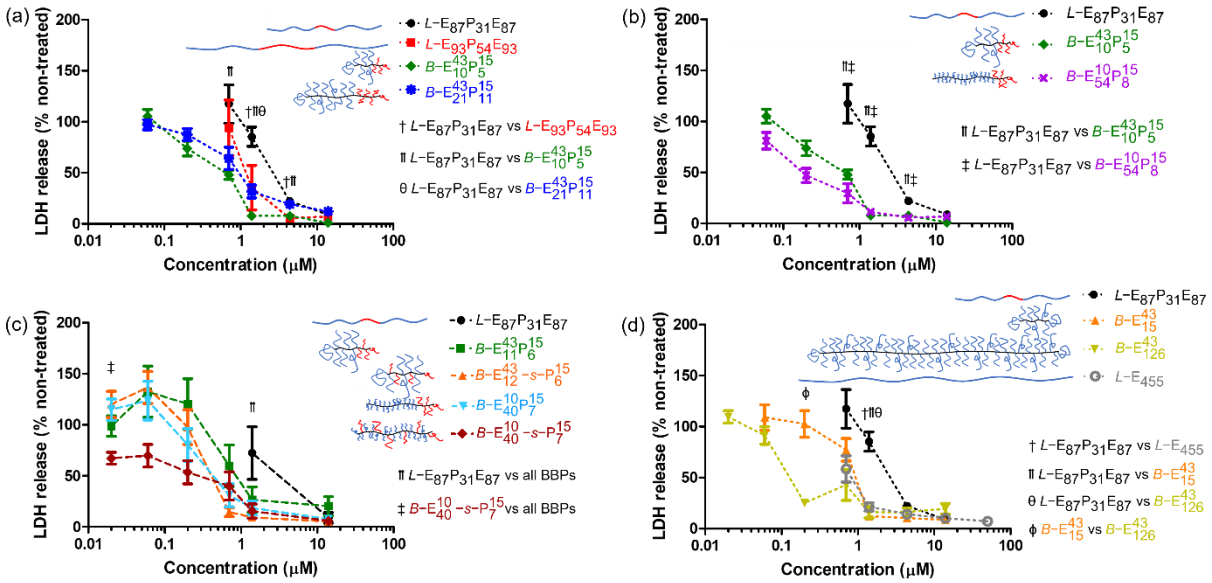

Figure 4.6: Osmotic stress assay demonstrates that BBPs can protect cell membranes under stress. LDH release is taken during the isotonic recovery step and is normalized to the non-treated (no polymer) control. (a) Comparison between linear and bottlebrush architectures and effect of molecular weight in the bottlebrush architecture. (b) Effect of shortening the PEO side chain. (c) Effect of BBP architecture (statistical versus block copolymers). (d) Effect of bottlebrush PEO homopolymers and their molecular weight. Error bars are the standard error of 9 independent replicates and statistical significance indicates results from a one-way analysis of variance with Tukey's post hoc test ($p < 0.01$).

We also explored the effect of BBP architectural parameters on protection efficacy. Figure 4.6b shows that shortening the PEO side chains leads to a nominal improvement in protection efficacy. This result is interesting because the BBP with shorter PEO side chains (B-$E_{54}^{10}P_{8}^{15}$) did not bind to a detectable level in the PFG-NMR assay (Figure S4.6), yet it does have a protective effect (which is also true for B-$E_{21}^{43}P_{11}^{15}$ and the statistical BBPs). This could be because the single component POPC liposome model neglects the effects of transmembrane proteins, surface receptors, glycolipids, and lipid phase coexistence that exist on a physiological membrane which could impact polymer-cell membrane interactions.[1,3,47] Additionally, as temperature increases one might expect binding to increase due to the reduced solvent quality of water for both PPO and PEO, so it is possible that by increasing the temperature from 27 °C to 37 °C in the PFG-NMR assay, binding of B-$E_{54}^{10}P_{8}^{15}$ and/or B-$E_{21}^{43}P_{11}^{15}$ to liposomes would be observed. Furthermore, the

relationship between abiotic membrane binding and cellular protection is poorly understood, so one should interpret the results of the liposomal PFG-NMR and the *in vitro* osmotic stress assays separately. However, we can conclude that this is another example of low-affinity polymers having a protective effect.[69,87]

Figure 4.6c indicates that protection efficacy is not unique to the block architecture, as statistical copolymer bottlebrushes are also significantly more protective than *L*-$E_{87}P_{31}E_{87}$ on a molar basis. Furthermore, for the pair of molecules with long PEO side chains, the block and statistical architectures showed similar protection efficacy (green vs. orange points). However, when the PEO side chain length was shortened, the statistical copolymer performed significantly better than the corresponding block polymer at very low concentrations (red vs. blue points, $p < 0.01$). Interestingly, it remained protective even down to 0.014 μM, which is the lowest protective polymer concentration of any polymer tested to date.[6,178] All other molecules follow the recently reported threshold effect, where polymers lose protective efficacy somewhere between 0.8 – 4 μM.[178] Future experiments will be conducted on a tissue-level protection assay with dystrophic mouse muscle fibers, which is a step closer to a physiological situation.[131]

Finally, Figure 4.6d shows that bottlebrush PEO polymers can be protective even without the PPO block. Additionally, a linear PEO homopolymer and a brush PEO polymer of similar molecular weights have the same protection efficacy. At low polymer concentrations, increasing the molecular weight of the brush PEO homopolymer from 30 kDa to over 200 kDa significantly improves the per molecule protection efficacy ($p < 0.01$). As discussed above, it is unlikely that the backbone alone imparts sufficient hydrophobicity to affect binding; therefore, these results suggest that polymers that only weakly associate with POPC liposomes can be protective of cellular membranes.

4.3 Discussion

The fraction of chains in micelles and bound to liposomes for all polymer+POPC PFG-NMR experiments are summarized in Table 4.2. Using the PFG-NMR results from the BBP architectural variants described, we can deduce useful information about the mechanism of BBP-phospholipid interactions. First, the hydrophobic norbornene backbone by itself is too sterically hindered to insert into the membrane; the hydrophobic PPO block is necessary for binding to occur. This result is consistent with the anchor-and-chain hypothesis, although in the bottlebrush architecture the conformation of a PPO anchoring block has two distinct limiting possibilities, which are illustrated in Figure 4.7a. In the "flagpole" conformation the backbone orients normal to the liposome surface, while the PPO block occupies a relatively large cylindrical volume within the bilayer. On the other hand, in the "in-plane" conformation the backbone lies largely in the bilayer plane and the side chains interdigitate with the lipids parallel to the lipid tails. Understanding whether either conformation is preferred is important to further engineer the molecular design, because polymer-lipid interactions are likely different between these conformations. For example, in the flagpole conformation the lateral surface area covered by a single chain is related to the side chain length of the PEO block and the insertion depth is dictated by the PPO block contour length. Meanwhile, for the in-plane conformation, the surface area coverage can be estimated by projecting a rectangle with dimensions proportional to the side chain and backbone lengths and the insertion depth by the side chain lengths of both blocks. Based on the side chain lengths and grafting density, we expect the BBPs are loose brushes, so the side chains are Gaussian coils while the backbone is extended.[246] Prior work has shown that the core dimensions of BBP micelles reflect behavior of a worm-like chain with a persistence length of ~10 nm, which is significantly higher than the 0.7 nm persistence length of linear polynorbornene.[109]

Table 4.2: Summary of Micelle and Bound Populations

Polymer	$f_{micelle}$ [mol%][a]	f_{bound} [mol%][a]
L-$E_{93}P_{54}E_{93}$	0[b]	2.3 ± 0.9[b]
B-$E_{10}^{43}P_{5}^{15}$	21 ± 9	7.3 ± 1.3
B-$E_{21}^{43}P_{11}^{15}$	56 ± 23	0
B-$E_{11}^{43}P_{6}^{15}$	77 ± 11[d]	0
B-E_{12}^{43}-*s*-P_{6}^{15}	0	0
B-$E_{40}^{10}P_{7}^{15}$	29 ± 13[d]	8.3 ± 4.1[d]
B-E_{40}^{10}-*s*-P_{7}^{15}	5.1 ± 5.1[d]	0
L-E_{455}	0[c]	0[c]
B-E_{15}^{43}	0[c]	0[c]

[a]Calculated via the constrained tri-exponential fitting procedure described in the methods section unless otherwise noted. [b]Unconstrained bi-exponential model, as the polymer-only control showed a single exponential decay. [c]Single exponential model applied. Error is the standard deviation of 3 independent replicates unless otherwise noted. [d]Error is the standard deviation of 2 independent replicates.

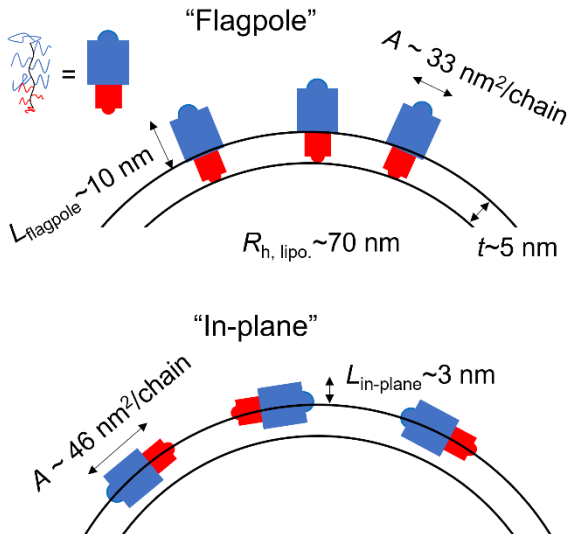

Figure 4.7: Two possible limiting conformations of membrane-bound BBPs: flagpole and in-plane. $R_{h,\ lipo.}$ is the hydrodynamic radius of liposomes extruded through a 100 nm diameter filter (this size was used only in the conformation assessment experiments described in the discussion section below and presented in Section 4.5), L is an estimate of the distance the polymer protrudes normal to the liposome surface, A is an estimate of the surface area occupied per chain, and t is the bilayer thickness.

We suspect that the in-plane conformation is more likely because it would enable the PPO side chains to intercalate between lipid molecules parallel to the acyl tails. In contrast, for the BBP to occupy the flagpole conformation, the polymer would have to overcome both van der Waals and hydrophobic forces[12,135] to create the open volume in the lipid bilayer required for the PPO block to insert. Therefore, the in-plane conformation likely has a lower free energy than the flag-pole conformation. Additionally, the relationships between architectural parameters and membrane binding affinity that we have found are more consistent with the in-plane conformation. For example, in the flagpole architecture one would not expect the PEO side chain length to have as significant of an impact on binding ability as we observed, namely, that shortening the PEO block side chain length by a factor of ~4 eliminates binding ability. Furthermore, this effect is consistent with the in-plane conformation because as side chain length is increased the flexibility on the periphery of the brush would enable the PEO chains to intercalate into the bilayer, while shorter PEO chains might be too stiff and therefore would be excluded. Finally, if BBPs adopted the

flagpole conformation, then when the contour length of the PPO block exceeds the bilayer thickness, the polymer would likely disrupt the bilayer.[184] Cryo-TEM images of POPC liposomes incubated with *B*-$E_{168}^{43}P_{43}^{15}$, a BBP whose PPO block contour length is ~6 times longer than the acyl region of the bilayer, showed no membrane perturbations or open vesicles. Although *B*-$E_{168}^{43}P_{43}^{15}$ likely has very low membrane affinity, due to the relationship between M_n and f_{bound} described above, liposome stability in its presence suggests this molecule does not assume the flagpole conformation.

Direct experimental evidence of the conformation of membrane-bound BBPs is difficult to obtain due to the dynamic nature of phospholipid bilayers and the relatively low fraction of chains bound. We performed PFG-NMR experiments on liposomes treated with *B*-$E_{11}^{43}P_{6}^{15}$ over a series of lipid concentrations to estimate the number of polymers bound to each liposome. Based on polymer characterization data, we can calculate the surface area coverage for both conformations using simple geometrical approximations. For both conformations, a wide range of surface areal coverage (~25%–100%) was observed. DLS experiments conducted at the same concentrations revealed that the R_h of the liposomes were independent of polymer treatment and within error of the neat liposome control. Because the flagpole conformation protrudes from the liposome surface by ~10 nm while the in-plane conformation protrudes by only ~3 nm, this preliminary result is consistent with the in-plane conformation. However, this analysis should be viewed cautiously because the R_h of polymer-treated liposomes cannot be described simply as the sum of the liposome radius and the contour length of the polymer, since it is unknown how an incompletely coated brush layer would impact diffusion. Details of this experiment and analysis are shown in Figure S4.7. Due to these experimental challenges, it may be that molecular dynamics simulations are a more promising route to assess the conformation of bound BBPs.

In both linear and bottlebrush poloxamers, the block architecture is necessary for binding to occur, with a proposed mechanism in which the hydrophobic PPO block acts as an anchor and the PEO block interacts with the hydrophilic headgroups and the bound water layer. However, based

on the effect of PEO side chain length on BBP-liposome binding, the PEO block likely also plays a role in providing additional interpenetration with phospholipids. The enhanced membrane affinity of *B*-$E_{10}^{43}P_5^{15}$ relative to an analogous linear poloxamer is attributable to this enhanced interdigitation effect.

All liposome models are distant abstractions from a living membrane, but they are useful because their simplicity allows one to ask targeted questions by specifying the desired bilayer constituents. In this work, we chose to focus on single component POPC liposomes because we were primarily interested in comparing membrane binding ability of bottlebrush and linear poloxamers and exploring the effect of bottlebrush architectural parameters. Previous work has established mechanisms by which lipid head and tail-group identities affect interactions between linear poloxamers and lipid bilayers.[82,146] Linear poloxamers have a higher affinity for POPG liposomes than POPC liposomes, likely due to hydrogen bonding between the ether groups of the polymer and the alcohol of the POPG.[146] We hypothesize that BBPs would also have a higher affinity towards a POPG bilayer (or any lipid bilayer with hydrogen bond donors in the headgroup region) than a POPC bilayer since BBPs contain many ether groups in close proximity to the lipid bilayer. Additionally, linear poloxamers have a higher affinity towards bilayers composed of DOPC than POPC because the additional unsaturated tail in DOPC reduces the bending modulus, facilitating polymer insertion.[82] We anticipate that this effect is independent of polymer architecture, and therefore BBPs would show a similar relationship between binding and lipid tail unsaturation.

4.4 Conclusion

We systematically varied molecular structure to explore the effects of several bottlebrush polymer architectural parameters including side chain length, overall molecular weight, and monomer distribution (statistical vs block). The membrane binding ability of a BBP can be significantly modified by adjusting the side chain length and backbone degree of polymerization.

The highest affinity BBP found in this study has approximately a three times higher membrane affinity than an analogous linear poloxamer, despite a more rigid and crowded architecture. The hydrophobic backbone of the bottlebrush does not participate significantly in membrane binding. A more likely explanation for the increased binding is the ability for side chains to interdigitate between neighboring phospholipids. These results are an important step towards tuning membrane affinity of amphiphilic macromolecules by providing mechanistic insight about which parts of the molecule drive binding.

Additionally, we have demonstrated that BBPs can protect cell membranes from osmotic stress. The bottlebrush polymers tested in this study ranged in total molecular weight from 26 kDa to 260 kDa, and they maintained protective ability throughout this range. Previously, linear block copolymer amphiphiles have only demonstrated protection efficacy up to ~20−30 kDa.[69,178] The dramatic extension in molecular weight of protective BBPs is notable given the well-established dependence of renal clearance on molecule size.[247] Finally, unlike liposome binding, cell membrane protection is not unique to the block architecture as bottlebrush PEO homopolymers and statistical copolymers with PEO and PPO side chains do outperform *L*-$E_{87}P_{31}E_{87}$ (P188) in an osmotic stress assay on a molar basis. This is another example of low affinity polymers being protective *in vitro*,[69,87] and re-emphasizes the fact that there remain important differences between studies of polymer-liposome binding and *in vitro* cellular protection.

4.5 Supplementary Materials for Chapter 4

Characterization of m-PEO(0.6k)-NB macromonomer

The m-PEO_{2k}-NB and t-PPO_{1k}-NB macromonomers were synthesized and reported in detail in a prior publication.[109] The same batches as reported in this earlier publication were used in this study and thus the characterization data are omitted here. The characterization data for m-$PEO_{0.6k}$-NB are shown below.

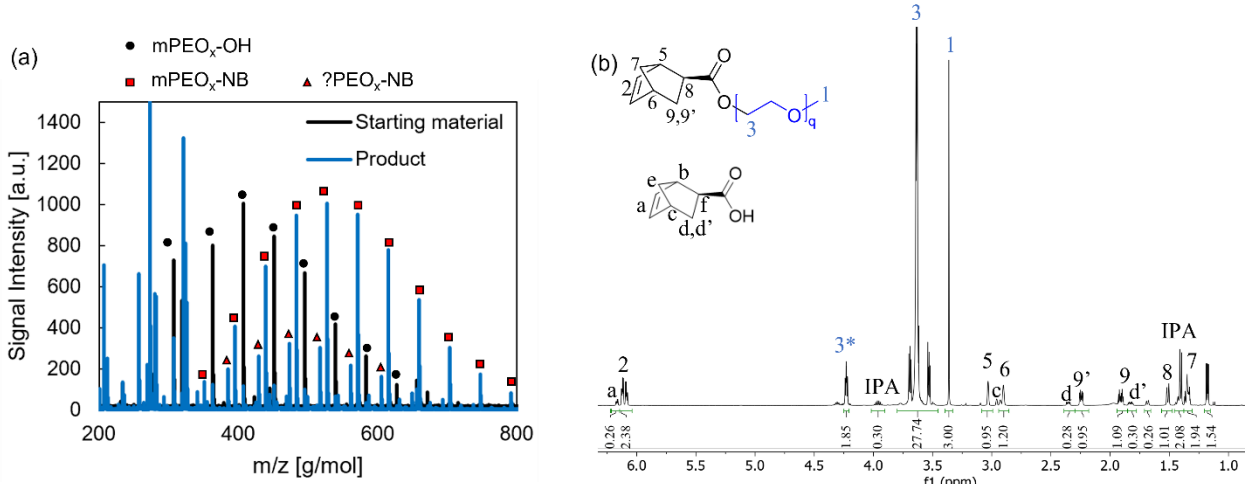

Figure S4.1: Characterization of esterification reaction to functionalize PEO ($M_n \approx 350$ g/mol) with norbornene. (a) MALDI ToF characterization of the starting material (black) and the purified product (blue). For the product, M_n = 604.9 g/mol ($N_{sc} \approx 10$) and $Đ$ = 1.07. The family of peaks labelled with red squares is the desired product and constitutes 69 mol% of the sample. (b) ^{1}H NMR spectrum of purified product. The integration and shape of the peaks at 6.0-6.2 ppm indicate that there is residual NB-COOH in the sample. This impurity is difficult to remove and makes up < 20% of the total norbornene present so was deemed acceptable.

Note the red triangle population in the MALDI-ToF spectrum for the product. This family of peaks makes up 31% (mol) of the sample and we are uncertain what the chain ends are. We suspect that the ω-chain end was successfully functionalized with norbornene because we can hit targeted molecular weights without accounting for 31% of dead chains. It is possible that a counterion impurity was introduced to the sample resulting in a shifted population in MALDI.

Dynamic light scattering (DLS) confirms liposome quality

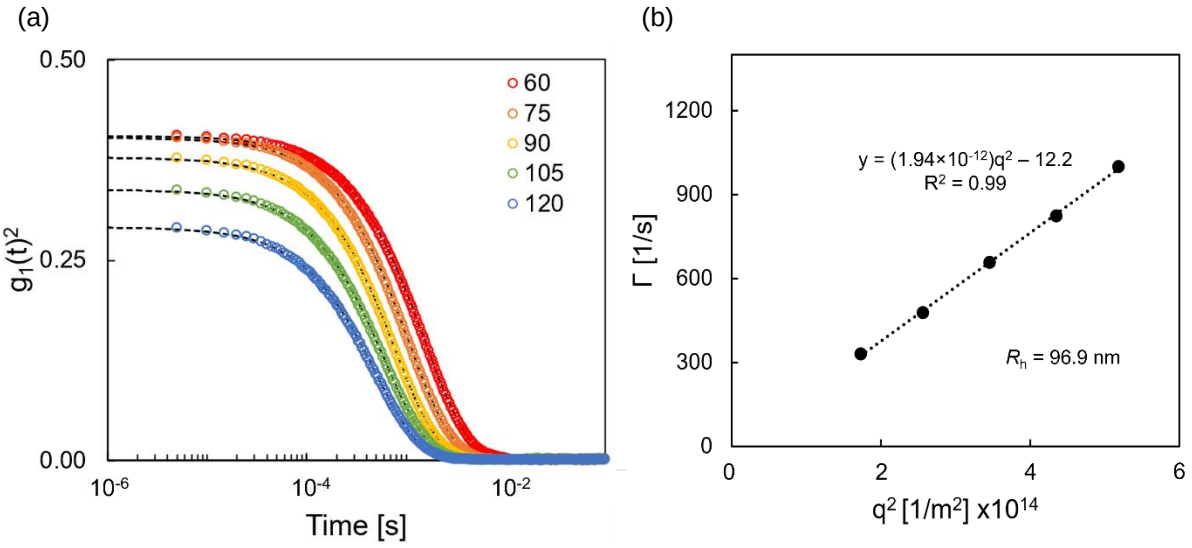

Figure S4.2: Representative multi-angle DLS data confirms that liposome size distribution is unimodal with an $R_h \approx 96.9$ nm and a dispersity of 1.03. (a) Intensity autocorrelation functions at each angle. The data were fit with the second cumulant model and the residuals were small. (b) The first cumulant as a function of the scattering vector. The linearity and near zero y-intercept indicate that the single relaxation process being observed is diffusive.

The measured intensity autocorrelation function ($g_2(t)$) was converted to the electric field autocorrelation function ($g_1(t)$) via the Siegert relation. Then, the autocorrelation function was fit to the second-order cumulant expansion model described by:

$$g_1(t)=\exp(-2\Gamma t+k_2 t^2) \tag{S.1}$$

where t is time, Γ and k_2 are the first and second cumulants which capture the mean and width of the relaxation rate in g_1, respectively. The mutual diffusion coefficient, D_m, can be obtained by dividing Γ by the slope of the relationship between Γ and q^2 shown in Figure S4.2b. For dilute solutions, the mutual diffusion coefficient is approximately equal to the tracer diffusion coefficient, D_t, which can then be related to the hydrodynamic radius of the particles via the Stokes-Einstein equation given by:

$$R_h=\frac{kT}{6\pi\eta_s D_t} \tag{S.2}$$

where k is Boltzmann's constant, T is the temperature in Kelvin, and η_s is the viscosity of the solvent. A representative value for R_h of the liposomes is 97 nm, which is consistent with the pore sized used during extrusion. Finally, the dispersity of the liposomes can be estimated by:

$$Đ=1+k_2/\Gamma^2 \quad \text{(S.3)}$$

The linearity and y-intercept of zero (within error) of the relationship between the first cumulant (Γ) and the scattering vector squared (q^2) indicate that a single diffusive process was observed.

Summary of PFG-NMR model fitting:

Table S4.1: Summary of the summation of exponentials model fits

Polymer	$f_{micelle}$ [mol%]	f_{bound} [mol%]	$R_{h,\ free}$ [nm]	$R_{h,\ micelle}$ [nm]	$R_{h,\ lipo}$ [nm]	CMC^a [mg/mL]
L-$E_{93}P_{54}E_{93}$	0	N/A	3.1 ± 0.1*	-	N/A	0.5 ± 0.1
L-$E_{93}P_{54}E_{93}$ + POPC	0	2.3 ± 0.9	3.2 ± 0.1*	-	26± 6*	
B-$E_{10}^{43}P_5^{15}$	27 ± 9	N/A	3.9 ± 0.5	8.0 ± 1.5	N/A	8 ± 3
B-$E_{10}^{43}P_5^{15}$ + POPC	21 ± 9	6.8 ± 1.5	3.9 ± 0.5	8.0 ± 1.5	25 ± 11	
B-$E_{21}^{43}P_{11}^{15}$	39 ± 2	N/A	6.3 ± 0.6	13 ± 1	N/A	2 ± 0.5
B-$E_{21}^{43}P_{11}^{15}$ + POPC	56 ± 23	0	6.4 ± 0.5*	13 ± 1	-	
B-$E_{54}^{10}P_8^{15}$	83	N/A	2.5	12	N/A	0.4 ± 0.1
B-$E_{54}^{10}P_8^{15}$ + POPC	84*	0	1.7*	11	-	
B-$E_{11}^{43}P_6^{15}$	18 ± 12	N/A	4.4 ± 1.1	11 ± 1	N/A	
B-$E_{11}^{43}P_6^{15}$ + POPC	29 ± 13	8.3 ± 4.1	4.4 ± 1.1	11 ± 1	28 ± 12	
B-E_{12}^{43}-*s*-P_6^{15}	0	N/A	4.7	-	N/A	
B-E_{12}^{43}-*s*-P_6^{15} + POPC	5.1 ± 5.1	0	4.6 ± 0.1*	10*	-	
B-$E_{40}^{10}P_7^{15}$	80 ± 9	N/A	2.6 ± 0.3	13 ± 1	N/A	
B-$E_{40}^{10}P_7^{15}$ + POPC	77 ± 11	0	2.4 ± 1	13 ± 2	-	
B-E_{40}^{10}-*s*-P_7^{15}	0	N/A	4.2 ± 0.1	-	N/A	
B-E_{40}^{10}-*s*-P_7^{15} + POPC	0	0	4.5 ± 0.1*	-	-	
L-E_{455}	0	N/A	4.3	-	N/A	
L-E_{455} + POPC	0	0	4.6*	-	-	
B-E_{15}^{43}	0	N/A	3.9	-	N/A	
B-E_{15}^{43} + POPC	0	0	3.7 ± 0.1*	-	-	

All polymer + liposome fits were done with the constrained tri-exponential model as described in the main text unless otherwise noted. All polymer-only fits were done with the biexponential model. In several cases, this model collapses to the single exponential model.
*unconstrained biexponential model

Error is the range of two independent replicates for the statistical vs. linear molecules and standard deviation of three independent replicates elsewhere.
[a]*CMC* was measured at 37 °C via dynamic light scattering.

Note the discrepancy in the estimated $R_{h,\ liposome}$ between PFG-NMR (~25 nm) and DLS (~95 nm). We have observed this discrepancy previously and believe it is due to light scattering techniques weighting larger species more heavily than smaller species, whereas PFG-NMR is known to give an underestimate of vesicle size because the slow relaxation of large vesicles leads to signal broadening.[20,85,87]

The apparent critical micelle concentration (CMC_a) was measured for selected polymers via dynamic light scattering. The CMCs are provided for context, but the CMC is a poor predictor of membrane affinity because it convolutes the effects of molecular weight and hydrophobicity, its value is sensitive to the technique employed, and because micellization is not a phase transition, so a single onset concentration does not exist. Furthermore, in all cases where micelles were observed via PFG-NMR, they coexisted with free chains, suggesting that a micelle is not in so deep a free energy minimum that interactions between free chains and liposomes are prevented.

Cryo-TEM of POPC liposomes and POPC liposomes treated with a high M_n BBP

The cryo-TEM studies reported here had two goals. First, prior literature has reported that extrusion leads to a small fraction of multilamellar vesicles.[248] This will impact the surface area covered by polymer, so the first goal of cryo-TEM was to assess the fraction of the lipid surface area that is in the outer leaflet. Second, we wanted to obtain a real-space image of a BBP bound to a liposome. The model BBP chosen for this study was *B*-E_{168}^{43}-P_{43}^{15} because previous results have shown that the corona of micelles formed by this polymer clearly shows individual chains.[109] Therefore, we thought that if the flagpole conformation exists, this polymer gives us the best chance of observing it.

To estimate the fraction of surface area in the outer leaflet, we analyzed over 200 objects from 5 representative TEM micrographs of neat POPC liposomes. We fit each bilayer observed with the circle tool in ImageJ and calculated the surface area. From this procedure, we estimate that roughly 68% of the liposome surface area is on the outer leaflet and exposed to the polymer solution. This represents the parameter *f* in Equation S4 below.

In the TEM micrographs of liposomes treated with *B*-E_{168}^{43}-P_{43}^{15} we did not observe any protrusions from the membrane. Therefore, no evidence of the flagpole conformation was observed. However, given the relationship between overall molecular weight and binding fraction reported in the main text, it is possible that this polymer does not bind to the liposomes. We cannot analyze PFG-NMR decay curves for liposomes incubated with *B*-E_{168}^{43}-P_{43}^{15} in a meaningful way because the micelles and liposomes are of similar size, as can be seen in Figures S4.3c and S4.3d. It is also worth noting that we did not observe any broken or open liposomes, which suggests that prolonged exposure to high M_n BBPs is not disruptive to the lipid bilayer structure. If this polymer adopted the flagpole conformation, it would almost certainly be disruptive as the contour length of the PPO block is ~30 nm, which is roughly six times longer than the thickness of the acyl region of the bilayer.[249]

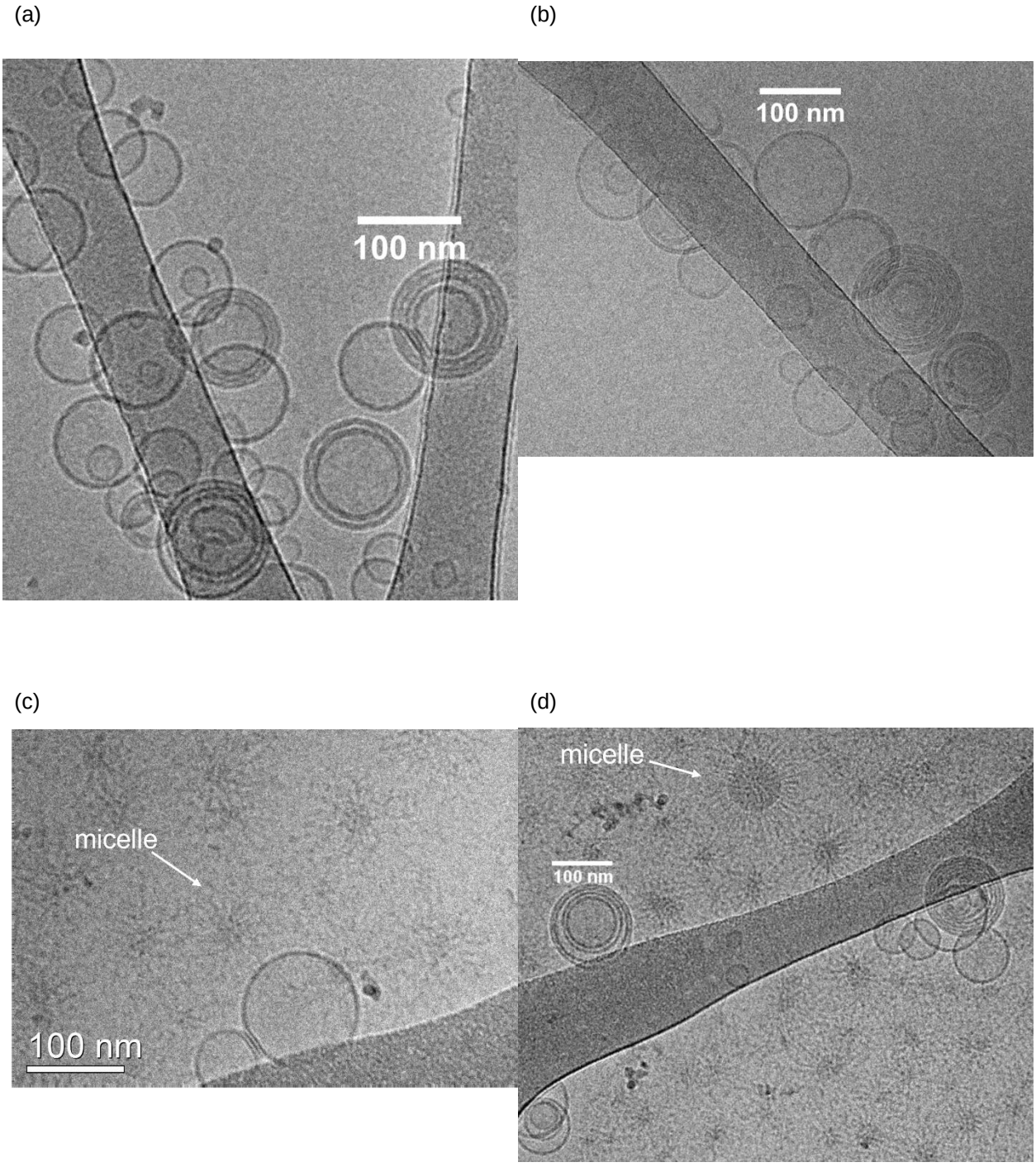

Figure S4.3: Representative cryo-TEM micrographs from (a−b) neat POPC liposomes and (c−d) POPC liposomes treated with *B*-E_{168}^{43}-P_{43}^{15} for 4 hours prior to vitrification.

Cloud point measurements

The norbornene backbone is hydrophobic, so we performed cloud point measurements on 3 mg/mL solutions of a linear PEO homopolymer, a bottlebrush PEO homopolymer, and a diblock bottlebrush poloxamer. Assuming each of these polymers have the same density, these solutions were at identical volume concentrations. Since PEO and PPO in water are lower critical solution temperature systems, a lower cloud point at a given volumetric concentration indicates a more hydrophobic polymer. These studies were initially performed in distilled water; however, no clouding was observed below the boiling point. We then performed the cloud point measurements in 1 M potassium fluoride solution, which is known to depress the cloud point.[99,244] This effect is attributed to K^+ cations complexing with the ether groups, disrupting the bound water hydration shell, rendering the polymer more hydrophobic.[99,244]

We defined the cloud point as the temperature at which the normalized transmittance falls below 75% on the heating trace. Following this definition, the cloud point in 1 M potassium fluoride solution of linear PEO is 60 °C while for bottlebrush PEO it drops to 48 °C. The BBP copolymer has a cloud point of 46 °C. The hydrophobic backbone reduces the cloud point temperature, and therefore renders the molecule more hydrophobic. Note that there is a two-step reduction in the transmittance for bottlebrush PEO, and this result was reproduced twice. A similar widening of the temperature range over which liquid-liquid phase separation occurs was reported for densely grafted poly(2-isopropyl-2-oxazoline) polymers in aqueous solutions.[250]

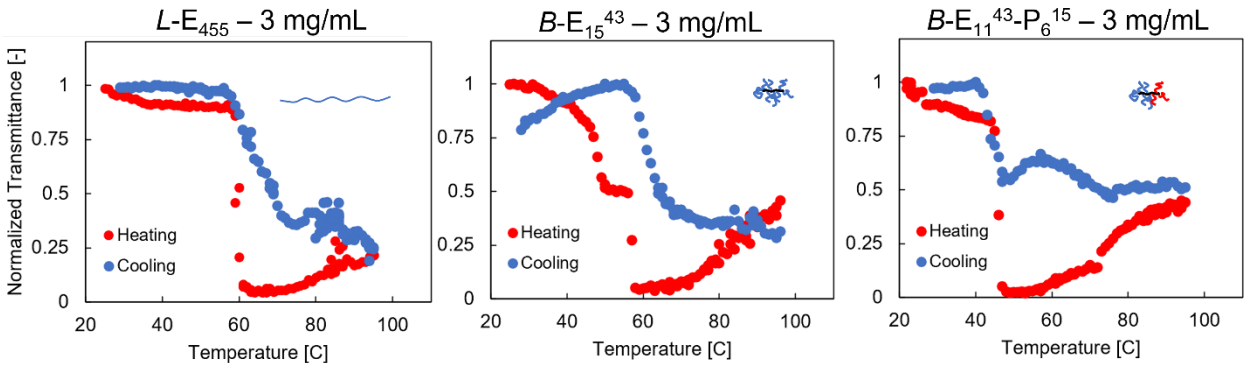

Figure S4.4: Cloud point measurements of solutions of polymer in 1M KF. From left to right: linear PEO (M_n = 20 kDa), bottlebrush PEO (M_n = 30.6 kDa), and a bottlebrush poloxamer (M_n = 29.4 kDa).

Osmotic stress assay results in mass units

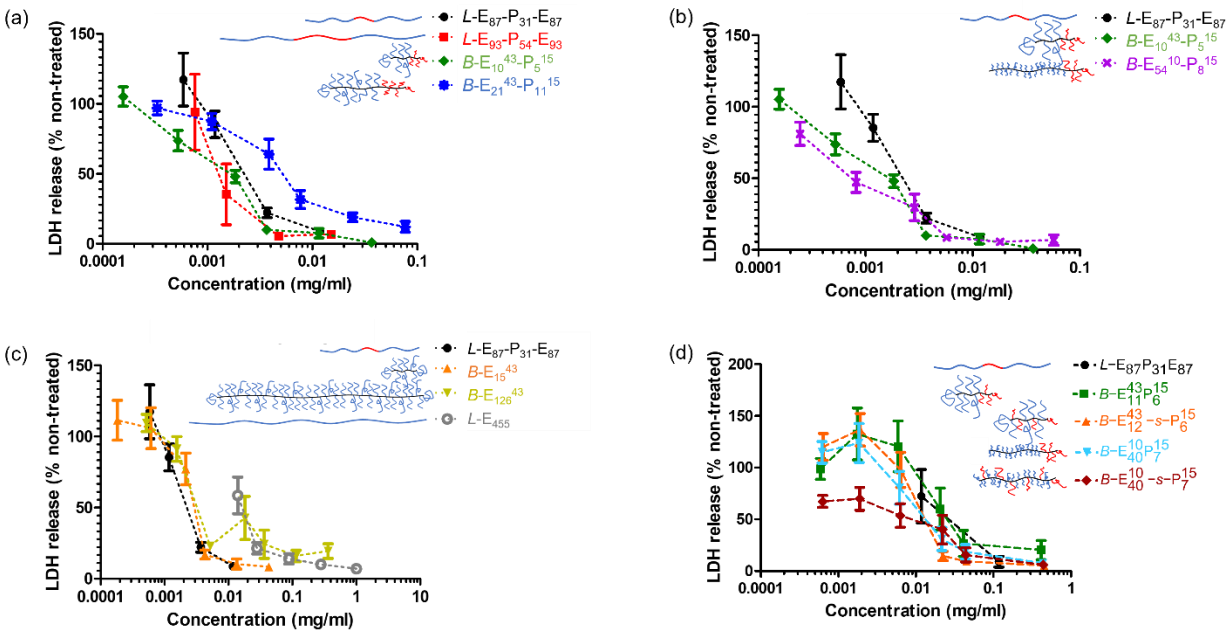

Figure S4.5: Osmotic stress protection assay displayed in mass units instead of molar units. This is the same data as in Figure 4.6 of the main text, but with different units of mg/mL instead of μM on the x-axis. LDH release is taken during the isotonic recovery step and is normalized to the no-polymer treated control. (a) Comparison between linear and bottlebrush architectures and effect of molecular weight in the bottlebrush architecture. (b) Effect of shortening the PEO side chain. (c) Effect of BBP architecture (statistical versus block copolymers). (d) Effect of bottlebrush PEO homopolymers and their molecular weight. Error bars are the standard error of 9 independent replicates.

PFG-NMR binding assay result for *B*-$E_{54}^{10}P_8^{15}$

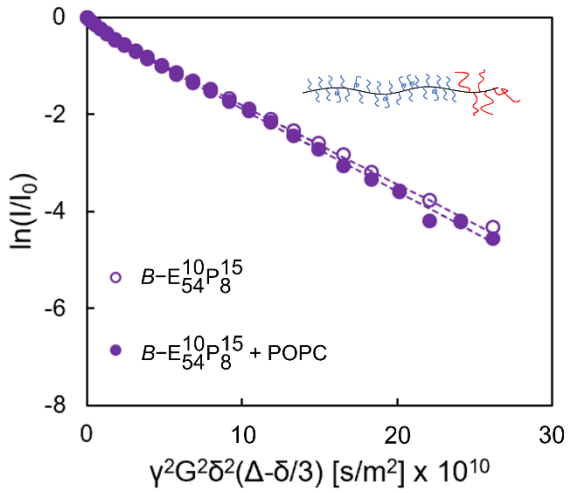

Figure S4.6: PFG-NMR decay curves for *B*-$E_{54}^{10}P_8^{15}$. The polymer-only control and the polymer + liposome samples agree within experimental error, indicating that this polymer does not bind to a detectable extent.

Conformation of bound BBPs via PFG-NMR and DLS

To obtain experimental insight into the conformation of bound BBPs, we performed PFG-NMR and dynamic light scattering experiments over a series of POPC concentrations to determine if the R_h of the liposomes is a function of polymer surface coverage. If the flagpole conformation exists, we hypothesized that at a high surface coverage a BBP with a PEO block contour length of ~10 nm would impact the R_h of the liposomes in an observable way.

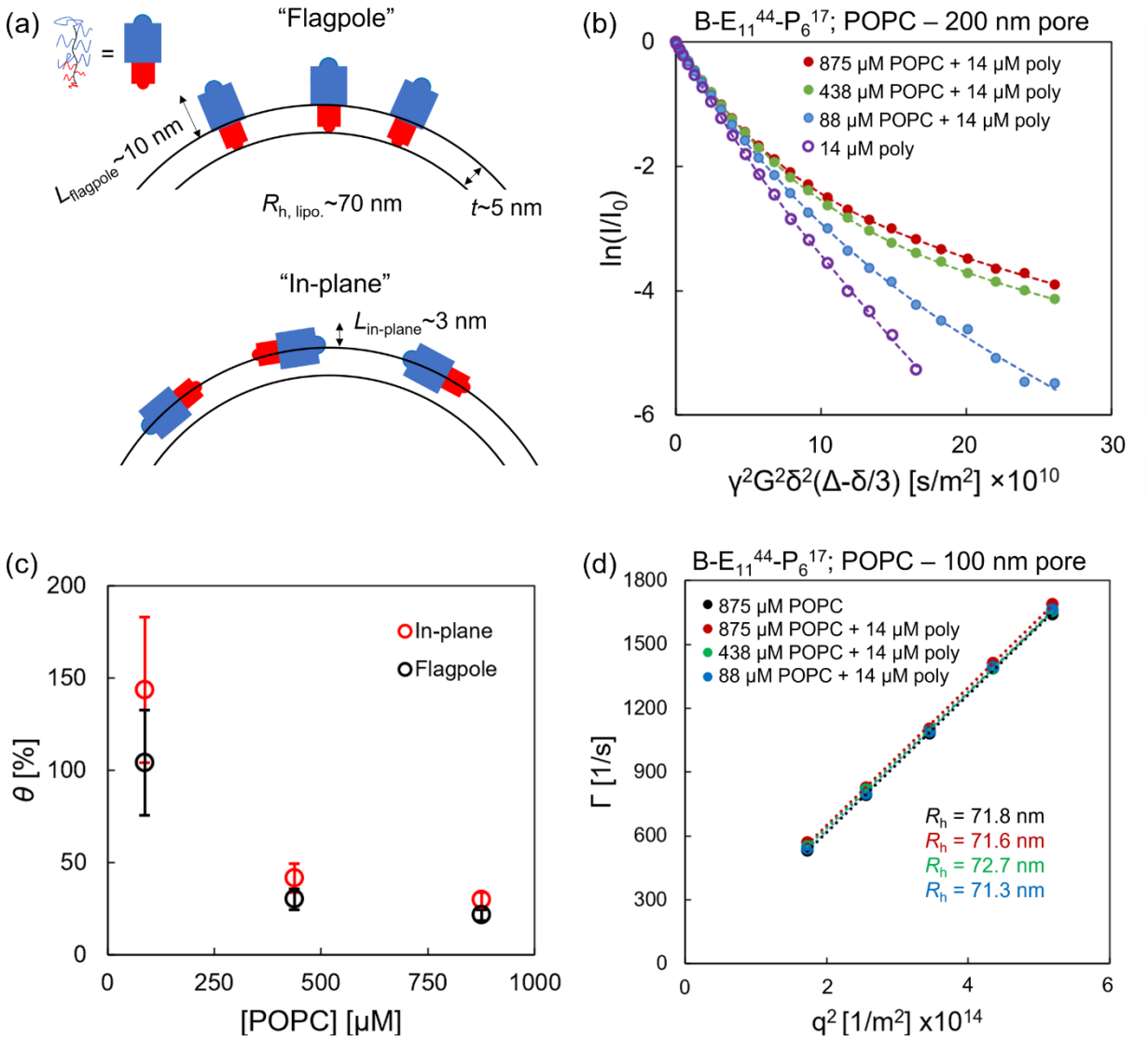

Figure S4.7: Conformation assessment suggests that bound BBPs lie flat in the bilayer plane. (a) Two hypothesized conformations for bound BBP: "flagpole" and "in-plane." $R_{h, lipo.}$ is the hydrodynamic radius of liposomes extruded through a 100 nm filter, L is an estimate of the distance the polymer protrudes normal to the liposome surface, A is an estimate of the surface area occupied per chain, and t is the bilayer thickness. (b) PFG-NMR decay curves over a series of liposome concentrations. Each dataset was fit to the sum of exponentials model and showed evidence of polymer binding to liposomes. (c) Estimated surface area coverage for both conformations based on the number of polymer chains bound to each liposome from the fits to the PFG-NMR data in panel (b). Error estimated by propagating the standard deviation in f_{bound} through the calculation outlined in the text (Eqs. 3–7). (d) DLS data for liposomes treated with *B*-E$_{11}^{43}$-P$_6^{15}$ under the same conditions as in panel (b).

We chose *B*-E_{11}^{43}-P_6^{15} as a model polymer due to its proven membrane affinity. We first performed the PFG-NMR binding assay over a range of liposome concentrations. The decay curves are shown in Figure S4.7b, and binding was detected in all cases except for the polymer-only control. As the liposome concentration decreases there are fewer binding sites, thus the amount of polymer bound per liposome was expected to increase. The number of polymers bound to each liposome can be calculated based on the PFG-NMR data, lipid and polymer concentrations, the fraction of the liposome surface area that is exposed to the solution (estimated via cryo-TEM) and an estimate of the number of lipid molecules per liposome.[85,87,249,251,252] Then, the surface area per chain in the flagpole and in-plane conformations were estimated from BBP characterization data. Finally, the fraction of the liposome surface area covered by polymer was calculated for both proposed conformations, and the results are shown in Figure S4.7c. Details of this calculation can be found in the next section.

If BBPs adopt the in-plane conformation, then the surface area coverage ranges from complete coverage, 144 ± 39%, to only 30 ± 4% at the lowest and highest concentrations of liposomes, respectively. If the flagpole conformation predominates, the surface area coverage ranges from 104 ± 28% to only 22 ± 3%. Thus, for both conformations a wide range of surface area coverages was observed. Multi-angle DLS results for POPC liposomes incubated with *B*-E_{11}^{43}-P_6^{15} at the same three POPC concentrations and a neat liposome control are shown in Figure S4.7d. The slopes of the Γ vs q^2 relationships are identical within error, indicating that polymer incubation does not change the R_h of the liposomes. Therefore, the R_h of the liposomes is independent of polymer surface coverage. This result is more consistent with the in-plane conformation; however, it should be treated as inconclusive for two reasons: (*i*) the R_h of polymer treated liposomes cannot be described simply as the sum of the liposome radius and the contour length of the polymer since, it is not clear how much an incompletely coated brush layer would impact diffusion, and (*ii*) the difference in polymer dimensions normal to the bilayer between the two conformations is small for *B*-E_{11}^{43}-P_6^{15} (~10 nm for flagpole vs. ~3 nm for the in-plane). Due to these experimental

challenges, the dynamic nature of phospholipid bilayers, and the low fraction of polymer chains that bind to the bilayer, we cannot draw definitive conclusions about conformation.

Note, the radius of the liposomes used in the PFG-NMR experiment was twice that of those used in the DLS experiment. The larger liposomes help discriminate between micelles and liposome-bound polymer in the PFG-NMR experiment by increasing the difference in size of these two states. Prior work has established that as the curvature of the liposome increases, binding increases.[86] Thus, the fraction of surface area coverage shown in Figure S4.7c is an underestimate of what is occurring in the DLS experiment. The smaller pore size was chosen in the DLS experiment to increase the % change in radius expected if the flagpole conformation persists.

Calculation of liposome surface area coverage by BBPs in the flagpole and in-plane conformations

The number of polymers bound to each liposome (N_{poly}) was calculated by:

$$N_{poly}=\frac{c}{M_n}*\frac{f_{bound}}{n_{lipid}f}*N_{tot} \quad (S.4)$$

where c is the polymer concentration (14 μM), f_{bound} is the mol fraction of chains bound to liposomes which was estimated by the triexponential model, M_n is the number average molecular weight, n_{lipid} is the concentration of lipid (875 μM), f is the fraction of liposome surface area that is on the exterior bilayer and thus available for polymer binding (estimated via cryo-TEM in Figure S4.3), and N_{tot} is the number of lipids per liposome. N_{tot} was estimated by:

$$N_{tot}=\frac{4\pi R_{lipo}^2}{A}+\frac{4\pi(R_{lipo}-t)^2}{A} \quad (S.5)$$

where R_{lipo} is the hydrodynamic radius of the liposomes measured by DLS, A is the surface area per lipid (0.683 nm^2)[251], and t is the bilayer thickness (5.2 nm).[249,252] This calculation has been employed by our group in the past to calculate the fraction of the liposome surface that is covered by polymers.[85,87] Knowing the chain dimensions and the number of polymers bound to the surface, we can now estimate the surface area coverage for the two hypothesized conformations. For the flagpole conformation, we approximated the PEO side chains as Gaussian coils, and projected the circle with radius of $2R_{g,\ PEO\ side\ chains}$ onto the liposome surface. Thus, the area occupied by a single chain in the flagpole conformation was estimated by:

$$A_{flagpole}=4\pi N_{sc,\ PEO}b_{PEO}^2/6 \quad (S.6)$$

where $N_{sc,\ PEO}$ is the side chain degree of polymerization for the PEO block and b_{PEO} is the statistical segment length of PEO (0.6 nm).[163] For the in-plane conformation, we approximated each bound polymer by adjoined rectangles and semi-circles. In this model, the rectangle represents the cross section of the cylindrical bottlebrush and the semi-circle the terminal side chain, which can protrude in the axial direction. Rectangle dimensions were estimated by the contour length of the backbone and $4R_{g,\ sc}$, and the semicircle had a radius of $2R_{g,\ sc}$ described by:

$$A_{in\text{-}plane}=4L_{bb,PPO}\left(\frac{N_{sc,PPO}b_{PPO}^2}{6}\right)^{\frac{1}{2}}+\frac{1}{2}\pi\left(4\frac{N_{sc,PPO}b_{PPO}^2}{6}\right)+4L_{bb,PEO}\left(\frac{N_{sc,PEO}b_{PEO}^2}{6}\right)^{\frac{1}{2}}+\frac{1}{2}\pi(4\frac{N_{sc,PEO}b_{PEO}^2}{6}) \quad (S.7)$$

where L_{bb} is the contour length, N_{sc} is the side chain degree of polymerization, and b is the statistical segment length for the given block. Now, the fraction of the liposome surface that is covered by the BBP in each conformation was calculated as:

$$\theta_x = \frac{N_{poly} A_x}{4\pi R_{lipo}^2} \tag{S.8}$$

where A_x represents the area occupied by a chain in the conformation of interest. Figure S4.7c shows the relationship between the lipid concentration and surface area coverage for both conformations.

Multiangle DLS data for liposomes treated with high M_n BBP

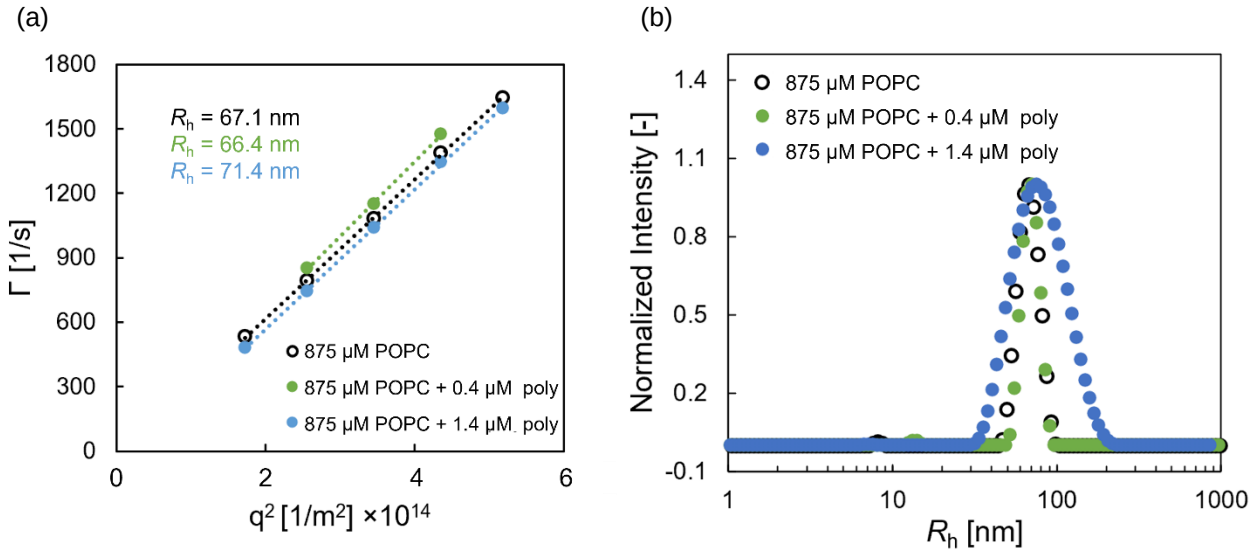

Figure S4.8: (a) Multi-angle DLS data for POPC liposomes and POPC liposomes treated with *B*-E_{168}^{43}-P_{43}^{15}. (b) REPES analysis of the correlation function collected at 90°. A 100 nm diameter membrane was used to prepare the liposomes in this experiment.

To further assess the bound BBP conformation, we repeated the DLS experiment described in the sections above with *B*-E_{168}^{43}-P_{43}^{15} which has a contour length of roughly 120 nm which is ten times longer than that of *B*-E_{11}^{43}-P_6^{15}. Thus, if this polymer adopts the flagpole conformation, it will protrude much further from the liposome surface and be more likely to affect diffusion. Due to the high *Mn* of *B*-E_{168}^{43}-P_{43}^{15}, we had to reduce the polymer concentration to minimize scattering from unimers. Figure S4.8a shows the multi-angle DLS data for three conditions of POPC liposomes treated with *B*-E_{168}^{43}-P_{43}^{15}, and the R_h of all conditions are within error; thus, there is no evidence of a flagpole conformation. Furthermore, REPES analysis shown in Figure S4.8b shows that *B*-E_{168}^{43}-P_{43}^{15} treatment does not change the liposome size distribution. This corroborates the TEM result that *B*-E_{168}^{43}-P_{43}^{15} is not disruptive to lipid bilayers.

Effect of extending PEO block backbone on binding affinity and protection efficacy

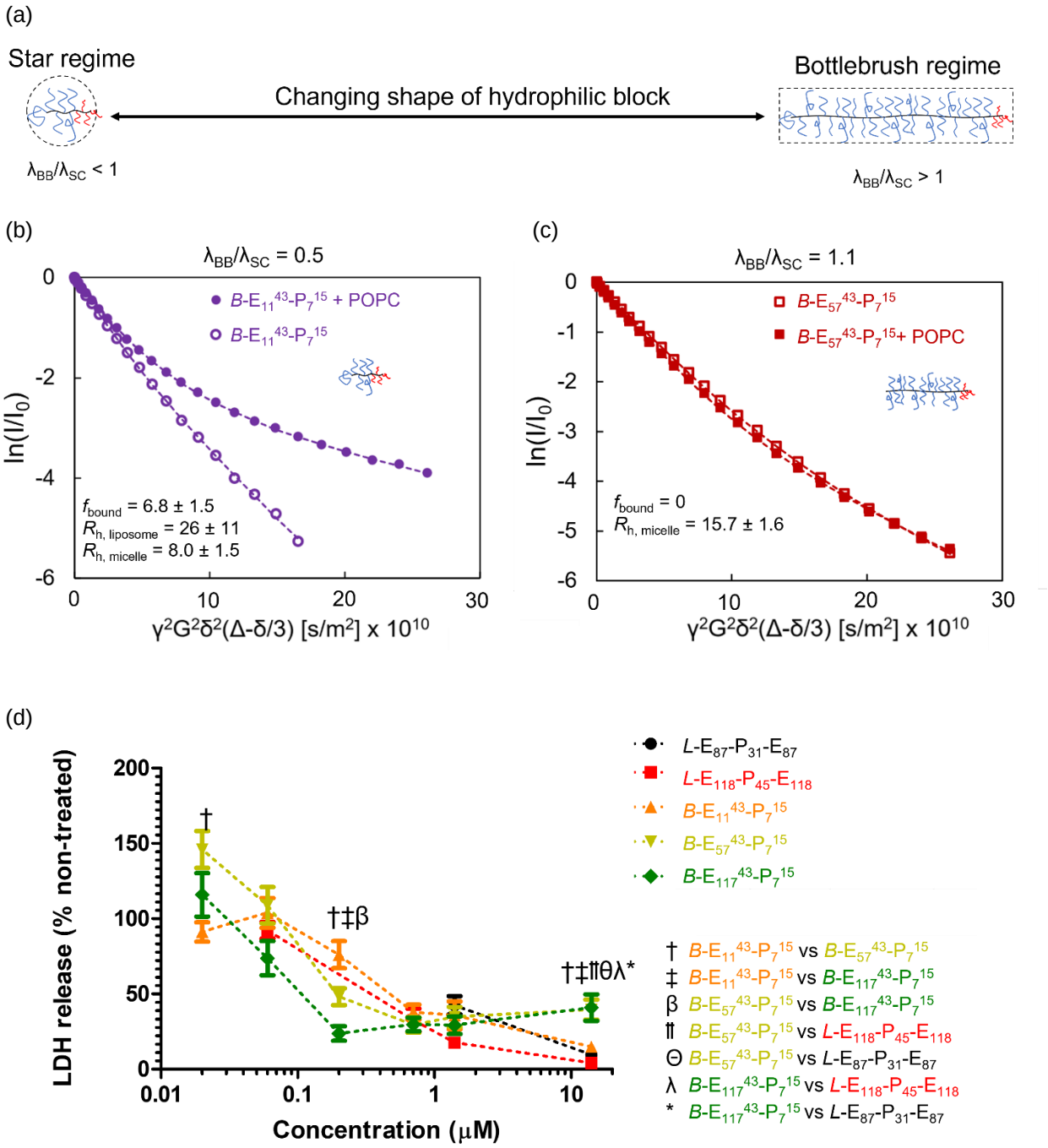

Figure S4.9: Extending the PEO brush block reduces protection efficacy at high concentrations, while improving protection at low concentrations. (a) Sketch of how extending the backbone of the PEO block changes the molecular shape.[152] (b) Representative PFG-NMR decay curves for *B*-E_{10}^{43}-P_5^{15} and liposomes treated with *B*-E_{10}^{43}-P_5^{15}. (c) Representative PFG-NMR decay curves for *B*-E_{57}^{43}-P_5^{15} and liposomes treated with *B*-E_{57}^{43}-P_5^{15}. (d) Osmotic stress protection data over a series of polymer concentrations.

Extending the backbone of the hydrophilic block causes a shape change of the molecule. When the side chain length is longer than the backbone, the molecule occupies a roughly spherical conformation, and this is called the star-like regime. When the backbone is extended and becomes longer than the side chains, the molecule is cylindrical and this is the bottlebrush regime.[152]

Unfortunately, when we extend the backbone past the star-to-brush transition, the size of micelles (R_h ~ 20 nm) approaches that of the liposomes (R_h ~ 30 nm); therefore, the PFG-NMR binding assay is unable to distinguish polymers between these two states. In other words, the overlap between the polymer-only control and the polymer + liposome samples for *B*-E_{57}^{43}-P_5^{15} in Figure S4.9c is not evidence that no polymer binds because chains in the micelle state and liposome state are indistinguishable. However, given the relationship between molecular weight and binding discussed in the main text, we suspect that no detectable binding occurred for *B*-E_{57}^{43}-P_5^{15}.

The osmotic stress protection assay data in Figure S4.9d clearly demonstrate that the protective ability is not lost when the PEO block backbone is extended. In fact, the polymer with the longest PEO backbone (*B*-E_{117}^{44}-P_5^{17}) is significantly more protective than the shortest backbone polymer at a polymer concentration of 0.2 μM. It is interesting that the protective efficacy of *B*-E_{117}^{43}-P_5^{15} and *B*-E_{57}^{43}-P_5^{15} decreases relative to the linear controls and *B*-E_{10}^{43}-P_5^{15} at higher concentrations. As there is little correlation between binding affinity in the PFG-NMR assay and protection in the osmotic stress assay, a decrease in membrane affinity is unlikely the explanation and other factors must be in play.[87]

Finally, this dataset is interesting because it highlights the difference between plotting the osmotic stress protection data in mass vs molar units. Figure S4.9 below shows the same data as in Figure S4.8d but in mass units. When the data are plotted this way, the higher molecular weight BBPs are less protective than the smaller ones. This may suggest that distributing PEO/PPO mass among more chains is beneficial because it leads to more binding sites across the membrane surface. This could allow the polymer to manipulate the mechanical properties of the membrane in more locations and therefore more uniformly.

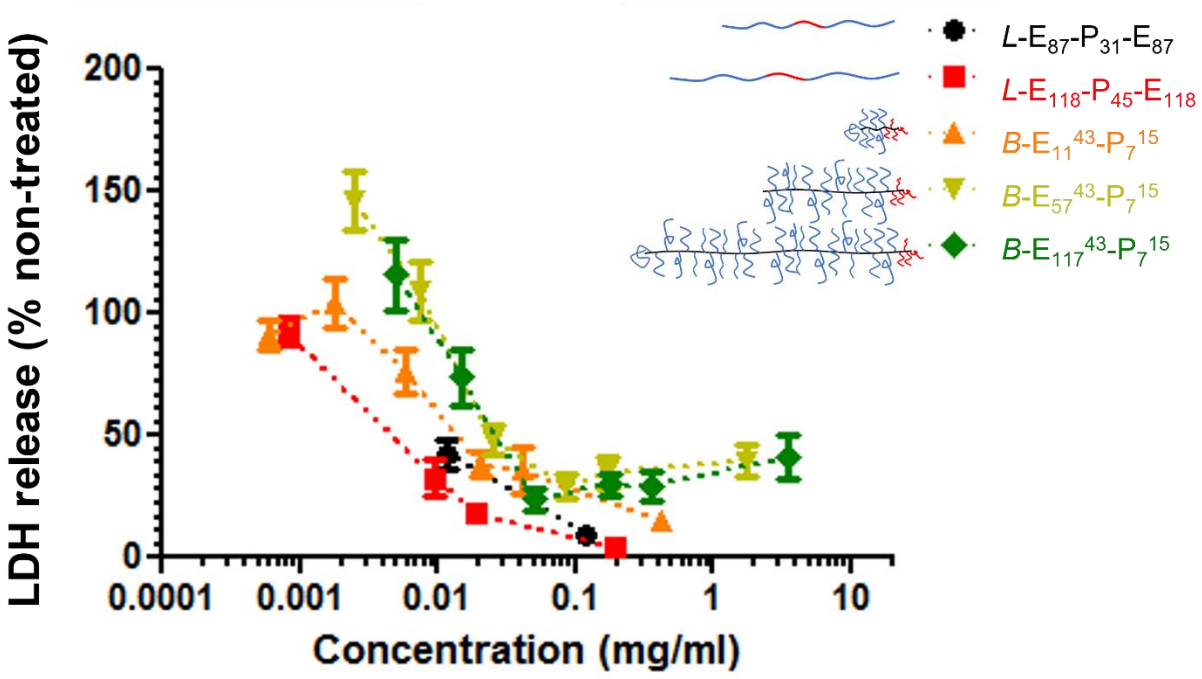

Figure S4.10: Effect of extending the PEO brush block on *in vitro* protection efficacy in mass units. Data are identical to Figure S4.9d, but now plotted in mass units on the x-axis.

Polymer characterization data

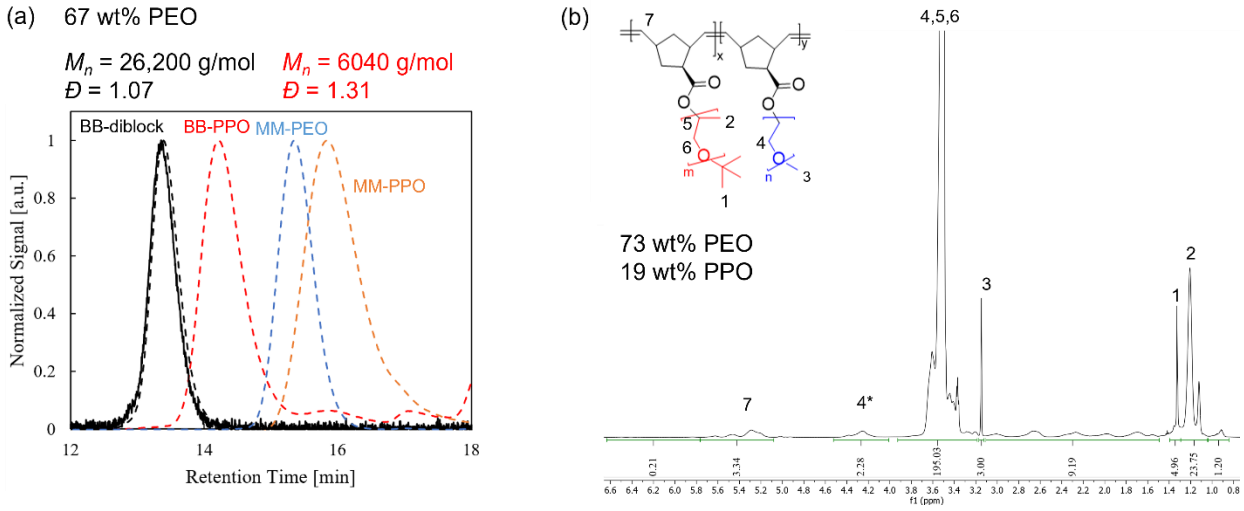

Figure S4.11: Characterization data for ***B*-E$_{10}^{44}$-P$_5^{17}$**. (a) SEC traces of both macromonomers "MM", an aliquot of the PPO block, and the resulting diblock copolymer. Dashed lines are traces from the differential refractive index detector and solid lines from the light scattering detector. (b) ^{1}H NMR spectrum of the purified final product. Peaks 1 and 4* were used to estimate the composition of the diblock, where * denotes the side chain unit adjacent to the ester. This figure was reproduced with permission from a prior publication.[109]

All wt% PEO and wt% PPO reported exclude the mass of norbornene backbone from the numerator of the mass fraction, and thus are exclusively the mass fraction of EO/ PO units respectively. For SEC, the mass fraction of PEO was calculated by:

$$\text{wt\% PEO} = \left(1 - \frac{M_{\text{n,PPO}}}{M_{\text{n,diblock}}}\right) \times \left(\frac{M_{\text{n,PEO-OH}}}{M_{\text{n,PEO-NB}}}\right)_{\text{MALDI}} \quad \text{(S.9)}$$

To estimate the composition of the polymer from the ^{1}H NMR spectrum either the PEO methyl side chain terminus or the PPO t-butyl side chain terminus was used as the integration basis, depending on which had better resolution from the baseline. Then, the ratio of PEO to PPO units with the bottlebrush was calculated by comparing the intensities of the PPO t-butyl peak (1) and the PEO methylene adjacent to the ester of the backbone (4*). The fraction of PPO macromonomer

without the t-butyl α-chain end was accounted for. This calculation is shown in Equation S.10 below:

$$\frac{N_{PEO}}{N_{PPO}} = \frac{\left(\frac{I_{4*}}{2}\right)}{\frac{I_1}{9} * \frac{1}{1-\alpha}} \tag{S.10}$$

where I_x indicates the integral of the corresponding NMR peak, and α is the mol fraction of PPO chains without the t-butyl α-chain end (0.07). Finally, the mass fraction of PEO and PPO can be estimated from the product of the ratio of PEO to PPO units and the molecular weights of both macromonomers as determined by MALDI-ToF spectrometry.

$$\text{wt\% PEO} = \frac{\frac{N_{PEO}}{N_{PPO}} M_{n,PEO\text{-}NB}}{\frac{N_{PEO}}{N_{PPO}} M_{n,PEO\text{-}NB} + M_{n,PPO\text{-}NB}} \times \frac{M_{n,PEO\text{-}OH}}{M_{n,PEO\text{-}NB}} \tag{S.11}$$

$$\text{wt\% PPO} = \left(1 - \frac{\frac{N_{PEO}}{N_{PPO}} M_{n,PEO\text{-}NB}}{\frac{N_{PEO}}{N_{PPO}} M_{n,PEO\text{-}NB} + M_{n,PPO\text{-}NB}}\right) \times \frac{M_{n,PPO\text{-}OH}}{M_{n,PPO\text{-}NB}} \tag{S.12}$$

where $M_{n,\,PEO\text{-}OH}$ and $M_{n,\,PPO\text{-}OH}$ are the number-averaged molecular weights of the MM starting materials prior to functionalization with norbornene while $M_{n,\,PEO\text{-}NB}$ and $M_{n,\,PPO\text{-}NB}$ are the number-averaged molecular weight of the functionalized MMs.

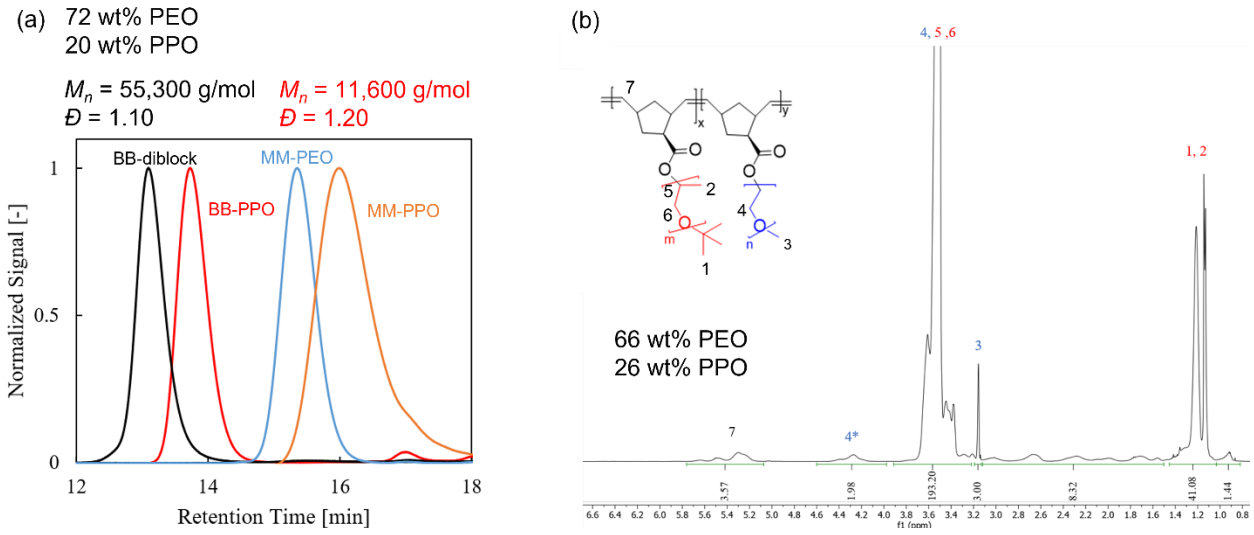

Figure S4.12: Characterization data for ***B*-E$_{21}^{43}$-P$_{11}^{15}$**. (a) SEC traces of both macromonomers "MM", an aliquot of the PPO block, and the resulting diblock copolymer. (b) ^{1}H NMR spectrum of the purified final product. Peaks 3 and 7 were used to estimate the composition of the diblock. This figure was reproduced with permission from a prior publication.[109]

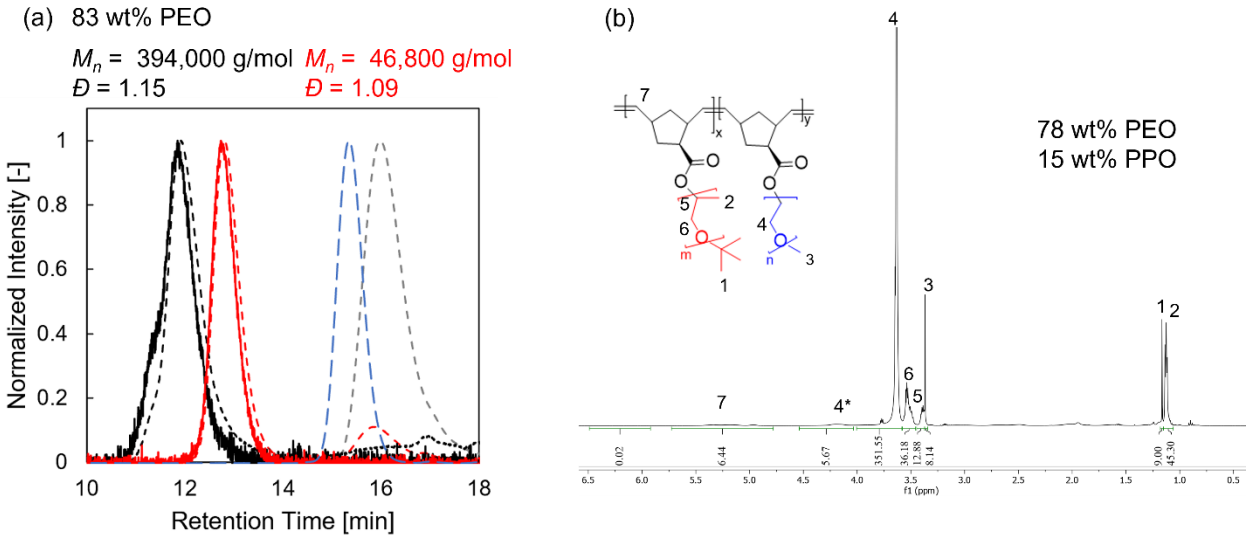

Figure S4.13: Characterization data for ***B*-E$_{168}^{43}$-P$_{43}^{15}$**. (a) SEC traces of both macromonomers "MM", an aliquot of the PPO block, and the resulting diblock copolymer. Dashed lines are traces from the differential refractive index detector and solid lines from the light scattering detector. (b) ^{1}H NMR spectrum of the purified final product. Peaks 1 and 4* were used to estimate the composition of the diblock, where * denotes the side chain unit adjacent to the ester. This figure was reproduced with permission from a prior publication.[109]

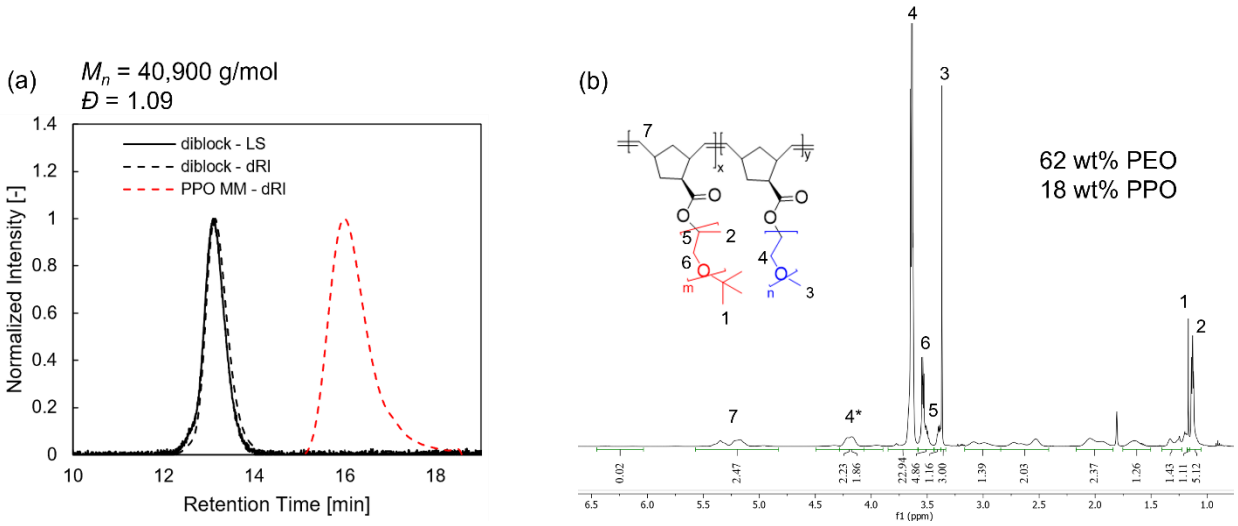

Figure S4.14: Characterization data for ***B*-E$_{54}^{10}$-P$_8^{15}$**. (a) SEC traces of the PPO macromonomer and the resulting diblock copolymer. Dashed lines are traces from the differential refractive index detector and the solid line is the light scattering detector. (b) ^{1}H NMR spectrum of the purified final product. Peaks 1 and 4* were used to estimate the composition of the diblock, where * denotes the side chain unit adjacent to the ester.

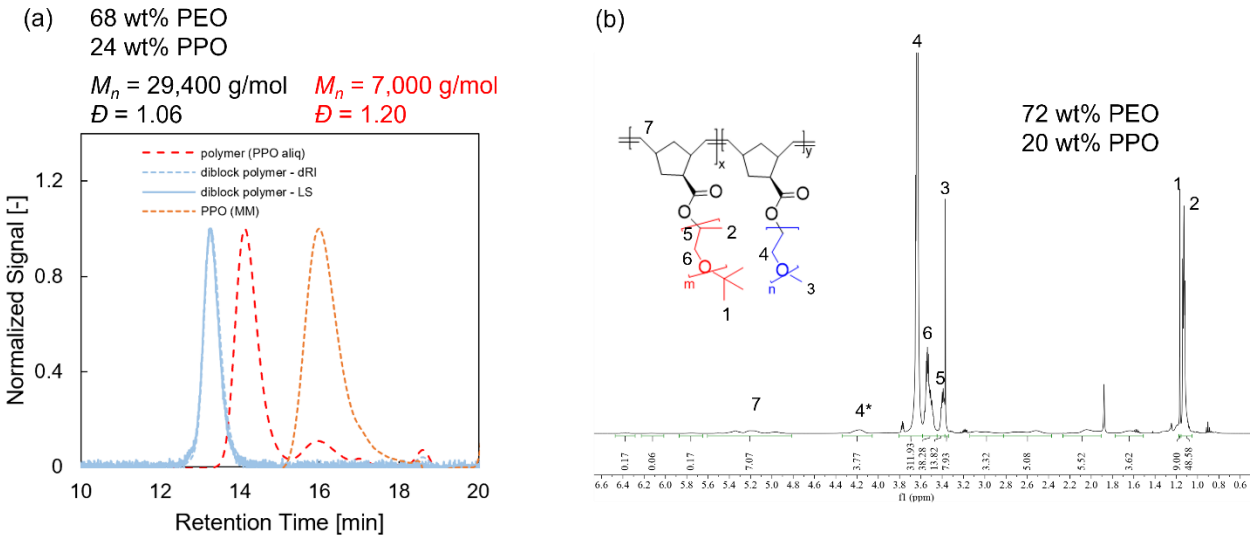

Figure S4.15: Characterization data for ***B*-E$_{11}^{43}$-P$_6^{15}$**. (a) SEC traces of the PPO macromonomer, an aliquot of the PPO block, and the resulting diblock copolymer. Dashed lines are traces from the differential refractive index detector and the solid line is the light scattering detector. (b) ^{1}H NMR spectrum of the purified final product. Peaks 1 and 4* were used to estimate the composition of the diblock, where * denotes the side chain unit adjacent to the ester.

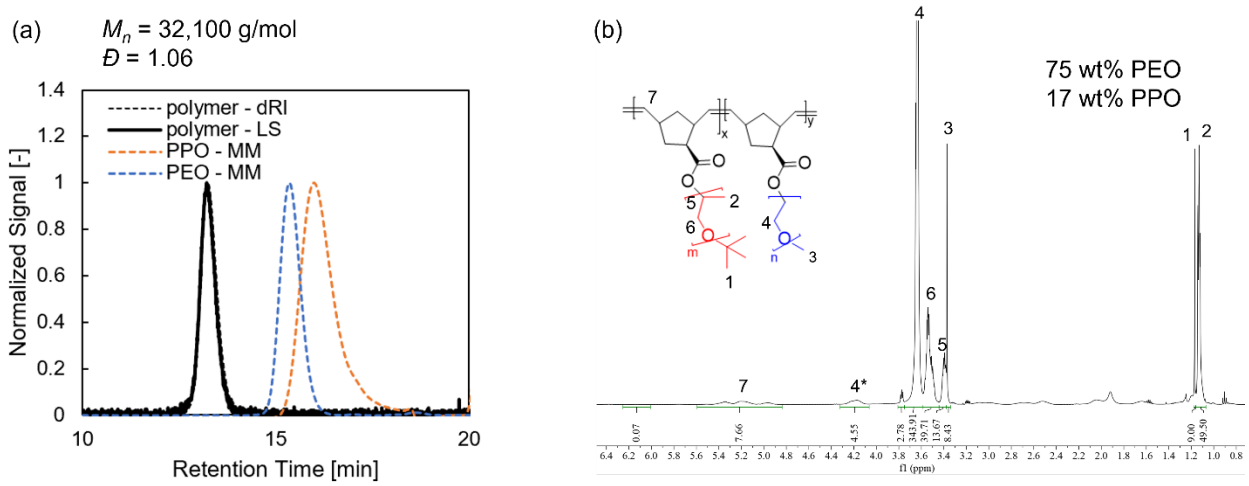

Figure S4.16: Characterization data for ***B*-E$_{12}^{43}$-*s*-P$_6^{15}$**. (a) SEC traces of both macromonomers and the resulting diblock copolymer. Dashed lines are traces from the differential refractive index detector and the solid line is the light scattering detector. (b) ^{1}H NMR spectrum of the purified final product. Peaks 1 and 4* were used to estimate the composition of the diblock, where * denotes the side chain unit adjacent to the ester.

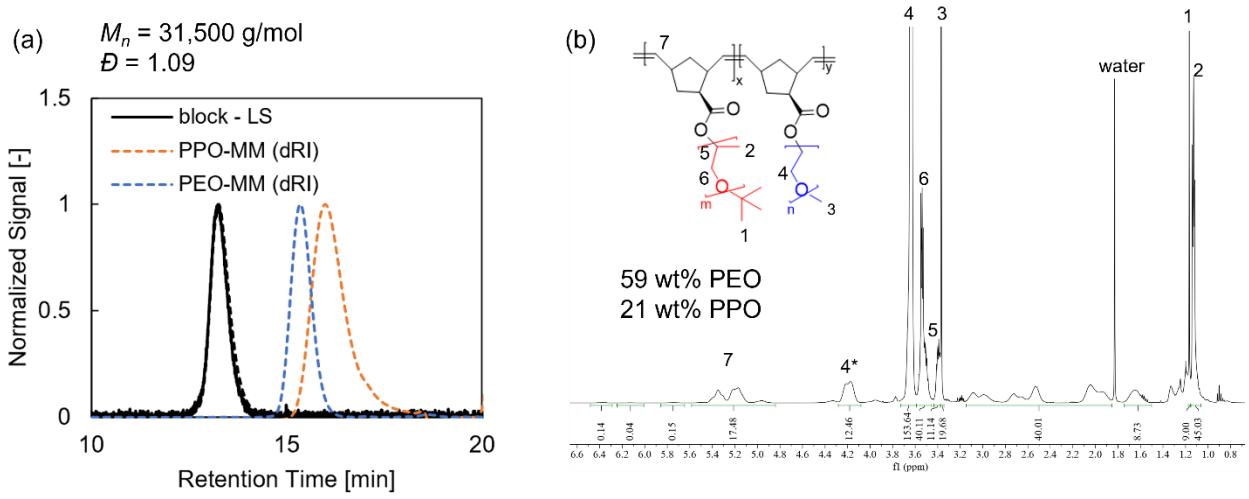

Figure S4.17: Characterization data for ***B*-E$_{40}^{10}$-P$_{7}^{15}$**. (a) SEC traces of both macromonomers and the resulting diblock copolymer. Dashed lines are traces from the differential refractive index detector and the solid line is the light scattering detector. (b) ^{1}H NMR spectrum of the purified final product. Peaks 1 and 4* were used to estimate the composition of the diblock, where * denotes the side chain unit adjacent to the ester.

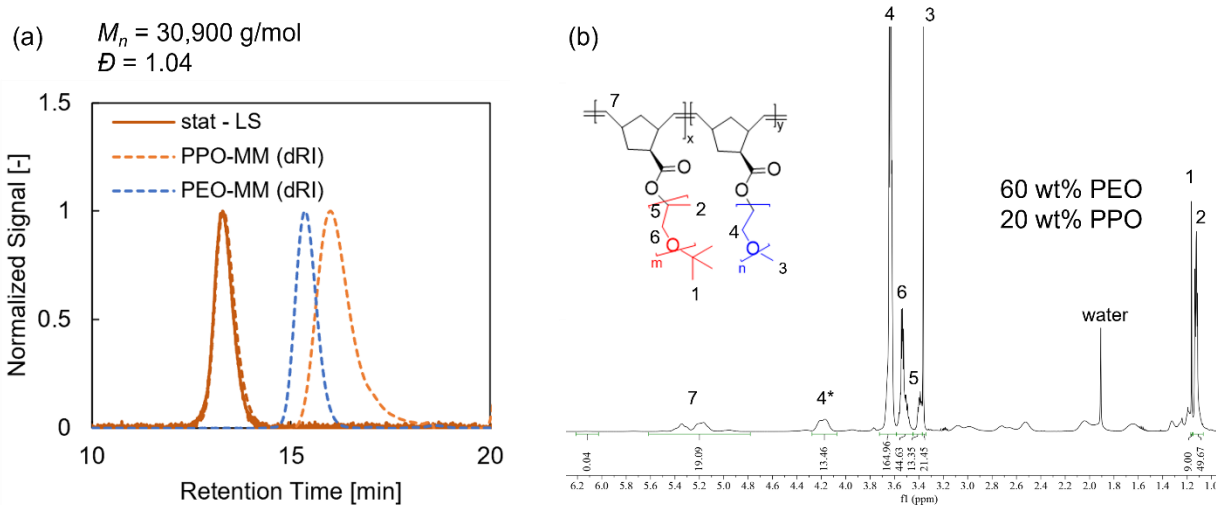

Figure S4.18: Characterization data for ***B*-E$_{40}^{10}$-*s*-P$_7^{15}$**. (a) SEC traces of both macromonomers and the resulting diblock copolymer. Dashed lines are traces from the differential refractive index detector and the solid line is the light scattering detector. (b) ^{1}H NMR spectrum of the purified final product. Peaks 1 and 4* were used to estimate the composition of the diblock, where * denotes the side chain unit adjacent to the ester.

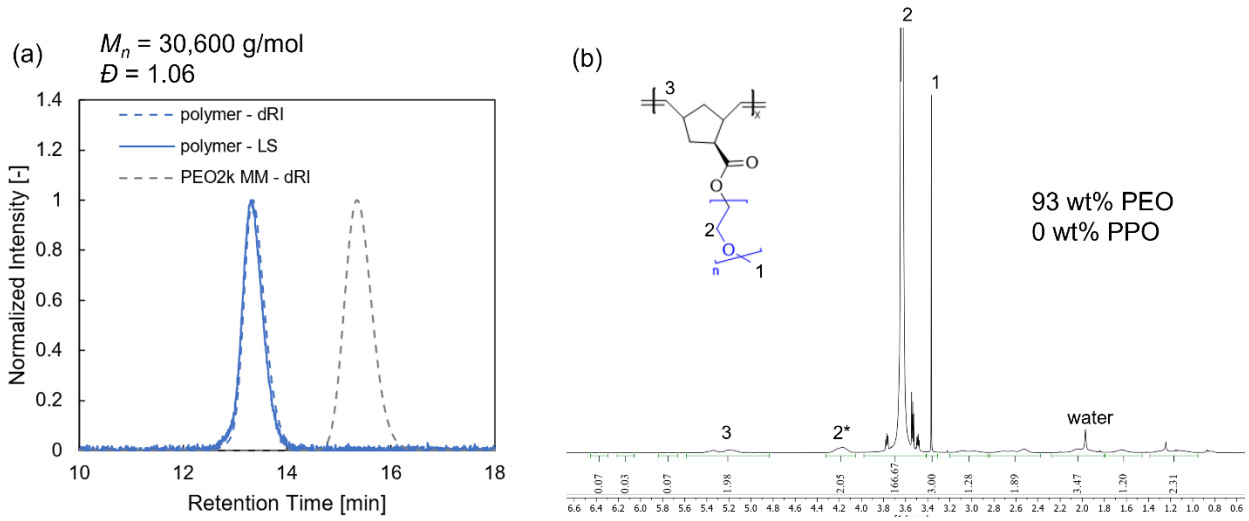

Figure S4.19: Characterization data for ***B*-E$_{15}$^{43}**. (a) SEC traces of the PEO macromonomer and the resulting bottlebrush PEO. Dashed lines are traces from the differential refractive index detector and the solid line is the light scattering detector. (b) ^{1}H NMR spectrum of the purified final product. The composition of PEO matches the composition of the PEO in the macromonomer since this is a brush "homo-polymer."

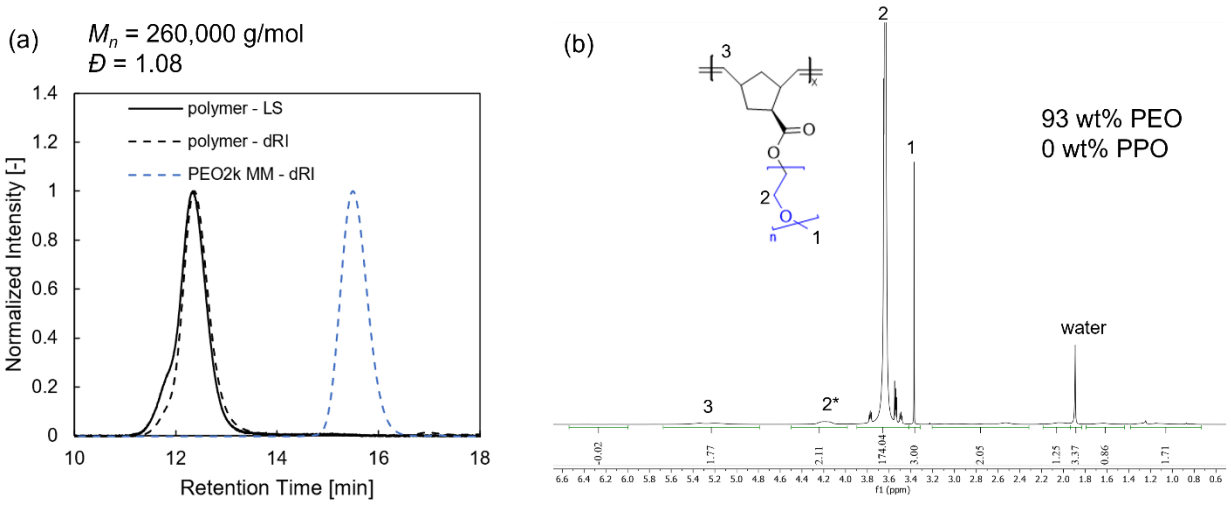

Figure S4.20: Characterization data for ***B*-E$_{126}$[43]**. (a) SEC traces of the PEO macromonomer and the resulting bottlebrush PEO. Dashed lines are traces from the differential refractive index detector and the solid line is the light scattering detector. (b) ^{1}H NMR spectrum of the purified final product. The composition of PEO matches the composition of the PEO in the macromonomer since this is a brush "homo-polymer."

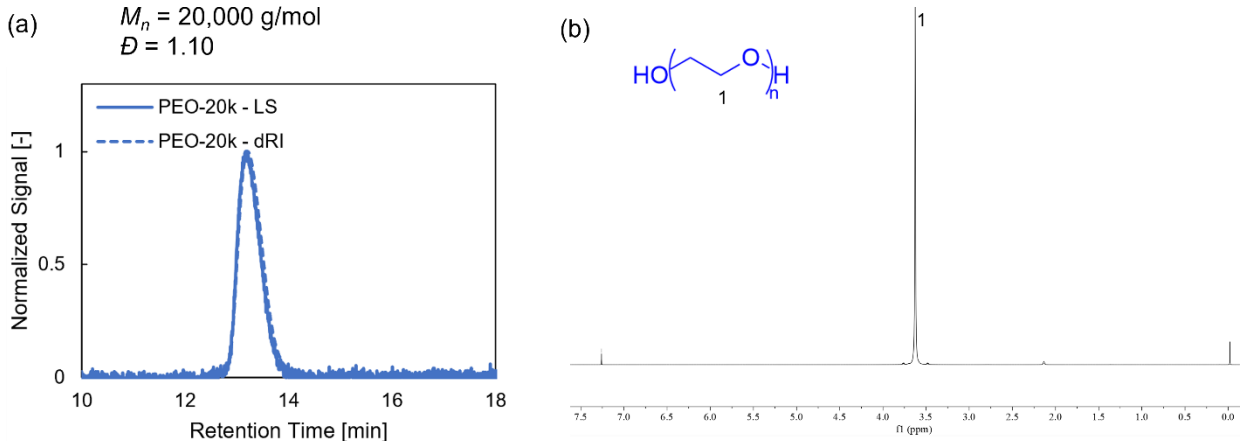

Figure S4.21: Characterization data for ***L*-E$_{455}$**. (a) SEC trace of the commercially available PEO-20k as received. Dashed lines are traces from the differential refractive index detector and the solid line is the light scattering detector. (b) ^{1}H NMR spectrum of the received material.

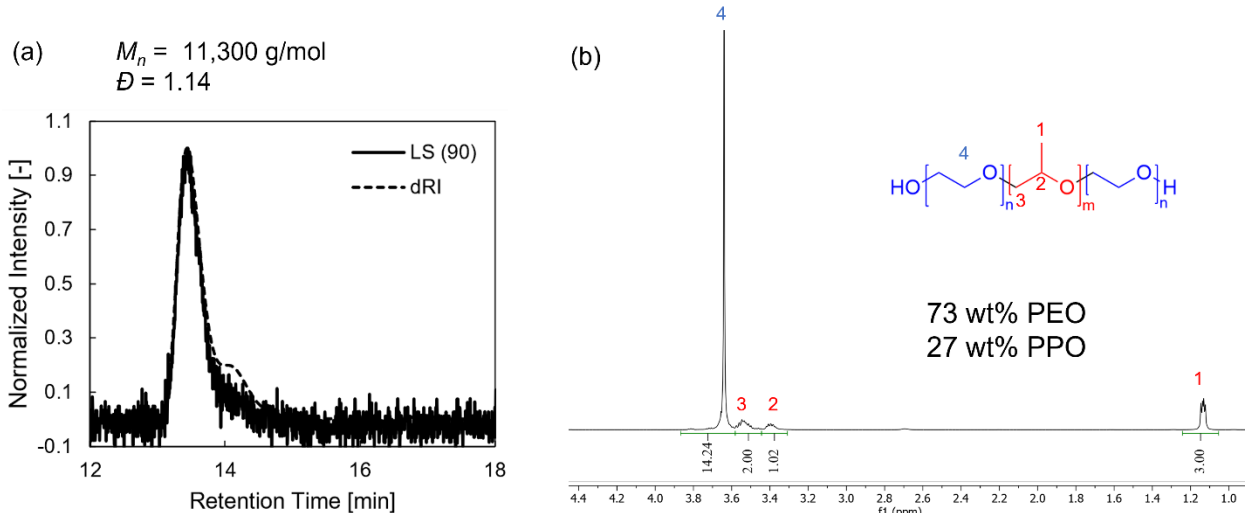

Figure S4.22: Characterization data for ***L*-E$_{93}$-P$_{54}$-E$_{93}$ (F127)**. (a) SEC trace of the commercially available material as received. Dashed lines are traces from the differential refractive index detector and the solid line is the light scattering detector. (b) ^{1}H NMR spectrum of the received material.

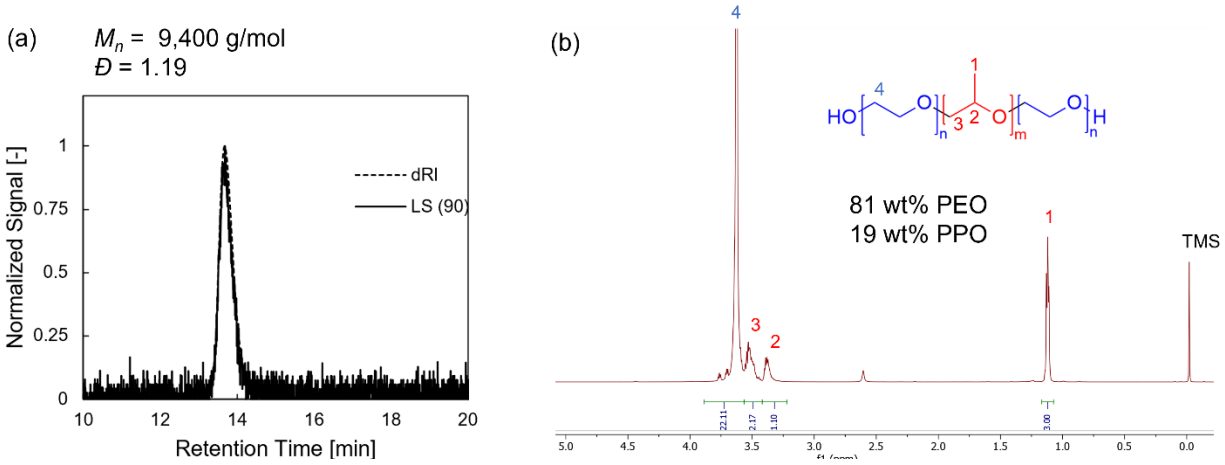

Figure S4.23: Characterization data for ***L*-E$_{87}$-P$_{31}$-E$_{87}$ (P188)**. (a) SEC trace of the commercially available material as received. Dashed lines are traces from the differential refractive index detector and the solid line is the light scattering detector. (b) ^{1}H NMR spectrum of the received material.

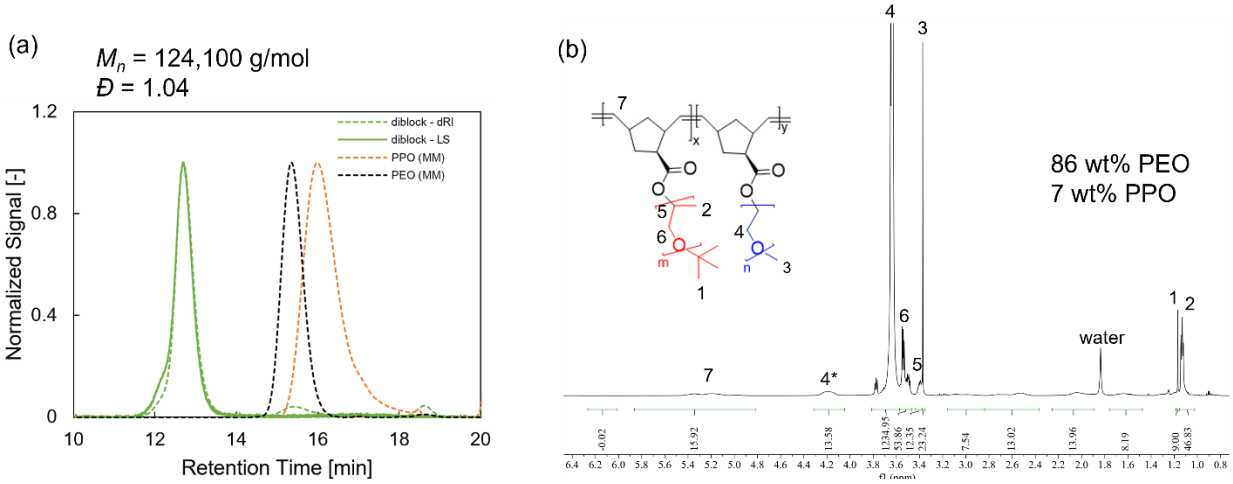

Figure S4.24: Characterization data for ***B*-E$_{57}^{43}$-P$_{7}^{15}$**. (a) SEC traces of both macromonomers and the resulting diblock copolymer. Dashed lines are traces from the differential refractive index detector and the solid line is the light scattering detector. (b) ^{1}H NMR spectrum of the purified final product. Peaks 1 and 4* were used to estimate the composition of the diblock.

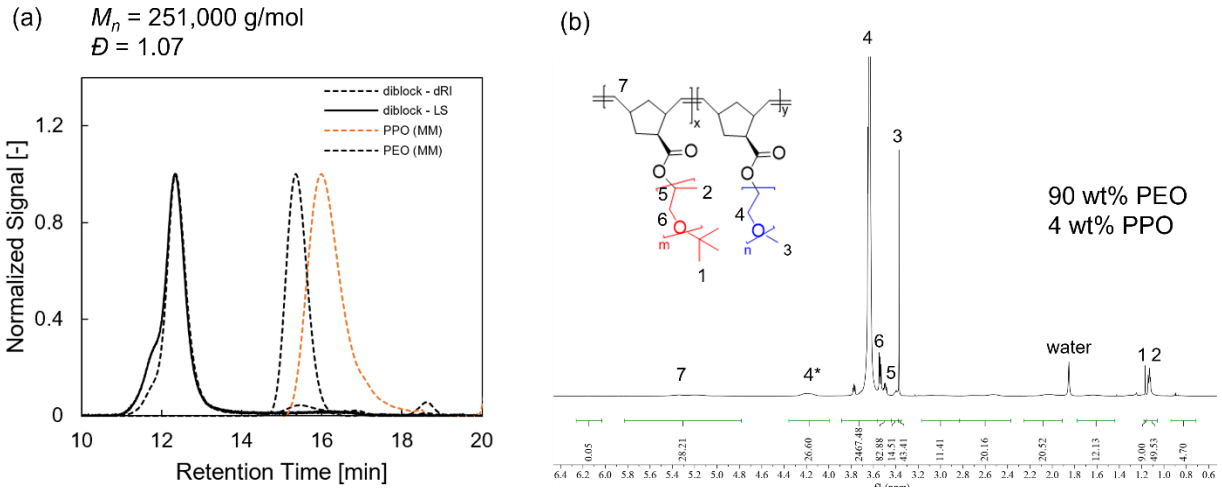

Figure S4.25: Characterization data for ***B*-E$_{117}^{43}$-P$_7^{15}$**. (a) SEC traces of both macromonomers and the resulting diblock copolymer. Dashed lines are traces from the differential refractive index detector and the solid line is the light scattering detector. (b) ^{1}H NMR spectrum of the purified final product. Peaks 1 and 4* were used to estimate the composition of the diblock.

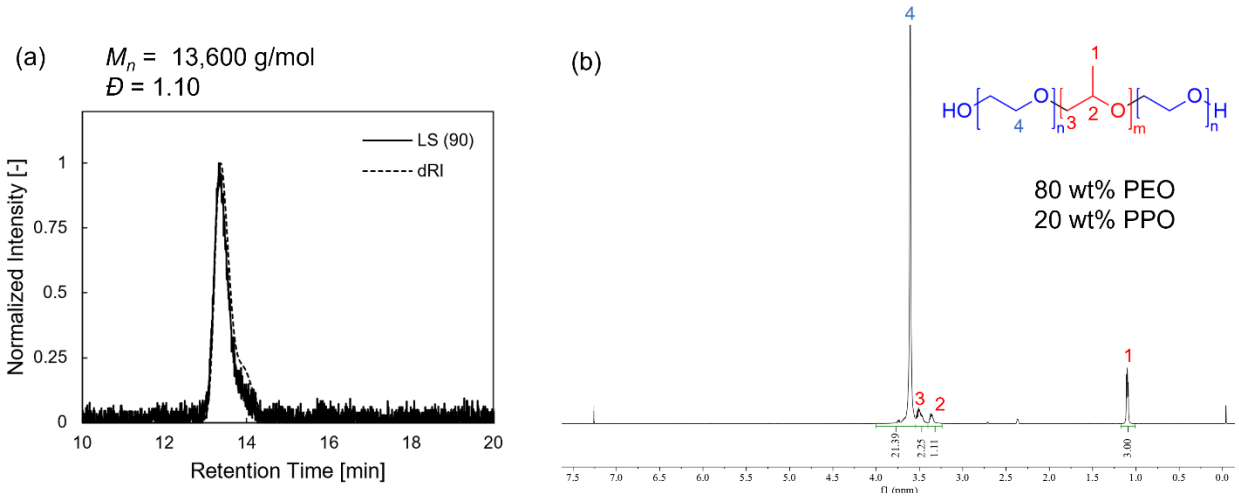

Figure S4.26: Characterization data for ***L*-E$_{118}$-P$_{45}$-E$_{118}$ (F98)**. (a) SEC trace. Dashed lines are traces from the differential refractive index detector and the solid line is the light scattering detector. (b) ^{1}H NMR spectrum of the received material.

Assessment of BBP stability in D_2O

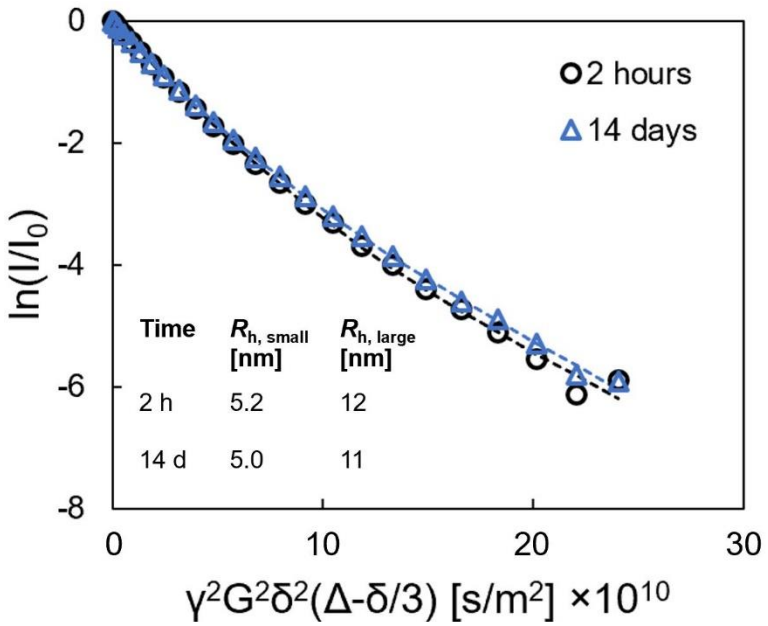

Figure S4.27: PFG-NMR decay curves of a 1 mg/mL solution of ***B*-E_{11}^{43}-P_6^{15}** in D_2O. 2 hours after dissolution (black circles) and 14 days after dissolution (blue triangles). The decay curves and fittings to the biexponential model are within error, indicating that the same two populations are present: free chains and micelles. Additionally, when the 14-day decay curve was fit to the unconstrained triexponential model only two of the populations had non-zero coefficients, again indicating two populations: free chains and micelles.

Chapter 5: Discovery of kinetic trapping of poloxamers inside liposomes via thermal treatment

This chapter was reproduced from Hassler, J.F.; Lawson, M.; Cerna Arroyo, E.; Bates, F.S.; Hackel, B.J.; Lodge, T.P. "Discovery of kinetic trapping of poloxamers inside liposomes via thermal treatment." *Submitted.*

5.1 Motivation

Fundamental understanding of interactions between amphiphilic block copolymers (ABPs) and phospholipids is important for a range of fields including cosmetics,[253] food,[254] nano-reactors,[255] and drug delivery.[256–259] Due to the amphiphilic nature of both ABPs and phospholipids, ABPs can self-assemble with phospholipids to make hybrid polymer-lipid bilayers[190,260,261] or can bind to vesicle surfaces after fabrication.[69,80,85,89,185] In both cases, ABPs have a profound impact on the structure and dynamics of lipid packing,[261,236,80,81,83] manipulate mechanical properties such as the bending and stretching moduli,[69,94,185] and can alter the vesicle morphology.[185] Therefore, ABPs can be used to tailor the mechanical and surface properties of lipid and polymer-lipid vesicles for the specific application. Understanding how polymer parameters such as chemistry, composition, and architecture as well as environmental variables such as temperature impact ABP-vesicle interactions is essential to optimize these systems.

Many amphiphilic polymers such as PEO-PPO, poly(*N*-isopropylacrylamide), and glycopolymers contain moieties that form hydrogen bonds with water. Due to the entropic cost of constraining translation of water molecules bonded to the polymer, as temperature increases the hydrogen bonded water shell dehydrates, making aqueous solutions of these materials thermoresponsive, lower critical solution temperature systems.[88,262–268,97] One consequence of this effect is the decreasing critical micelle concentration (CMC) with increasing temperature.[97] Poloxamers are non-ionic ABPs consisting of PEO-PPO-PEO that are commercially available over a range of molecular weights and compositions and are biocompatible.[269,270] Poloxamer binding to phospholipid bilayers is endothermic,[81] driven by entropically dominated hydrophobic forces.[143,188] Since the hydrophobic effect and the hydrogen-bonded water shell of PEO and PPO

are sensitive to temperature, it is important to understand how temperature and thermal history affects poloxamer-lipid bilayer interactions. However, many mechanistic studies of polymer-lipid bilayer interactions have been conducted at a single temperature, often room temperature, for experimental convenience or because the effects of other variables were the focus.[17,69,273,71,73,81,83,141,145,271,272,87,88,146]

Some previous studies have explored the role of temperature in poloxamer-lipid bilayer systems. Small-angle X-ray scattering (SAXS) experiments performed by Firestone and co-workers found that increasing the temperature of concentrated lipid-polymer mixtures (diblocks and triblocks) led to broadening of the Bragg peaks associated with a lamellar morphology and a contraction of the lamellar spacing.[189,190] These experiments were conducted using samples prepared by mixing the solid components prior to solvation with water, bypassing any binding-unbinding equilibrium and potentially altering the membrane-bound configuration. Wu and co-workers observed that insertion of a triblock poloxamer into lipid monolayers was very sensitive to temperature due to the gel-fluid transition of the acyl tails;[89] however the impact of the changing solvent quality of the polymer was not isolated. Finally, Wang *et al*. reported an increase in the equilibrium association coefficient, K_{eq}, and a decrease in lipid lateral diffusivity with increasing temperature upon exposing two triblock poloxamers (over a range of M_n) to a POPC lipid bilayer supported on a silicon dioxide substrate.[80] They concluded that higher temperatures led to deeper insertion of the PPO block into the membrane; however, because there was only one free surface, diffusion of the polymer through the bilayer was not possible, constraining the bound polymer to hairpin conformations where both PEO blocks remain on the exterior leaflet. Finally, Chandaroy *et al.* demonstrated that temperature impacts the amount of F127 ($M_n \cong$ 12,600 g/mol and 70 wt% PEO) that adheres to the surface of multilamellar vesicles and noted that some chains remain associated with the lipid bilayer when the sample is cooled. Furthermore, incubating F127 with liposomes at high concentrations and elevated temperature limited liposome adhesion to cell

surfaces, demonstrating the potential for using poloxamers to modify liposome surface properties to reduce the immune response.[274]

In this study, we explore the impact of temperature and thermal history on PEO-PPO block copolymer interactions with POPC liposomes, which do not undergo any phase transitions over the temperature range studied (T_m = −2 °C) or place any constraints on bound-polymer configuration. Our results reveal a surprising effect of thermal history on polymer binding to liposomes. A short incubation at 50 °C or 37 °C leads to a kinetically trapped state upon lowering the temperature, with remarkably slow expulsion from the liposome, occurring on a timescale of weeks. Identification and quantification of this phenomenon could have ramifications for liposome mechanical and surface properties and for the cellular distribution of ABPs.

5.2 Materials and Methods

Materials: Poloxamers P188 and P407 (also known as Pluronics F68 and F127, respectively) were generously provided by BASF. 16:0-18:1 1-palmitoyl-2-oleoyl-glycero-3-phosphocholine (POPC) and cholesterol were purchased from Avanti Polar Lipids. Deuterium oxide and deuterated chloroform were purchased from Cambridge Isotope Laboratories. SiliaMetS DMT was purchased from Silicycle. The following materials were obtained from Fisher Scientific and used without further purification: methanol (HPLC grade), diatomaceous earth, diethyl ether (anhydrous), sodium sulfate (anhydrous), and dichloromethane (ACS reagent, anhydrous, 99.8%). The following materials were obtained from Sigma and used without further purification unless otherwise noted: propylene oxide (>99.0%), potassium tert-butoxide, 18-crown-6, butyl-magnesium chloride, palladium (10% on activated charcoal), exo-5-norbornene-2-carboxylic acid (97%), N,N' diisopropylcarbodiimide (99%), tetrahydrofuran (ACS reagent, 97%), methyl ether poly(ethylene glycol) (M_n = 2000 g/mol), ethyl vinyl ether (99%), benzene (ACS reagent, 99%), α-cyano-4-hydroxycinnamic acid, sodium trifluoroacetate, pyridine (>99%), and second generation Grubbs Catalyst® M204. Propylene oxide was distilled twice over butyl magnesium chloride and tetrahydrofuran was dried using an alumina column prior to use in anionic

polymerization. Methyl ether poly(ethylene glycol) was freeze dried from benzene prior to any reactions. Hydrogen gas was obtained from Airgas. $P_{14}E_{118}$ was synthesized via anionic polymerization as reported in a prior publication.[178]

Liposome production: POPC and cholesterol solutions in chloroform were mixed to achieve the desired molar ratio, then the chloroform was gently evaporated using a stream of filtered nitrogen (0.2 μm PTFE filter) to leave a film on the vial walls. Residual chloroform was removed by placing the film under high vacuum for 1 h. The film was then hydrated with deuterium oxide on a vortex plate for 1 h. Finally, liposomes were obtained by extruding the lipid suspension 29 times through an Avanti mini-extruder setup with 50 nm pore diameter. The hydrodynamic radius and dispersity of the liposomes were assessed using multi-angle dynamic light scattering (DLS). The liposome stock solution was diluted to ~1.5 mg/mL and filtered through a 0.2 μm wwPTFE filter into a glass test tube (200 mm × 7 mm with 5 mm inner diameter). DLS experiments were performed using a Brookhaven BI-200SM instrument equipped with a refractive index matching bath and a 637 nm laser. The autocorrelation functions collected at 60°, 75°, 90°, 105°, and 120° were analyzed using the second-order cumulant model (Eq. S1). For all samples the first cumulant scaled linearly with q^2, where q is the scattering vector, and the scaling relationship passed through the origin, consistent with a single diffusive process. Representative DLS data and analysis are shown in Figure S5.1.

Pulsed-field gradient NMR binding assay: PFG-NMR experiments were performed on a Bruker Avance III 500 MHz spectrometer equipped with a 5 mm TBO triple-resonance PFG probe. The ledbpg2s pulse sequence was applied with a 700 ms diffusion time (Δ), 5 ms gradient pulse duration (δ), a gradient strength that varied linearly from 2−95%, an acquisition time and relaxation delay of 1 s, and 32 scans at each gradient strength. For all data analysis, the integral of the PEO peak at ~3.70 ppm was selected because it has the highest signal-to-noise ratio. All samples were mixed at the desired concentrations and allowed to equilibrate at 25 °C for a minimum of 2 h prior

to any thermal treatment or measurement. Previous work has determined that this is sufficiently long to reach a steady state.[85]

All PFG-NMR experiments where data acquisition was performed at 10 °C, 37 °C, or 50 °C were done at 1 mg/mL polymer and 10 mM POPC. A Shigemi tube was used to minimize the effects of convection currents, which we do not expect to be significant over the experimental temperature range (10−50 °C). Samples were held in the probe at the specified temperature for a minimum of 30 min, then locked, tuned, and shimmed prior to data collection.

For kinetic trapping experiments, the samples were prepared at 1 mg/mL polymer and 1.25 mM POPC. Polymer and liposomes were mixed, incubated on a hotplate at the specified temperature for 2 h, and then brought to 25 °C. All PFG-NMR measurements for the kinetic studies were done at 27 °C, which is the standby temperature of the probe and enables automation of the experiments. Within each timepoint, the 3 datasets (50 °C, 37 °C, and 25 °C incubations) were fit to a global two-term expansion of Equation 5.2 where the diffusion coefficients of free and bound polymer were shared among all fits.

PFG-NMR is a 2-dimensional NMR technique where each experiment consists of many (~15-25) 1-D NMR spectra. In each spectrum there is a magnetic field gradient along the z-axis of the sample, which encodes spatial information into the excited nuclei. This leads to decay of all NMR signals as a function of the magnetic field gradient strength and the diffusion coefficient of the species, according to Equation 5.1:[85,165]

$$\ln\left(\frac{I}{I_0}\right) = -\gamma^2\delta^2 G^2(\Delta - \frac{\delta}{3})D \tag{5.1}$$

where I and I_0 are the integral of a chosen NMR signal at the given gradient strength and a gradient strength of 0 respectively, δ is the duration of the magnetic field gradient pulse, Δ is the time between magnetic field gradient pulses (diffusion time), G is the magnetic field gradient strength, γ is the gyromagnetic ratio of a proton (42.6 MHz/T), and D is the translational diffusion coefficient of the species associated with the chosen NMR signal. Previous studies have demonstrated that PFG-NMR is a robust technique for measuring the fraction of polymer chains that bind to a

liposome.[85–88] When multiple populations are present, as long as their characteristic sizes differ by at least a factor of ~2, multiple rates of diffusion can be extracted by fitting the signal decay to a sum of exponentials given by Equation 5.2:

$$\ln\left(\frac{I}{I_0}\right) = \ln(\sum_i f_i \exp(-\gamma^2\delta^2 G^2(\Delta - \frac{\delta}{3})D_i) \quad (5.2)$$

where f_i is the mol fraction of chains in state i (i.e. solvated free chain, in a micelle, or bound to a liposome) and D_i is the corresponding translational diffusion coefficient.

SAXS: X-ray scattering experiments were performed on beamline 5-ID-D at the Advanced Photon Source, Argonne National Lab. The incident wavelength was $\lambda = 0.7293$ Å and two detectors were used at distances of 1.0 m and 8.5 m, affording a q-range of 0.0025−0.195 $Å^{-1}$. Samples were loaded into quartz capillaries and sealed with epoxy resin. Temperature was controlled using a custom-built multi-capillary stage to obtain SAXS patterns along the following thermal sequence: 25 °C, 10 °C, 37 °C, 50 °C, 25 °C with a 10 min equilibration period between changes in setpoint. Three 1 s beam exposures were performed at different locations along the capillary. The 2-D scattering vector was calibrated using a Au-coated silicon chip with a 7200 lines/mm grating. 2-D patterns were azimuthally integrated to give 1-D traces of scattering intensity, $I(q)$, as a function of the scattering vector $q = 4\pi\lambda^{-1}\sin(\theta/2)$, where θ is the scattering angle.

Bottlebrush synthesis: The synthesis of the bottlebrush poloxamers (BBPs) has been reported elsewhere.[109] Briefly, PPO with a single terminal alcohol group was synthesized by anionic polymerization in tetrahydrofuran at 25 °C, with the addition of 18-crown-6 (2 eqv). The resulting PPO had M_n = 1090 g/mol, $Đ$ = 1.12, and 7% of the α-chain ends were an alkene impurity which was removed via a hydrogenation reaction catalyzed by palladium on carbon. Mono-alcohol functionalized PPO and methyl ether poly(ethylene oxide) (M_n ~ 2000 g/mol) were then functionalized with norbornene using an established esterification protocol.[109,181] PPO macromonomer was purified by vacuum drying at 50 °C, and PEO macromonomer was purified via precipitation into cold diethyl ether. Ring opening metathesis polymerization reactions were

carried out with Grubbs 3rd generation catalyst to yield the diblock BBP (M_n = 29,400 g/mol, $Đ$ = 1.06, wt% PEO = 72%). Catalyst was removed by chelation with SiliaMetS DMT and then the effluent was passed through a column of diatomaceous earth. Grubbs 3rd generation catalyst was prepared from Grubbs 2nd generation catalyst by reaction with pyridine.[233]

Polymer characterization: All polymers were characterized by ^{1}H NMR spectroscopy with $CDCl_3$ as the solvent to estimate the composition. Size exclusion chromatography (SEC) with multi-angle light scattering detection was used to assess the molecular weight distribution. SEC samples were prepared at 5 mg/mL in THF and were filtered through a 0.2 μm PTFE filter. The instrument was equipped with a Wyatt Dawn Heleos II multiangle light scattering detector. The differential refractive index (*dn/dc*) of all block copolymers was calculated as the weighted average of the *dn/dc* values of PEO (0.068 mL/g) and PPO (0.087 mL/g) in THF.[202] MALDI-ToF spectrometry was performed using α-cyano-4-hydroxycinnamic acid as the matrix (30 mg/mL in THF) and sodium trifluoroacetate as the counterion source (1 mg/mL in THF), which were mixed with polymer (3 mg/mL in THF) at a matrix:polymer:counterion volume ratio of 3:1:0.1. Characterization data are summarized in Table 5.1 and all data can be found in Figures S5.18-S5.22. The expected chain hydrodynamic radius (R_h) was estimated assuming the chains are Gaussian coils and by applying Equation 5.3 below:

$$R_{h,o} = \frac{2}{3} R_g = \frac{2}{3} \left(\frac{Nb^2}{6}\right)^{\frac{1}{2}} \tag{5.3}$$

where R_g is the radius of gyration, N is the number averaged degree of polymerization, and b is the statistical segment length which is 6.0 Å for PEO and 5.9 Å for PPO.[163]

Table 5.1: Polymer Characteristics

Polymer	Commercial Name	M_n [kDa][a]	$Đ$[a]	wt% PEO[b]	$R_{h,o}$ [nm][c]
L-$E_{93}P_{54}E_{93}$	F127	11.3	1.14	73	2.5
B-$E_{11}^{43}P_{6}^{15}$	-	29.4	1.06	72	5.5[d]
L-E_{455}	-	20.0	1.10	100	3.5
L-$E_{87}P_{31}E_{87}$	P188	9.4	1.19	81	2.3
L-$P_{14}E_{118}$	-	6.2[e]	1.02[e]	84	1.9

[a]SEC(MALS + dRI)
[b]NMR
[c]Estimated assuming polymer is a Gaussian coil using Eq. 3
[d]Estimated as half the contour length
[e]MALDI-ToF spectrometry
Polymer nomenclature: The first letter denotes architecture (*L* = linear and *B* = bottlebrush). E and P indicate PEO and PPO, respectively. For the bottlebrush architecture, the subscript and superscript give the number averaged degree of polymerization of the backbone and sidechain, respectively.

5.3 Results and Discussion

Impact of thermal history on F127 binding to liposomes: We employed an established liposome binding assay based on PFG-NMR[82,85,87,88,146] to assess the impact of thermal history on F127 binding to POPC liposomes. Figure 5.1a shows the thermal history of two otherwise identical F127 + POPC samples at 1 mg/mL polymer and 10 mM POPC. Figure 5.1b shows the PFG-NMR data for these two samples and a 1 mg/mL F127 solution without liposomes (negative control). Both F127 + POPC samples (solid symbols) show two rates of relaxation, indicating co-existence of free chains and polymer bound to the liposomes; meanwhile, the F127 solution control (open symbols) shows a single rate of decay. Clearly, the two F127 + POPC samples have distinct PFG-

NMR decay curves and fitting the data to a two-term expansion of Equation 5.2 reveals that the sample with thermal history (red) has 29 ± 3 mol% of chains bound to liposomes (corresponding to 220 ± 10 chains per liposome), whereas the sample that was held exclusively at 25 °C prior to the measurement (grey) only has 4 ± 1 mol% bound chains (30 ± 10 chains per liposome).

DLS performed before and after incubation at 50 °C for 2 h confirmed that the R_h and $Đ$ of the liposomes does not change during this protocol (Figure S5.2). Furthermore, SAXS experiments performed *in situ* with a similar thermal protocol found no qualitative change to the scattering patterns (Figure S5.3). Thus, we conclude that the bilayer form factor, which is dependent on the electron density and width of the headgroup and tailgroup regions averaged over the entire liposome surface, and over all liposomes in the sample, did not change.[16] Therefore, the liposomes are stable during the thermal treatment, and the difference between the thermal history and control samples is not due to liposome damage.

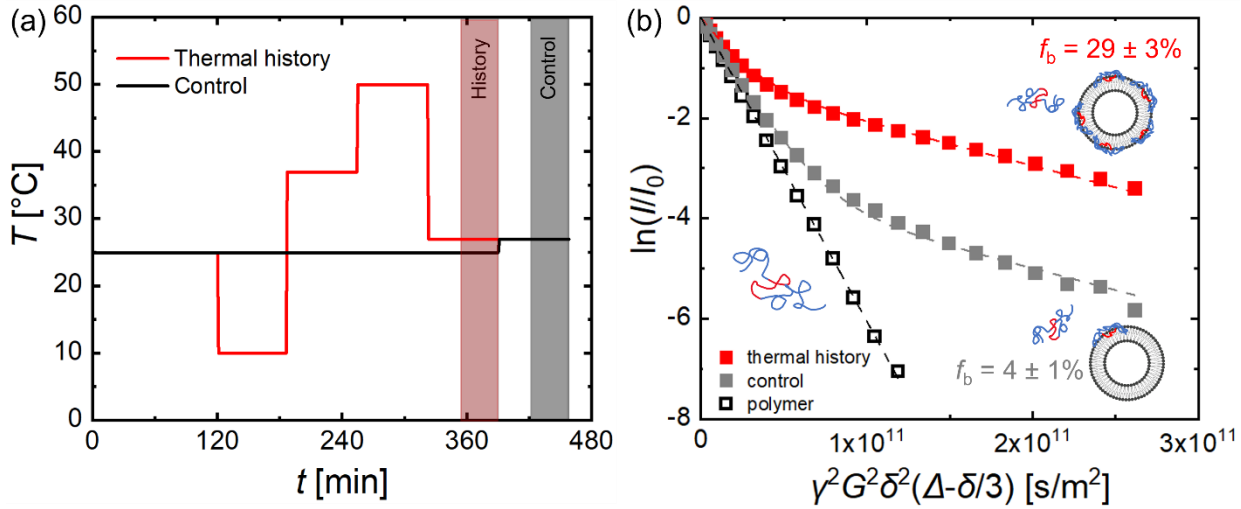

Figure 5.1: (a) Thermal history imposed on two F127 + POPC samples to assess the impact of thermal history. Shaded regions indicate the duration of the PFG-NMR data acquisition. (b) PFG-NMR result of F127 in solution at 1 mg/mL (open) and two F127 + POPC samples both at 1 mg/mL F127 and 10 mM POPC (filled). All PFG-NMR data were acquired at 27 °C.

To understand the effect of temperature on the liposome binding affinity of F127, we also performed PFG-NMR measurements at each of the temperatures shown in Figure 5.1a. We found that chains desorb completely within 30 min upon cooling to 10 °C following a 25 °C incubation period. Then, as temperature increases to 37 °C, f_b reaches a maximum at 45 ± 2 mol%. Based on the PFG-NMR measurements performed on F127 + POPC at 37 °C (f_b = 45 ± 2 mol%) and the control sample in Figure 5.1b (gray solid: f_b = 4 ± 1 mol%), the binding affinity of F127 towards liposomes increases by a factor of 11 ± 3 over a temperature increase of only 10 °C. This striking effect is particularly notable as the higher temperature corresponds to physiological conditions. Upon further heating to 50 °C formation of copolymer micelles becomes favorable, and at the elevated temperature chains can desorb to occupy micelles, leading to a decrease in binding to f_b = 13 ± 3 mol%, but still well above the 25 °C result. The variable temperature PFG-NMR data are presented in Figure S5.4 and the fits to Equation 5.2 are summarized in Table S5.1 and Figure S5.5. Based on the increase in binding observed at elevated temperatures and the thermal path dependence shown in Figure 5.1, we conclude that a significant fraction of the chains that bind at elevated temperatures remain attached to the membrane after the system is cooled.

Relaxation kinetics of thermally treated F127 + POPC samples: To assess whether this remarkable difference in binding between the thermal history and control samples decays over time, we mixed F127 and POPC liposomes, incubated them at 50 °C, 37 °C, or 25 °C for 2 h, then allowed the samples to recover at 25 °C, and performed PFG-NMR measurements at 27 °C as a function of time following the incubation, which we call the recovery time (t_{rec}). This protocol is summarized schematically in Figure 5.2a.

Figures 5.2b-e display representative timepoints of this experiment, and a full dataset is shown in Figure S5.7. Figure 5.2b shows that 24 h into the recovery period there are still significantly more chains bound to the liposomes in the 50 °C and 37 °C incubated samples (f_b = 9.0 ± 0.9 mol% and f_b = 12.6 ± 1.3 mol%, respectively) than in the control sample maintained at 25 °C (f_b = 2.5 ±

0.3 mol%). Importantly, this confirms that the onset of thermal history dependence does occur near 37 °C, emphasizing that this phenomenon is physiologically relevant.

Figure 5.2e shows that after 768 h of recovery at 25 °C the PFG-NMR decay curves of all thermal histories overlap, and at this time point f_b is within 1 mol% for all datasets. Since the excess bound polymers in the samples incubated at 50 °C and 37 °C do eventually desorb, we conclude that the bound state accessed at the elevated temperature is not lower in free energy at 25 °C than the bound state reached with a 25 °C incubation. The extremely slow desorption kinetics after thermal treatment ($t_{1/2}$ ~ O(100 h)) are surprising because lipid bilayers are dynamic systems with facile lateral diffusion of lipid molecules ($D_L \sim 10^{-13}$ m^2/s),[18] and the polymer is associated with the bilayer by relatively weak hydrophobic forces. Therefore, we conclude that at elevated temperatures the chains access a liposome-bound state that is inaccessible at 25 °C, and then upon cooling the system chains in this state become kinetically trapped.

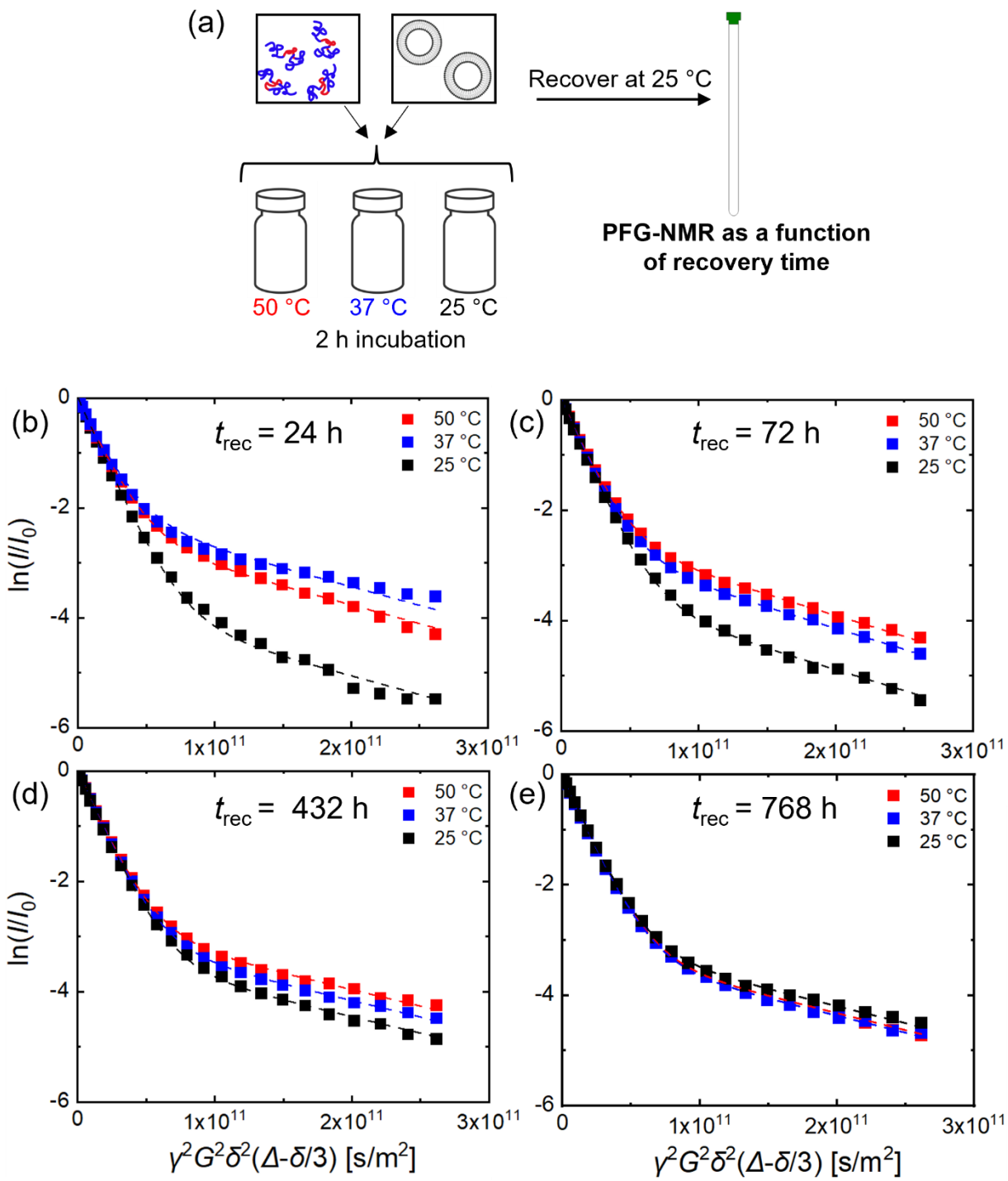

Figure 5.2: (a) Schematic of the incubation and PFG-NMR measurement protocol used for the kinetic trapping experiment. (b-e) Representative PFG-NMR data of F127 + POPC samples (1 mg/mL F127 + 1.25 mM POPC) with different incubation temperatures as a function of recovery time, t_{rec}. All PFG-NMR data were collected at 27 °C.

We can quantify the rate of F127 desorption from the kinetically trapped state by modelling the process as a first order reaction. We performed three independent replicates of the experiment outlined in Figure 5.2a. The resulting f_b vs t_{rec} curves are shown in Figure 3 and the data were fit to Equation 5.4, which was derived from a first order rate law.

$$f_b(t_{rec}, T_{inc}) = f_{b,0} \exp[-k_{rec} t_{rec}] + \overline{f_b}(T_{inc}=25\ °C) \quad (5.4)$$

Here, $f_{b,0}$ and k_{rec} are fitting parameters that represent the amount of polymer in the trapped state and the rate constant of desorption from the trapped state, respectively. $f_b(t_{rec}, T_{inc})$ is the measured amount of bound polymer resulting from the fit to the PFG-NMR data, and $\overline{f_b}(T_{inc}=25\ °C)$ is the amount of bound polymer in the sample that was maintained at 25 °C averaged over all time points. This term was included to satisfy the long-time limit where the samples incubated at 50 °C and 37 °C reach the same steady state as the sample maintained at 25 °C.

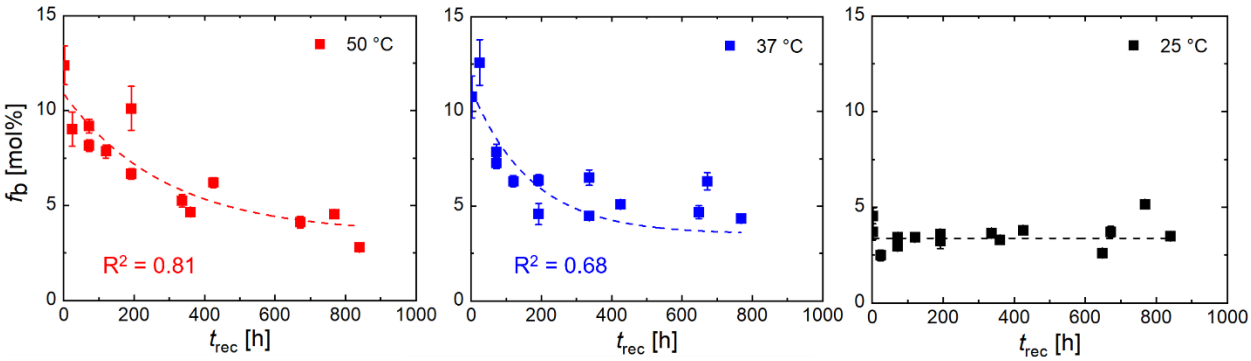

Figure 5.3: Kinetic analysis of the desorption reaction monitored by PFG-NMR as a function of recovery time. Each data point is an independent replicate and error bars are the 95% confidence interval on the fit to the PFG-NMR data.

Notably, the 25 °C control shows a flat line within experimental uncertainty, and $f_{b,0} = 0$. This is consistent with previous results showing that a steady state is reached within 2 h of mixing polymer and liposomes.[85] On the other hand, $f_{b,0}$ and k_{rec} for the samples incubated at 50 °C and 37 °C are significantly different from 0, indicating that the elevated temperatures have a

measurable effect on the fraction of bound chains, and that this method yields a quantitative measurement of the desorption kinetics. The fitting parameters are summarized in Table 5.2. Based on the 95% confidence intervals, we do not observe a significant difference in either $f_{b,0}$ or k_{rec} between the 50 °C and 37 °C datasets. Thus, both incubation temperatures lead to equal prevalence of the same non-equilibrium, kinetically trapped state.

Table 5.2: Fit Parameters for Data in Figure 5.3

Incubation Temp. [°C]	$k_{rec} \times 10^{-3}$ **[h^{-1}]**	$f_{b,0}$ **[mol%]**
50	3.5 (1.6 – 5.4)	7.4 (5.6 – 9.1)
37	5.9 (2.1 – 10.1)	7.7 (5.3 – 10.1)
25	-	0 (0 – 0.4)

Parentheses are 95% confidence intervals

Figure 5.4a shows a sketch of a proposed mechanism for this kinetic trapping effect. First it is important to understand that poloxamer insertion into phospholipid bilayers is endothermic and therefore is an entropically dominated process.[81] As a polymer contacts the liposome, hydrogen bonds between the ether units and water are broken, and the resulting translational freedom of the water molecules leads to an overall increase in entropy. Because the methyl units of PPO result in weaker hydrogen bonds with water, the PPO block primarily drives binding by inserting into the acyl region.[85,188,191] During a 25 °C incubation, we believe the adsorbed polymer occupies a "hairpin" conformation where the PPO adsorbs and inserts into the acyl region, and both PEO blocks remain solvated on the exterior side of the lipid bilayer. When the system is cooled to 10 °C, more water molecules surround the exposed PEO units and the increased solvent quality creates an enthalpic driving force for desorption, and the hairpin state can be pulled out of the bilayer, leading to complete desorption of the polymer (Fig. S4).

However, if the system is heated above a critical temperature, T_{crit}, between 27−37 °C, we have observed that F127 becomes kinetically trapped upon cooling the system to 25 °C. As temperature increases, the hydrogen-bonded water shell surrounding both PEO and PPO units is dehydrated. Dehydrating the PEO units lowers the free energy barrier associated with this block traversing the hydrophobic acyl region of the bilayer. This enables a triblock PEO-PPO-PEO copolymer to access the transbilayer conformation where the PEO blocks are in solution on opposite sides of the bilayer, with the PPO block spanning the acyl region as shown in the upper-left of Figure 5.4a. Monte Carlo simulations performed by Rabbel *et al.* found that as the PPO block fraction of triblock copolymers increases, the transmembrane conformation can have a lower free energy than the hairpin conformation.[184] Furthermore, neutron reflectivity measurements by Kim *et al.* found that a PEO homopolymer can insert into the acyl region at sufficiently high concentrations.[17] If one of the PEO blocks can traverse the bilayer, it is reasonable to assume that the second one could as well; therefore, a triblock could also adopt a hairpin conformation on the interior leaflet. Then, because bound polymer is in equilibrium with free polymer, chains in the interior leaflet hairpin state could desorb into the liposome. Thus, the elevated temperature leads to 3 new states: transmembrane, interior leaflet hairpin, and freely diffusing in the intraliposomal space.

When the system is cooled to 25 °C following an incubation above T_{crit}, we hypothesize that all three of these non-equilibrium states are kinetically trapped. The osmotic pressure difference across the membrane due to internalized polymer (~3 kPa) provides a driving force for polymer expulsion. Expulsion of intra-liposomal polymer is likely a step wise process proceeding sequentially through the interior leaflet hairpin, to the transmembrane, to the exterior leaflet hairpin to dissociated from the liposome (Figure 5.4b). At 25 °C the PEO blocks are hydrated, leading to unfavorable enthalpic interactions as the PEO block traverses the acyl region. This creates two large free energy barriers in this reaction pathway: in going from the interior leaflet hair pin to the transbilayer and then from the transbilayer to the exterior leaflet hairpin configurations. These steps are likely very slow, explaining why it takes weeks for the system to re-equilibrate following

a thermal incubation above T_{crit}. At equilibrium the polymer concentration will be equal on both sides of the liposomal membrane. Based on the lipid concentration, liposome size, and the number of lipids per liposome, an internalized polymer concentration of 1 mg/mL corresponds to 0.3 mol% of the chains. This is below the resolution of the PFG-NMR assay, therefore after a recovery period of several weeks, the samples incubated above T_{crit} fully relax to the non-thermally treated sample.

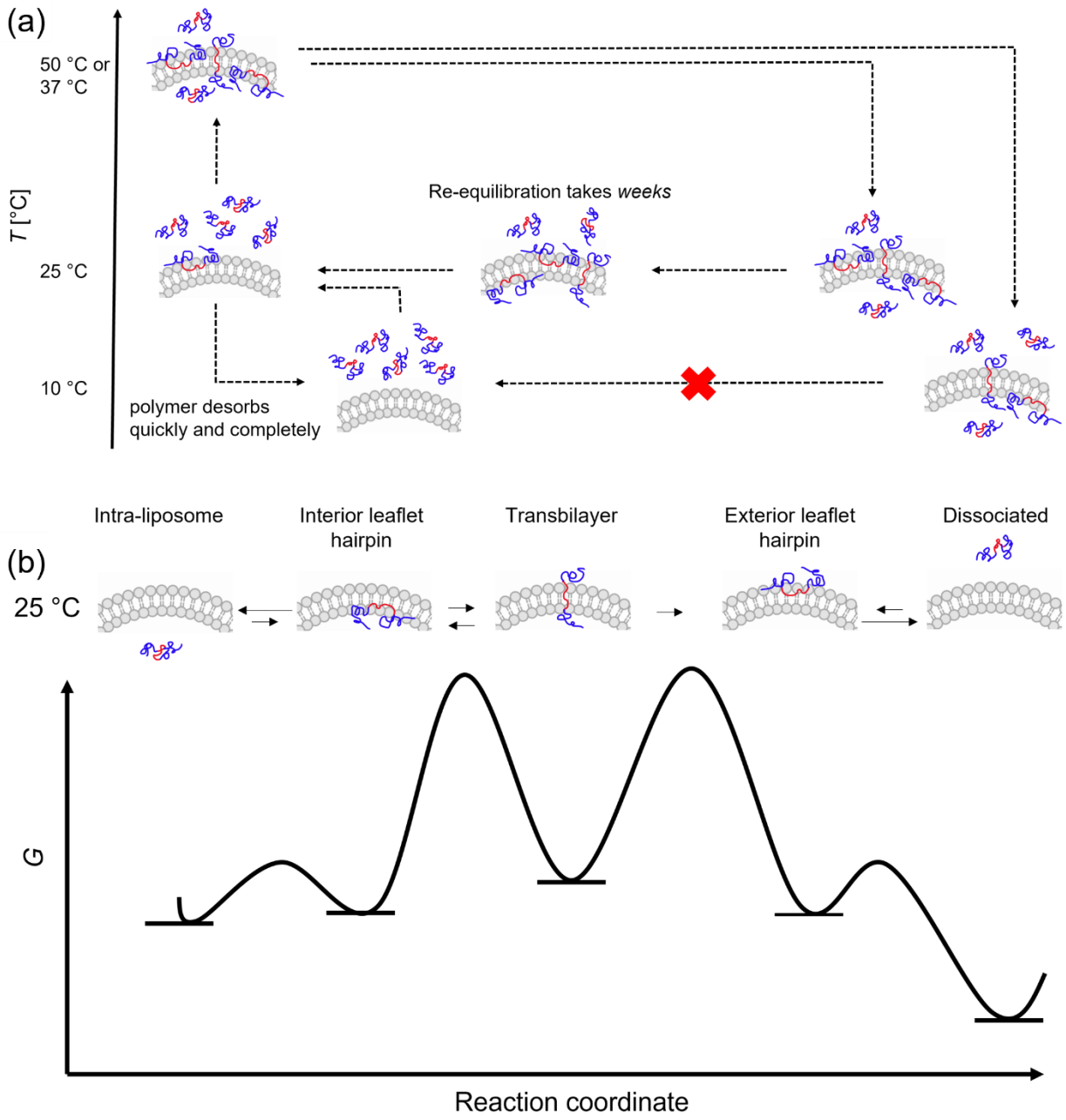

Figure 5.4: Proposed mechanism for kinetic trapping effect upon thermal treatment of a triblock poloxamer with liposomes. (a) Schematic describing the effect of temperature on polymer binding and the bound configuration. (b) Sketch of the hypothesized reaction pathway of a single polymer from inside the liposome to completely dissociated at 25 °C.

Effect of thermal cycling between 10 °C and 37 °C: To test this hypothesized mechanism, we performed a PFG-NMR experiment with *in situ* thermal cycling. If the transition state to polymer

desorbing from the kinetically trapped state involves the PEO block traversing the acyl region of the bilayer, then we further hypothesized that the polymer will not desorb if the system is cooled to 10 °C following incubation at 37 °C. Therefore, we investigated the effect of repeated cycles between 10 °C and 37 °C as shown by the thermal pathway in Figure 5.5a.

As the F127 + POPC system is incubated at 25 °C, an observable number of chains adsorb to the bilayer (~4 mol% based on Figure 5.1b). However, the PFG-NMR data for step 1 at 10 °C (dark blue) shows a single rate of decay with R_h = 4.5 ± 1 nm, consistent with exclusively free chains. Therefore, when the system is cooled to 10 °C following incubation at 25 °C, all polymer chains desorb within 30 min. Thus, as the temperature decreases and the solvent quality of water towards both PEO and PPO increases, there is an enthalpic driving force for desorption and the PPO block is pulled out of the bilayer as the chains enter the solution. The first measurement done at 37 °C (step 2 – pink diamonds), shows f_b = 37 ± 4 mol%. Both the step 1 and step 2 results are consistent with the variable temperature PFG-NMR results presented in Figure S5.4. Then, when the system is cooled to 10 °C following incubation at 37 °C (steps 3, 5, and 7 – light blue, green, and purple squares, respectively), there remains a substantial amount of polymer bound to the liposomes, f_b = 32 ± 4 mol%. This result provides indirect support of the proposed mechanism in Figure 5.4, because significant binding was observed at 10 °C following the 37 °C treatment, despite the thermodynamic driving force for desorption. The fit parameters for each step of this experiment are shown in Table 5.3. An identical thermal cycling experiment was performed using DLS to confirm that the R_h of the liposomes does not change substantially as a function of temperature (Figure S5.8).

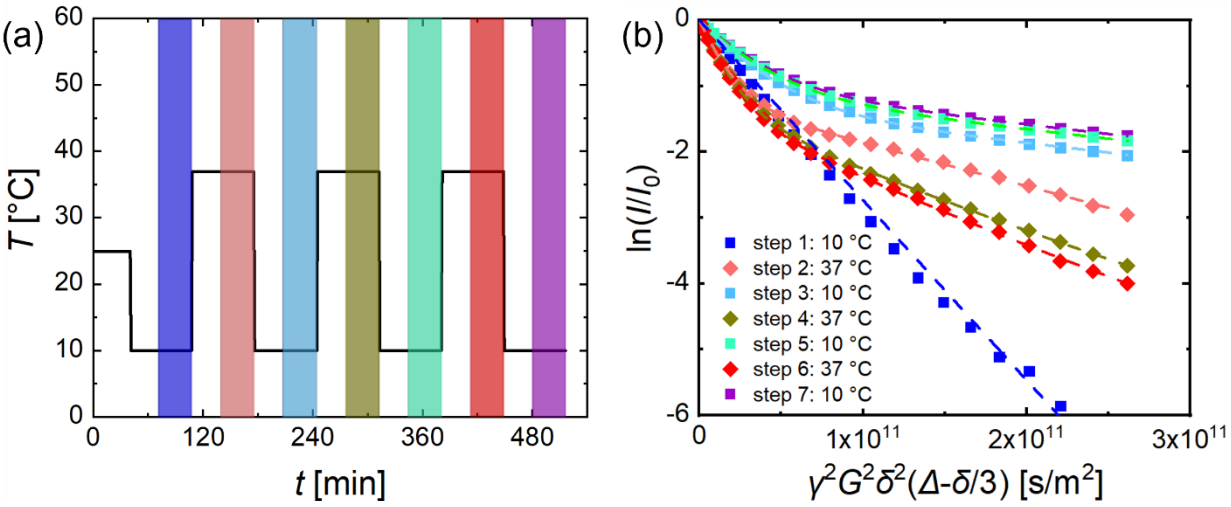

Figure 5.5: (a) Thermal pathway for the thermal cycling PFG-NMR experiment. We performed a room temperature incubation of 1 mg/mL F127 with 10 mM POPC, followed by an initial measurement at 10 °C followed by cycles of 37 °C to 10 °C. (b) PFG-NMR data from sequential steps in the experiment sequence. Squares in cool colors are data collected at 10 °C while diamonds in warm colors are data collected at 37 °C. All 37 °C data sets were fit to a two-term expansion of Equation 5.2 with D_{free} and D_{bound} shared as global parameters. Step 1 was fit to a single exponential decay while the remaining 10 °C datasets were fit to a two-term expansion of Equation 5.2 with D_{free} and D_{bound} shared as global parameters.

Table 5.3: Summary of Fit Parameters for the PFG-NMR Thermal Cycling Experiment.

Step #	Temperature [°C]	f_b [mol%][a]
1	10	0[b]
2	37	37 ± 4
3	10	27 ± 1
4	37	22 ± 2
5	10	34 ± 1
6	37	19 ± 2
7	10	36 ± 1

[a]Biexponential fit with D_{free} and $D_{liposome}$ as global parameters
[b]Single exponential fit
$R_{h,\ liposome}$(T=10 °C) = 44 ± 1 nm
$R_{h,\ liposome}$(T=37 °C) = 41 ± 1 nm
Error is 95% confidence interval on the fitting parameter.

Impact of cholesterol incorporation on the kinetics of desorption from trapped state: Since the hypothesized free energy barrier to desorption from the kinetically trapped state involves passage of a PEO block through the acyl region of the bilayer, we hypothesized that the bending and stretching moduli of the bilayer will impact the rate of desorption from the trapped state and/ or the ability of the chains to access it. Since cholesterol has a known rigidification and thickening effect on lipid bilayers,[18,35,40,275,276] we investigated the impact of cholesterol content on the kinetics of polymer desorption over a range of cholesterol incorporation from 0−14 mol%. Above this level of cholesterol content, binding of F127 to the liposomes was not observed.

Figure 5.6a shows the f_b vs t_{rec} curves of F127 + liposomes with 5, 9, and 14 mol% cholesterol, and the corresponding PFG-NMR decay curves are shown in Figures S5.9-11. As with the 100% POPC results presented in Figure 5.3, at early times the samples incubated at 50 °C and 37 °C

show elevated f_b compared to the 25 °C control. Then, the excess bound polymer in the samples incubated at elevated temperatures decays over time as the samples rest at 25 °C. For 5 and 9 mol% cholesterol liposomes, f_b in the thermally treated samples decays to the same steady state that was achieved in the 25 °C control; however, for 14 mol% cholesterol, the decay was incomplete even after 2000 h. Comparing the 25 °C datasets (black) across the three panels of Figure 5.6a, demonstrates that increasing cholesterol content from 5 to 14 mol%, leads to a decrease in $\overline{f_b}(T_{inc}=25\ °C)$ from 1.7 ± 0.3 mol% to 0 mol%, respectively. This effect has been observed before and was attributed to cholesterol stiffening the bilayer, therefore making insertion more difficult.[86] Because of the similarities between the 100% POPC and POPC/chol datasets, we conclude that the same kinetic trapping mechanism is likely occurring in both systems.

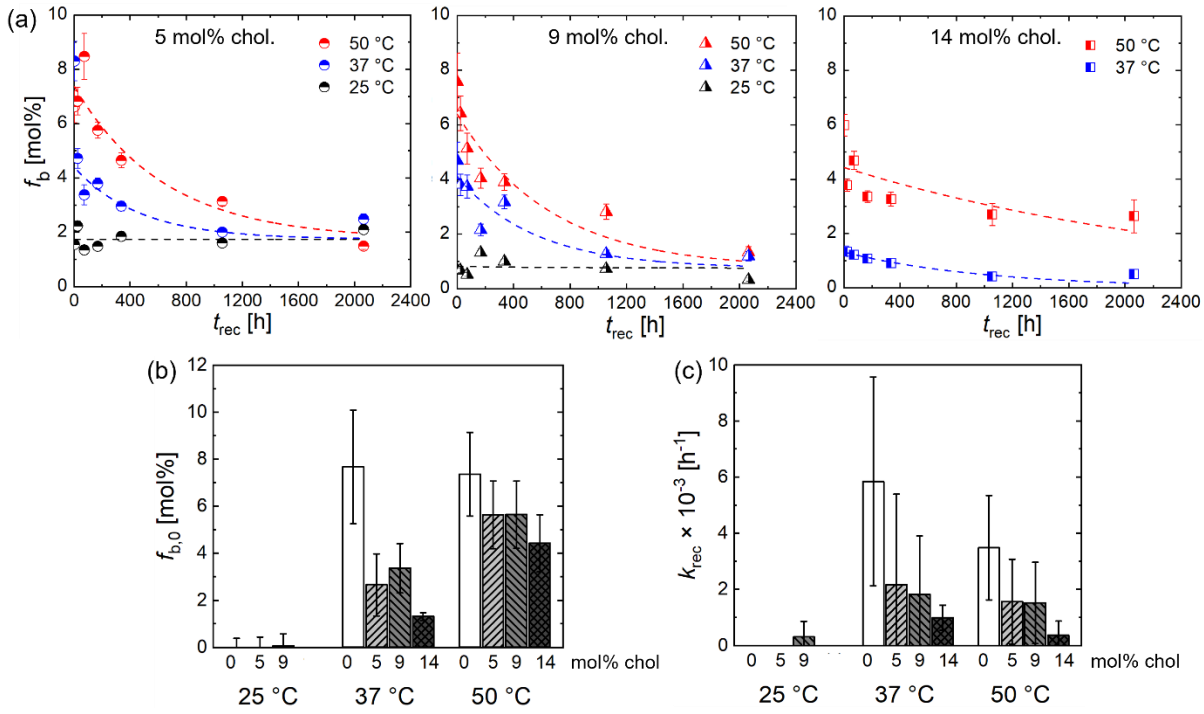

Figure 5.6: Effect of cholesterol incorporation on the rate of F127 desorption from POPC/ chol mixed bilayers after thermal treatment. (a) f_b vs recovery time for 5 mol%, 9 mol% and 14 mol% cholesterol. Error bars indicate the 95% confidence interval on f_b from fitting the PFG-NMR decay curves to a two-term expansion of Equation 5.2. (b and c) Summary of the fitting parameters from Equation 5.4 to the data in panel (a). Error bars indicate the 95% confidence interval of the fit.

Figures 5.6b and 5.6c summarize the results from fitting the kinetic relaxation data in Figure 5.6a to Equation 5.4. Figure 5.6b shows that for the 25 °C control, the excess bound polymer due to the incubation ($f_{b,0}$) is within error of 0 for all levels of cholesterol content. By the definition of the model in Equation 5.4, this parameter must be 0 if the sample incubated at 25 °C is at steady state. Additionally, Figures 5.6b and 5.6c suggest that for the samples incubated at elevated temperatures, $f_{b,0}$ and k_{rec} decrease as cholesterol content increases. Figure S5.12 shows a linear fit to the relationships between these fitting parameters and cholesterol content. For the 50 °C dataset, the slopes are significantly less than zero (p = 0.049 and p = 0.029 for $f_{b,0}$ and k_{rec}, respectively using ANOVA). This indicates that cholesterol inhibits the polymer from entering the trapped state

and slows the kinetics of desorption. As cholesterol content increases over this range of incorporation into POPC bilayers, molecular dynamics simulations have shown a 14% increase in the bilayer thickness[40] and neutron spin echo experiments have shown that the bending modulus increases by ~20%.[35] Thus, the observed reduction in $f_{b,0}$ and k_{rec} with increasing cholesterol content is consistent with a mechanism where the PEO block must pass through the bilayer since it should take longer for a chain to pass through a thicker, stiffer membrane.

Effect of polymer composition and architecture on thermal trapping: We investigated the effect of removing the PPO block by repeating the kinetic trapping experiment outlined in Figure 5.2a with a PEO homopolymer (M_n = 20.0 kDa). Figure 5.7a shows the PFG-NMR decay curves 2 h after incubation at 50 °C and a control sample maintained at 25 °C. The single rate of decay and nearly perfect superposition of the polymer control and polymer + POPC samples subjected to both treatments indicates that no binding occurred. Therefore, a PPO block is necessary for detectable binding in the PFG-NMR assay, even at elevated temperatures. Thus, a linear PEO homopolymer by itself does not traverse the bilayer.

We also explored the effect of composition (wt% PEO) and the diblock architecture on $f_{b,0}$ and k_{rec}. The PFG-NMR data for P188 and $P_{14}E_{118}$ (~80 wt% PEO triblock and diblock respectively) show no evidence of binding following incubation at 25 °C and 37 °C, but both polymers show observable binding after incubation at 50 °C, and this outcome persisted for at least 360 h into the recovery period at 25 °C. (Figures S5.13 and S5.14, respectively). Because f_b is so low (f_b < 0.5 mol%) we could not perform any quantitative kinetic analysis for P188 or $P_{14}E_{118}$.

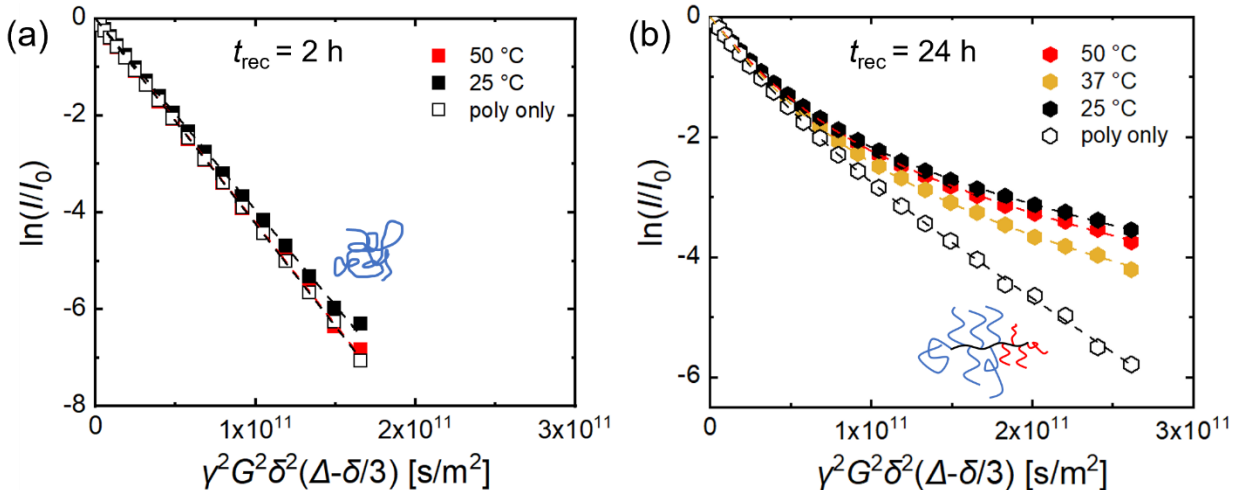

Figure 5.7: (a) Effect of removing the PPO block. PFG-NMR decay curves of *L*-E_{455}, a PEO homopolymer with M_n = 20.0 kDa. (b) Effect of bottlebrush poloxamer architecture on kinetic trapping effect. Representative PFG-NMR data of *B*-$E_{11}^{43}P_6^{15}$ + POPC samples (1 mg/mL *B*-$E_{11}^{43}P_6^{15}$ + 1.25 mM POPC) with different incubation temperatures. All data were collected at 27 °C. The data were fit to a constrained 3-component expansion of Equation 5.2, and f_b = 11 ± 3 mol%, 6 ± 2 mol%, and 9 ± 3 mol% for 50 °C, 37 °C, and 25 °C incubations, respectively. $R_{h,\,bound}$ = 37 ± 2 nm was a global parameter for all three conditions.

The effects of polymer composition within the linear triblock and diblock architectures are consistent with the proposed mechanism. Without the PPO block, the extent of dehydration of the PEO units with increasing temperature is insufficient to drive binding to a detectable level. However, the presence of even a small PPO block (N_{PPO} = 14 in the case of $P_{14}E_{118}$) leads to a kinetic trapping effect (Figure S5.16). The PPO block dehydrates to a greater extent and therefore is likely the first part of the chain to adsorb to the bilayer. Thus, the PPO block brings the PEO block(s) into closer proximity to the bilayer, facilitating further dehydration as the chain samples configurations that draw the PEO units into the membrane. While a diblock cannot form a transbilayer configuration, the PEO block can traverse the acyl region, providing access to the interior leaflet hairpin state and then desorbing into the intraliposomal space; hence a diblock polymer also can exhibit the thermal trapping effect.

Finally, we hypothesized that a bulky PEO-PPO bottlebrush block copolymer, would not traverse the lipid bilayer, which would eliminate the effects of thermal history on f_b. Therefore, we synthesized *B*-$E_{11}^{43}P_6^{15}$, a bottlebrush analogue to F127 with a comparable wt% PEO and a similar number of PPO units using previously established methods.[88,109] This bottlebrush poloxamer contains an average of 43 PEO units for each of 11 backbone norbornene units and 15 PPO units for each of 6 backbone norbornene units. As shown in Figure 5.7b, *B*-$E_{11}^{43}P_6^{15}$ does bind to POPC liposomes; however, samples incubated at 50 °C and 37 °C do not show excess binding compared to the 25 °C control 24 h into the recovery period at 25 °C. Figure S5.15 shows that there is also no difference in f_b between the samples incubated at 37 °C and 25 °C 2 h into the recovery period. Thus, bottlebrush poloxamers do not exhibit the same thermal path dependence exhibited by linear poloxamers, and we conclude that the kinetic trapping effect is not operative with a bottlebrush architecture. We believe this is due to a significantly stiffer and bulkier molecular structure of the bottlebrush poloxamer versus flexible linear poloxamers, leaving bottlebrush poloxamers unable to traverse the bilayer and shutting off the thermal trapping effect.

PFG-NMR measurements were also performed at 10 °C, 37 °C, 50 °C, and 27 °C with *B*-$E_{11}^{43}P_6^{15}$ treated POPC liposomes (Figure S5.16). Compared to F127, f_b for *B*-$E_{11}^{43}P_6^{15}$ was much less sensitive to temperature, only ranging from 14 ± 2 to 19 ± 2 mol% over 10−37 °C. Furthermore, *B*-$E_{11}^{43}P_6^{15}$did not desorb from the bilayer at 10 °C, irrespective of the thermal history (Figure S5.17). This is likely because the bottlebrush occupies a bound conformation where the backbone lies parallel to the bilayer plane, enabling multiple PPO and PEO side chains to intercalate into the acyl region.[88] Thus, for desorption to occur every side chain must simultaneously pull out of the bilayer, an unlikely event that would also result in significant steric crowding.

5.4 Conclusion

We report that poloxamers can traverse lipid bilayers at or above 37 °C, but not at 25 °C. This results in chains that are kinetically trapped onto (and into) liposomes. Furthermore, we developed an experimental method for quantifying the rate constant of desorption from the kinetically trapped

states (k_{rec}) and found that $k_{rec} \cong 3 \times 10^{-3}$ h^{-1}, which is remarkably slow given the relatively weak forces that drive polymer binding and the dynamic nature of lipid bilayers. The ability to access the trapped states, and the rate of desorption from them, are sensitive to polymer architecture and bilayer cholesterol content. We propose that at elevated temperatures, the PEO block(s) can traverse the hydrophobic acyl region of the bilayer, enabling a linear triblock copolymer to access the transmembrane configuration, the interior leaflet hairpin state, and the intra-liposomal space. The rate limiting step to escaping from these states is the PEO block(s) re-traversing the acyl region, which has a high free energy barrier upon cooling the system to room temperature due to the hydrogen bonded water shell.

This mechanistic investigation is of practical importance because there are conflicting reports of whether poloxamers enter the intracellular space. Prior studies have documented that poloxamers and PEO homopolymers are internalized by both stressed and non-stressed living cells,[116,117] and internalization was believed to occur by endocytosis.[116] On the other hand, a recent study by Bez Batti Angulski *et al.* employed confocal microscopy and showed that P188 localizes at the exterior membrane of cardiomyocytes and skeletal muscle cells.[158] The thermal trapping effect we observed, and the proposed mechanism reported here suggests that poloxamers can traverse lipid bilayers via a passive transport mechanism at the physiological temperature. It is possible that in some cellular systems, additional membrane components (*e.g.* the dense glycocalyx and/or actin cytoskeleton) could slow passive diffusion of ABPs across the cell membrane. This could have caused the accumulation of P188 at the exterior membrane observed by Bez Batti Angulski *et al.* and led to an internalized concentration of P188 that was below the detection threshold in their confocal microscopy experiment. Passive diffusion of poloxamers across a lipid bilayer has important ramifications for the cellular distribution of poloxamers. It is possible that intracellular membranes, organelles, or processes are impacted by poloxamer presence and play a role in protecting cells from stress. We speculate that this thermal trapping effect and passive lipid bilayer

diffusion could take place in any polymer system with thermoresponsive character due to a hydrogen bonded water shell.

We also systematically studied the effect of temperature on the affinity of poloxamers towards POPC bilayers and observed that increasing temperature leads to 11 ± 3× more polymer chains bound to the bilayer at 37 °C compared to 27 °C. These results will help the community compare the results of previous mechanistic studies of polymer-lipid bilayer interactions that may have been done at different temperatures. Additionally, in designing future experiments involving thermoresponsive block polymers and lipid bilayers one should carefully consider the desired temperature, and for physiological applications we suggest including 37 °C wherever experimentally possible.

Finally, we have demonstrated that it is possible to achieve a wide range of PEO surface coverage post liposome fabrication via addition of commercially available poloxamers and heat. This could present a facile and scalable method to manipulate liposome mechanical and surface properties without needing to change the formulation or compromise on encapsulation efficiency.[256] Furthermore, we hypothesize that the significant amount of triblock polymers in the transbilayer conformation will increase interleaflet friction,[32] and this could have beneficial implications for applications where lipid bilayers are subjected to shear stresses.

5.5 Supporting Information for Chapter 5

Dynamic light scattering assessment of liposome preparations:

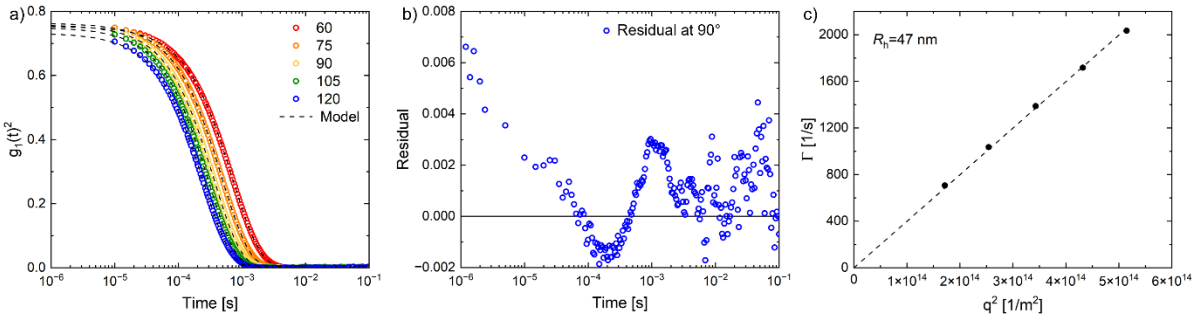

Figure S5.1: Representative multi-angle dynamic light scattering data and analysis. (a) Correlation functions collected over a series of 5 angles. Data is fit to the second cumulant model described by equation S5.1. (b) Residual (data−fit) for the 90° dataset. (c) Relationship between the first cumulant (Γ) and the scattering vector squared (q^2). The best fit line was forced through the origin, and the slope gives the diffusion coefficient and the corresponding R_h value is given. The linearity and y-intercept of zero indicate a diffusive relaxation process.

All DLS data were fit to the second-order cumulant model shown below:

$$g_1^2 = B \exp(-2\Gamma t + k_2 t^2) \quad \text{(S5.1)}$$

where g_1 is the autocorrelation function which is calculated from the fluctuations in the observed scattering intensity, Γ is the first cumulant which in dilute solutions is related to the translational diffusion coefficient, k_2 is the second cumulant which accounts for dispersity in the sample, and t is time.

Dynamic light scattering assessment of liposome stability upon 50 °C incubation

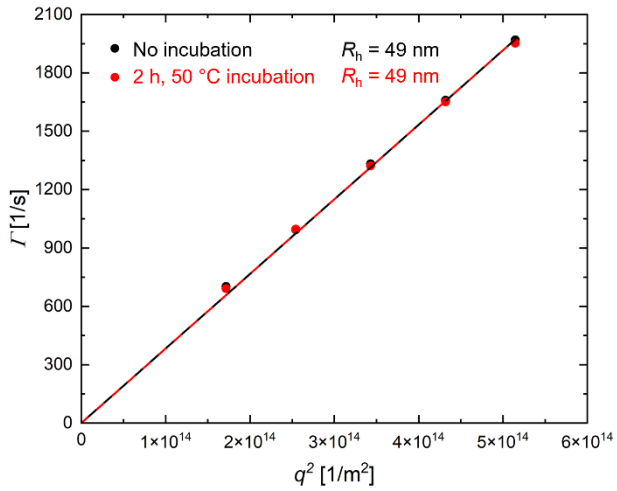

Figure S5.2: Multi-angle DLS data of POPC liposomes pre (black) and post (red) a 2 h incubation at 50 °C. The dispersity before and after the incubation were both 1.01 as estimated by the ratio of the second cumulant to the square of the first cumulant resulting from the fit to the 90° data.

Small angle X-ray scattering assessment of bilayer form factor during thermal incubation

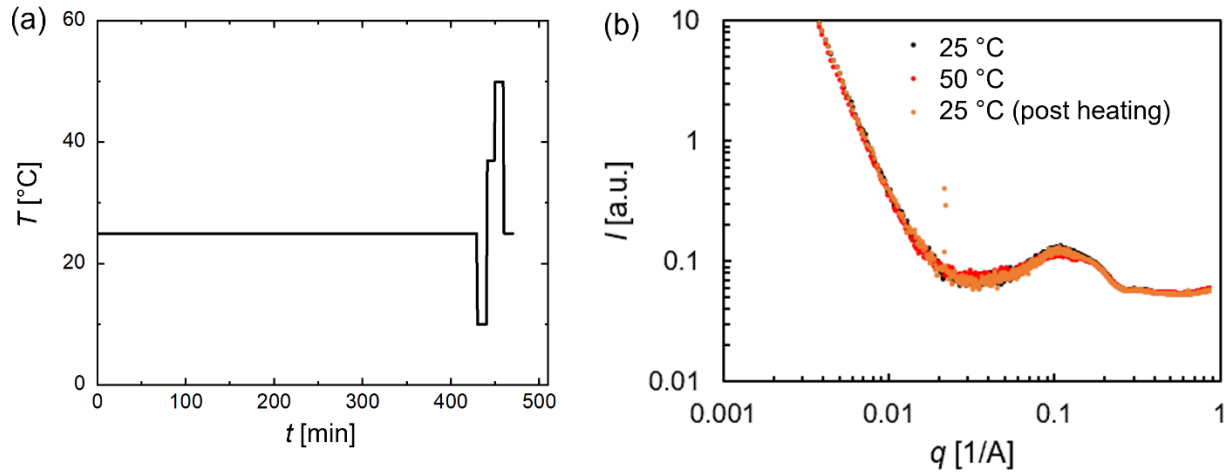

Figure S5.3: (a) Thermal sequence for the experiment. SAXS data was collected at the end of every temperature. Liposomes were prepared roughly 7 hours prior to the start of the experiment. (b) Scattering profiles of the first 25 °C scan, the 50 °C scan, and the 25 ° C scan following the thermal protocol. The curves overlap within error, indicating qualitatively that there is no change to the bilayer.

We deem this system to have too low of an electron density contrast, and therefore too low of a signal-to-noise ratio, to quantitatively fit the SAXS data to a bilayer form factor model, as these models have at least 6 fitting parameters.[16]

Variable temperature PFG-NMR measurements:

The anchor-and-chain model, which describes poloxamer lipid bilayer interactions, asserts that entropically dominated hydrophobic forces are the primary driving force for polymer binding to lipid bilayers.[6,85,143,144] Therefore, we hypothesized that as PPO-water interactions become less favorable with increasing temperature, f_b would increase. We evaluated this hypothesis using the thermal pathway described by Figure S5.4a. We mixed F127 with POPC liposomes, and incubated the solution at 25 °C for 2 hours to establish a steady state.[85] We then inserted the sample into the NMR probe, set to 10 °C, and allowed the sample to incubate for 30 minutes prior to starting the PFG-NMR data acquisition, which takes 37 minutes. After each temperature change, the sample asymptotically approaches a new steady state during the incubation period. We performed an experiment with a 3 h incubation period and periodic PFG-NMR measurements at 37 °C (Figure S5.6) and found that the 30-minute period is sufficient to reach at least 75% of the steady state. This 30-minute incubation and 37-minute acquisition cycle was repeated at 37 °C, 50 °C, and finally 27 °C. The same thermal pathway was followed for the F127 solution without liposomes control experiment (open symbols).

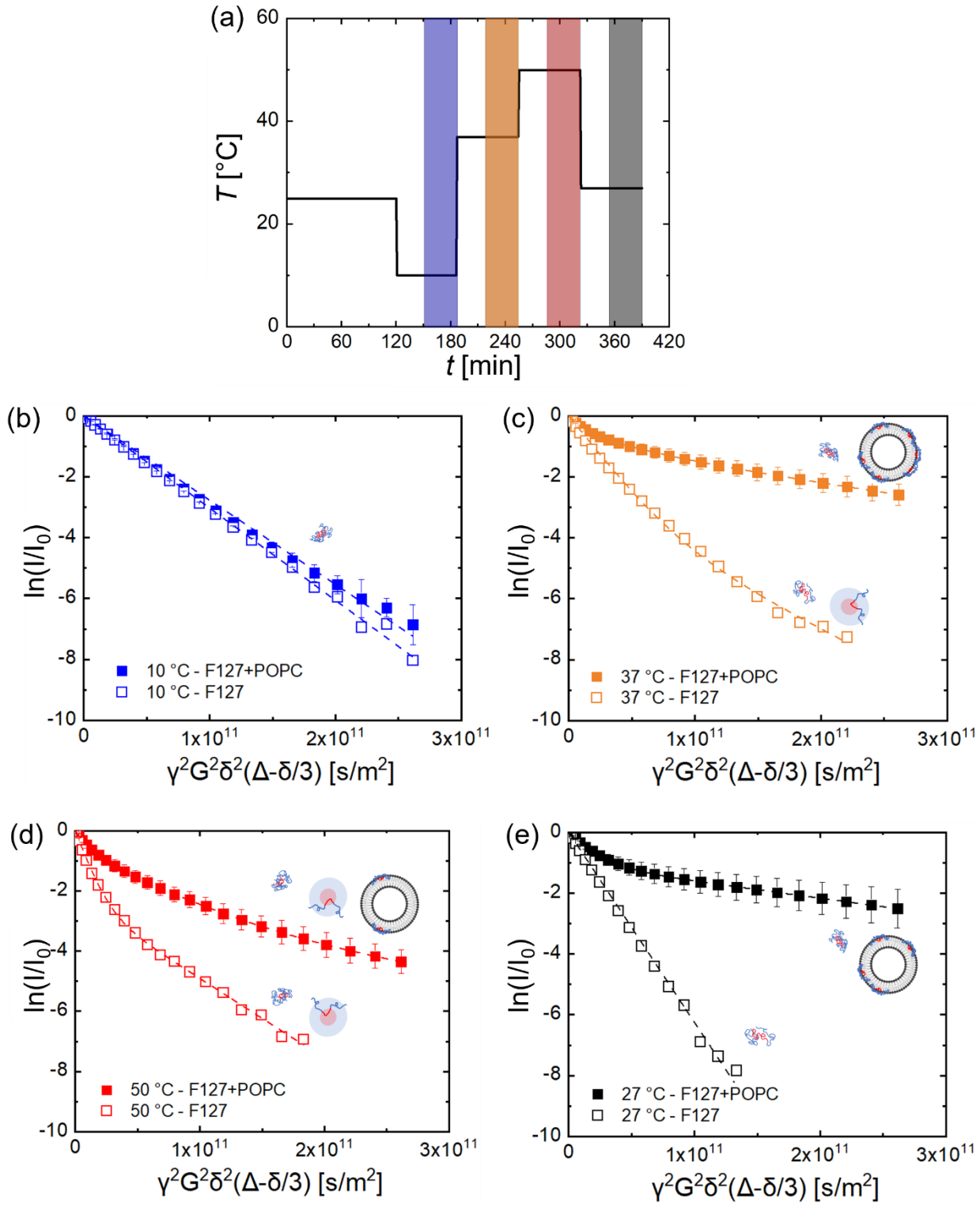

Figure S5.4: (a) Summary of thermal pathway. Shading indicates timing of PFG-NMR data acquisition. (b-e) Variable temperature PFG-NMR data of 1 mg/mL F127 (open) and 1 mg/mL

F127 + 10 mM POPC (closed). Error bars indicate the standard deviation of 3 independent experiments.

Based on the linearity and close superposition of the F127 solution without POPC and F127 + POPC sample at 10 °C shown in Figure S5.4b, we conclude that F127 chains do not adsorb to the liposomes at this temperature. At 10 °C, both blocks are solvated, thus it is thermodynamically favorable for the chains to exist as unimers diffusing freely in solution; the diffusion coefficient from the fit gives $R_h = 4 \pm 1$ nm (based on the Stokes-Einstein relationship), consistent with free chains. All fitting parameters are summarized in Table S5.1 and are presented graphically in Figure S5.5. The results shown in Figures 1b (gray) and S5.4a conclusively demonstrate that F127 chains adsorbed to liposomes at 27 °C completely desorb within 30 minutes after being cooled to 10 °C.

Table S5.1: Summary of fitting parameters for the PFG-NMR experiments with F127 and F127 + POPC solutions at various temperatures.

Temp. [°C]	Sample	$f_{micelle}$ [mol%]	f_{bound} [mol%]	$R_{h,\ free\ chain}$ [nm]	$R_{h,\ micelle}$ [nm]	$R_{h,\ bound}$ [nm]	$N_{poly/\ liposome}$
10	F127	0	-	4 ± 1	-	-	-
	F127 + POPC	0	**0**	4 ± 1	-	-	0
37	F127	7 ± 5	-	5 ± 1	13 ± 3	-	-
	F127 + POPC	0	**45 ± 2**	5 ± 1	-	40 ± 2	340 ± 10
50	F127	11 ± 2	-	3 ± 1	14 ± 1	-	-
	F127 + POPC	47 ± 2	**13 ± 3**	3 ± 1	14 ± 1	41 ± 2	100 ± 20
27	F127	0	-	3 ± 1	-	-	-
	F127 + POPC	0	**37 ± 1**	3 ± 1	-	36 ± 1	280 ± 10

$N_{poly/liposome}$ is an estimate for the number of polymers bound to each liposome. The calculation is based on literature relationships between liposome size and the number of lipids per liposome.[85,87]

Increasing the temperature to 37 °C demonstrates the thermoresponsive nature of F127. In Figure S5.4c, the curve corresponding to the F127 solution without liposomes (open symbols) is non-linear which indicates the existence of more than one population of chains, assumed to be unimers and micelles based on a wealth of prior characterization of poloxamer solutions.[97,101] Fitting this data to a sum of two exponentials indicates a relatively small fraction of chains are present in micelles, $f_{\text{micelles}} = 7 \pm 5$ mol%, and the hydrodynamic radii of the two populations are $R_{\text{h, free chains}} = 5 \pm 1$ nm and $R_{\text{h, micelles}} = 13 \pm 1$ nm, consistent with the assignment of free chains and micelles. Comparing the F127 and the F127 + POPC decay curves at 37 °C (Figure S5.4c) shows that there is a substantial amount of polymer bound to the liposomes. To reduce the number of fitting parameters in a three-term expansion of Equation 2, we assumed that the free chains and micelles do not change in size in the presence of liposomes; $D_{\text{free chain}}$ and D_{micelle} were assigned values obtained from the F127 solution without POPC. This protocol results in $f_{\text{bound}} = 45 \pm 2$ mol% and $f_{\text{micelles}} = 0$ mol% based on the fit shown in Figure S5.4c. As temperature increases from 10 °C to 37 °C, the critical micelle concentration (CMC) decreases as the chains become more amphiphilic.[97] In the F127 sample without liposomes, the poloxamer concentration is greater than the CMC, resulting in micelle formation. However, when liposomes are present, no micelles were detected. We conclude that the relatively high affinity of F127 chains to liposomes at this temperature reduces the concentration of free chains below the CMC, thus eliminating micelle formation.

Increasing the temperature to 50 °C leads to stronger micellization in the F127 control solution, with 11 ± 2 mol% of the chains now present in micelles (Figure S5.4d). Following the same fitting protocol described above indicates a co-existence of unimers, micelles, and liposome-bound polymer with $f_{\text{free chains}} = 40 \pm 5$ mol%, $f_{\text{micelles}} = 47 \pm 2$ mol%, and $f_{\text{bound}} = 13 \pm 3$ mol%. The reduction in f_{bound} at 50 °C compared to 37 °C suggests that the associated reduction in PEO and PPO miscibility energetically favors micelles over liposome bound polymer, leading to rapid desorption of chains from the liposome surface to form micelles at 50 °C. Curiously, the fraction

of polymer chains in micelles is higher in the F127 + POPC sample than the F127 control solution at 50 °C. Micellization is not a phase transition and micelle creation is a multi-molecular process that can be slow.[104,277] Therefore, it may be possible that as chains desorb from the liposomes at 50 °C there is a boundary layer region near the liposome surface with a higher local concentration of chains than far from the liposomes, increasing the probability of a micelle formation event.

When the sample is cooled to 27 °C following the 50 °C data acquisition, no micelles are detected in the F127 or F127 + POPC samples, indicating that the concentration of polymer is below the CMC and the timescale of micelle dissolution at 27 °C is shorter than 30 minutes. Surprisingly, f_{bound} = 37 ± 1 mol% at 27 °C after cooling from 50 °C, which is remarkably higher than the 4 ± 1 mol% binding observed at 27 °C without prior heating (Figure 1b).

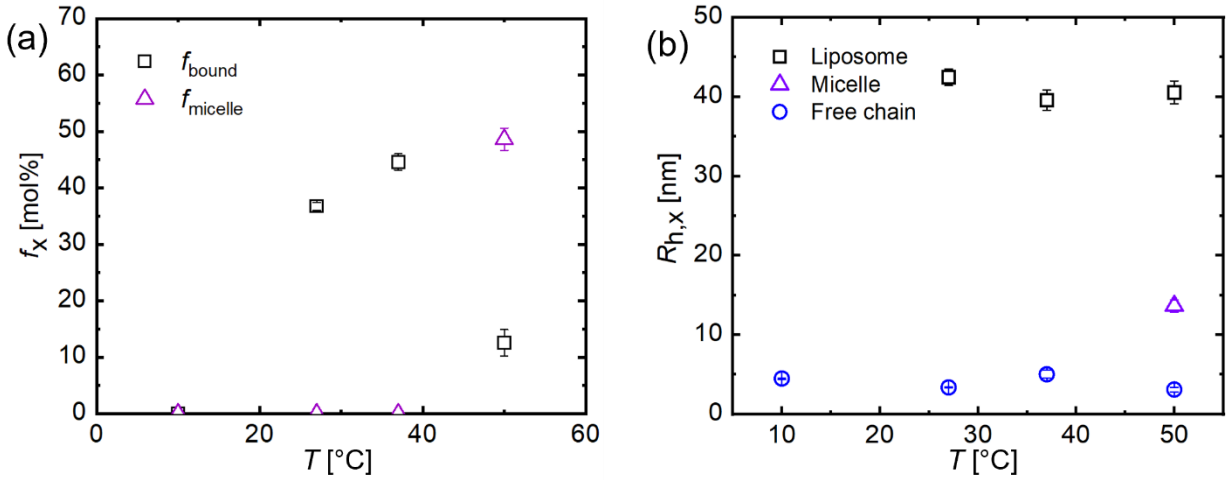

Figure S5.5: Summary of the fitting parameters for the PFG-NMR data presented in Figure 2.

Impact of incubation time in variable temperature PFG-NMR experiments

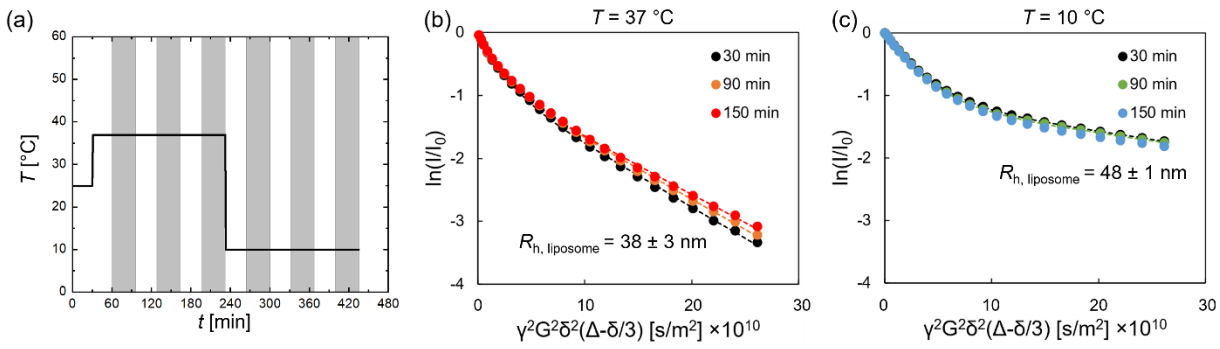

Figure S5.6: (a) Thermal sequence for the experiment. Shading indicates data acquisition period. (b) PFG-NMR data collected during the first 3 steps of the experiment which were done at 37 °C. Data were fit to a three-term expansion of Equation 2 with all diffusion coefficients as global parameters. (c) PFG-NMR data collected during the final 3 steps of the experiment which were done at 10 °C. Data were fit to a two-term expansion of Equation 2 with both diffusion coefficients as global parameters.

Table S5.2: Summary of fitting parameters for PFG-NMR data in Figure S5.6.

Temperature [°C]	Incubation time [min]	$f_{micelle}$ [mol%]	f_b [mol%]
37	30	46 ± 2	22 ± 3[a]
37	90	44 ± 3	26 ± 4[a]
37	150	40 ± 3	29 ± 4[a]
10	30	-	35 ± 1[b]
10	90	-	33 ± 1[b]
10	150	-	32 ± 1[b]

[a]Triexponential fit with D_{free}, $D_{micelle}$, and $D_{liposome}$ as global parameters.
[b]Biexponential fit with D_{free} and $D_{liposome}$ as global parameters.
Error is 95% confidence interval on the fitting parameter.

During each change in temperature, the polymer + liposome system asymptotically approaches a new steady state. We were interested in how quickly it reaches the new steady state to determine an efficient incubationing time for variable temperature PFG-NMR experiments. The data in Table S5.2 shows that there is roughly a 25% increase in f_b at 37 °C between the 30 minute and 150 minute incubations. Since the variable temperature NMR protocol involves 4 changes in the set point each requiring an incubation period and a data acquisition period, we decided that reaching

~75% of the steady state is sufficient to observe the trends between f_b and temperature. Therefore, a 30 minute incubation time was chosen.

Notice, the R_h of the liposomes reported in Figure S5.6b and S5.6c appears to change as a function of temperature. We hypothesize that this is an artifact of fitting the PFG-NMR data to a multiparameter model and is not significant. Therefore, we performed a similar thermal cycling experiment and observed the R_h of liposomes alone via DLS (Fig S8).

Representative dataset for kinetic trapping of F127 onto 100−0 POPC−Chol (mol%) liposomes

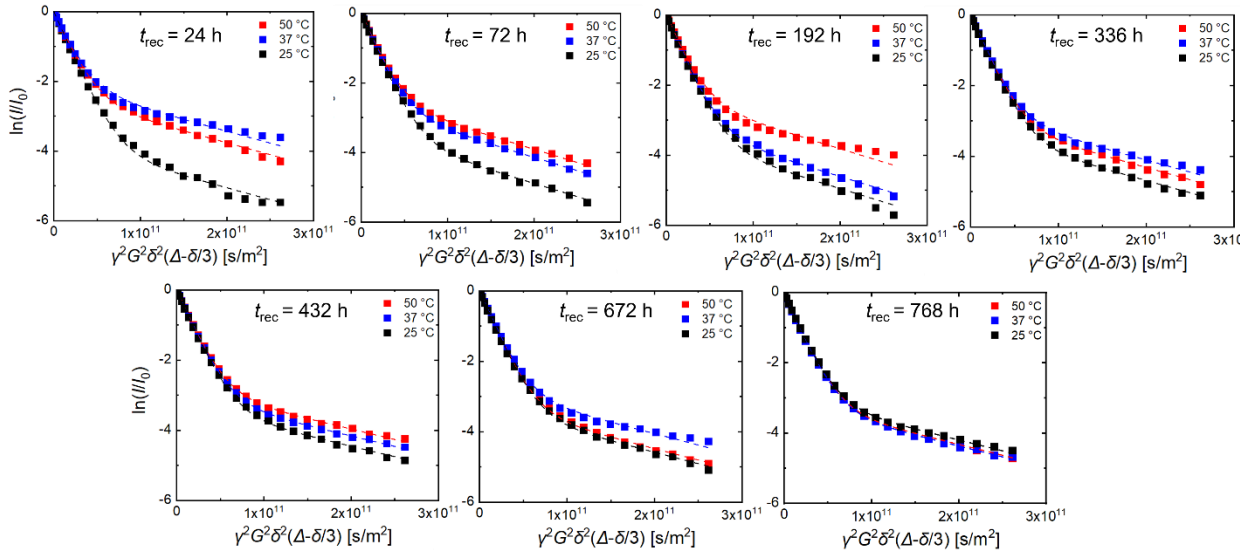

Figure S5.7: All timepoints for a single representative kinetic trapping PFG-NMR experiment of F127 onto pure POPC liposomes (100−0 POPC−Chol (mol%)).

Thermal cycling DLS experiment to assess R_h of liposomes as a function of temperature

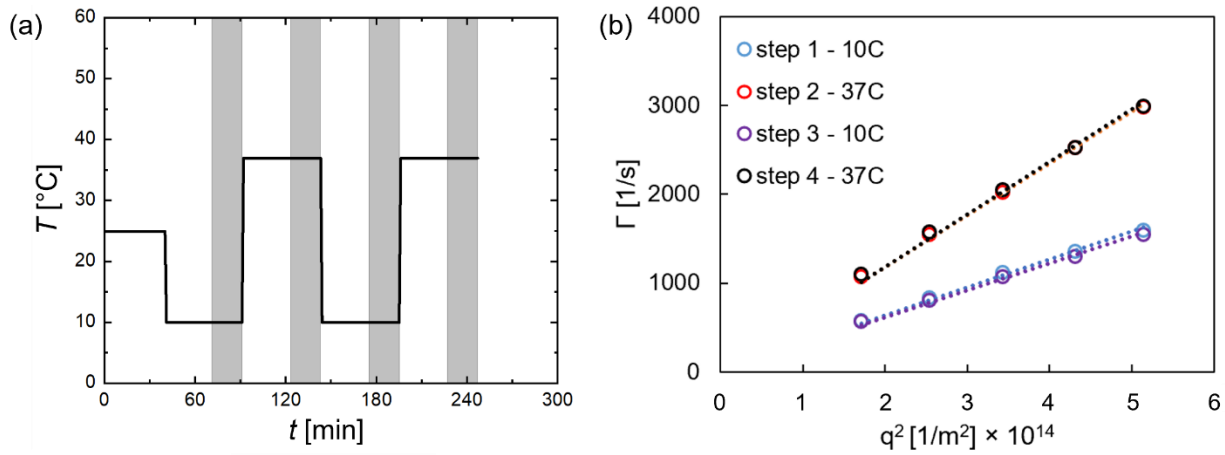

Figure S5.8: (a) Thermal sequence for the experiment. Shading indicates data acquisition period. Sample is 1 mg/mL F127 + 10 mM POPC liposomes. (b) Multi-angle DLS data for each step of the experiment. The linearity and near-zero intercept indicate that a diffusive process is being observed. The overlap between the curves corresponding to the same temperatures indicates that the liposome size is stable to thermal perturbations over this temperature range. The R_h and dispersity are summarized in Table S5.3.

Table S5.3: Summary of DLS results from Figure S5.8b.

Step #	Temperature [°C]	R_h [nm][a]	D[b]
1	10	41	1.02
2	37	46	1.01
3	10	42	1.02
4	37	46	1.01

[a]Calculated by applying the Stokes-Einstein equation using the slope of best fit to Γ vs q^2 as the translational diffusion coefficient, D_t. Error is ~10%. [b]Calculated as $1+k_2/k_1^2$ from the second-cumulant fit (Eq. S1) to the 90° data.

The DLS results reported in Table S5.3 suggest that the R_h of the liposomes changes by ~10% as the temperature is increased from 10 °C to 37 °C. This is very close to a typical error in a DLS measurement. Notably, DLS shows that R_h of the liposomes increases as a function of temperature while PFG-NMR suggests the opposite. As temperature increases, the area per lipid increases, so we trust the trend observed in the DLS data; however, any change that does occur is small and reversible.

Kinetic trapping of F127 onto 86:14 (POPC:Chol mol%) liposomes

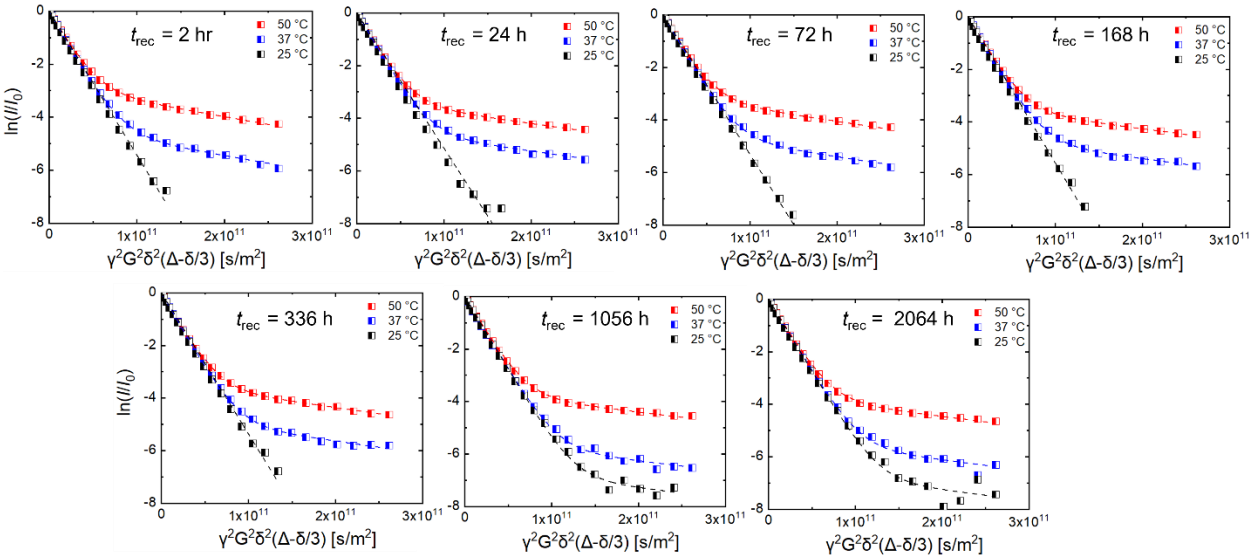

Figure S5.9: Kinetic trapping PFG-NMR experiment of F127 onto 86:14 (POPC:Chol mol%) liposomes. Note the onset of a second mode of relaxation in the 25 °C dataset at 1056 hr post incubation. This appears to be a very small fraction of chains bound to the liposomes (f_{bound} ~ 0.1 mol%) which is the lower limit of detection in this assay. It is likely that this level of adsorption was occurring in every dataset, but due to fluctuations in noise at this low of a s:n (99.99% signal decay) it cannot be consistently observed. Data corresponds to the right panel in Figure 5.6a of the main text.

Kinetic trapping of F127 onto 91:9 (POPC:Chol mol%) liposomes

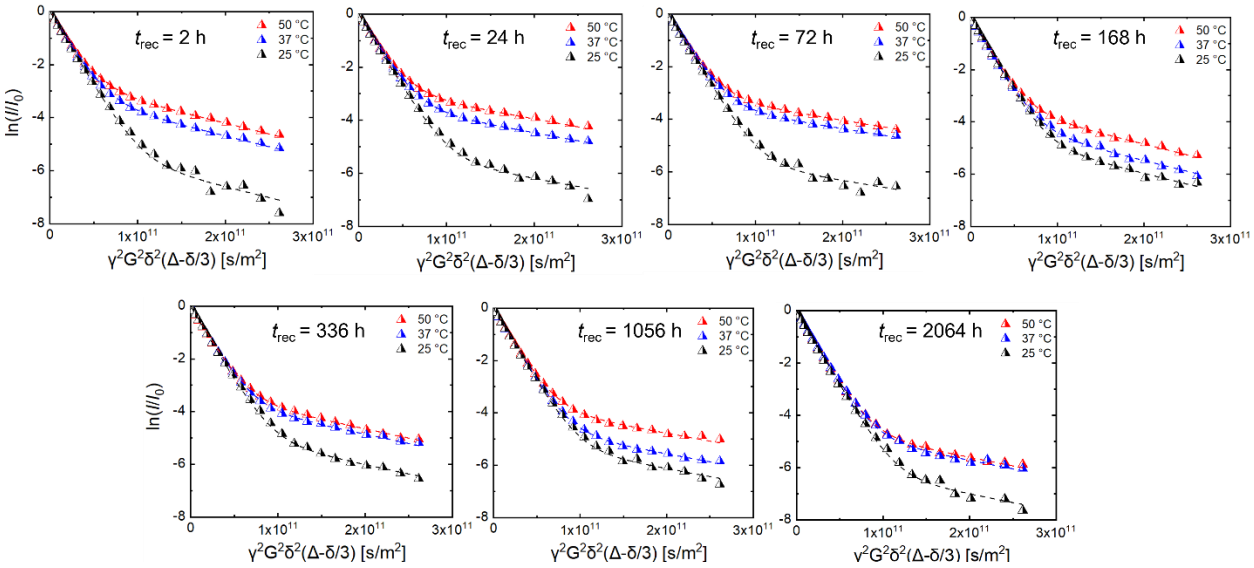

Figure S5.10: Kinetic trapping PFG-NMR experiment of F127 onto 91:9 (POPC:Chol mol%) liposomes. Data corresponds to the middle panel in Figure 5.6a of the main text.

Kinetic trapping of F127 onto 95:5 (POPC:Chol mol%) liposomes

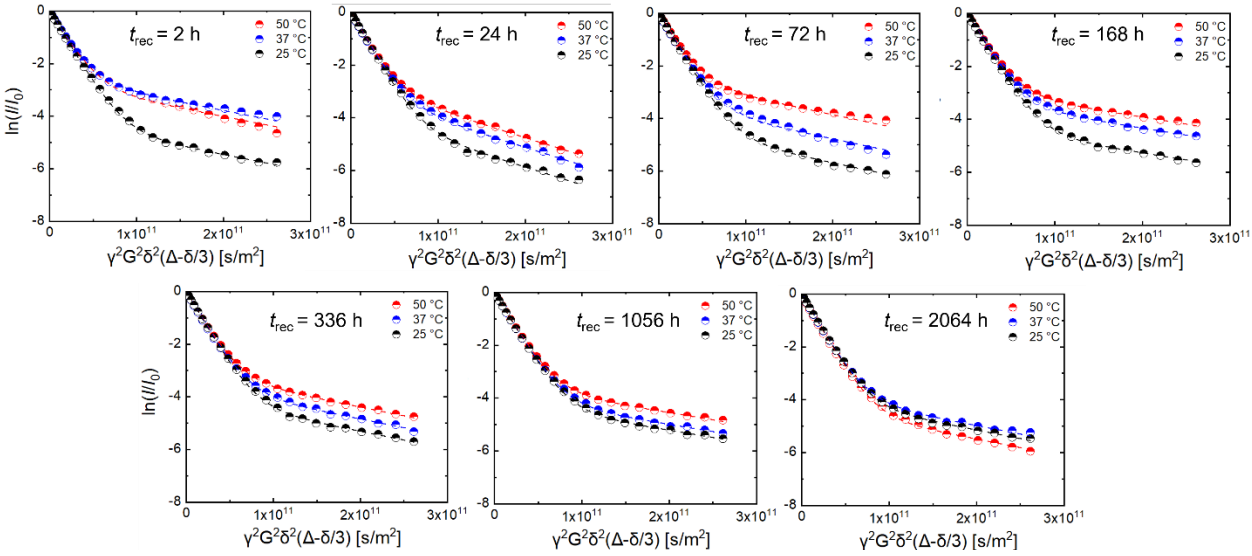

Figure S5.11: Kinetic trapping PFG-NMR experiment of F127 onto 95:5 (POPC:Chol mol%) liposomes. Data corresponds to the left panel in Figure 5.6a of the main text.

Statistical analysis of the effect of cholesterol on $f_{bound,0}$ and $k_{off,\ incubation}$

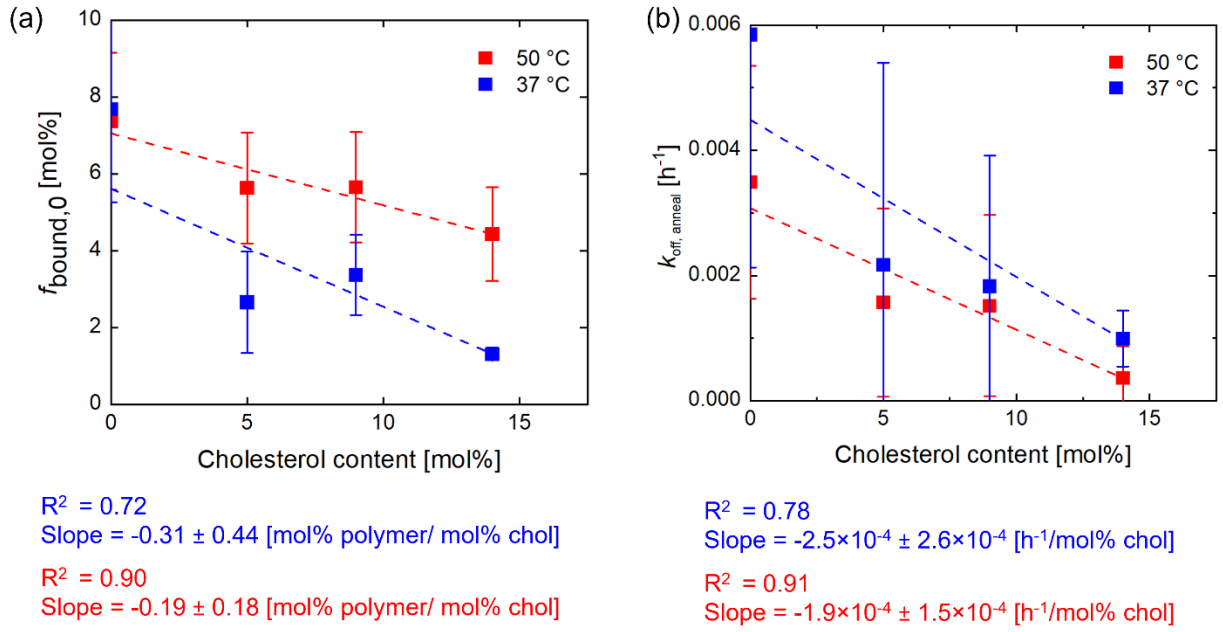

Figure S5.12: Statistical analysis of the effect of cholesterol incorporation on fitting parameters to Equation 4; error is the 95% confidence interval. (a) Effect of cholesterol content on $f_{bound,0}$, the amount of excess polymer bound due to the incubation. The slope of the linear best fit to the 50 °C dataset is significantly different from 0 (p = 0.049 via ANOVA). For the 37 °C dataset, the slope is not significantly different from 0 (p = 0.097 via ANOVA); although the same trend exists. (b) Effect of cholesterol content on $k_{off,incubation}$, the rate constant of desorption from the trapped state. For the 50 °C dataset, the slope is significantly different from 0 (p = 0.029 via ANOVA) while for the 37 °C dataset, it is not (p = 0.076); although the same trend exists.

Kinetic trapping of P188 onto 100:0 POPC:Chol liposomes

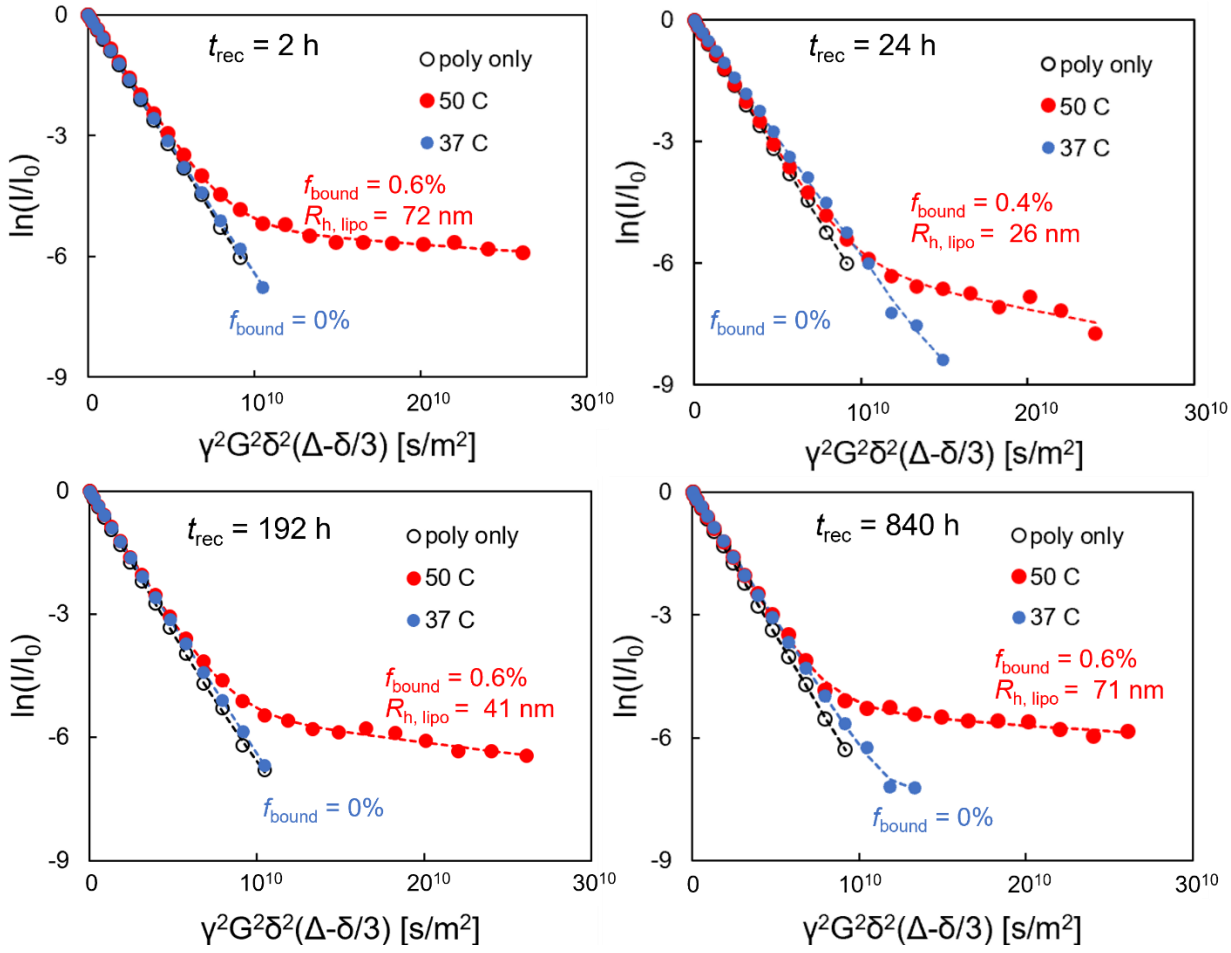

Figure S5.13: Kinetic trapping of P188 onto pure POPC liposomes. The kinetic trapping effect occurs only at 50 °C, indicating that the critical temperature for the effect to occur is dependent on copolymer composition. Since the affinity of this polymer is so low, it is impossible to quantify the rate constant of desorption; however, desorption does occur very slowly as no change in f_{bound} was observed over 192 hours in the 50 °C incubation dataset.

Kinetic trapping of $P_{14}E_{118}$ onto 100:0 POPC: Chol bilayers

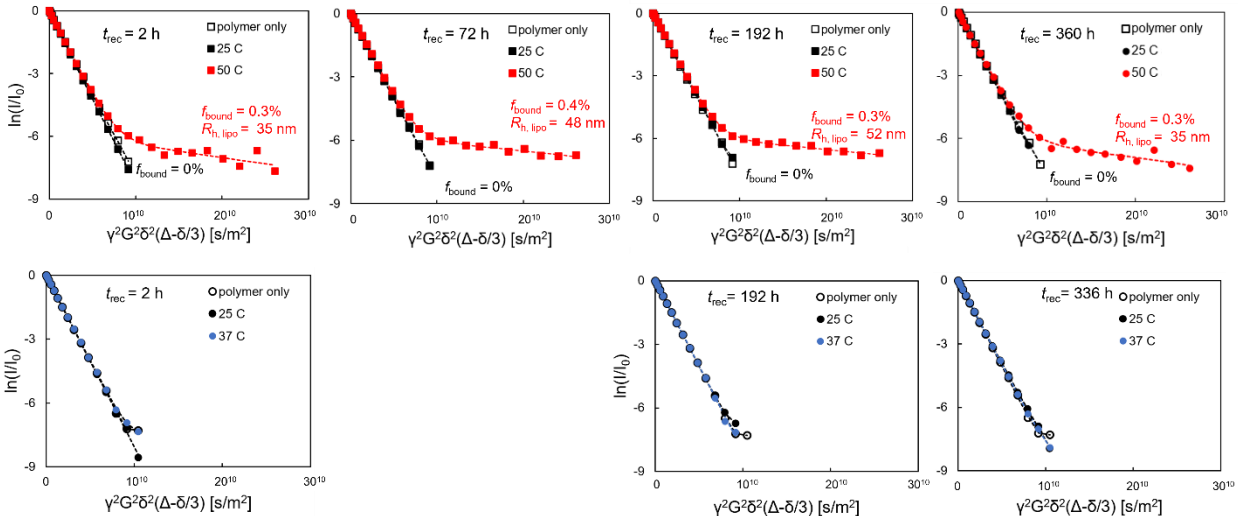

Figure S5.14: Kinetic trapping of $P_{14}E_{118}$ onto pure POPC liposomes. The kinetic trapping effect occurs only at 50 °C, indicating that the critical temperature for the effect to occur is dependent on copolymer composition. Since the affinity of this polymer is so low, it is impossible to quantify the rate constant of desorption; however, desorption does occur very slowly as no change in f_{bound} was observed over 360 hours in the 50 °C incubation dataset.

Kinetic trapping of *B*-$E_{11}^{43}P_6^{15}$ 2 h after incubation

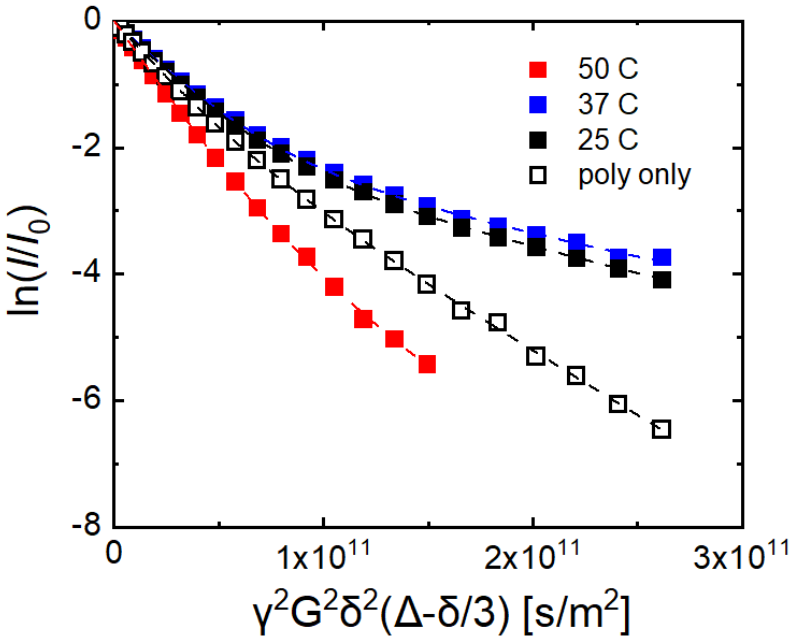

Figure S5.15: Kinetic trapping PFG-NMR experiment of POPC liposomes treated with *B*-$E_{11}^{43}P_6^{15}$, 2 h post incubation. All PFG-NMR data acquisition were done at 27 °C. Decay curves corresponding to 37 °C and 25 °C incubations (yellow and black, respectively) overlap indicating that over this temperature range the incubation does not affect f_{bound}. The decay curve of the 50 °C incubation is significantly different and does not show any binding to the liposomes. Thus, for a bottlebrush poloxamer, a 50 °C incubation leads to desorption. In all cases, thermal incubating did not lead to a bottlebrush polymer in the kinetically trapped state.

Table S5.4: Summary of the fits to data in Figure S5.15 to Equation 2

Incubation Condition	$f_{micelle}$ **[mol%]**	f_{bound} **[mol%]**	$R_{h,\ free\ chain}$ **[nm]**	$R_{h,\ micelle}$ **[nm]**	$R_{h,\ bound}$**[nm]**
50 °C - *B*-$E_{11}^{43}P_6^{15}$+ POPC	10 ± 5	0	4 ± 1	10 ± 2	-
37 °C - *B*-$E_{11}^{43}P_6^{15}$+ POPC	0	16 ± 3	6 ± 1	-	25 ± 4
25 °C - *B*-$E_{11}^{43}P_6^{15}$+ POPC	0	15 ± 3	6 ± 1	-	25 ± 4
B-$E_{11}^{43}P_6^{15}$	30 ± 5	-	5 ± 1	10 ± 1	-

Variable temperature PFG-NMR of *B*-$E_{11}^{43}P_6^{15}$ treated POPC liposomes

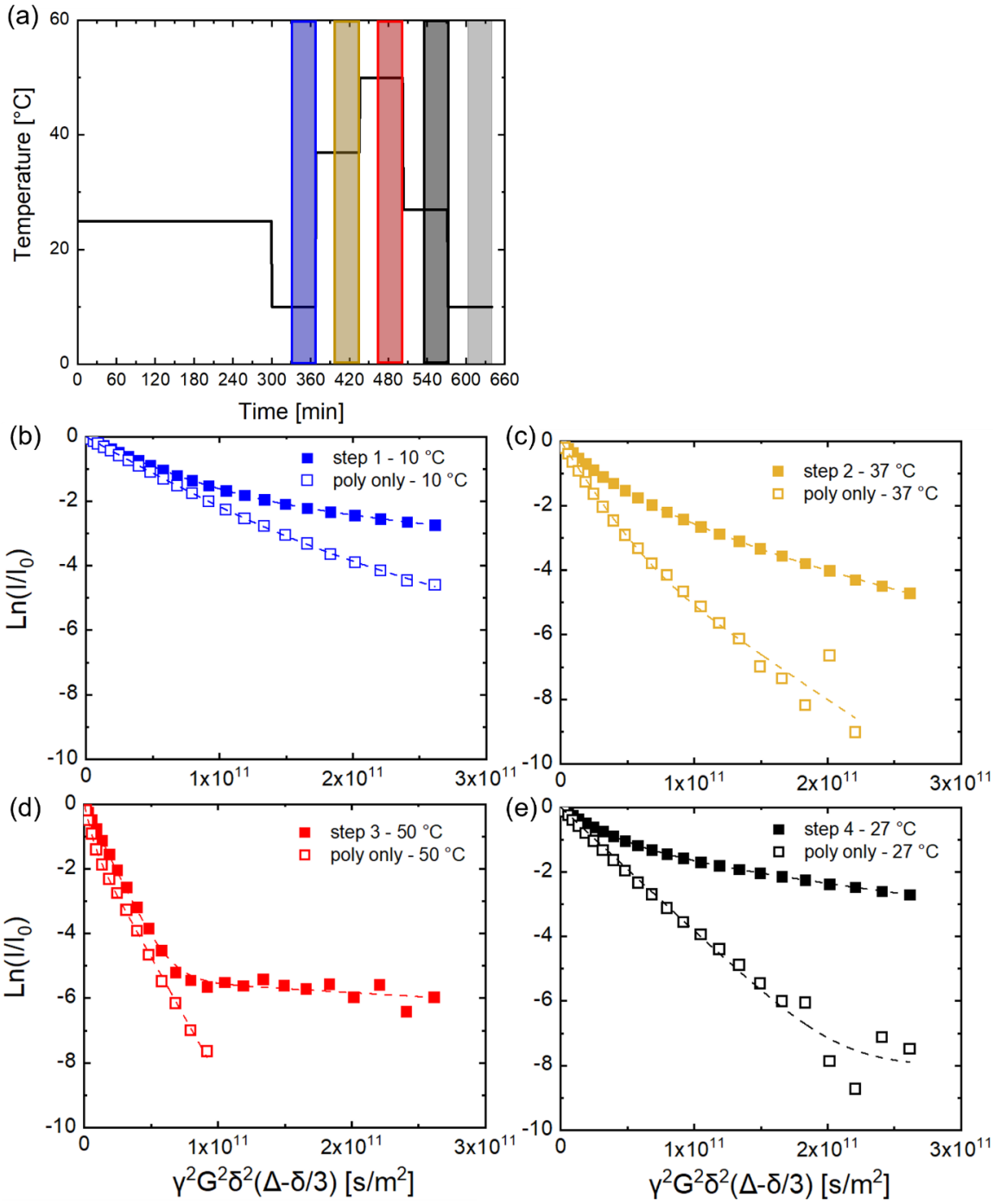

Figure S5.16: Variable temperature PFG-NMR experiment performed on POPC liposomes treated with *B*-$E_{11}^{43}P_6^{15}$. (a) Thermal path which is identical to that performed for F127. (b-e) PFG-NMR data collected at 10 °C (b), 37 °C (c), 50 °C (d), and 27 °C (e) open symbols is polymer only control and filled is polymer + liposome.

Table S5.5: Summary of fitting the PFG-NMR data in Figure S5.16 to Equation 2.

Temp. [°C]	Sample	$f_{micelle}$ [mol%]	f_{bound} [mol%]	$R_{h,\ free\ chain}$ [nm]	$R_{h,\ micelle}$ [nm]	$R_{h,\ bound}$ [nm]
10	*B*-$E_{11}^{43}P_{6}^{15}$[a]	9 ± 5	-	5 ± 1	13 ± 3	-
	B-$E_{11}^{43}P_{6}^{15}$ + POPC[a]	-	19 ± 1	5 ± 1	-	30 ± 1
37	*B*-$E_{11}^{43}P_{6}^{15}$[a]	8 ± 8	-	4 ± 2	10 ± 4	-
	B-$E_{11}^{43}P_{6}^{15}$ + POPC[b]	44 ± 2	14 ± 2	4	10	26 ± 1
50	*B*-$E_{11}^{43}P_{6}^{15}$[c]	0	-	5 ± 1	-	-
	B-$E_{11}^{43}P_{6}^{15}$ + POPC[d]	0	0	4 ± 1	-	-
27	*B*-$E_{11}^{43}P_{6}^{15}$[a]	2 ± 1	-	5 ± 1	16 ± 5	-
	B-$E_{11}^{43}P_{6}^{15}$ + POPC[b]	22 ± 2	19 ± 2	5	16	47 ± 2

[a]2-term expansion of Equation 2

[b]Constrained 3-term expansion of Equation 2

[c]Equation 1

[d]2-term expansion of Equation 2 yielded an unphysically slow diffusion for the bound state. The flat region in Figure S5.16d is an artifact.

Effect of thermal path on *B*-$E_{11}^{43}P_6^{15}$ binding to POPC liposomes

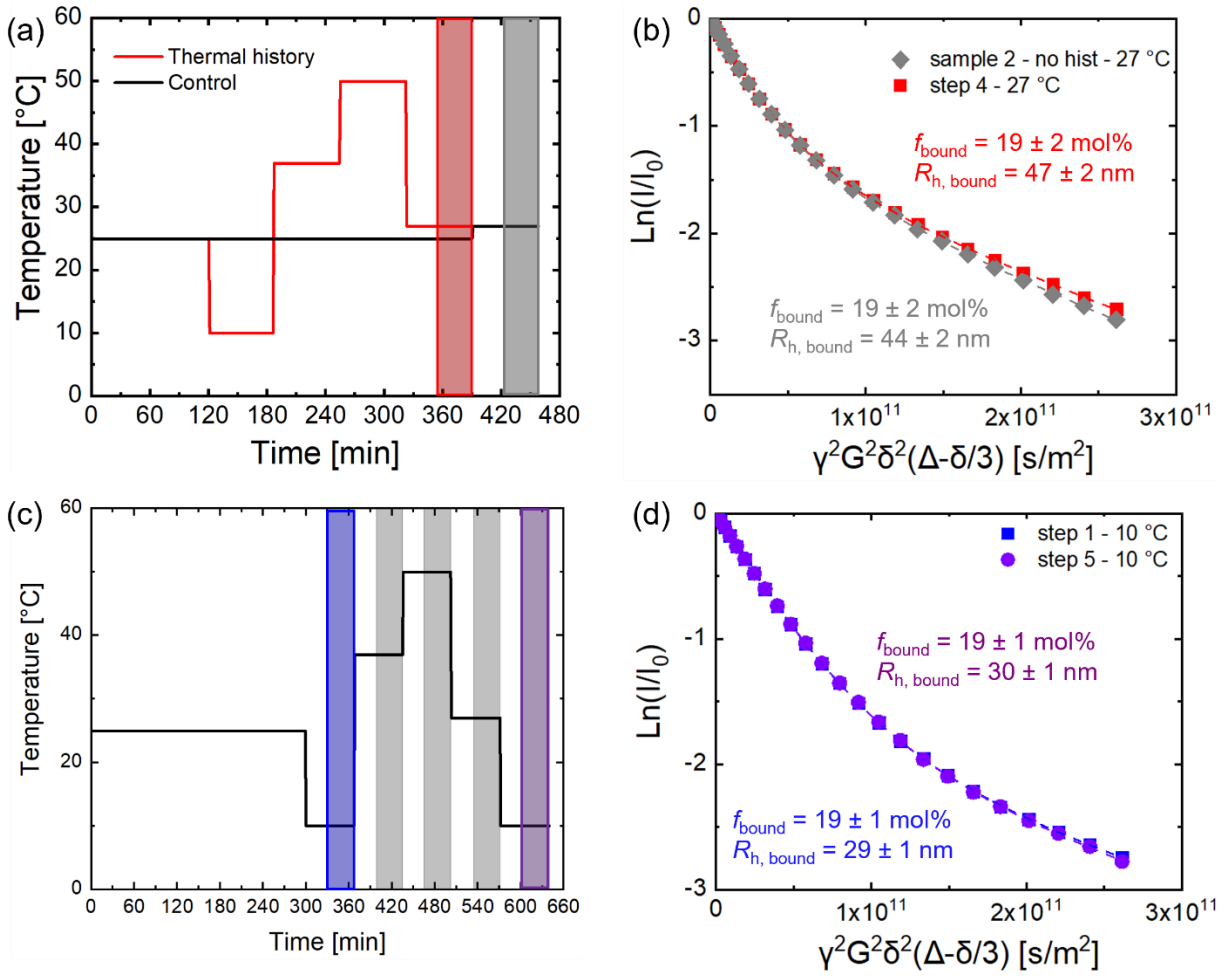

Figure S5.17: (a) Thermal path for 2 samples of POPC liposomes treated with *B*-$E_{11}^{43}P_6^{15}$: thermal history and a control sample. (b) PFG-NMR data for the two highlighted timepoints from panel (a). The decay curves are within error, indicating that there is no thermal path dependence for the bottlebrush architecture. (c) Thermal path for a single sample of POPC liposomes treated with *B*-$E_{11}^{43}P_6^{15}$. (d) PFG-NMR decay curves collected at the corresponding shaded regions of panel (c). The decay curves are within error and both show significant binding, indicating that *B*-$E_{11}^{43}P_6^{15}$ does not desorb at 10 °C nor does it exhibit path dependence.

F127 characterization data

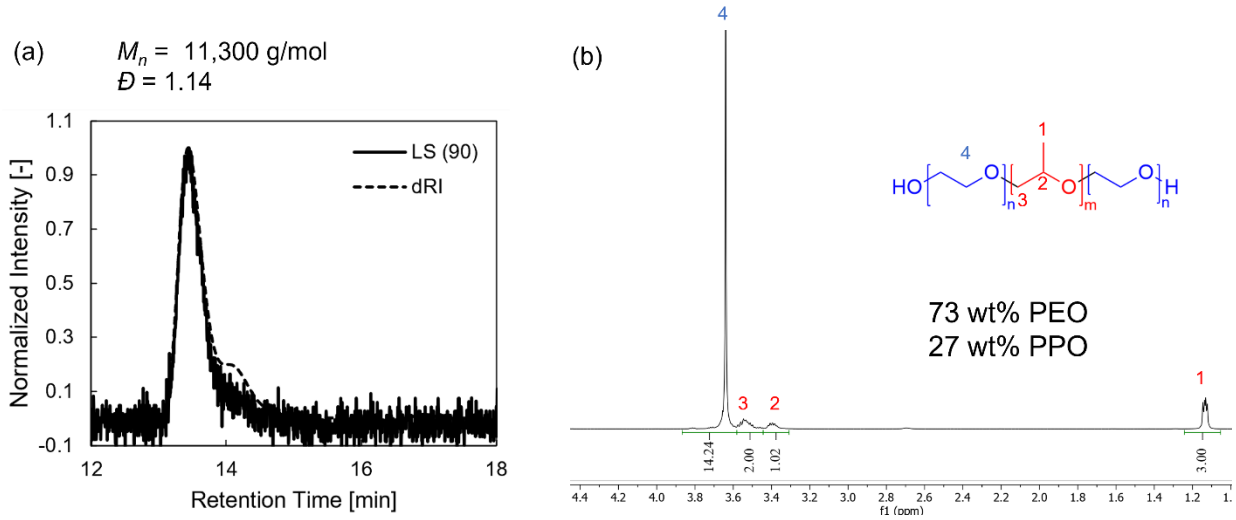

Figure S5.18: Characterization of F127. (a) SEC data; M_n and $Đ$ was determined using multi-angle light scattering and differential refractometer detectors. (b) ^{1}H NMR spectroscopy of F127 in $CDCl_3$. The ratio of PEO to PPO signals was used to estimate the composition. Data used with permission from Hassler et al.[88]

P188 characterization data

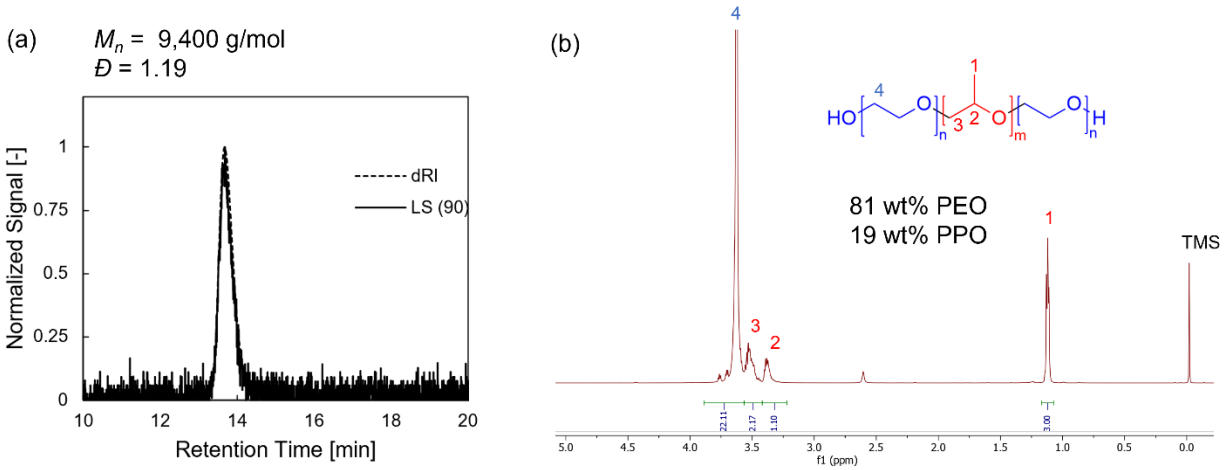

Figure S5.19: Characterization of P188. (a) SEC data; M_n and $Đ$ was determined using multi-angle light scattering and differential refractometer detectors. (b) ^{1}H NMR spectroscopy of P188 in $CDCl_3$. The ratio of PEO to PPO signals was used to estimate the composition. Data used with permission from Hassler et al.[88]

Characterization of bottlebrush poloxamer that is analogous to F127

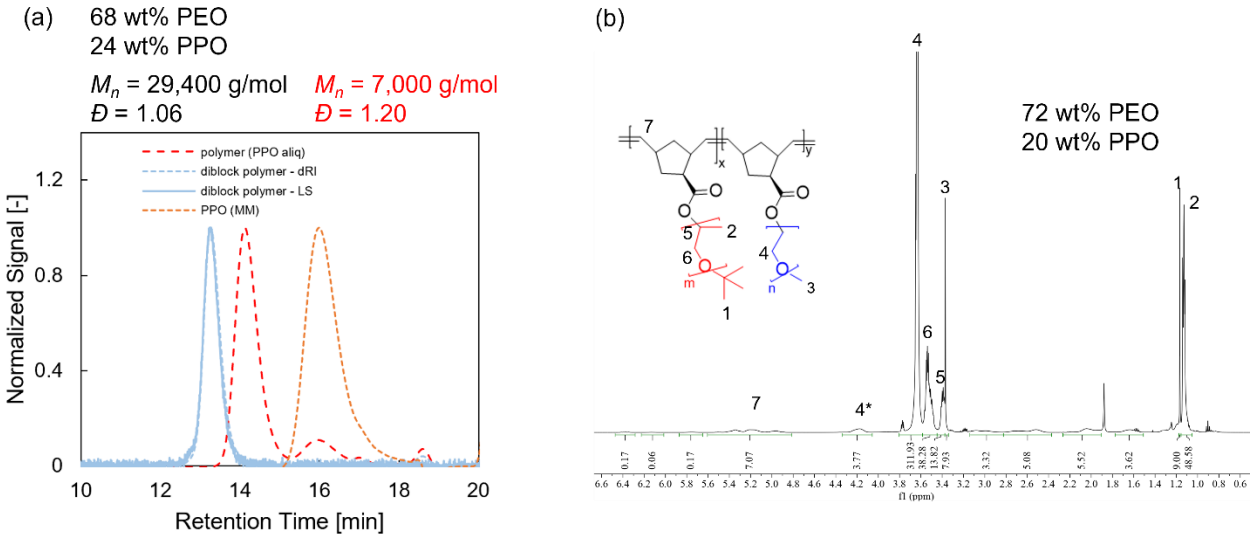

Figure S5.20: Characterization of *B*-$E_{11}^{43}P_6^{15}$. (a) SEC data; M_n and *Đ* was determined using multi-angle light scattering and differential refractometer detectors. (b) ^{1}H NMR spectroscopy of *B*-$E_{11}^{43}P_6^{15}$ in $CDCl_3$. The ratio of PEO to PPO signals was used to estimate the composition. Data used with permission from Hassler et al.[88]

Characterization of *L*-E_{455} (PEO-20k)

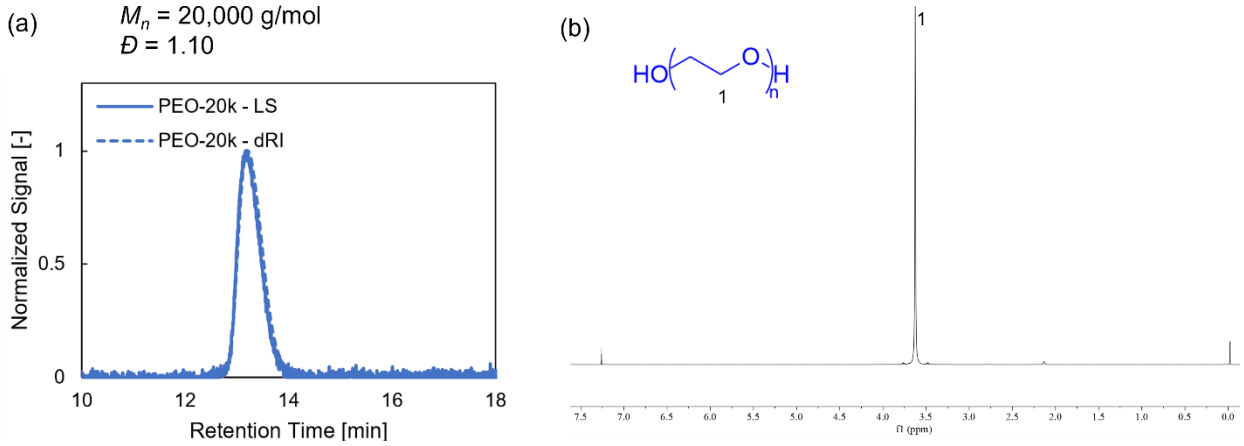

Figure S5.21: Characterization of *L*-E_{455}. (a) SEC data; M_n and *Đ* was determined using multi-angle light scattering and differential refractometer detectors. (b) ^{1}H NMR spectroscopy of *L*-E_{455} in $CDCl_3$. The ratio of PEO to PPO signals was used to estimate the composition. Data used with permission from Hassler et al.[88]

Characterization of *L*-$P_{14}E_{118}$

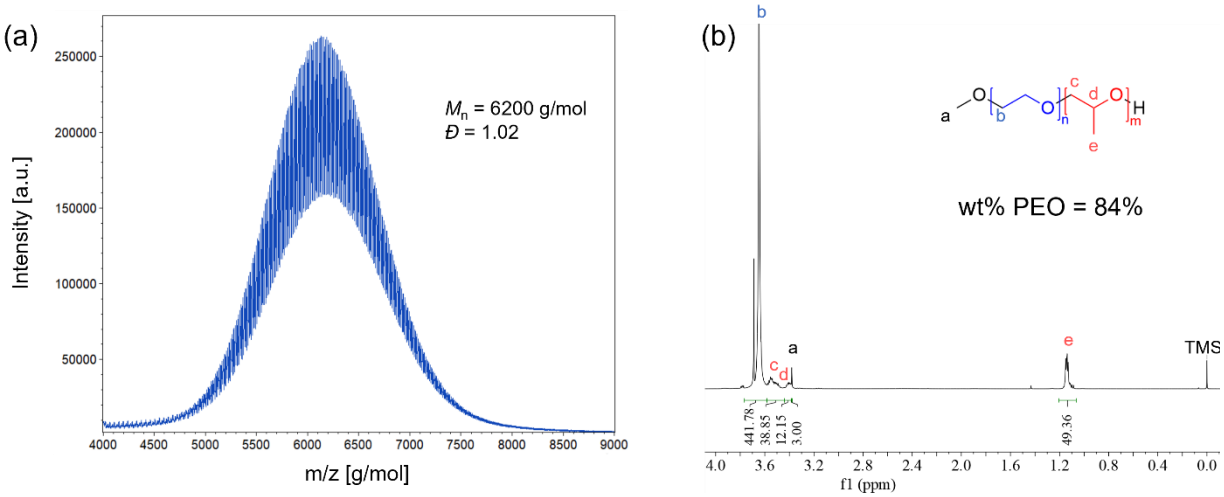

Figure S5.22: Characterization of $P_{14}E_{118}$. (a) MALDI-ToF spectrometry data. (b) ^{1}H NMR spectroscopy in $CDCl_3$. The ratio of PEO to PPO signals was used to estimate the composition. The number average degree of polymerization of the PEO and PPO blocks was then calculated using the composition from NMR and M_n from MALDI-ToF (N_{PEO} = 118 and N_{PPO} = 14).

Chapter 6: Impact of lipid phase behavior on polymer binding to liposomes

6.1 Motivation

The cell membrane of living cells is a non-equilibrium mixture of up to thousands of lipid species, proteins, and cholesterol.[53,278] Lipids with distinct tail and headgroup structures have different interaction energies with each other and with cholesterol, leading to phase separation into liquid-ordered (L_o), liquid disordered (L_d), and solid ordered (S_o) phases.[45–47,53] The phase behavior is sensitive to both temperature and membrane composition, and for many abiotic membranes the phase space is well mapped.[47] In the L_d phase, lipid molecules have a high degree of translational and rotational freedom; in the L_o phase, translation is slower and rotation is hindered; in the S_o phase, both translation and rotation are restricted.[52] This leads to different mechanical, structural, and dynamic properties. Although these properties are sensitive to temperature and composition, representative literature values for each phase are summarized in Table 6.1. The L_o phase is enriched in saturated lipids and cholesterol, has more organized packing, a smaller area per lipid, a higher bending modulus, and has slower lateral diffusion of lipid species relative to the L_d phase.[2,15,40,41] The differences in mechanical properties between the L_o domains, often referred to as lipid rafts, and the L_d matrix can alter protein conformation and therefore have implications for cell motility,[49] cell signalling,[2,279] and transport across the membrane.[280] In living cells, lipid rafts have diameters on the order of 10 nm and exist on short timescales, rapidly dissolve into the surrounding matrix and then re-form in a different location.[52] Because of the critical roles of lipid rafts, it is important for cells to have control over the distribution between L_o and L_d phases.

Table 6.1: Summary of differences in structural and mechanical properties between liquid disordered (L_d), liquid ordered (L_o), and solid ordered (S_o) phases.

		L_d	L_o	S_o
Bending modulus	κ [k_BT]	20[a]	25[d]	300[a]
Stretching modulus	κ_A [mN/m]	780[c]	1720[c]	
Thickness	t [nm]	3.8[e]	5.1[e]	5.6[a]
Lipid lateral diffusivity	$D_{lipid} \times 10^{-12}$ [m^2/s]	12[b]	4[b]	
Area per lipid	A [nm^2/lipid]	0.68[b]	0.53[b]	0.40[f]

[a]Woodka *et al. Phys. Rev. Lett.* 2012.[15]
[b]Lindblom G. and Oradd G. *Biochimica et Biophysica Acta.* 2009.[41]
[c]Needham D. and Nunn R.S. *Biophy. J.* 1990.[42]
[d]Baumgart *et al. Nature.* 2003.[134]
[e]Van der Paal *et al. Chem. Sci.* 2016.[40] Garcia-Saez *et al. J Bio. Chem.* 2007.[281]
[f]Filippov *et al. Biophys. J.* 2007.[282]

Interfacial energy is high at the L_o-L_d borders due to the height mismatch between the two phases and the high surface tension, creating a driving force for two L_o domains to coalesce, while entropy and electrostatic forces oppose it.[134,281] Garcia-Saez *et al.* used confocal microscopy to measure domain size and raft formation kinetics in 3-component supported lipid bilayers and found that as the height mismatch between the ordered and disordered phases increases, raft domains form more quickly upon cooling from above the miscibility temperature and are more circular.[281] A cell has mechanisms to manipulate its membrane composition, enabling cells to adjust surface tension and control the distribution between the L_o and L_d phases.[283] When a cell is exposed to stresses such as pore-forming toxins,[284,285] oxidative stress,[121,125] or a transmembrane gradient in osmotic pressure,[286] the distribution between L_o and L_d phases is disrupted and the cell loses its ability to control the lipid raft fraction and size, affecting cell signaling and having detrimental implications for many cell processes.

As described in Section 1.4.2, many studies have reported that the presence of PEO-PPO block copolymers during stress attenuates changes in cell signaling across many diverse pathways governing processes such as cytoskeleton reorganization and apoptosis.[118,121,128] Since these block copolymers are flexible, non-polar, molecules with a gaussian coil conformation, they are unlikely to have specific interactions with proteins. However, upon polymer insertion into the cell membrane, the surface tension decreases[137,136] and the area per lipid must decrease due to the occupied volume of the polymer. By manipulating surface tension, polymer insertion could affect the balance between L_o and L_d phases, which could non-specifically alter cell signaling. Therefore, it is important to understand how lipid phases affect polymer-liposome interactions and how polymer binding affects lipid phase behavior in the presence and absence of stress. In this chapter, I utilize 3-component liposomes to determine how lipid phase coexistence affects the fraction of F127 chains that bind to the liposome surface. To my knowledge, this is the first study of poloxamer-lipid bilayer interactions using 3-component membrane models and therefore is the first to incorporate the effects of lipid phase coexistence.

6.2 Liposome model to study effect of lipid phase behavior

Co-existing liquid phases require a saturated lipid (high melting temperature - T_m), an unsaturated lipid (low T_m), and cholesterol. Therefore, throughout this chapter, liposomes were prepared from different ratios of 3 components: 16:0-18:1 1-palmitoyl-2-oleoyl-glycero-3-phosphocholine (POPC: T_m = −2 °C), sphingomyelin (PSM: T_m = 40 °C), and cholesterol. The nomenclature used to describe the membrane composition is X/Y/Z where X, Y, and Z represent the mol% of POPC, PSM, and cholesterol in the liposomes, respectively. This model system was chosen because the composition-temperature space has been studied extensively using techniques such as fluorescence microscopy, confocal microscopy, Förster resonance energy transfer, and differential scanning calorimetry.[46–48,58,287,288] As shown by Figure 6.1, at both room temperature (23 °C) and physiological temperature (37 °C) there are windows of L_o/L_d coexistence (solid

circles) which can serve as models for lipid rafts.[47] Additionally, the headgroup identity and tail group lengths of POPC and PSM are identical, eliminating potential confounding effects. Zhang *et al.* reported the effect of adding cholesterol to POPC liposomes on poloxamer binding using pulsed field gradient NMR (PFG-NMR), exploring the left edge of the phase diagram in Figure 6.1.[86] PSM is an important saturated lipid that plays a role in cell signaling, makes up ~5−20 mol% of all lipids in mammalian cells, is enriched in the outer leaflet, and is particularly important in the myelin sheath of axons in the nervous system and the sarcolemma of muscle tissue.[289,290] Therefore, choosing PSM as the third component is a natural and biologically relevant extension of the POPC/Chol system which can be used to assess how lipid phase behavior affects polymer-liposome interactions.

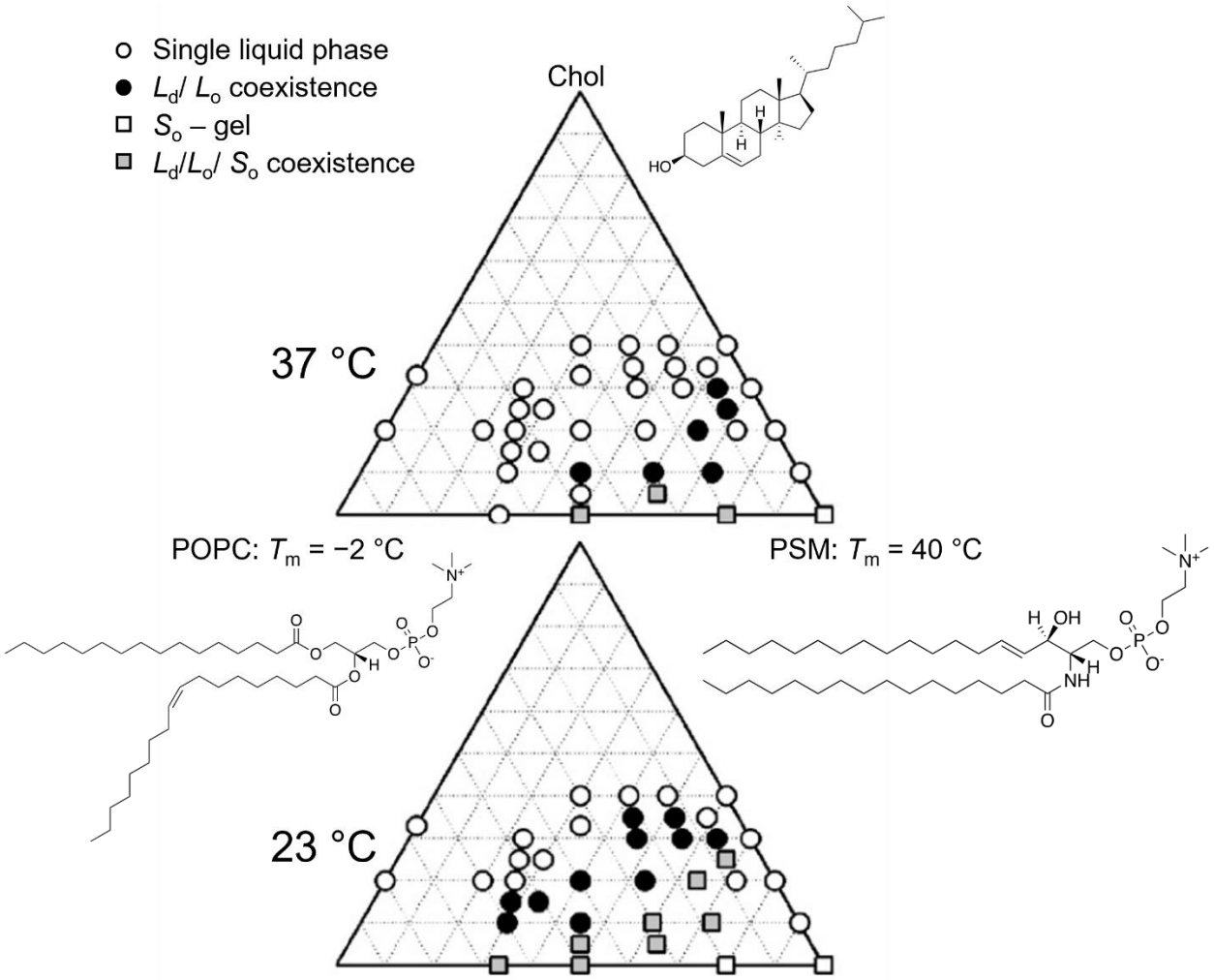

Figure 6.1: Ternary phase diagram for lipid vesicles prepared from POPC-PSM-Chol at 37 °C (top) 23 °C (bottom). Figure adapted from Keller and Veatch. *Phys. Rev. Lett.* 2005.[47]

Throughout this chapter, liposomes were prepared using the extrusion technique described in Chapter 2. Due to the high melting temperature of PSM (T_m = 40 °C), the lipid film was maintained at 50 °C throughout the hydration and extrusion steps. During the hydration step, the vial was placed in a 50 °C water bath for 30 s, then placed on a vortex plate for 30 s, and this cycle was repeated for a total of 1 h. Then, the extrusion step was performed at 50 °C using the heating block provided with the Avanti mini-extruder setup. It is critical to ensure that all lipid components are in the fluid phase during these steps to ensure incorporation of all components and to minimize liposome-to-liposome variation in composition, which is thought to be ~2 mol% deviation of each

component.[291] After preparation, liposomes were cooled to room temperature and the hydrodynamic radius and dispersity were measured via DLS. For all liposome preparations, the size distribution had a single peak, and the dispersity was narrow ($Đ \leq 1.02$). DLS data for all compositions are summarized in Table 6.2. Cholesterol incorporation leads to roughly a 10% increase in R_h, relative to the pure POPC liposomes, due to the membrane-stiffening effect of cholesterol.[86] Otherwise, the R_h of all liposome preparations are within error, thus liposome size is independent of composition along the isocholesterol slice. Pure PSM liposomes have higher bending and stretching moduli than POPC, so the stiffening effect of cholesterol is less pronounced, leading to no difference in the R_h of 0/86/14 and 0/100/0 liposomes.

Table 6.2: Summary of DLS characterization of liposomes

Membrane composition (POPC/PSM/Chol) [mol%]	R_h **[nm]**[a]	$Đ$[b]
100/0/0	43 ± 1	1.01 ± 0.01
86/0/14	52	1.01
60/26/14	56 ± 1	1.02 ± 0.01
36/50/14	46	1.01
21/65/14	47 ± 4	1.01 ± 0.01
0/86/14	52	1.02
0/100/0	51 ± 2[*]	1.01 ± 0.01[*]

[a]Mutliangle DLS measurement. Slope of relationship between the first cumulant (Γ) and the scattering vector squared (q^2).
[b]Determined via the ratio of the first and second cumulants from the fit to the DLS data acquired at a scattering angle of 90°.
Error is the standard deviation of at least 3 independent replicates unless otherwise noted.
[*]Range of 2 independent replicates

This chapter will focus exclusively on F127 (M_n = 11.3 kDa; $Đ$ = 1.14; 73 wt% PEO) binding to liposomes. Zhang *et al.* observed that cholesterol incorporation significantly reduced the fraction of chains that bind to the liposome.[86] Therefore, we chose F127 for this study because it has the highest membrane affinity of any linear poloxamer tested.[85] Furthermore, we chose to extrude the liposomes through the smallest pore diameter possible, 50 nm, because the increased membrane curvature increases the amount of binding; thus, the smallest liposomes maximizes the signal.[86] All experiments in this chapter were performed at 1 mg/mL F127 and 10 mM total lipid concentration with at least a 2 h incubation period at room temperature prior to PFG-NMR acquisition. All PFG-NMR data were acquired at 27 °C.

6.3 Single component liposome control experiments

Before we can explore the effects of lipid phase coexistence, it is first important to understand if there are any differences in F127 binding to pure POPC compared to pure PSM liposomes. Based on the T_m of POPC and PSM, at 27 °C, POPC liposomes will be exclusively in the L_d state ($T > T_{m,\,POPC}$) while PSM will be in the S_o state ($T < T_{m,\,PSM}$). Previous studies using lipid monolayers and Langmuir trough experiments have shown that poloxamers preferentially insert into monolayers at low surface pressures, corresponding to a large area per lipid.[66,71] Furthermore, Ka Yee Lee and co-workers performed isothermal titration calorimetry experiments on liposomes prepared with dimyristoylphosphocholine (DMPC: T_m = 24 °C) and showed that P338, a hydrophilic poloxamer with M_n = 14,600 g/mol and 80 wt% PEO, bound to the liposomes at $T > T_m$ (fluid phase – L_d) but not at $T < T_m$ (gel phase – S_o).[89] Based on this result and because the S_o state has a higher bending modulus, tighter lipid packing, and reduced lateral mobility of lipid molecules, we hypothesized that F127 binding would be significantly lower towards PSM compared to POPC liposomes at 27 °C.

Figure 6.2a shows the PFG-NMR decay curves of POPC liposomes treated with F127. The open symbols are the F127 solution control containing no liposomes, which shows a single rate of decay corresponding to free chains. Upon adding POPC liposomes, there is a second, slower decay which dominates at large values of the x-axis. The slower mode of relaxation corresponds to polymer adsorbed to the liposome surface, and the fraction of chains that bind to the liposomes can be quantified by fitting this data to a 2-term expansion of the sum of exponentials model (Eq. 6.2). This suggests that the fraction of chains bound to the POPC liposomes is $f_b = 9 \pm 3$ mol%. Since the temperature of incubation and data acquisition (27 °C) is greater than the melting temperature of POPC (T_m = −2 °C), the liposomes will be in the L_d phase. The bilayers have a relatively low bending modulus, so there will be spontaneous fluctuations in bilayer height, neighboring lipid molecules can translate and rotate with a high degree of freedom, and the area per lipid is relatively high. Based on the anchor and chain mechanism and previous literature results, these factors facilitate binding and lead to the relatively high bound fraction observed.

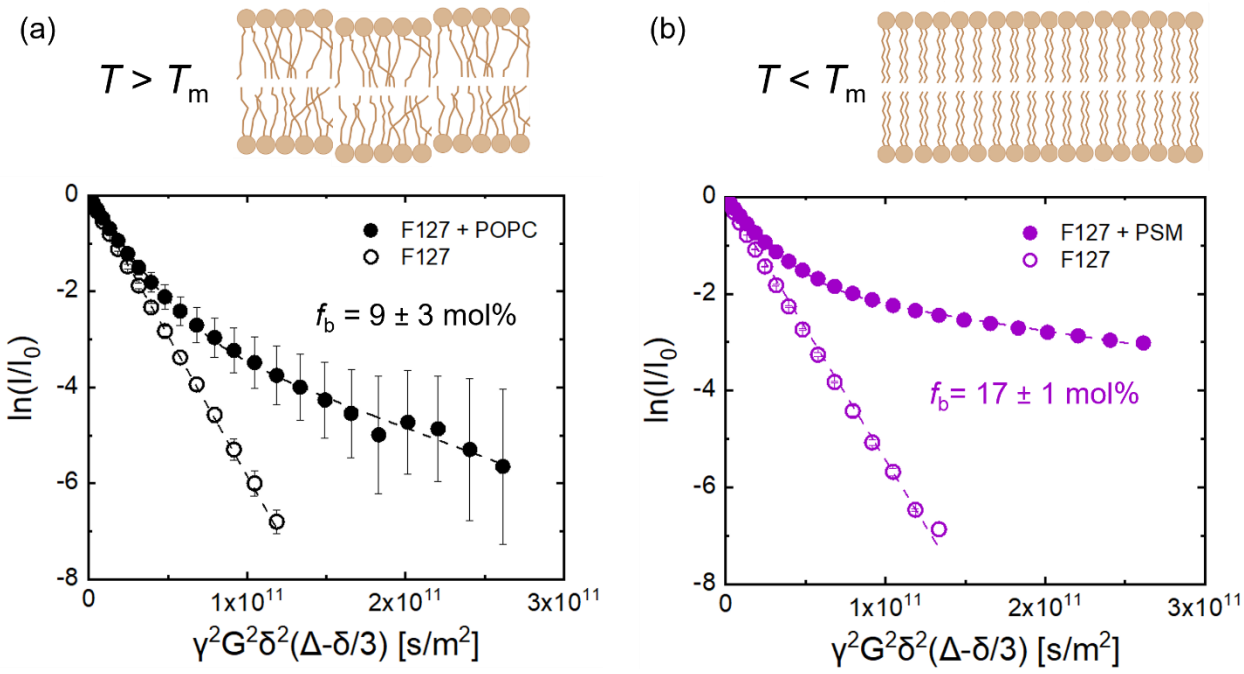

Figure 6.2: (a) PFG-NMR data for POPC liposomes treated with F127. (b) PFG-NMR data for PSM liposomes treated with F127. Error bars are the range of two independent replicates and the error reported is from the 95% confidence interval from the biexponential model.

For PSM liposomes on the other hand, the measurement was performed below the melting temperature (T_m = 40 °C); therefore, the PSM liposomes will be in the gel phase (S_o). As shown by the schematic in Figure 6.2b, the S_o phase has fewer spontaneous fluctuations in height, translation and rotation of lipids is more restricted, there is less area per lipid, and the bilayer is thicker. Figure 6.2b shows the PFG-NMR decay curve of F127 solution (open symbols) and F127 + PSM liposomes (closed symbols). This data is the average of two independent experiments. The F127 solution decay curve shows a single rate of relaxation that is consistent with the F127 solution in Figure 6.2a. When the PSM liposomes are added, a slow mode of relaxation appears and fitting this data to a 2-term expansion of Equation 6.2 suggests that f_b = 17 ± 1 mol%. Surprisingly, we found that F127 binds to pure PSM liposomes at $T < T_m$ with considerably high affinity. Furthermore, F127 has a higher affinity towards gel-phase PSM liposomes than towards fluid-phase POPC liposomes at the same temperature.

A possible explanation for the increased affinity of F127 towards PSM compared to POPC liposomes is faceting of the surface as the PSM liposomes are cooled past T_m. The PSM liposomes were prepared above T_m, existing as homogeneous L_d, then they were cooled to room temperature. As T_m is traversed, the S_o phase will nucleate at many sites along the liposome surface, then grow into each other resulting in a faceted surface due to grain boundaries. Figure 6.3a shows a cryo-TEM image of faceted DMPC liposomes (T_m = 24 °) that were prepared via extrusion above their T_m, then cooled to 4 °C.[89] At the facets, neighboring lipid headgroups are not aligned, resulting in an open volume for polymer insertion, as shown in Figure 6.3b. We speculate that the facets are attractive binding sites; since the acyl tails are exposed at the grain boundaries, the polymer does not need to push neighboring lipids apart to access the hydrophobic region, perhaps explaining why F127 has a higher f_b towards S_o phase PSM than for L_d phase POPC. It is curious that Ka Yee Lee and co-workers observed substantial binding of P338 to DMPC liposomes above T_m (L_d) but not below T_m (S_o), despite faceting of the DMPC liposome surface (Figure 6.3a), using ITC experiments.[89] The most likely explanation of this result is competing effects between temperature and lipid phase behavior. As temperature is reduced, the solvent quality of water towards PEO-PPO increases, dramatically reducing the binding affinity of poloxamers (Chapter 5). Therefore, comparing poloxamer binding to liposomes composed of lipids with dramatically different T_m at the same temperature, as was done in this Chapter, is a more direct comparison of how lipid phase affects poloxamer binding. Furthermore, F127 has a significantly higher membrane affinity than P338. Zhang *et al.* found that F127 had a 14× higher fraction bound than P338.[85] It is possible that PFG-NMR can more sensitively measure binding of low affinity polymers than ITC. Finally, in the PFG-NMR experiments reported here, polymer and liposome were mixed and incubated for 2 h to achieve a steady state, whereas an ITC experiment consists of a series of injections where the endotherm associated with adsorption occurs over a span of minutes. Therefore, kinetic effects could also contribute to the different results observed here and in Ka Yee Lee's work.[89]

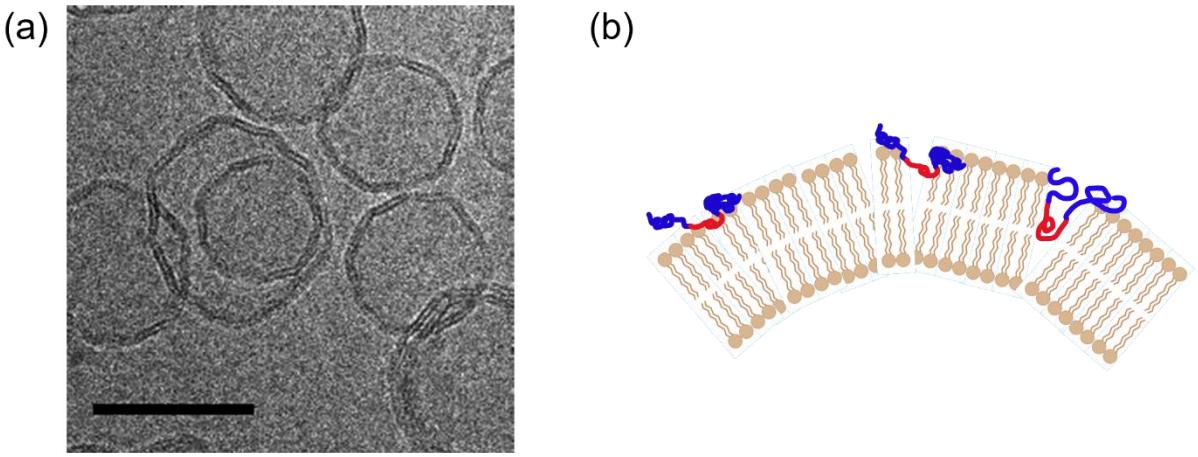

Figure 6.3: (a) cryo-TEM image of DMPC liposomes prepared above T_m then cooled into the gel phase. The scale bar is 100 nm. This figure was taken from Wu *et al. Soft Matter.* 2009.[89] (b) Schematic of a faceted gel phase lipid bilayer and the poloxamer preferentially inserting at the grain boundaries due to the exposed acyl tails and the available volume.

6.4 Results for isothermal-isocholesterol slice of the phase space

The phase space of POPC/PSM/Chol shown in Figure 6.1 is expansive, so we chose a single isocholesterol slice to probe the effects of lipid phase behavior on f_b of F127 at a single temperature (27 °C). Based on the phase diagram and previous results on how F127 binding changes with cholesterol content, we chose 14 mol% cholesterol. This level of cholesterol content was chosen for two reasons. First, based on previous PFG-NMR results, at 14 mol% cholesterol F127 will still exhibit observable binding (2 % < f_b < 10 %), depending on the concentrations of polymer and lipid employed.[86] Second, as shown by Figure 6.4a, there is diverse phase behavior along the 14 mol% cholesterol slice, i.e. regions of L_d, L_d/L_o, $L_d/L_o/S_o$, and L_o are present in traversing the phase diagram from left to right at 23 °C. Note, the literature phase diagram was constructed at 23 °C, and the PFG-NMR experiments performed here were done at 27 °C; thus, the phase boundaries will be similar, but not identical, to the phase boundaries shown in Figure 6.4a. It is important to note that the tie lines in the coexisting region of the ternary phase diagram are roughly parallel to the x-axis. Therefore, although the composition of the L_d and L_o phases in each sample will be similar, they will not be identical. Because of the dramatic effect of cholesterol content on binding,[86] we elected to study an isocholesterol slice of the phase diagram instead of a tie line.

On the far-left side of the isocholesterol slice, 86/0/14, the liposomes are exclusively in the L_d phase. As the saturated lipid component is added, L_o and S_o appear and occupy a larger and larger fraction of the surface area. Since the ordered phases have a higher cholesterol content, less space per lipid, and a higher bending modulus, we hypothesize that f_b will monotonically decrease in going from left to right on the phase diagram as the ordered phases occupy more and more surface area.

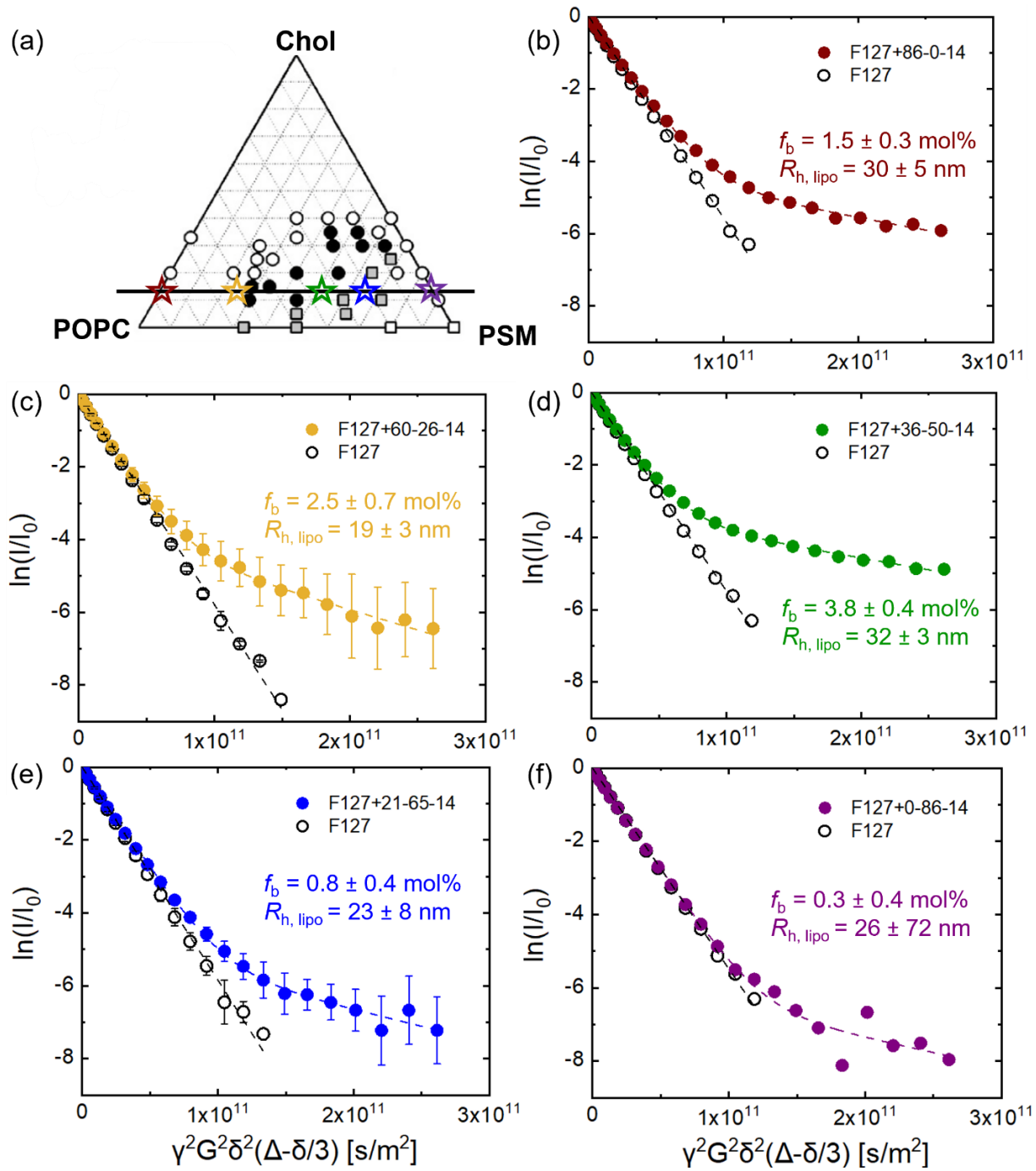

Figure 6.4: (a) Phase diagram for the POPC/PSM/Chol system with the experimental membrane compositions indicated with stars along the chosen isocholesterol slice. Figure adapted from Keller and Veatch. *Phys. Rev. Lett.* 2005.[47] (b-f) PFG-NMR decay curves of F127 solutions (open symbols) and F127 + liposomes (closed symbols) of various compositions. Compositions are given as POPC/PSM/Chol in mol%. Error bars are the standard deviation of 3 independent replicates. Absence of error bars indicates that a single replicate was performed at that membrane composition. Error is the 95% confidence interval from the fit to a 2-term expansion of Eq. 6.2.

Figures 6.4b−6.4f show PFG-NMR data corresponding to different points along the isocholesterol slice. In all cases, the F127 solution without liposomes (open symbols) shows a single rate of decay (R_h is consistent with free chains) while all the F127 + liposomes (closed symbols) show two rates of decay, indicating that F127 does bind to a detectable extent to liposomes of all compositions across the chosen slice of the phase space. All datasets were fit to an unconstrained 2-term expansion of Eq. 6.2.

Fitting the F127 + 86/0/14 liposome decay curve (maroon) results in f_b = 1.5 ± 0.3 mol% and $R_{h,\,lipo}$ = 30 ± 5 nm. Adding 14 mol% cholesterol dramatically reduced f_b compared to the 100% POPC control experiment shown in Figure 6.2a (f_b = 9 ± 3 mol%). This is consistent with previous results and is due to cholesterol stiffening the bilayer.[82,86] When some PSM is added to create liposomes with a 60/26/14 composition (yellow), the phase behavior is still, likely, exclusively L_d at 27 °C. The PFG-NMR data for this composition is shown in Figure 6.4c and the fitting result suggests that f_b = 2.5 ± 0.7 mol%, which is nominally higher than the result for 86/0/14. The green and blue points (36/50/14 and 21/65/14, respectively) are in regions where the liposome surface will phase separate into coexisting domains. For 36/50/14 (green), there are coexisting L_d and L_o domains. Since both domains are liquid, neighboring lipids can rotate and translate unhindered compared to the S_o domains that appear in 21/65/14 liposomes (blue). Interestingly, the fit to the PFG-NMR data for F127 + 36/50/14, shows a local maximum in f_b at f_b = 3.8 ± 0.4 mol% which is significantly higher than all other membrane compositions tested along this isocholesterol slice. As the boundary between L_d/L_o coexistence and L_d/L_o/S_o is crossed, f_b significantly decreases to f_b = 0.8 ± 0.4 mol%, possibly because the S_o domains are too stiff for the polymer to insert, effectively reducing the number of binding sites available. Finally, F127 binding to 0/86/14 liposomes (purple) was barely detected, f_b = 0.3 ± 0.4 mol%, equivalent to 0 within the 95% confidence interval for this membrane composition. At a membrane composition of 0/86/14, the membrane is exclusively in the L_o phase. Since the membrane is in a homogeneous liquid phase, there are no grain boundaries as depicted for the pure S_o phase in Figure 6.3. Since minimal to no binding occurred

at this membrane composition, we assert that polymer binding into a L_o matrix is unfavorable, likely due to the high bending and stretching moduli, the small area per lipid, and the ordered lipid packing.

Figure 6.5a summarizes the f_b results for all membrane compositions along the 14 mol% cholesterol slice. Clearly, there is a non-monotonic relationship between the PSM fraction and f_b, indicating that our original hypothesis was incorrect. Instead, f_b is maximized at intermediate compositions where there are coexisting liquid domains, decreases as a solid phase nucleates, and then approaches zero when there are exclusively L_o domains in the 0/86/14 membrane.

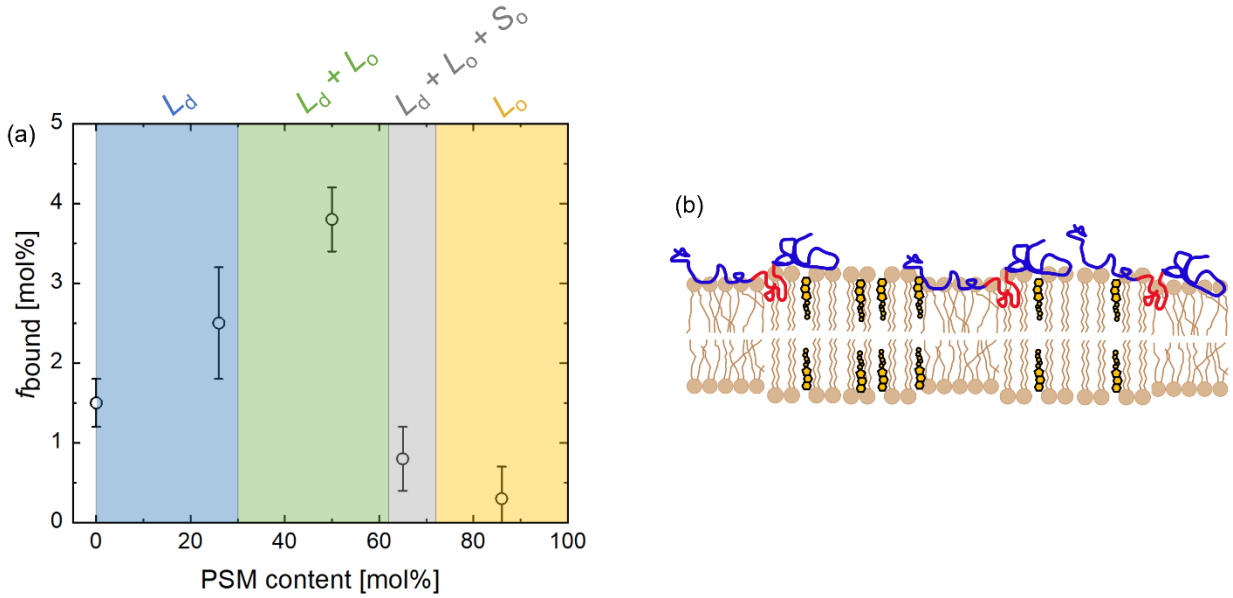

Figure 6.5: (a) Relationship between f_b and the percent incorporation of the saturated lipid component (PSM). Error bars are the 95% confidence interval on fitting the PFG-NMR data averaged over all replicates. (b) Sketch of the hypothesized mechanism behind the effect of lipid phase behavior on F127 binding.

Figure 6.5b shows a sketch of a possible explanation for this observation. We hypothesize that f_b is maximized in the region with coexisting liquid domains because the borders between the L_d and L_o domains are attractive binding sites. At the $L_d - L_o$ border, there is a mismatch in bilayer thickness, leading to a high interfacial energy.[40,292] This thickness difference is particularly

dramatic in sphingomyelin containing bilayers, and in POPC/PSM/Chol bilayers atomic force microscopy measurements revealed a height difference of 1.3 nm between the L_o and L_d phases.[281] This is significant, as it is roughly a 30% difference in bilayer thickness and is commensurate with the R_g of the PPO block of F127 ($R_{g,\,PPO}$ = 1.8 nm). The height mismatch minimizes the distance that the chain must push neighboring lipids apart before it can access the acyl region. Furthermore, given the surfactancy of poloxamers, they will likely accumulate at the $L_d - L_o$ interface to minimize the interfacial energy. Thus, in POPC/PSM/Chol liposomes with phase coexistence, the $L_d - L_o$ borders play a similar role to the facets in a S_o phase PSM liposomes. Therefore, the results presented in Sections 6.3 and 6.4 share a common mechanism.

6.5 Conclusion and next steps

In this chapter, we have begun to explore the effects of lipid phase behavior on polymer affinity towards liposomes. We studied F127 (M_n = 11.3 kDa, 72 wt% PEO) as the model polymer and various mixtures of POPC/PSM/Chol as model membranes. We employed PFG-NMR to measure f_b as a function of PSM content along an isocholesterol slice of the ternary phase diagram mapped by Keller *et al.*[47]

Surprisingly, F127 binds to S_o phase PSM liposomes with higher affinity than it does towards L_d phase POPC liposomes. Previous studies have shown that an 80 wt% PEO poloxamer was excluded from the gel phase due to the high bending modulus and small area per lipid.[66,71] However this study compared poloxamer binding to DMPC liposomes over a wide temperature range, confounding effects of changing solvent quality of water towards PEO-PPO polymers and membrane phase transitions.[89] As a single component liposome is cooled through its T_m, the surface facets as S_o domains from different nucleation sites grow into each other. We propose that these facets could be attractive binding sites and therefore explain why F127 has a higher affinity towards S_o phase PSM than for L_d phase POPC at the same temperature.

In 3-component POPC/PSM/Chol liposomes, we found that there is a non-monotonic relationship between f_b and the percent of the saturated lipid component, PSM, in the bilayer. Furthermore, the local maximum in binding affinity coincides very closely with the region of L_d – L_o phase coexistence. We assert that this is indirect evidence of poloxamer localization to the borders between these domains which could be caused by the height mismatch and high interfacial energy. Poloxamer localization at the interface between L_d – L_o domains could attenuate changes to the lipid raft fraction and domain size upon osmotic swelling or oxidative stress, providing a non-specific mechanism for poloxamers minimizing changes in cell signaling upon membrane damage. However, direct evidence of this hypothesized mechanism is needed.

Confocal and fluorescence microscopy have been successfully used to image phase coexistence in ternary lipid vesicles.[48,55,134,286,291,293,58,292] These techniques require a small fraction (0.1−1 mol%) of a fluorescently labelled lipid dye. Based on the tail group of the dye labelled lipid, the dye will prefer either the L_o or L_d phase, and the partitioning coefficient has been recently reviewed by Baumgart *et al* for a variety of dyes.[55] Figure 6.6 shows an example fluorescence microscopy study from the literature which obtained clear evidence of macroscopic lipid phase separation in 3-component vesicles.[292] Here, the dye selectively partitions into the L_d phase; hence L_d is bright and L_o or S_o is dark. As the content of the saturated component (DPPC) increases from ~15−55 mol%, the matrix transitions from light to dark as the ordered phases become the major component. By conjugating a fluorophore to the chain ends of F127, we could employ fluorescence microscopy to directly visualize the spatial distribution of F127 across the liposome surface relative to the L_o and L_d domains. Bez Batti *et al.* recently reported a synthetic scheme to functionalize poloxamer chain ends with a fluorophore.[158] It is important that the dye label and the lipid label emit at different wavelengths, so their signals can be distinguishable. I propose to use 18:1 lissamine rhodamine PE which selectively partitions into the L_d phase and emits at 583 nm (red) as the label for the lipid phase behavior and carboxyfluorescein as the polymer label because it emits at 515 nm (green) and has a been shown to have minimal interactions with lipid bilayers.[294]

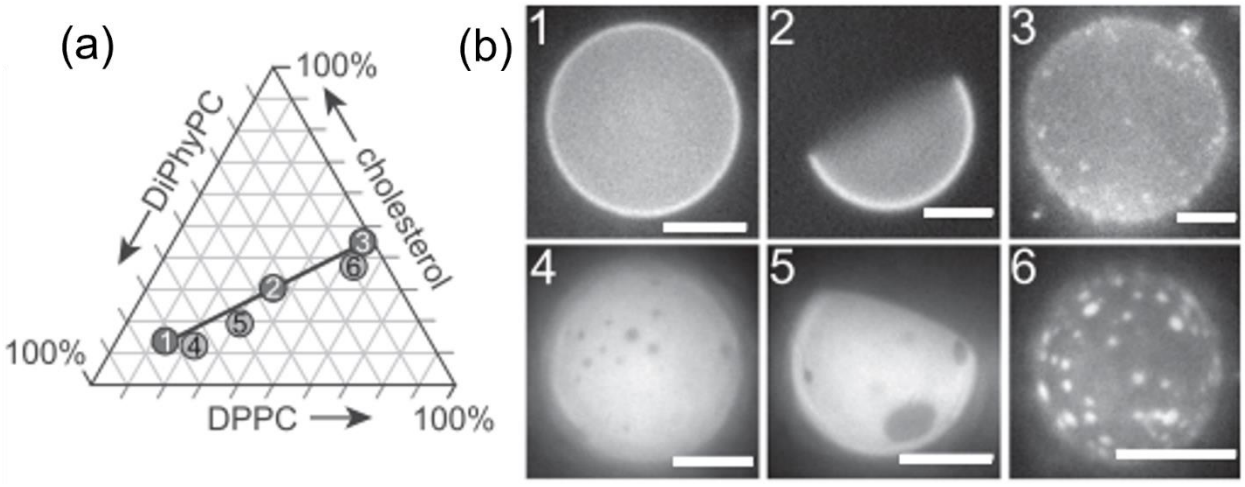

Figure 6.6: Fluorescence microscopy images along a tie line of the phase diagram, showing coexisting phases. 0.8 mol% of Texas Red DHPE was incorporated into the vesicles which selectively partitions into the L_d phase. Scale bar is 20 μm. Figure adapted from Cornell *et al.*[292]

There are several challenges that must be overcome to perform this experiment successfully. First, all the PFG-NMR results were done with liposomes prepared by direct dissolution followed by extrusion through 50 nm diameter pores at 50 °C. The preparation method has been observed to impact the lipid ratio in the resulting liposomes,[292] so it will be important to prepare all liposomes using the direct dissolution + extrusion method. Second, it is imperative to hydrate and extrude above the highest T_m in the system. This ensures that the lipid film is homogeneous as it hydrates, leading to as little variation in lipid composition liposome-to-liposome as possible (~2 mol% deviation of each component).[48] As the liposomes are cooled past the miscibility temperature, the L_o/L_d domains form and coarsen over time to minimize interfacial energy. Thus, the cooling rate and timing of imaging relative to vesicle preparation will affect the domain size and distribution, so these experimental details should be controlled for and consistent across all

datasets. Third, the 50 nm pore size was needed to induce an observable level of binding in the PFG-NMR assay at 14 mol% cholesterol, 1 mg/mL F127 and 10 mM total lipid. The high membrane curvature leads to an increase in binding which offsets the stiffening effect of cholesterol.[86] Due to the diffraction limit and the wavelength of visible light, obtaining quantitative images of lipid phase coexistence on the surface of 50 nm liposomes is not possible. Fortunately, vesicles with diameters of 1−10 μm can be prepared using the same direct dissolution + extrusion method.[295] However, the fraction of chains that will bind to micron scale vesicles will be dramatically lower than that observed for the liposomes reported in Figure 6.5. To increase the number of polymers bound to each vesicle, high polymer: lipid ratios may need to be employed.[94] Furthermore, since PEO-PBO polymers are thought to follow the anchor and chain mechanism, we speculate that these higher affinity polymers would also localize to the borders of L_o and L_d domains. Thus, due to their higher binding affinity,[87] this proposed fluorescence microscopy experiment could also be done with a dye-labelled PEO-PBO polymer.

6.6 Materials and Methods

Materials: Pluronic F127 (also known as Poloxamer 407) was provided by BASF. 16:0-18:1 1-palmitoyl-2-oleoyl-glycero-3-phosphocholine (POPC), porcine brain sphingomyelin (PSM), and cholesterol were purchased from Avanti Polar Lipids. Deuterium oxide was purchased from Cambridge Isotope Laboratories. All materials were used as received.

Liposome fabrication: Stock solutions of each lipid component in chloroform were prepared with known concentrations ([lipid] ~ 0.1 M) and were mixed to yield a chloroform solution with the desired molar ratio of POPC/PSM/Chol. Then, the chloroform was evaporated using a gentle stream of N_2 to yield a lipid film on the walls of a glass vial. To ensure all residual chloroform was removed, the vial was placed under vacuum for > 1 h. For all lipid mixtures containing PSM (T_m = 40 °C), the lipid film and D_2O were heated to 50 °C prior to hydration. Then, the film was hydrated by placing the vial on a vortex plate for 30 s then in a 50 °C bath for 30 s to ensure the

hydration step was done above the highest T_m in the system. This cycle was repeated for 1 h. After hydration, the lipid suspension was extruded 29× through a membrane with 50 nm diameter pores using the Avanti mini-extruder on a heating block at 50 °C. For lipid preparations without PSM, the hydration and extrusion were done at room temperature.

Dynamic light scattering: The hydrodynamic radius and dispersity of all liposome preparations were assessed using dynamic light scattering. The liposome stock solution after extrusion was diluted to ~1.5 mg/mL in D_2O, filtered with a 0.2 μm wwPTFE filter to remove dust, and placed in a glass test tube (200 mm × 7 mm with 5 mm inner diameter). All DLS experiments were performed at room temperature on a Brookhaven BI-200SM instrument equipped with a 637 nm laser. Data were collected at incident-to-detector angles of 60°, 75°, 90°, 105°, and 120°, and the autocorrelation functions were analyzed using the second-order cumulant model (Eq. 2.3). For all samples, the size distribution has a single peak, and the size dispersity is low ($Đ \leq 1.02$). Furthermore, the first cumulant scales linearly with the scattering vector squared ($\Gamma \sim q^2$), and the relationship passes through the origin, consistent with a diffusive process.

Pulsed-field gradient NMR: All PFG-NMR experiments were performed at 1 mg/mL polymer and 10 mM total lipid concentration. Polymer and liposomes were incubated together at room temperature for a minimum of 2 h prior to data acquisition. Data was acquired using a Bruker Avance III 500 MHz spectrometer which was equipped with a 5 mm TBO triple-resonance PFG probe. The probe temperature was set to 300 K to enable automation of experiments. The ledbpg2s pulse sequence was employed with a 5 ms gradient pulse duration (δ), a 700 ms diffusion time (Δ), a gradient strength that varied linearly from 2−95% with 25 distinct gradient strengths, a relaxation delay and acquisition time of 1 s, and 32 scans were recorded at each gradient strength.

In a PFG-NMR experiment, the magnetic field gradient along the z-axis of the sample encodes spatial information into the phase of the excited spins. This leads to signal decay according to Equation 6.1:

$$\ln\left(\frac{I}{I_0}\right) = -\gamma^2\delta^2G^2(\Delta - \frac{\delta}{3})D \tag{6.1}$$

where I and I_0 are the integrals of the chosen NMR peak (PEO at ~ 3.70 ppm) at the given gradient strength and a gradient strength of 0, respectively, γ is the gyromagnetic ratio of the nucleus (42.6 MHz/T for a proton), δ is the duration of the magnetic field gradient pulse, G is the strength of the magnetic field gradient, Δ is the diffusion time, and D is the translational diffusion coefficient of the species associated with the chosen NMR signal.[85,87,88,165] Since the signal decay is a function of D, if multiple populations are present with distinct sizes (difference of at least a factor of 2), then the fraction of the material in each state can be resolved by fitting the data to a sum of exponentials model given by Equation 6.2:

$$\ln\left(\frac{I}{I_0}\right) = \ln\left(\sum_i f_i \exp\left(-\gamma^2\delta^2G^2\left(\Delta-\frac{\delta}{3}\right)D_i\right)\right) \tag{6.2}$$

where fi and Di are the mol fraction of material in state i and the translational diffusion coefficient of state i, respectively. The translational diffusion coefficient can then be related to the hydrodynamic radius using the Stokes-Einstein equation:

$$R_h = \frac{k_B T}{6\pi\eta_s D} \tag{6.3}$$

where k_B is Boltzmann's constant, T is absolute temperature, η_s is the viscosity of the solvent at the given temperature,[296] and D is the translational diffusion coefficient resulting from the fit to the PFG-NMR data. All PFG-NMR data in this chapter were fit to an unconstrained 2-term expansion of Equation 6.2.

Chapter 7: Summary and future directions

7.1 Summary

The research presented in this thesis has advanced understanding of interactions between amphiphilic block polymers and phospholipid bilayers. The cell membrane, including how the structures of its constituent molecules lead to its mechanical and structural properties and its role in maintaining homeostasis, was introduced in Chapter 1. Furthermore, I discussed poloxamers and related their amphiphilic nature and membrane interacting capabilities to the structure of the repeat units. Namely, due to hydrogen bonding between the oxygen atoms in PEO and PPO to water, these polymers are surrounded by a water shell. As temperature increases, the strength of these hydrogen bonds decreases, leading to thermoresponsive behavior in aqueous PEO-PPO systems.

Chapter 2 discusses the fundamentals and practical considerations of techniques that are used throughout this thesis, and that may not be common knowledge for some polymer scientists. Liposomes are useful as model cell membranes because they expand the set of characterization techniques that can be employed and reduce the complexity of the system to enable fundamental studies. Throughout this thesis liposomes of various sizes and compositions were prepared by extrusion as described in Section 2.1. Dynamic light scattering is a solution characterization technique that relates temporal fluctuations in scattered light intensity to the rate of translational diffusion of particles in solution. Sample preparation and careful comparison of different models are required for meaningful results, as described in Section 2.2. I employed PFG-NMR spectroscopy throughout Chapters 4-6 of this thesis, so the fundamentals of this technique, a description of how to qualitatively and quantitatively interpret a dataset for polymer + liposome samples, and details on the parameter optimization protocol to enable the reader to choose appropriate parameters for their system of interest were also discussed in Chapter 2. Finally, an *in vitro* assay that imposes osmotic stress to cells and measures the release of an enzyme as a marker for membrane permeability was introduced. This assay uses a cell line that is relevant to human

muscle cells, is intermediate throughput (~100 conditions/ day), and can be used as a first-pass biological assessment of the protective ability of a polymer treatment.

In Chapter 3, a novel synthetic strategy to efficiently make bottlebrush poloxamers (BBPs) was outlined. Anionic polymerization yielded mono-alcohol functionalized PPO and PEO materials with narrow dispersity and control over the molecular weight and α-chain end. Then, for PPO, a hydrogenation step must be performed to eliminate an alkene α-chain end impurity arising during the anionic synthesis. The final step of macromonomer preparation was to convert the alcohol ω-chain end to a norbornene via an esterification reaction. Finally, ring opening metathesis polymerization (ROMP) reactions were performed with the desired macromonomer(s) and a Grubbs 3rd generation catalyst. This strategy avoids side reactions associated with radical polymerization of PPO, enabling a bottlebrush PPO polymer with high grafting density and complete conversion of monomer for the first time. Furthermore, because ROMP reaches full conversion in ~10 min and purification is relatively easy, this strategy enables the experimentalist to efficiently span a given parameter space. Once a set of macromonomers has been prepared, they can be combined in different ratios and combinations to create BBPs with varying molecular weights, side chain lengths, and arrangement of side chains, making this strategy a versatile synthetic platform for the preparation of BBPs.[109]

In Chapter 4, I employed this synthetic strategy to create a set of BBPs over a range of molecular weight, with two PEO block side chain lengths, and with block and statistical architectures. I then used the PFG-NMR assay to elucidate relationships between these parameters and the polymer affinity for POPC liposomes. This study culminated in understanding that the backbone of membrane-bound BBPs likely lies in the bilayer plane with the PPO and PEO side chains intercalating between neighboring lipids. This creates multiple anchoring units on the same molecule, explaining the increase in membrane affinity of a BBP relative to an analogous linear poloxamer. Additionally, I used an *in vitro* assay to screen this set of BBPs for their ability to protect cells against osmotic stress. All BBPs tested exhibited a protective effect, and surprisingly,

a statistical BBP showed a protective effect at concentrations as low as 20 nM, the lowest efficacious concentration observed to date using this assay.[88]

Chapter 5 explored the role of temperature and thermal history on polymer-liposome binding. I presented data demonstrating that the thermal history of a polymer-liposome sample has a remarkable effect on the amount of polymer bound to the liposome. During an incubation at an elevated temperature, the activation energy of a PEO block traversing the acyl region is relatively low, leading to polymer entering the intra-liposomal space. This leads to polymer kinetically trapped within the liposome and in new configurations on the liposome surface. I employed PFG-NMR to measure the extent of polymer in these kinetically trapped states ($f_{b,0}$) and the rate of expulsion from them (k_{rec}). These parameters are functions of the cholesterol content and polymer architecture, providing indirect support for the hypothesized mechanism. This fundamental insight suggests that poloxamers passively enter the cell, and it could be exploited to manipulate the surface and mechanical properties of liposomes. Furthermore, I showed that temperature has a dramatic effect on the fraction of chains bound to the liposome (f_b), with f_b increasing by a factor of 11 (± 3) in raising the temperature from 27 °C to 37 °C. This is particularly notable because much of the poloxamer-lipid bilayer literature has been performed at room temperature (near 27 °C) while 37 °C is close to body temperature. This information may help put previous mechanistic studies in context with each other wherever temperature is not the same.

Finally, in Chapter 6 I studied the role of lipid phase coexistence in poloxamer-liposome binding events. Living cell membranes are heterogeneous with liquid ordered domains (L_o - rafts) amongst a matrix of liquid disordered domains (L_d). Here, I employed 3-component liposomes consisting of POPC/PSM/Chol which has a well-mapped phase space as a model for cell membranes with lipid rafts. PFG-NMR results across an isocholesterol slice of the phase space showed that binding of a model poloxamer is maximized in the window of phase space with L_o-L_d coexistence. Then, when the S_o phase nucleates in a mixed liposome, binding decreases and when there is a homogenous L_o phase, binding is minimized. I hypothesize that the maximum binding in

the L_o-L_d coexistence region is because the border between the two liquid phases is an attractive binding site. The thickness mismatch between the two domains leads to a high line tension which the surfactant-like poloxamer will bind to minimize total surface energy. If the poloxamer localizes to the interface of L_o-L_d domains, then I speculate that poloxamer treatment will regulate the surface area fraction and domain shape of lipid rafts, thereby providing a non-specific mechanism by which poloxamers impact protein conformation and cell signaling pathways.

7.2 Continued exploration of bottlebrush poloxamer architecture

The initial exploration of the BBP parameter space presented in Chapter 4 yielded mechanistic insight into BBP-lipid bilayer interactions and a molecule with superior protection efficacy against osmotic stress.[88] To realize more efficacious treatments for DMD and heart attack patients, it is important to continue assessing the performance of these molecules in more physiologically relevant systems such as an *ex vivo* sarcomere length kinetics assay and *in vivo* models interrogating protection efficacy against isoproterenol insult.[131,158] Additionally, as shown by Figure 7.1, there are three bottlebrush parameters that could be explored using the synthetic platform described in Chapter 3 and the assays described in this thesis: multiblock BBPs, PPO side chain length ($N_{sc,\,PPO}$), and the spacing between grafts (N_g).

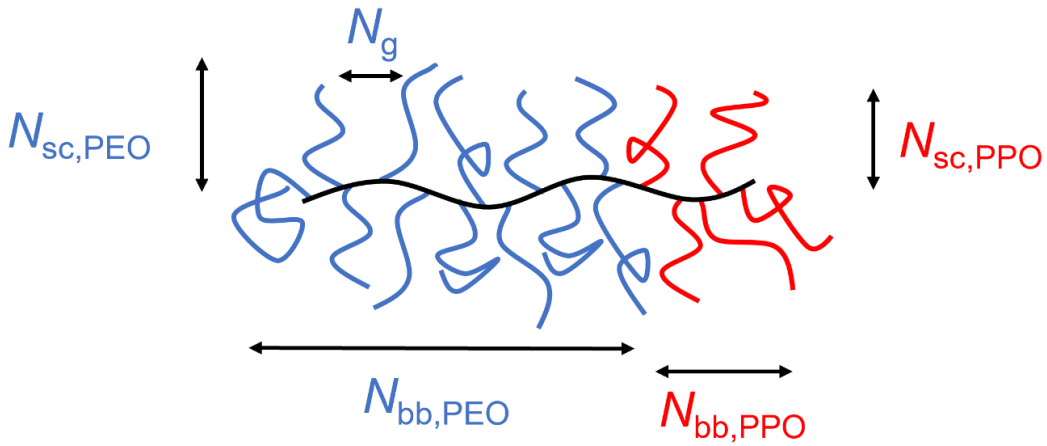

Figure 7.1: Schematic of the BBP architecture. In this section, I will propose future experiments to assess the impact of extending the chain to a multiblock architecture, varying the side chain length of the PPO block ($N_{sc,PPO}$), and increasing the spacing between side chains (N_g).

7.2.1 Multiblock bottlebrush poloxamers

Crabtree, *et al.* showed that the inverted linear poloxamer architecture led to minor improvements to protection efficacy against osmotic stress, possibly because of having two anchoring blocks on the ends of a single chain. In Chapter 4, I demonstrated that diblocks of a bottlebrush poloxamer architecture also had improved protection efficacy at low polymer concentrations. Therefore, I hypothesize that multiblock BBPs could combine the effects of multiple anchoring blocks and the bottlebrush architecture, leading to even greater protection efficacy than either of the aforementioned variants.

Previously, Miyamoto *et al.* and Rahman *et al.* have synthesized tetra- and pentablock copolymers using ROMP with a single mode in the molecular weight distributions and relatively small dispersities.[297,298] Furthermore, ROMP of the PEO-NB and PPO-NB macromonomers described in Chapter 3 achieves full conversion within minutes, making synthesis of a pentablock BBP with a monomodal molecular weight distribution achievable and relatively straightforward. Since the minimum degree of polymerization that can be achieved in any block synthesis is $N \sim 5$ and the macromonomers are large relative to monomers used in linear polymerizations, a pentablock BBP will necessarily have a relatively high molecular weight. This could make differentiating free and liposome bound polymer in the PFG-NMR assay challenging and lead to a lack of observable binding.[88] Importantly, the loss in binding affinity with increasing M_n of BBPs was not associated with a loss of performance in the osmotic stress assay. Additionally, by synthesizing PEO and PPO macromonomers with low molecular weights ($N_{sc} \sim 10$ for both blocks, $M_{n,\,PEO\text{-}NB} \sim 600$ and $M_{n,\,PPO\text{-}NB} \sim 700$ g/mol), one could prepare a pentablock with a molecular weight within the range of the molecules tested in Chapter 4. I propose *B*-$P_5^{10}E_{20}^{10}P_5^{10}E_{20}^{10}P_5^{10}$ as a promising starting point because it has telechelic PPO anchor blocks, an $M_n \sim 30$ kDa which is comparable to BBPs tested previously, and it is 52 wt% PEO and 26 wt% PPO.

7.2.2 PPO side chain length

The methyl group of PPO leads to fewer, and longer, hydrogen bonds with water than a PEO polymer. This makes the PPO block(s) less hydrophilic than PEO. Based on the anchor and chain hypothesis, the PPO block(s) are primarily responsible for driving binding. Furthermore, membrane-bound BBPs likely lie with their backbone tangent to the bilayer with the side chains intercalating between lipids.[88] Therefore, I hypothesize that the length of the PPO side chains ($N_{sc,\ PPO}$) will have a significant impact on binding affinity and protection efficacy.

A critical length scale to consider in designing a set of BBPs with variable $N_{sc,\ PPO}$ is the thickness of the lipid bilayer or cell membrane. This depends on the lipids used in the model membrane and on the lipid phase behavior as described in Chapter 6; however, the bilayer is roughly 50 nm in thickness, and the thickness of the acyl region is ~30−40 nm.[299] In the limit of high grafting density and short side chains ($N_{sc} < 5$), the bottlebrush will resemble a linear polymer with a higher persistence length. This regime is not very interesting, and it will be difficult to synthesize a PPO macromonomer with this small degree of polymerization. For intermediate and long $N_{sc,\ PPO}$, we can approximate the side chain dimensions by assuming that the chain will occupy a Gaussian conformation. This will underestimate the coil dimensions because near the backbone chains will extend due to steric repulsions between neighboring chains; however, for $N_{sc,\ PPO} = 17$, the distal units are assumed to be Gaussian because BBPs of this length have considerable binding affinity towards POPC liposomes, which would likely have been prevented if the side chains were extended and stiff.[88]

I hypothesize that at intermediate PPO side chain lengths ($10 < N_{sc,\ PPO} < 50$) increasing $N_{sc,\ PPO}$ will allow the polymer to insert more deeply into the bilayer, increasing membrane affinity. The effect of deeper insertion of a bottlebrush PPO block on protection efficacy is difficult to predict. It may be disruptive to lipid packing, leading to a detrimental effect, or it may reduce membrane permeability through pores or damage sites. However, as the length of the PPO block exceeds the length of the acyl region of the bilayer ($N_{sc,\ PPO} > 50$), I hypothesize that the polymer will associate too strongly and the ability of individual side chains to span the membrane will lead

to pore formation,[184] potentially leading to liposome rupture and therefore detrimental to cell health.

7.2.3 Grafting density

Grafting density (z) is inversely related to the spacing between grafts, $z \sim 1/N_g$. The proximity of neighboring side chains affects steric interactions, and therefore has implications for the persistence length, side chain conformation, entanglement molecular weight, and rheological properties.[150,192] Specifically, at low grafting densities the side chains do not affect one another much, therefore they adopt Gaussian conformations and the backbone conformation is almost unaffected. At intermediate grafting densities, loose comb and dense comb regimes exist where the conformations of the side chains and the backbone begin to extend. Finally, at high grafting densities the chain adopts an extended conformation with a significantly longer persistence length.[246,300] Scaling relationships between the grafting density and persistence length and plateau modulus have been developed for these regimes. [246,300] Experimentally, Haugen *et al.* showed that the transition between these regimes depends on the ratio of the side chain diameter to the average distance between grafts (N_g).[150]

In Chapter 4, I compared the liposome binding affinity and cell membrane protection efficacy of flexible, linear poloxamers to more rigid bottlebrush poloxamers with 100% grafting density ($N_g = 1$). By synthesizing BBPs with reduced grafting densities, one could achieve loose comb and dense comb architectures that have intermediate flexibilities to the linear and bottlebrush poloxamers tested thus far. Spacing PPO side chains further apart along the backbone will increase side chain and backbone flexibility, which could facilitate intercalation into the lipid bilayer. Lin, *et al.* demonstrated that copolymerizing a norbornene-macromonomer with a norbornene-small molecule diluent via ROMP can be used to synthesize bottlebrush polymers with controlled grafting density.[301] As with any copolymerization, the relative reaction rates of the two monomers, the reactivity ratios, dictate monomer incorporation into the growing chain. To ensure a controlled

and constant grafting density, the PEO/PPO side chains should be randomly distributed within their respective blocks, favoring macromonomer-diluent pairs with reactivity ratios close to 1.0.[163] Thus, the first step in this proposed direction would be assessing copolymerization reaction kinetics to find a norbornene-small molecule diluent partner that yields reactivity ratios close to 1.0 with all of the desired PEO/PPO macromonomers. Lin, *et al.* showed that the chemistry of the polymer appended to the norbornene and its length affects the propagation rate constant[301] and Radzinski, *et al.* showed that the anchor group of the norbornene, the functional group forming the linkage between the norbornene and the polymer chain, lead to different propagation rates with the same macromonomer chemistry and molecular weights.[302] Therefore, these are important considerations when designing the set of macromonomers. Fortunately, PPO and PEO are similar chemistries, and an identical anchor group can be used for all macromonomers, so I expect that a single small molecule norbornene diluent could be used for all desired macromonomers. The PPO/PEO macromonomers have very rapid propagation kinetics, making kinetic experiments challenging. Pyridine competes with the macromonomer for the active site of the Grubbs catalyst, hence slowing the propagation reaction.[303] Therefore, adding an excess of pyridine to the ROMP can slow the kinetics to an observable level for the purposes of assessing reactivity ratios.

A second consideration with this proposed study is the increasing exposure of the backbone to the aqueous environment and the lipid bilayer as the grafting density is decreased. The norbornene backbone is relatively hydrophobic so it will likely depress the cloud point and could lead to insolubility in water at low grafting density. In Chapter 4, I showed that a bottlebrush PEO homopolymer with 100% grafting density did not bind to the liposomes despite the hydrophobicity of the backbone.[88] This is because the densely grafted PEO side chains prevent the backbone from contacting the acyl region of the bilayer; however, this may not be the case as the side chains are spaced further apart.

7.3 Effect of diblock architecture on thermal trapping effect

In Chapter 5, I reported the effect of thermal history on the fraction of poloxamer chains bound to liposomes and proposed a mechanism behind this effect. At elevated temperatures, the PEO blocks are more dehydrated and therefore the free energy associated with traversing the bilayer is reduced, enabling chains to enter the intraliposomal space. Then, when the system is returned to 25 °C the PEO blocks are re-hydrated, presenting a high kinetic barrier for chain expulsion. Figure 7.2a shows a schematic of this proposed molecular mechanism for a triblock poloxamer being expelled from the intraliposomal space. Notably, there are two high energy intermediates: one for each of the hydrated PEO blocks being pulled through the bilayer. Additionally, when a triblock is in the transmembrane state, it is equally likely to enter the hairpin state on the exterior (towards expulsion) or interior (towards intraliposomal) leaflet. On the other hand, because a diblock only has one PEO block, it cannot occupy the transmembrane conformation, eliminating one of the high free energy intermediates and minimizing the likelihood of the chain returning to the intraliposomal space after it passes the single maximum in free energy (Figure 7.2b). Therefore, I hypothesize that liposomes incubated with a diblock PEO-PPO polymer at elevated temperatures will have a substantially greater recovery rate at 25 °C, k_{rec}, than liposomes incubated with a comparable triblock.

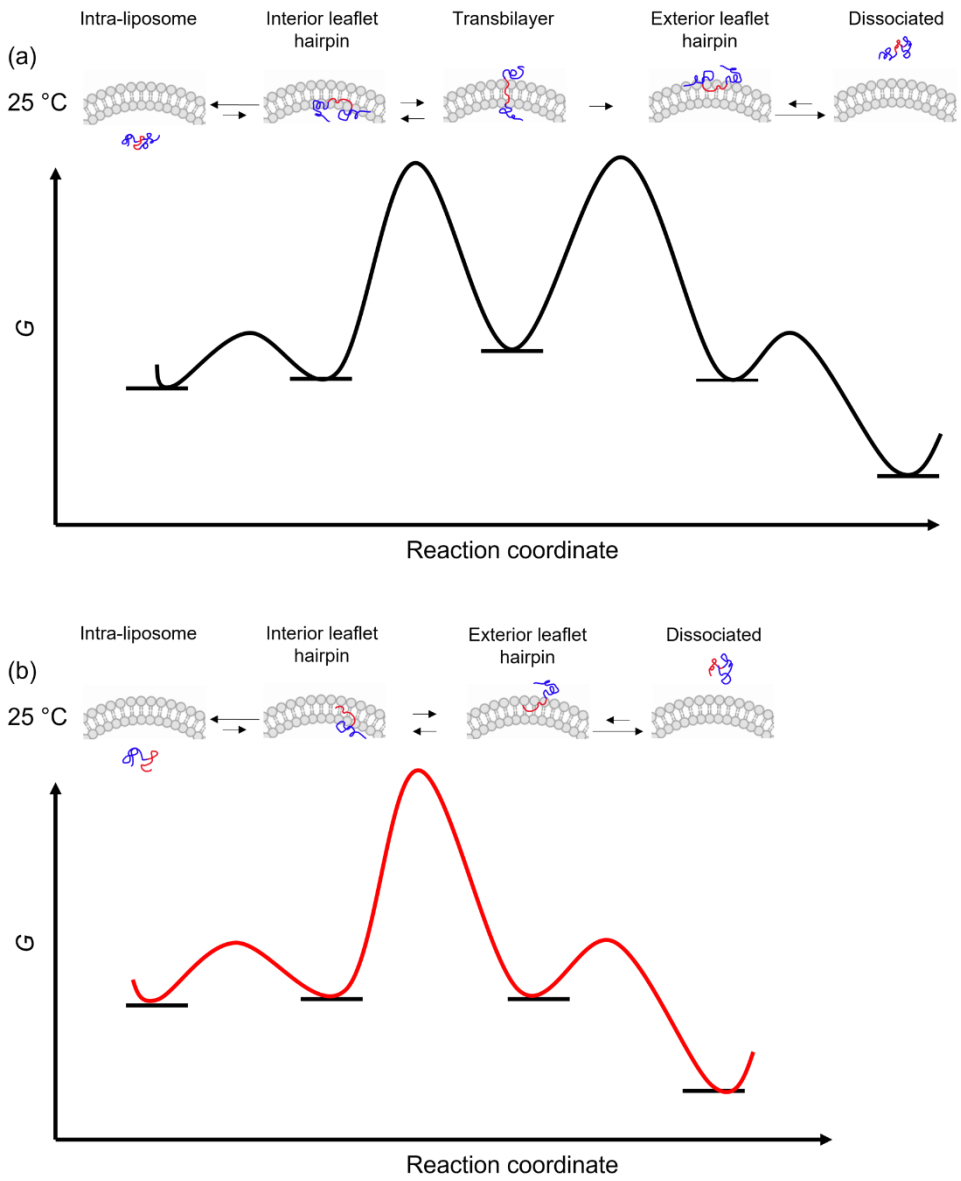

Figure 7.2: Comparison of the hypothesized mechanism of escape from the intraliposomal space of (a) a triblock poloxamer and (b) a diblock PEO-PPO polymer.

The choice of PEO-PPO diblock is very important to the success of this study. One must choose a diblock that has a substantial amount of binding to the model liposome with just a 25 °C incubation. Furthermore, it should be analogous to F127 for comparison to the dataset in Chapter 5. Hence, I propose $t\mathrm{P}_{54}\mathrm{E}_{186}$, where *t* indicates a tert-butyl endgroup on the PPO block. This molecule has an identical molecular weight, composition, and number of each repeat unit as F127

(M_n = 11.3 kDa, 70 wt% PEO). This molecule could be synthesized via anionic polymerization with potassium tert-butoxide as the initiator in the presence of 18-crown-6 as previously reported.[6,109,132] Based on established relationships between M_n and PPO content on binding affinity, I expect this diblock will have substantial binding with a 25 °C incubation,[85] enabling an identical thermal incubation kinetic recovery experiment as detailed in Chapter 5.

7.4 Effect of polymer on lipid phase behavior under osmotic stress

When vesicles, or cells, are placed in a hypotonic environment, they swell due to the difference in osmotic pressure across the lipid bilayer. This increases the membrane tension, which can lead to pore formation if the areal strain exceeds a critical value.[304,305] Once the pore forms, solute and solvent leak out via convective transport, shrinking the vesicle and reducing the osmotic gradient across the membrane. As the membrane tension is relaxed as the vesicle shrinks, the pore closes, typically well before the osmotic pressure gradient is fully dissipated. Then the vesicle begins to swell again, restarting the swelling/pore formation/shrinking cycle. These cycles have been observed with periods between 50−500 s that increase in duration with cycle number as the osmotic gradient is reduced, ultimately eliminating the osmotic pressure gradient across the membrane on the time scale of 10−60 min.[306]

As described in Chapter 6.1, surface tension influences the coexistence of L_d and L_o domains and domain size, therefore the swell/pore formation/burst cycles also impact lipid phase behavior. Oglęcka, *et al.* used time-lapse fluorescence microscopy with a phase-sensitive fluorophore to image lipid phase coexistence in 33.3/33.3/33.3 POPC/PSM/Chol vesicles in isotonic and hypotonic environments. At 25 °C under isotonic conditions the dye partitions uniformly into the vesicles, indicating a homogeneous L_d phase. This is consistent with the phase diagram shown in Figure 6.1, as this composition is in the L_d region very near the L_o-L_d coexistence window.[48] When the vesicles were placed in a hypotonic bath, the phase behavior oscillates between a well-mixed, L_d phase and L_d−L_o coexistence, coinciding with the swelling/pore formation/shrinking cycles as

shown by Figure 7.3.[286] Since poloxamers reduce the stretching modulus of lipid bilayers,[94] I hypothesize that poloxamer presence will increase the critical strain at which pore formation occurs. Therefore, the swell-pore-shrink cycles and cycles of phase separation will have a longer period in the presence of F127 or other poloxamers with a documented protective effect. This could explain why poloxamers limit diffusion of enzymes across the cell membrane of cells exposed to a hypotonic shock and serve as a non-specific mechanism by which polymers could affect cell signaling.

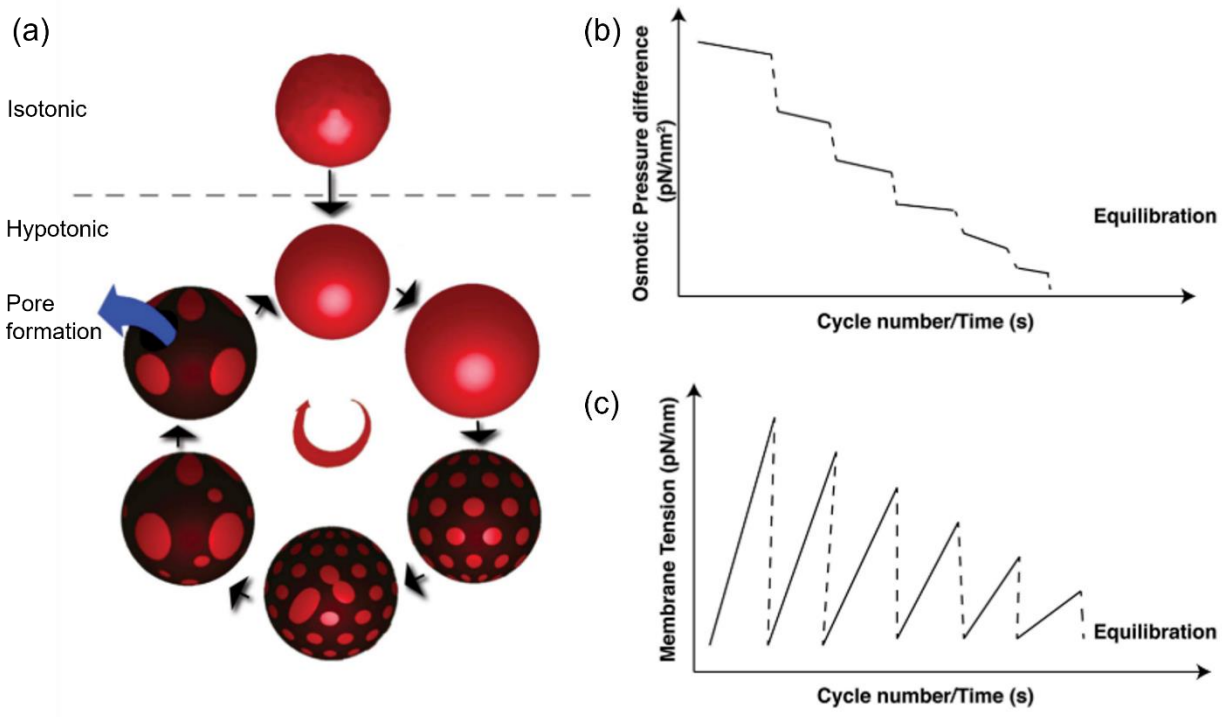

Figure 7.3: (a) Schematic of the cyclic phase behavior associated with swell-burst cycles in vesicles placed in a hypotonic environment. (b) Decay of osmotic pressure gradient due to pore formation in swell-burst cycles. (c) Membrane tension associated with the swell-burst cycles. Figure adapted from Oglęcka *et al. eLife.* 2014.[286]

Preliminary work has been performed to image co-existing L_d/L_o domains using confocal and fluorescence microscopy with two phase selective dyes: 18:1 lissamine rhodamine

phosphoethanolamine for the L_d phase (λ_{ex}/ λ_{em} = 560/583 nm) and 16:0 nitro-benzoxadiazol phosphoethanolamine for the L_o phase (λ_{ex}/ λ_{em} = 460/535 nm). Preparing the vesicles via extrusion or electroformation in a 100 mM sucrose solution then dropping them into either a 100 mM glucose solution (isotonic) or distilled water (hypotonic) will cause the vesicles to sink, enabling imaging via microscopy.[94] Once a reliable method to observe lipid phase coexistence is established, the same experimental methodology could be applied to observe the lipid phase behavior and vesicle radius as a function of time after imposing the osmotic stress. The periods of the swell-burst and phase separation, and domain size and shape could then be quantified and compared across various poloxamer treatments and concentrations.

References

(1) Maxfield, F. R.; Tabas, I. Role of Cholesterol and Lipid Organization in Disease. *Nature* **2005**, *438*, 612–621.

(2) Niemela, P.S.; Ollila, S.; Hyvonen, M.T.; Karttunen, M.; Vattulainen, I. Assessing the Nature of Lipid Raft Membranes. *PloS Comput. Biol.* **2007**, *3* (2).

(3) Sengupta, P.; Baird, B.; Holowka, D. Lipid Rafts, Fluid/Fluid Phase Separation, and Their Relevance to Plasma Membrane Structure and Function. *Semin. Cell Dev. Biol.* **2007**, *18* (5), 583–590.

(4) De La Haba, C.; Palacio, J. R.; Martínez, P.; Morros, A. Effect of Oxidative Stress on Plasma Membrane Fluidity of THP-1 Induced Macrophages. *Biochim. Biophys. Acta - Biomembr.* **2013**, *1828* (2), 357–364.

(5) Mcneil, P. L.; Steinhardt, R. A. PLASMA MEMBRANE DISRUPTION : Repair, Prevention, Adaptation. **2003**, 697–731.

(6) Kim, M.; Haman, K. J.; Houang, E. M.; Zhang, W.; Yannopoulos, D.; Metzger, J. M.; Bates, F. S.; Hackel, B. J. PEO-PPO Diblock Copolymers Protect Myoblasts from Hypo-Osmotic Stress in Vitro Dependent on Copolymer Size, Composition, and Architecture. *Biomacromolecules* **2017**, *18* (7), 2090–2101.

(7) Yasuda, S.; Townsend, D. W.; Michele, D. E.; Favre, E. G.; Day, S. M.; Metzger, J. M. Dystrophic Heart Failure Blocked by Membrane Sealant Poloxamer. *Nature* **2005**, *436* (7053), 1025–1029.

(8) Tsao, C. W.; Aday, A. W.; Almarzooq, Z. I.; Alonso, A.; Beaton, A. Z.; Bittencourt, M. S.; Boehme, A. K.; Buxton, A. E.; Carson, A. P.; Commodore-Mensah, Y.; Elkind, M. S. V.; Evenson, K. R.; Eze-Nliam, C.; Ferguson, J. F.; Generoso, G.; Ho, J. E.; Kalani, R.; Khan, S. S.; Kissela, B. M.; Knutson, K. L.; Levine, D. A.; Lewis, T. T.; Liu, J.; Loop, M. S.; Ma, J.; Mussolino, M. E.; Navaneethan, S. D.; Perak, A. M.; Poudel, R.; Rezk-Hanna, M.; Roth, G. A.; Schroeder, E. B.; Shah, S. H.; Thacker, E. L.; Vanwagner, L. B.; Virani, S. S.; Voecks, J. H.; Wang, N. Y.; Yaffe, K.; Martin, S. S. *Heart Disease and Stroke Statistics-2022 Update: A Report from the American Heart Association*; 2022; Vol. 145.

(9) Lee, R. C.; River, L. P.; Pan, F. S.; Ji, L.; Wollmann, R. L. Surfactant-Induced Sealing of Electropermeabilized Skeletal Muscle Membranes in Vivo. *Proc. Natl. Acad. Sci. U. S. A.* **1992**, *89* (10), 4524–4528.

(10) Kalappurakkal, J. M.; Sil, P.; Mayor, S. Toward a New Picture of the Living Plasma Membrane. *Protein Sci.* **2020**, *29* (6), 1355–1365.

(11) Benabdellah, F.; Yu, H.; Brunelle, A.; Laprévote, O.; De La Porte, S. MALDI Reveals Membrane Lipid Profile Reversion in MDX Mice. *Neurobiol. Dis.* **2009**, *36* (2), 252–258.

(12) Maskarinec, S. A.; Wu, G.; Lee, K. Y. C. Membrane Sealing by Polymers. *Ann. N. Y. Acad. Sci.* **2005**, *1066*, 310–320.

(13) Houang, E. M.; Sham, Y. Y.; Bates, F. S.; Metzger, J. M. Muscle Membrane Integrity in Duchenne Muscular Dystrophy: Recent Advances in Copolymer-Based Muscle

Membrane Stabilizers. *Skelet. Muscle* **2018**, *8* (1), 1–19.

(14) Marsh, D. Thermodynamics of Phospholipid Self-Assembly. *Biophys. J.* **2012**, *102* (5), 1079–1087.

(15) Woodka, A. C.; Butler, P. D.; Porcar, L.; Farago, B.; Nagao, M. Lipid Bilayers and Membrane Dynamics: Insight into Thickness Fluctuations. *Phys. Rev. Lett.* **2012**, *109* (5), 1–5.

(16) Narayanan, T.; Weerakkody, D.; Karabadzhak, A. G.; Anderson, M.; Andreev, O. A.; Reshetnyak, Y. K. PHLIP Peptide Interaction with a Membrane Monitored by SAXS. *J. Phys. Chem. B* **2016**, *120* (44), 11484–11491.

(17) Kim, M.; Heinrich, F.; Haugstad, G.; Yu, G.; Yuan, G.; Satija, S. K.; Zhang, W.; Seo, H. S.; Metzger, J. M.; Azarin, S. M.; Lodge, T. P.; Hackel, B. J.; Bates, F. S. Spatial Distribution of PEO − PPO − PEO Block Copolymer and PEO Homopolymer in Lipid Bilayers. *Langmuir* **2020**, *36* (13), 3393–3403.

(18) Filippov, A.; Orädd, G.; Lindblom, G. The Effect of Cholesterol on the Lateral Diffusion of Phospholipids in Oriented Bilayers. *Biophys. J.* **2003**, *84* (5), 3079–3086.

(19) Gaede, H. C.; Gawrisch, K. Lateral Diffusion Rates of Lipid, Water, and a Hydrophobic Drug in a Multilamellar Liposome. *Biophys. J.* **2003**, *85* (3), 1734–1740.

(20) Hinton, D.P. and Johnson, C. S. Diffusion Ordered 2D NMR Spectroscopy of Phospholipid Vesicles: Determination of Vesicle Size Distributions. *J. Phys. Chem.* **1993**, *97*, 9064–9072.

(21) Gurtovenko, A. A.; Vattulainen, I. Molecular Mechanism for Lipid Flip-Flops. *J. Phys. Chem. B* **2007**, *111* (48), 13554–13559.

(22) Allhusen, J. S.; Conboy, J. C. The Ins and Outs of Lipid Flip-Flop. *Acc. Chem. Res.* **2017**, *50* (1), 58–65.

(23) Nagle, J. F. Theory of Lipid Monolayer and Bilayer Phase Transitions " Effect of Headgroup Interactions Experimental Results for MonoIayers. **1976**, *250*.

(24) Rawicz, W.; Olbrich, K. C.; McIntosh, T.; Needham, D.; Evans, E. A. Effect of Chain Length and Unsaturation on Elasticity of Lipid Bilayers. *Biophys. J.* **2000**, *79* (1), 328–339.

(25) Clarke, T. S. Æ. R. J. Effect of Headgroup on the Dipole Potential of Phospholipid Vesicles. **2009**, 103–110.

(26) Rand, R. P.; Pars, V. A. Hydration Forces between Phospholipid Bilayers. **1989**, *988* (19159).

(27) Yeagle, P. L.; Hutton, W. C.; Huang, C.; Martin, R. B. Phospholipid Head-Group Conformations ; Intermolecular Interactions. **1976**, No. 20.

(28) Valentine, M. L.; Waterland, M. K.; Fathizadeh, A.; Elber, R.; Baiz, C. R. Interfacial Dynamics in Lipid Membranes: The E Ff Ects of Headgroup Structures. **2021**.

(29) Lee, A. G. How Lipids Affect the Activities of Integral Membrane Proteins. **2004**, *1666*, 62–87.

(30) Takasaki, S.; Yamashita, K.; Kobata, A. The Sugar Chain Structures of ABO Blood Group Obtained from Human Erythrocyte Membrane * Active Glycoproteins. *J. Biol. Chem.* **1978**, *253* (17), 6086–6091.

(31) Allender, D. W.; Sodt, A. J.; Schick, M. Cholesterol-Dependent Bending Energy Is Important in Cholesterol Distribution of the Plasma Membrane. *Biophysj* **2019**, *116* (12), 2356–2366.

(32) Anthony, A. A.; Sahin, O.; Yapici, M. K.; Rogers, D.; Honerkamp-Smith, A. R. Systematic Measurements of Interleaflet Friction in Supported Bilayers. *Biophys. J.* **2022**, *121* (15), 2981–2993.

(33) Risselada, H. J. New and Notable Cholesterol : The Plasma Membrane ' s Constituent That Chooses Sides. *Biophysj* **2019**, *116* (12), 2235–2236.

(34) Sarangi, N. K.; Ilanila, P. I.; Ayappa, K. G.; Visweswariah, S. S.; Basu, J. K. Super-Resolution Stimulated Emission Depletion-Fluorescence Correlation Spectroscopy Reveals Nanoscale Membrane Reorganization Induced by Pore-Forming Proteins. *Langmuir* **2016**, *32* (37), 9649–9657.

(35) Arriaga, L. R.; López-Montero, I.; Monroy, F.; Orts-Gil, G.; Farago, B.; Hellweg, T. Stiffening Effect of Cholesterol on Disordered Lipid Phases: A Combined Neutron Spin Echo + Dynamic Light Scattering Analysis of the Bending Elasticity of Large Unilamellar Vesicles. *Biophys. J.* **2009**, *96* (9), 3629–3637.

(36) Chakraborty, S.; Doktorova, M.; Molugu, T. R.; Heberle, F. A.; Scott, H. L. How Cholesterol Stiffens Unsaturated Lipid Membranes. **2020**, *117* (36).

(37) Andrews, N. W.; Almeida, P. E.; Corrotte, M. Damage Control: Cellular Mechanisms of Plasma Membrane Repair. *Trends Cell Biol.* **2014**, *24* (12), 734–742.

(38) Woldring, D. R.; Holec, P. V.; Stern, L. A.; Du, Y.; Hackel, B. J. A Gradient of Sitewise Diversity Promotes Evolutionary Fitness for Binder Discovery in a Three-Helix Bundle Protein Scaffold. *Biochemistry* **2017**, *56* (11), 1656–1671.

(39) Anglin, T. C.; Liu, J.; Conboy, J. C. Facile Lipid Flip-Flop in a Phospholipid Bilayer Induced by Gramicidin A Measured by Sum-Frequency Vibrational Spectroscopy. *Biophys. J.* **2007**, *92* (1), L01–L03.

(40) Van Der Paal, J.; Neyts, E. C.; Verlackt, C. C. W.; Bogaerts, A. Effect of Lipid Peroxidation on Membrane Permeability of Cancer and Normal Cells Subjected to Oxidative Stress. *Chem. Sci.* **2016**, *7* (1), 489–498.

(41) Lindblom, G.; Orädd, G. Lipid Lateral Diffusion and Membrane Heterogeneity. *Biochim. Biophys. Acta - Biomembr.* **2009**, *1788* (1), 234–244.

(42) Needham, D.; Nunn, R. S. Elastic Deformation and Failure of Lipid Bilayer Membranes Containing Cholesterol. *Biophys. J.* **1990**, *58* (4), 997–1009.

(43) Lingwood, D.; Ries, J.; Schwille, P.; Simons, K. Plasma Membranes Are Poised for Activation of Raft Phase Coalescence at Physiological Temperature. *Proc. Natl. Acad. Sci. U. S. A.* **2008**, *105* (29), 10005–10010.

(44) Sezgin, E.; Levental, I.; Mayor, S.; Eggeling, C. The Mystery of Membrane Organization: Composition, Regulation and Roles of Lipid Rafts. *Nat. Rev. Mol. Cell Biol.* **2017**, *18* (6), 361–374.

(45) Veatch, S. L.; Keller, S. L. Organization in Lipid Membranes Containing Cholesterol. *Phys. Rev. Lett.* **2002**, *89* (26), 1–4.

(46) Veatch, S. L.; Keller, S. L. Separation of Liquid Phases in Giant Vesicles of Ternary Mixtures of Phospholipids and Cholesterol. *Biophys. J.* **2003**, *85* (5), 3074–3083.

(47) Veatch, S. L.; Keller, S. L. Miscibility Phase Diagrams of Giant Vesicles Containing Sphingomyelin. *Phys. Rev. Lett.* **2005**, *94* (14), 3–6.

(48) Veatch, S. L.; Keller, S. L. Seeing Spots: Complex Phase Behavior in Simple Membranes. *Biochim. Biophys. Acta - Mol. Cell Res.* **2005**, *1746* (3), 172–185.

(49) Gaus, K.; Gratton, E.; Kable, E. P. W.; Jones, A. S.; Gelissen, I.; Kritharides, L.; Jessup, W. Visualizing Lipid Structure and Raft Domains in Living Cells with Two-Photon Microscopy. *Proc. Natl. Acad. Sci. U. S. A.* **2003**, *100* (26), 15554–15559.

(50) K, S.; E., I. Functional Rafts in Cell Membranes. *Nature* **1997**, *387* (6633), 569–572.

(51) Dutta, D.; Donaldson, J. G. Intended Specificity and Unintended Consequences. *Cell. Logist.* **2012**, *2* (4), 203–208.

(52) Goñi, F. M. "Rafts": A Nickname for Putative Transient Nanodomains. *Chem. Phys. Lipids* **2019**, *218* (October 2018), 34–39.

(53) Levental, Ilya; Veatch, S. The Continuing Mystery of Lipid Rafts. *J Mol Bio* **2016**, *428* (10), 4749–4764.

(54) Bagatolli, L. A. To See or Not to See: Lateral Organization of Biological Membranes and Fluorescence Microscopy. *Biochim. Biophys. Acta - Biomembr.* **2006**, *1758* (10), 1541–1556.

(55) Baumgart, T.; Hunt, G.; Farkas, E. R.; Webb, W. W.; Feigenson, G. W. Fluorescence Probe Partitioning between Lo/Ld Phases in Lipid Membranes. *Biochim. Biophys. Acta - Biomembr.* **2007**, *1768* (9), 2182–2194.

(56) Klymchenko, A. S.; Kreder, R. Fluorescent Probes for Lipid Rafts: From Model Membranes to Living Cells. *Chem. Biol.* **2014**, *21* (1), 97–113.

(57) Sanchez, S. A.; Tricerri, M. A.; Gratton, E. Laurdan Generalized Polarization Fluctuations Measures Membrane Packing Micro-Heterogeneity in Vivo. *Proc. Natl. Acad. Sci. U. S. A.* **2012**, *109* (19), 7314–7319.

(58) Pinto, S. N.; Fernandes, F.; Fedorov, A.; Futerman, A. H.; Silva, L. C.; Prieto, M. A Combined Fluorescence Spectroscopy, Confocal and 2-Photon Microscopy Approach to Re-Evaluate the Properties of Sphingolipid Domains. *Biochim. Biophys. Acta - Biomembr.*

2013, *1828* (9), 2099–2110.

(59) Kim, H. M.; Cho, B. R. Two-Photon Probes for Intracellular Free Metal Ions, Acidic Vesicles, and Lipid Rafts in Live Tissues. *Acc. Chem. Res.* **2009**, *42* (7), 863–872.

(60) Meder, D.; Moreno, M. J.; Verkade, P.; Vaz, W. L. C.; Simons, K. Phase Coexistence and Connectivity in the Apical Membrane of Polarized Epithelial Cells. *Proc. Natl. Acad. Sci. U. S. A.* **2006**, *103* (2), 329–334.

(61) Ratto, T. V.; Longo, M. L. Obstructed Diffusion in Phase-Separated Supported Lipid Bilayers: A Combined Atomic Force Microscopy and Fluorescence Recovery after Photobleaching Approach. *Biophys. J.* **2002**, *83* (6), 3380–3392.

(62) Singer, S. J.; Nicolson, G. L. The Fluid Mosaic Model of the Structure of Cell Membranes. *Science (80-.).* **1972**, *175*, 720–731.

(63) Kusumi, A.; Fujiwara, T. K.; Chadda, R.; Xie, M.; Tsunoyama, T. A.; Kalay, Z.; Kasai, R. S.; Suzuki, K. G. N. Dynamic Organizing Principles of the Plasma Membrane That Regulate Signal Transduction : Commemorating the Fortieth Anniversary of Singer and Nicolson's Fluid-Mosaic Model. *Annu. Rev. Cell Dev. Biol.* **2012**, *28*, 215–250.

(64) Kusumi, A.; Suzuki, K. G. N.; Kasai, R. S.; Ritchie, K.; Fujiwara, T. K.; Bragg, L. Hierarchical Mesoscale Domain Organization of the Plasma Membrane. *Trends Biochem. Sci.* **2011**, *36* (11), 604–615.

(65) Wu, G.; Majewski, J.; Ege, C.; Kjaer, K.; Weygand, M. J.; Lee, K. Y. C. Interaction between Lipid Monolayers and Poloxamer 188: An X-Ray Reflectivity and Diffraction Study. *Biophys. J.* **2005**, *89* (5), 3159–3173.

(66) Wu, G.; Majewski, J.; Ege, C.; Kjaer, K.; Weygand, M. J.; Lee, K. Y. C. Lipid Corralling and Poloxamer Squeeze-out in Membranes. *Phys. Rev. Lett.* **2004**, *93* (2), 2–5.

(67) Eeman, M.; Deleu, M. From Biological Membranes to Biomimetic Model Membranes. *Biotechnol. Agron. Soc. Environ.* **2010**, *14* (4), 719–736.

(68) Brockman, H. Lipid Monolayers: Why Use Half a Membrane to Characterize Protein-Membrane Interactions? *Curr. Opin. Struct. Biol.* **1999**, *9* (4), 438–443.

(69) Wang, J.-Y.; Chen, W.; Nagao, M.; Shelat, P.; Hammer, B. A. G.; Tietjen, G. T.; Cao, K. D.; Henderson, J. M.; He, L.; Lin, B.; Akgun, B.; Meron, M.; Qian, S.; Ward, S.; Marks, J. D.; Emrick, T.; Lee, K. Y. C. Tailoring Biomimetic Phosphorylcholine-Containing Block Copolymers as Membrane-Targeting Cellular Rescue Agents. *Biomacromolecules* **2019**, *20* (9), 3385–3391.

(70) Frey, S. L.; Zhang, D.; Carignano, M. A.; Szleifer, I.; Lee, K. Y. C. Effects of Block Copolymer's Architecture on Its Association with Lipid Membranes: Experiments and Simulations. *J. Chem. Phys.* **2007**, *127* (11).

(71) Maskarinec, S. A.; Hannig, J.; Lee, R. C.; Lee, K. Y. C. Direct Observation of Poloxamer 188 Insertion into Lipid Monolayers. *Biophys. J.* **2002**, *82* (3), 1453–1459.

(72) Barletti, B.; Lucchesi, G.; Muscat, S.; Errico, S.; Barbut, D.; Danani, A.; Zasloff, M.;

Grasso, G.; Chiti, F.; Caminati, G. Reorganization of the Outer Layer of a Model of the Plasma Membrane Induced by a Neuroprotective Aminosterol. *Colloids Surfaces B Biointerfaces* **2023**, *222* (October 2022), 113115.

(73) Kim, M.; Vala, M.; Ertsgaard, C. T.; Oh, S.-H.; Lodge, T. P.; Bates, F. S.; Hackel, B. J. Surface Plasmon Resonance Study of the Binding of PEO–PPO–PEO Triblock Copolymer and PEO Homopolymer to Supported Lipid Bilayers. *Langmuir* **2018**, *34* (23), 6703–6712.

(74) Hardy, G.J.; Nayak, R.; Zauscher, S. Model Cell Membranes: Techniques to Form Complex Biomimetic Supported Lipid Bilayers via Vesicle Fusion. *Curr. Opin. Colloid Interface Sci.* **2013**, *18* (1), 448–458.

(75) Kakimoto, Y.; Tachihara, Y.; Okamoto, Y.; Miyazawa, K.; Fukuma, T.; Tero, R. Morphology and Physical Properties of Hydrophilic-Polymer-Modified Lipids in Supported Lipid Bilayers. *Langmuir* **2018**, *34* (24), 7201–7209.

(76) Brown, J. S.; Mohamed, Z. J.; Artim, C. M.; Thornlow, D. N.; Hassler, J. F.; Rigoglioso, V. P.; Daniel, S.; Alabi, C. A. Antibacterial Isoamphipathic Oligomers Highlight the Importance of Multimeric Lipid Aggregation for Antibacterial Potency. *Commun. Biol.* **2018**, *1* (1).

(77) Henriques, S. T.; Peacock, H.; Benfield, A.; Wang, C. K.; Craik, D. J.; Henriques, S. T.; Peacock, H.; Benfield, A. H.; Wang, C. K.; David, J. Is the Mirror Image a True Reflection ? Intrinsic Membrane Chirality Modulates Peptide Binding Is the Mirror Image a True Reflection ? Intrinsic Membrane Chirality Modulates Peptide Binding. *J Am Chem Soc* **2019**.

(78) Grage, S. L.; Sani, M. A.; Cheneval, O.; Henriques, S. T.; Schalck, C.; Heinzmann, R.; Mylne, J. S.; Mykhailiuk, P. K.; Afonin, S.; Komarov, I. V.; Separovic, F.; Craik, D. J.; Ulrich, A. S. Orientation and Location of the Cyclotide Kalata B1 in Lipid Bilayers Revealed by Solid-State NMR. *Biophys. J.* **2017**, *112* (4), 630–642.

(79) Mallikarjunaiah, K. J.; Leftin, A.; Kinnun, J. J.; Justice, M. J.; Rogozea, A. L.; Petrache, H. I.; Brown, M. F. Solid-State 2H NMR Shows Equivalence of Dehydration and Osmotic Pressures in Lipid Membrane Deformation. *Biophys. J.* **2011**, *100* (1), 98–107.

(80) Wang, J.; Segatori, L.; Biswal, S. L. Probing the Association of Triblock Copolymers with Supported Lipid Membranes Using Microcantilevers. *Soft Matter* **2014**, *10* (34), 6417–6424.

(81) Wang, J.; Marks, J.; Lee, K. Y. C. Nature of Interactions between PEO-PPO-PEO Triblock Copolymers and Lipid Membranes: (I) Effect of Polymer Hydrophobicity on Its Ability to Protect Liposomes from Peroxidation. *Biomacromolecules* **2012**, *13*, 2616–2623.

(82) Zhang, W. Interactions of Ethylene Oxide-Propylene Oxide Block Copolymers with Lipid Bilayers. *Univ. Minnesota* **2019**.

(83) Cheng, C.; Wang, J.; Kausik, R.; Lee, K. Y. C.; Han, S. Nature of Interactions between PEO-PPO-PEO Triblock Copolymers and Lipid Membranes: (II) Role of Hydration

Dynamics Revealed by Dynamic Nuclear Polarization. *Biomacromolecules* **2012**, *13*, 2624–2633.

(84) Kang, J. Y.; Choi, I.; Seo, M.; Lee, J. Y.; Hong, S.; Gong, G.; Shin, S. S.; Lee, Y.; Kim, J. W. Enhancing Membrane Modulus of Giant Unilamellar Lipid Vesicles by Lateral Co-Assembly of Amphiphilic Triblock Copolymers. *J. Colloid Interface Sci.* **2020**, *561*, 318–326.

(85) Zhang, W.; Haman, K. J.; Metzger, J. M.; Hackel, B. J.; Bates, F. S.; Lodge, T. P. Quantifying Binding of Ethylene Oxide-Propylene Oxide Block Copolymers with Lipid Bilayers. *Langmuir* **2017**, *33* (44), 12624–12634.

(86) Zhang, W.; Coughlin, M. L.; Metzger, J. M.; Hackel, B. J.; Bates, F. S.; Lodge, T. P. Influence of Cholesterol and Bilayer Curvature on the Interaction of PPO–PEO Block Copolymers with Liposomes. *Langmuir* **2019**, *35* (22), 7231–7241.

(87) Van Zee, N. J.; Peroutka, A. S.; Crabtree, A.; Hillmyer, M. A.; Lodge, T. P. Lipid Membrane Binding and Cell Protection Efficacy of Poly(1,2-Butylene Oxide)-b-Poly(Ethylene Oxide) Copolymers. *Biomacromolecules* **2022**, *23* (3), 1433–1442.

(88) Hassler, J. F.; Crabtree, A.; Liberman, L.; Bates, F. S.; Hackel, B. J.; Lodge, T. P. Effect of Bottlebrush Poloxamer Architecture on Binding to Liposomes. *Biomacromolecules* **2023**, *24* (1), 449–461.

(89) Wu, G.; Khant, H. A.; Chiu, W.; Lee, K. Y. C. Effects of Bilayer Phases on Phospholipid-Poloxamer Interactions. *Soft Matter* **2009**, *5* (7), 1496–1503.

(90) Zou, Y.; Pan, R.; Ruan, Q.; Wan, Z.; Guo, J.; Yang, X. Interaction of Soybean 7S Globulin Peptide with Cell Membrane Model via Isothermal Titration Calorimetry, Quartz Crystal Microbalance with Dissipation, and Langmuir Monolayer Study. *J. Agric. Food Chem.* **2018**, *66* (19), 4913–4922.

(91) Drabik, D.; Przybyło, M.; Chodaczek, G.; Iglič, A.; Langner, M. The Modified Fluorescence Based Vesicle Fluctuation Spectroscopy Technique for Determination of Lipid Bilayer Bending Properties. *Biochim. Biophys. Acta - Biomembr.* **2016**, *1858* (2), 244–252.

(92) Arriaga, L. R.; Rodríguez-García, R.; López-Montero, I.; Farago, B.; Hellweg, T.; Monroy, F. Dissipative Curvature Fluctuations in Bilayer Vesicles: Coexistence of Pure-Bending and Hybrid Curvature-Compression Modes. *Eur. Phys. J. E* **2010**, *31* (1), 105–113.

(93) Lu, L.; Doak, W. J.; Schertzer, J. W.; Chiarot, P. R. Membrane Mechanical Properties of Synthetic Asymmetric Phospholipid Vesicles. *Soft Matter* **2016**, *12* (36), 7521–7528.

(94) Van Zee, N. J. Pharmaceutically Relevant Amphiphilic Copolymers and Their Applications : Crystal Inhibition and Membrane Stabilization. *Univ. Minnesota* **2022**.

(95) Israelachvili, J. The Different Faces of Poly(Ethylene Glycol). *Proc. Natl. Acad. Sci. U. S. A.* **1997**, *94* (16), 8378–8379.

(96) Hezaveh, S.; Samanta, S.; Milano, G.; Roccatano, D. Molecular Dynamics Simulation

Study of Solvent Effects on Conformation and Dynamics of Polyethylene Oxide and Polypropylene Oxide Chains in Water and in Common Organic Solvents. *J. Chem. Phys.* **2012**, *136* (12).

(97) Alexandridis, P.; Holzwarth, J. F.; Hatton, T. A. Micellization of Poly(Ethylene Oxide)-Poly(Propylene Oxide)-Poly(Ethylene Oxide) Triblock Copolymers in Aqueous Solutions: Thermodynamics of Copolymer Association. *Macromolecules* **1994**, *27* (9), 2414–2425.

(98) McLain, V. C. Safety Assessment of Poloxamers 101, 105, 108, 122, 123, 124, 181, 182, 183, 184, 185, 188, 212, 215, 217, 231, 234, 235, 237, 238, 282, 284, 288, 331, 333, 334, 335, 338, 401, 402, 403, and 407, Poloxamer 105 Benzoate, and Poloxamer 182 Dibenzoate as Use. *Int. J. Toxicol.* **2008**, *27* (SUPPL. 2), 93–128.

(99) Florin, E.; Kjellander, R.; Eriksson, J. C. Salt Effects on the Cloud Point of the Poly(Ethylene Oxide) + Water System. *J. Chem. Soc. Faraday Trans. 1 Phys. Chem. Condens. Phases* **1984**, *80* (11), 2889–2910.

(100) Alexandridis, P.; Hatton, T. A. Block Copolymer Surfactants in Aqueous Solutions and at Interface: Thermodynamics, Structure, Dynamics and Modeling. *Colloids Surfaces A Physicochem. Eng. Asp.* **1995**, *96*, 1–46.

(101) White, J. M.; Calabrese, M. A. Impact of Small Molecule and Reverse Poloxamer Addition on the Micellization and Gelation Mechanisms of Poloxamer Hydrogels. *Colloids Surfaces A Physicochem. Eng. Asp.* **2022**, *638* (December 2021), 128246.

(102) Nagarajan, R.; Ganesh, K. Block Copolymer Self-Assembly in Selective Solvents: Spherical Micelles with Segregated Cores. *J. Chem. Phys.* **1989**, *90* (10), 5843–5856.

(103) Noolandi, J.; Hong, K. M. Theory of Block Copolymer Micelles in Solution. *Macromolecules* **1983**, *16* (9), 1443–1448.

(104) Lodge, T. P.; Seitzinger, C. L.; Seeger, S. C.; Yang, S.; Gupta, S.; Dorfman, K. D. Dynamics and Equilibration Mechanisms in Block Copolymer Particles. *ACS Polym. Au* **2022**, *2* (6), 397–416.

(105) Denkova, A. G.; Mendes, E.; Coppens, M. O. Non-Equilibrium Dynamics of Block Copolymer Micelles in Solution: Recent Insights and Open Questions. *Soft Matter* **2010**, *6* (11), 2351–2357.

(106) Malmsten, M; Lindman, B. Self-Assembly in Aqueous Block Copolymer Solutions. *Macromolecules* **1992**, *25*, 5440–5445.

(107) Rikiyama, K.; Horiuchi, T.; Koga, N.; Sanada, Y.; Watanabe, K.; Aida, M.; Katsumoto, Y. Micellization of Poly(Ethylene Oxide)-Poly(Propylene Oxide) Alternating Multiblock Copolymers in Water. *Polymer (Guildf).* **2018**, *156* (September), 102–110.

(108) Alaboalirat, M.; Qi, L.; Arrington, K. J.; Qian, S.; Keum, J. K.; Mei, H.; Littrell, K. C.; Sumpter, B. G.; Carrillo, J. M. Y.; Verduzco, R.; Matson, J. B. Amphiphilic Bottlebrush Block Copolymers: Analysis of Aqueous Self-Assembly by Small-Angle Neutron Scattering and Surface Tension Measurements. *Macromolecules* **2019**, *52* (2), 465–476.

(109) Hassler, J. F.; Van Zee, N. J.; Crabtree, A. A.; Bates, F. S.; Hackel, B. J.; Lodge, T. P.

Synthesis and Micellization of Bottlebrush Poloxamers. *ACS Macro Lett.* **2022**, *11*, 460–467.

(110) Pitsikalis, M.; Woodward, J.; Mays, J. W.; Hadjichristidis, N. Micellization of Model Graft Copolymers in Dilute Solution. *Macromolecules* **1997**, *30* (18), 5384–5389.

(111) Iyama, K.; Nose, T. Kinetics of Micelle Formation with Change of Micelle Shape in a Dilute Solution of Diblock Copolymers. *Macromolecules* **1998**, *31* (21), 7356–7364.

(112) Yang, Y. W.; Deng, N. J.; Yu, G. E.; Zhou, Z. K.; Attwood, D.; Booth, C. Micellization of Diblock and Triblock Copolymers in Aqueous Solution. New Results for Oxyethylene/Oxybutylene Copolymers E38B12 and E21B11E21. Comparison of Oxyethylene/Oxybutylene, Oxyethylene/Oxypropylene, and Oxyethylene/Alkyl Systems. *Langmuir* **1995**, *11* (12), 4703–4711.

(113) Papoutsakis, E. T. Fluid-Mechanical Damage of Animal Cells in Bioreactors. *Trends Biotechnol.* **1991**, *9* (1), 427–437.

(114) Zhang, Z.; Al-Rubeai, M.; Thomas, C. R. Effect of Pluronic F-68 on the Mechanical Properties of Mammalian Cells. *Enzyme Microb. Technol.* **1992**, *14* (12), 980–983.

(115) Serbest, G.; Horwitz, J.; Barbee, K. The Effect of Poloxamer-188 on Neuronal Cell Recovery from Mechanical Injury. *J. Neurotrauma* **2005**, *22* (1), 119–132.

(116) Inyang, E.; Abhyankar, V.; Chen, B.; Cho, M. Modulation of in Vitro Brain Endothelium by Mechanical Trauma: Structural and Functional Restoration by Poloxamer 188. *Sci. Rep.* **2020**, *10* (1), 1–16.

(117) Luo, J.; Borgens, R.; Shi, R. Polyethylene Glycol Improves Function and Reduces Oxidative Stress in Synaptosomal Preparations Following Spinal Cord Injury. *J. Neurotrauma* **2004**, *21* (8), 994–1007.

(118) Shelat, P. B.; Plant, L. D.; Wang, J. C.; Lee, E.; Marks, J. D. The Membrane-Active Tri-Block Copolymer Pluronic F-68 Profoundly Rescues Rat Hippocampal Neurons from Oxygen-Glucose Deprivation-Induced Death through Early Inhibition of Apoptosis. *J. Neurosci.* **2013**, *33* (30), 12287–12299.

(119) Luo, C.; Li, Q.; Gao, Y.; Shen, X.; Ma, L.; Wu, Q.; Wang, Z.; Zhang, M.; Zhao, Z.; Chen, X.; Tao, L. Poloxamer 188 Attenuates Cerebral Hypoxia/Ischemia Injury in Parallel with Preventing Mitochondrial Membrane Permeabilization and Autophagic Activation. *J. Mol. Neurosci.* **2015**, *56* (4), 988–998.

(120) Palmer, J. S.; Cromie, W. J.; Lee, R. C. Surfactant Administration Reduces Testicular Ischemia-Reperfusion Injury. *J. Urol.* **1998**, *159* (6), 2136–2139.

(121) Malhotra, R.; Valuckaite, V.; Staron, M. L.; Theccanat, T.; D'Souza, K. M.; Alverdy, J. C.; Akhter, S. A. High-Molecular-Weight Polyethylene Glycol Protects Cardiac Myocytes from Hypoxia- and Reoxygenation-Induced Cell Death and Preserves Ventricular Function. *Am. J. Physiol. - Hear. Circ. Physiol.* **2011**, *300* (5), 1–18.

(122) Salzman, M. M.; Bartos, J. A.; Yannopoulos, D.; Riess, M. L. Poloxamer 188 Protects Isolated Adult Mouse Cardiomyocytes from Reoxygenation Injury. *Pharmacol. Res.*

Perspect. **2020**, *8* (6), 1–13.

(123) Martindale, J. J.; Metzger, J. M. Uncoupling of Increased Cellular Oxidative Stress and Myocardial Ischemia Reperfusion Injury by Directed Sarcolemma Stabilization. *J. Mol. Cell. Cardiol.* **2014**, *67*, 26–37.

(124) Bartos, J. A.; Matsuura, T. R.; Tsangaris, A.; Olson, M.; McKnite, S. H.; Rees, J. N.; Haman, K.; Shekar, K. C.; Riess, M. L.; Bates, F. S.; Metzger, J. M.; Yannopoulos, D. Intracoronary Poloxamer 188 Prevents Reperfusion Injury in a Porcine Model of ST-Segment Elevation Myocardial Infarction. *JACC Basic to Transl. Sci.* **2016**, *1* (4), 224–234.

(125) Valuckaite, V.; Zaborina, O.; Long, J.; Hauer-Jensen, M.; Wang, J.; Holbrook, C.; Zaborin, A.; Drabik, K.; Katdare, M.; Mauceri, H.; Weichselbaum, R.; Firestone, M. A.; Lee, K. Y.; Chang, E. B.; Matthews, J.; Alverdy, J. C. Oral PEG 15-20 Protects the Intestine against Radiation: Role of Lipid Rafts. *Am. J. Physiol. - Gastrointest. Liver Physiol.* **2009**, *297* (6), 1041–1052.

(126) Terry, M. A.; Hannig, J.; Carrillo, C. S.; Beckett, M. A.; Weichselbaum, R. R.; Lee, R. C. Oxidative Cell Membrane Alteration. Evidence for Surfactant-Mediated Sealing. *Ann. N. Y. Acad. Sci.* **1999**, *888*, 274–284.

(127) Hannig, J.; Yu, J.; Beckett, M.; Weichselbaum, R.; Lee, R. C. Poloxamine 1107 Sealing of Radiopermeabilized Erythrocyte Membranes. *Int. J. Radiat. Biol.* **1999**, *75* (3), 379–385.

(128) Wong, S. W.; Yao, Y.; Hong, Y.; Ma, Z.; Kok, S. H. L.; Sun, S.; Cho, M.; Lee, K. K. H.; Mak, A. F. T. Preventive Effects of Poloxamer 188 on Muscle Cell Damage Mechanics Under Oxidative Stress. *Ann. Biomed. Eng.* **2017**, *45* (4), 1083–1092.

(129) Spurney, C. F.; Guerron, A. D.; Yu, Q.; Sali, A.; van der Meulen, J. H.; Hoffman, E. P.; Nagaraju, K. Membrane Sealant Poloxamer P188 Protects Against Isoproterenol Induced Cardiomyopathy in Dystrophin Deficient Mice. *BMC Cardiovasc. Disord.* **2011**, *11* (2005).

(130) Call, J. A.; Warren, G. L.; Verma, M.; Lowe, D. A. Acute Failure of Action Potential Conduction in Mdx Muscle Reveals New Mechanism of Contraction-Induced Force Loss. *J. Physiol.* **2013**, *591* (15), 3765–3776.

(131) Houang, E. M.; Haman, K. J.; Filareto, A.; Perlingeiro, R. C.; Bates, F. S.; Lowe, D. A.; Metzger, J. M. Membrane-Stabilizing Copolymers Confer Marked Protection to Dystrophic Skeletal Muscle in Vivo. *Mol. Ther. - Methods Clin. Dev.* **2015**, *2* (June), 15042.

(132) Crabtree, A. A. Influence of Poly (Ethylene Oxide) - b -Poly (Propylene Oxide) Block Copolymers and Poly (Ethylene Oxide) Homopolymer on Cellular Function. *Univ. Minnesota* **2022**, No. December.

(133) Usery, R. D.; Enoki, T. A.; Wickramasinghe, S. P.; Weiner, M. D.; Tsai, W. C.; Kim, M. B.; Wang, S.; Torng, T. L.; Ackerman, D. G.; Heberle, F. A.; Katsaras, J.; Feigenson, G. W. Line Tension Controls Liquid-Disordered + Liquid-Ordered Domain Size Transition in Lipid Bilayers. *Biophys. J.* **2017**, *112* (7), 1431–1443.

(134) T. Baumgart; S. Hess; W. Webb. Imaging Coexisting Fluid Domains in Biomembrane Models Coupling Curvature and Line Tension. *Nature* **2003**, *425* (October), 821–824.

(135) Hristova, K.; Needham, D. The Influence of Polymer-Grafted Lipids on the Physical Properties of Lipid Bilayers: A Theoretical Study. *Journal of Colloid And Interface Science*. 1994, pp 302–314.

(136) Maatouk, C.; Ling, M.; Titushkin, I.; Cho, M.; McFaul, C. A.; Lee, R. C. Amphiphilic Block Copolymer-Catalyzed Cell Membrane Sealing Is Linked to Decreased Membrane Tension. *Regen. Eng. Transl. Med.* **2021**.

(137) Togo, T.; Alderton, J. M.; Bi, G. Q.; Steinhardt, R. A. The Mechanism of Facilitated Cell Membrane Resealing. *J. Cell Sci.* **1999**, *112* (5), 719–731.

(138) Togo, T.; Krasieva, T. B.; Steinhardt, R. A. A Decrease in Membrane Tension Precedes Successful Cell-Membrane Repair. *Mol. Biol. Cell* **2000**, *11* (12), 4339–4346.

(139) Kwiatkowski, T. A.; Rose, A. L.; Jung, R.; Capati, A.; Hallak, D.; Yan, R.; Weisleder, N. Multiple Poloxamers Increase Plasma Membrane Repair Capacity in Muscle and Nonmuscle Cells. *Am. J. Physiol. - Cell Physiol.* **2020**, *318* (2), C253–C262.

(140) Krylova, O. O.; Melik-Nubarov, N. S.; Badun, G. A.; Ksenofontov, A. L.; Menger, F. M.; Yaroslavov, A. A. Pluronic L61 Accelerates Flip-Flop and Transbilayer Doxorubicin Permeation. *Chem. - A Eur. J.* **2003**, *9* (16), 3930–3936.

(141) Demina, T.; Grozdova, I.; Krylova, O.; Zhirnov, A.; Istratov, V.; Frey, H. Relationship between the Structure of Amphiphilic Copolymers and Their Ability To Disturb Lipid Bilayers. *Biochemistry* **2005**, *44*, 4042–4054.

(142) Sandez-macho, I.; Casas, M.; Lage, E. V; Rial-hermida, M. I.; Concheiro, A.; Alvarez-lorenzo, C. Colloids and Surfaces B : Biointerfaces Interaction of Poloxamine Block Copolymers with Lipid Membranes : Role of Copolymer Structure and Membrane Cholesterol Content. **2015**, *133*, 270–277.

(143) Houang, E. M.; Haman, K. J.; Kim, M.; Zhang, W.; Lowe, D. A.; Sham, Y. Y.; Lodge, T. P.; Hackel, B. J.; Bates, F. S.; Metzger, J. M. Chemical End Group Modified Diblock Copolymers Elucidate Anchor and Chain Mechanism of Membrane Stabilization. *Mol. Pharm.* **2017**, *14* (7), 2333–2339.

(144) Houang, E. M.; Bates, F. S.; Sham, Y. Y.; Metzger, J. M. All-Atom Molecular Dynamics-Based Analysis of Membrane- Stabilizing Copolymer Interactions with Lipid Bilayers Probed under Constant Surface Tensions. *J. Phys. Chem. B* **2017**, *121*, 10657–10664.

(145) Cheng, C. Y.; Wang, J. Y.; Kausik, R.; Lee, K. Y. C.; Han, S. An Ultrasensitive Tool Exploiting Hydration Dynamics to Decipher Weak Lipid Membrane-Polymer Interactions. *J. Magn. Reson.* **2011**, *215*, 115–119.

(146) Zhang, W.; Metzger, J. M.; Hackel, B. J.; Bates, F. S.; Lodge, T. P. Influence of the Headgroup on the Interaction of Poly(Ethylene Oxide)-Poly(Propylene Oxide) Block Copolymers with Lipid Bilayers. *J. Phys. Chem. B* **2020**, *124* (12), 2417–2424.

(147) Henriksen, J.; Rowat, A. C.; Brief, E.; Hsueh, Y. W.; Thewalt, J. L.; Zuckermann, M. J.;

Ipsen, J. H. Universal Behavior of Membranes with Sterols. *Biophys. J.* **2006**, *90* (5), 1639–1649.

(148) Pietrasik, J.; Sumerlin, B. S.; Lee, H.; Gil, R. R.; Matyjaszewski, K. Structural Mobility of Molecular Bottle-Brushes Investigated by NMR Relaxation Dynamics. *Polymer (Guildf).* **2007**, *48* (2), 496–501.

(149) Bichler, K. J.; Jakobi, B.; Schneider, G. J. Dynamical Comparison of Different Polymer Architectures - Bottlebrush vs Linear Polymer. *Macromolecules* **2021**, *54* (4), 1829–1837.

(150) Haugan, I. N.; Maher, M. J.; Chang, A. B.; Lin, T. P.; Grubbs, R. H.; Hillmyer, M. A.; Bates, F. S. Consequences of Grafting Density on the Linear Viscoelastic Behavior of Graft Polymers. *ACS Macro Lett.* **2018**, *7* (5), 525–530.

(151) Fenyves, R.; Schmutz, M.; Horner, I. J.; Bright, F. V.; Rzayev, J. Aqueous Self-Assembly of Giant Bottlebrush Block Copolymer Surfactants as Shape-Tunable Building Blocks. *J. Am. Chem. Soc.* **2014**, *136* (21), 7762–7770.

(152) Levi, A. E.; Lequieu, J.; Horne, J. D.; Bates, M. W.; Ren, J. M.; Delaney, K. T.; Fredrickson, G. H.; Bates, C. M. Miktoarm Stars via Grafting-Through Copolymerization: Self-Assembly and the Star-to-Bottlebrush Transition. *Macromolecules* **2019**, *52* (4), 1794–1802.

(153) Li, X.; Shamsijazeyi, H.; Pesek, S. L.; Agrawal, A.; Hammouda, B.; Verduzco, R. Thermoresponsive PNIPAAM Bottlebrush Polymers with Tailored Side-Chain Length and End-Group Structure. *Soft Matter* **2014**, *10* (12), 2008–2015.

(154) Kang, J. J.; Jung, F. A.; Ko, C. H.; Shehu, K.; Barnsley, L. C.; Kohler, F.; Dietz, H.; Zhao, J.; Pispas, S.; Papadakis, C. M. Thermoresponsive Molecular Brushes with Propylene Oxide/Ethylene Oxide Copolymer Side Chains in Aqueous Solution. *Macromolecules* **2020**, *53* (10), 4068–4081.

(155) Heatley, F.; Lovell, P. A.; Yamashita, T. Chain Transfer to Polymer in Free-Radical Solution Polymerization of 2-Ethylhexyl Acrylate Studied by NMR Spectroscopy. *Macromolecules* **2001**, *34* (22), 7636–7641.

(156) Ding, J.; Heatley, F.; Price, C.; Booth, C. Use of Crown Ether in the Anionic Polymerization of Propylene Oxide-1. Rate of Polymerization. *Eur. Polym. J.* **1991**, *27* (9), 891–895.

(157) Yu, G. -E; Masters, A. J.; Heatley, F.; Booth, C.; Blease, T. G. Anionic Polymerisation of Propylene Oxide. Investigation of Double-bond and Head-to-head Content by NMR Spectroscopy. *Macromol. Chem. Phys.* **1994**, *195* (5), 1517–1538.

(158) Batti Angulski, A. B.; Cohen, H.; Kim, M.; Hahn, D.; Van Zee, N.; Lodge, T. P.; Hillmyer, M. A.; Hackel, B. J.; Bates, F. S.; Metzger, J. M. Molecular Homing and Retention of Muscle Membrane Stabilizing Copolymers by Non-Invasive Optical Imaging in Vivo. *Mol. Ther. - Methods Clin. Dev.* **2023**, *28* (March), 162–176.

(159) Grindel, J. M.; Jaworski, T.; Piraner, O.; Emanuele, R. M.; Balasubramanian, M. Distribution, Metabolism, and Excretion of a Novel Surface-Active Agent, Purified Poloxamer 188, in Rats, Dogs, and Humans. *J. Pharm. Sci.* **2002**, *91* (9), 1936–1947.

(160) Svetlovics, J. A.; Wheaten, S. A.; Almeida, P. F. Phase Separation and Fluctuations in Mixtures of a Saturated and an Unsaturated Phospholipid. *Biophys. J.* **2012**, *102* (11), 2526–2535.

(161) Fischer, K.; Schmidt, M. Pitfalls and Novel Applications of Particle Sizing by Dynamic Light Scattering. *Biomaterials* **2016**, *98*, 79–91.

(162) Early, J. T.; Lodge, T. P. Fragmentation of 1,2-Polybutadiene- Block-Poly(Ethylene Oxide) Micelles in Imidazolium-Based Ionic Liquids. *Macromolecules* **2019**, *52* (18), 7089–7101.

(163) Lodge, Timothy P.; Hiemenz, P. C. *Polymer Chemistry*, 3rd ed.; Taylor & Francis: Boca Raton, Fl, 2020.

(164) Malcolm H. Levitt. *Spin Dynamics*, 2nd ed.; John Wiley and Sons, 2009.

(165) Pagès, G.; Gilard, V.; Martino, R. Pulsed-Field Gradient Nuclear Magnetic Resonance Measurements (PFG NMR) for Diffusion Ordered Spectroscopy (DOSY) Mapping. *RSC Anal.* **2017**, *142*, 3771–3796.

(166) Bilia, A. R.; Camilla Bergonzi, M.; Vincieri, F. F.; Lo Nostro, P.; Morris, G. A. A Diffusion-Ordered NMR Spectroscopy Study of the Solubilization of Artemisinin by Octanoyl-6-O-Ascorbic Acid Micelles. *J. Pharm. Sci.* **2002**, *91* (10), 2265–2270.

(167) Ivanova, G.; Simeonova, M.; Cabrita, E. J.; Rangel, M. NMR Insight into the Supramolecular Structure of Daunorubicin Loaded Polymer Nanoparticles. *J. Phys. Chem. B* **2011**, *115* (5), 902–909.

(168) Scheidt, H. A.; Pampel, A.; Nissler, L.; Gebhardt, R.; Huster, D. Investigation of the Membrane Localization and Distribution of Flavonoids by High-Resolution Magic Angle Spinning NMR Spectroscopy. *Biochim. Biophys. Acta - Biomembr.* **2004**, *1663* (1–2), 97–107.

(169) Wu, D.; Chain, A.; Johnson, C. S. An Improved Diffusion-Ordered Spectroscopy Experiment Incorporating Bipolar-Gradient Pulses. 1995, pp 260–264.

(170) Lewis, A. K.; Harthorn, A.; Johnson, S. M.; Lobb, R. R.; Hackel, B. J. Engineered Protein-Small Molecule Conjugates Empower Selective Enzyme Inhibition. *Cell Chem. Biol.* **2022**, *29* (2), 328-338.e4.

(171) Golinski, A. W.; Mischler, K. M.; Laxminarayan, S.; Neurock, N. L.; Fossing, M.; Pichman, H.; Martiniani, S.; Hackel, B. J. High-Throughput Developability Assays Enable Library-Scale Identification of Producible Protein Scaffold Variants. *Proc. Natl. Acad. Sci. U. S. A.* **2021**, *118* (23), 1–11.

(172) Tresnak, D. T.; Hackel, B. J. Deep Antimicrobial Activity and Stability Analysis Inform Lysin Sequence-Function Mapping. *ACS Synth. Biol.* **2023**, *12* (1), 249–264.

(173) Dejong, M. P.; Ritter, S. C.; Fransen, K. A.; Tresnak, D. T.; Golinski, A. W.; Hackel, B. J. A Platform for Deep Sequence-Activity Mapping and Engineering Antimicrobial Peptides. *ACS Synth. Biol.* **2021**, *10* (10), 2689–2704.

(174) Kumar, R.; Le, N.; Tan, Z.; Brown, M. E.; Jiang, S.; Reineke, T. M. Efficient Polymer-Mediated Delivery of Gene-Editing Ribonucleoprotein Payloads through Combinatorial Design, Parallelized Experimentation, and Machine Learning. *ACS Nano* **2020**, *14* (12).

(175) Yang, J.; Mei, Y.; Hook, A. L.; Taylor, M.; Urquhart, A. J.; Bogatyrev, S. R.; Langer, R.; Anderson, D. G.; Davies, M. C.; Alexander, M. R. Polymer Surface Functionalities That Control Human Embryoid Body Cell Adhesion Revealed by High Throughput Surface Characterization of Combinatorial Material Microarrays. *Biomaterials* **2010**, *31* (34), 8827–8838.

(176) Dalal, R. J.; Oviedo, F.; Leyden, M. C.; Reineke, T. M. Polymer Design via SHAP and Bayesian Machine Learning Optimizes PDNA and CRISPR Ribonucleoprotein Delivery. *Res. Sq.* **2022**, 1–21.

(177) Boehnke, N.; Straehla, J. P.; Safford, H. C.; Kocak, M.; Rees, M. G.; Ronan, M.; Rosenberg, D.; Adelmann, C. H.; Chivukula, R. R.; Nabar, N.; Berger, A. G.; Lamson, N. G.; Cheah, J. H.; Li, H.; Roth, J. A.; Koehler, A. N.; Hammond, P. T. Massively Parallel Pooled Screening Reveals Genomic Determinants of Nanoparticle Delivery. *Science (80-.).* **2022**, *377* (6604).

(178) Crabtree, A. A.; Bates, F. S.; Hackel, B. J. Concentration Threshold for Membrane Protection by PEO − PPO Block Copolymers with Variable Molecular Architectures. *ACS Appl. Polym. Mater.* **2022**, *4*, 3259–3269.

(179) Wessels, M. G.; Jayaraman, A. Molecular Dynamics Simulation Study of Linear, Bottlebrush, and Star-like Amphiphilic Block Polymer Assembly in Solution. *Soft Matter* **2019**, *15* (19), 3987–3998.

(180) Adams, D. J.; Kitchen, C.; Adams, S.; Furzeland, S.; Atkins, D.; Schuetz, P.; Fernyhough, C. M.; Tzokova, N.; Ryan, A. J.; Butler, M. F. On the Mechanism of Formation of Vesicles from Poly(Ethylene Oxide)-Block-Poly(Caprolactone) Copolymers. *Soft Matter* **2009**, *5* (16), 3086–3096.

(181) Jiang, Y.; Lodge, T. P.; Reineke, T. M. Packaging PDNA by Polymeric ABC Micelles Simultaneously Achieves Colloidal Stability and Structural Control. *J. Am. Chem. Soc.* **2018**, *140* (35), 11101–11111.

(182) Maksym, P.; Neugebauer, D. Synthesis of Amphiphilic Semigrafted Pseudo-Pluronics for Self-Assemblies Carrying Indomethacin. *RSC Adv.* **2016**, *6* (91), 88444–88452.

(183) Cotanda, P.; Lu, A.; Patterson, J. P.; Petzetakis, N.; O'Reilly, R. K. Functionalized Organocatalytic Nanoreactors: Hydrophobic Pockets for Acylation Reactions in Water. *Macromolecules* **2012**, *45* (5), 2377–2384.

(184) Rabbel, H.; Werner, M.; Sommer, J. U. Interactions of Amphiphilic Triblock Copolymers with Lipid Membranes: Modes of Interaction and Effect on Permeability Examined by Generic Monte Carlo Simulations. *Macromolecules* **2015**, *48* (13), 4724–4732.

(185) De Mel, J. U.; Gupta, S.; Willner, L.; Allgaier, J.; Stingaciu, L. R.; Bleuel, M.; Schneider, G. J. Manipulating Phospholipid Vesicles at the Nanoscale: A Transformation from Unilamellar to Multilamellar by an n-Alkyl-Poly(Ethylene Oxide). *Langmuir* **2021**, *37* (7),

2362–2375.

(186) Adhikari, U.; Goliaei, A.; Tsereteli, L.; Berkowitz, M. L. Properties of Poloxamer Molecules and Poloxamer Micelles Dissolved in Water and next to Lipid Bilayers: Results from Computer Simulations. *J. Phys. Chem. B* **2016**, *120* (26), 5823–5830.

(187) Redhead, M.; Mantovani, G.; Nawaz, S.; Carbone, P.; Gorecki, D. C.; Alexander, C.; Bosquillon, C. Relationship between the Affinity of PEO-PPO-PEO Block Copolymers for Biological Membranes and Their Cellular Effects. *Pharm. Res.* **2012**, *29* (7), 1908–1918.

(188) Houang, E. M.; Bartos, J.; Hackel, B. J.; Lodge, T. P.; Yannopoulos, D.; Bates, F. S.; Metzger, J. M. Cardiac Muscle Membrane Stabilization in Myocardial Reperfusion Injury. *JACC Basic to Transl. Sci.* **2019**, *4* (2), 275–287.

(189) Firestone, M. A.; Wolf, A. C.; Seifert, S. Small-Angle X-Ray Scattering Study of the Interaction of Poly(Ethylene Oxide)-b-Poly(Propylene Oxide)-b-Poly(Ethylene Oxide) Triblock Copolymers with Lipid Bilayers. *Biomacromolecules* **2003**, *4* (6), 1539–1549.

(190) Firestone, M. A.; Seifert, S. Interaction of Nonionic PEO-PPO Diblock Copolymers with Lipid Bilayers. *Biomacromolecules* **2005**, *6* (5), 2678–2687.

(191) Houang, E. M.; Bates, F. S.; Sham, Y. Y.; Metzger, J. M. All-Atom Molecular Dynamics-Based Analysis of Membrane-Stabilizing Copolymer Interactions with Lipid Bilayers Probed under Constant Surface Tensions. *J. Phys. Chem. B* **2017**, *121* (47), 10657–10664.

(192) Lecommandoux, S.; Chécot, F.; Borsali, R.; Schappacher, M.; Deffieux, A.; Brûlet, A.; Cotton, J. P. Effect of Dense Grafting on the Backbone Conformation of Bottlebrush Polymers: Determination of the Persistence Length in Solution. *Macromolecules* **2002**, *35* (23), 8878–8881.

(193) Zhang, B.; Gröhn, F.; Pedersen, J. S.; Fischer, K.; Schmidt, M. Conformation of Cylindrical Brushes in Solution: Effect of Side Chain Length. *Macromolecules* **2006**, *39* (24), 8440–8450.

(194) López-Barrón, C. R.; Brant, P.; Eberle, A. P. R.; Crowther, D. J. Linear Rheology and Structure of Molecular Bottlebrushes with Short Side Chains. *J. Rheol. (N. Y. N. Y).* **2015**, *59* (3), 865–883.

(195) Sun, H.; Yu, D. M.; Shi, S.; Yuan, Q.; Fujinami, S.; Sun, X. Configurationally Constrained Crystallization of Brush Polymers with Poly(Ethylene Oxide) Side Chains. *Macromolecules* **2019**, *52*, 592–600.

(196) Chang, A. B.; Bates, F. S. Impact of Architectural Asymmetry on Frank-Kasper Phase Formation in Block Polymer Melts. *ACS Nano* **2020**, *14*, 11463–11472.

(197) Shemper, B. S.; Acar, A. E.; Mathias, L. J. Synthesis of Linear and Starlike Polymers from Poly(Propylene Glycol) Methacrylate Using Controlled Radical Polymerization. *J. Polym. Sci. Part A Polym. Chem.* **2002**, *40* (3), 334–343.

(198) París, R.; Quijada-Garrido, I. Synthesis and Aggregation Properties in Water Solution of Comblike Methacrylic Polymers with Oligo(Propylene Glycol)-Block-Oligo(Ethylene

Glycol) as Side Chains. *J. Polym. Sci. Part A Polym. Chem.* **2011**, *49* (8), 1928–1932.

(199) Truelsen, J. H.; Kops, J.; Batsberg, W.; Armes, S. P. Novel Polymeric Surfactants: Synthesis of Semi-Branched, Non-Ionic Triblock Copolymers Using ATRP. *Macromol. Chem. Phys.* **2002**, *203* (14), 2124–2131.

(200) Maksym-Bębenek, P.; Biela, T.; Neugebauer, D. Water Soluble Well-Defined Acidic Graft Copolymers Based on a Poly(Propylene Glycol) Macromonomer. *RSC Adv.* **2015**, *5* (5), 3627–3635.

(201) Loh, X. J. Poly(DMAEMA-Co-PPGMA): Dual-Responsive "Reversible" Micelles. *J. Appl. Polym. Sci.* **2013**, *127* (2), 992–1000.

(202) Heroguez, V.; Gnanou, Y.; Fontanille, M. Novel Amphiphilic Architectures by Ring-Opening Metathesis Polymerization of Macromonomers. *Macromolecules* **1997**, *30* (17), 4791–4798.

(203) Heroguez, V.; Breunig, S.; Gnanou, Y.; Fontanille, M. Synthesis of α-Norbornenylpoly(Ethylene Oxide) Macromonomers and Their Ring-Opening Metathesis Polymerization. *Macromolecules* **1996**, *29* (13).

(204) Ohnsorg, M. L.; Prendergast, P. C.; Robinson, L. L.; Bockman, M. R.; Bates, F. S.; Reineke, T. M. Bottlebrush Polymer Excipients Enhance Drug Solubility: Influence of End-Group Hydrophilicity and Thermoresponsiveness. *ACS Macro Lett.* **2021**, *10* (3), 375–381.

(205) Xia, Y.; Olsen, B. D.; Kornfield, J. A.; Grubbs, R. H. Efficient Synthesis of Narrowly Dispersed Brush Copolymers and Study of Their Assemblies: The Importance of Side Chain Arrangement. *J. Am. Chem. Soc.* **2009**, *131* (51), 18525–18532.

(206) Hillmyer, M. A.; Bates, F. S. Synthesis and Characterization of Model Polyalkane - Poly (Ethylene Oxide) Block Copolymers. *Macromolecules* **1996**, *29* (22), 6994–7002.

(207) Ding, J.; Heatley, F.; Price, C.; Booth, C. Use of Crown Ether in the Anionic Polymerization of Propylene Oxide-2. Molecular Weight and Molecular Weight Distribution. *Eur. Polym. J.* **1991**, *27* (9), 895–899.

(208) Ren, N.; Zhu, X. Hybrid Polymerization of Ring-Opening Metathesis and Cross-Metathesis for Polyolefins with Tunable Architectures. *Macromolecules* **2018**, *51* (23), 9555–9561.

(209) Zhang, H.; Zhang, Z.; Gnanou, Y.; Hadjichristidis, N. Well-Defined Polyethylene-Based Random, Block, and Bilayered Molecular Cobrushes. *Macromolecules* **2015**, *48* (11), 3556–3562.

(210) Yavitt, B. M.; Fei, H.; Kopanati, G.; Li, R.; Fukuto, M.; Winter, H. H.; Watkins, J. J. Long-Range Lamellar Alignment in Diblock Bottlebrush Copolymers via Controlled Oscillatory Shear. *Macromolecules* **2020**.

(211) Schillén, K.; Brown, W.; Johnsen, R. M. Micellar Sphere-to-Rod Transition in an Aqueous Triblock Copolymer System. A Dynamic Light Scattering Study of Translational and Rotational Diffusion. *Macromolecules* **1994**, *27* (17), 4825–4832.

(212) Zee, N. J. Van; Hillmyer, M. A.; Lodge, T. P. Role of Polymer Excipients in the Kinetic Stabilization of Drug-Rich Nanoparticles. *ACS Appl. Bio Mater.* **2020**, *3*, 7243–7254.

(213) Kangarlou, B.; Dahanayake, R.; Martin, I. J.; Ndaya, D.; Wu, C.-M.; Kasi, R. M.; Dormidontova, E. E.; Nieh, M.-P. Flower-like Micelles of Polyethylene Oxide End-Capped with Cholesterol. *Macromolecules* **2021**, *54* (19), 8960–8970.

(214) Topel, Ö.; Çakir, B. A.; Budama, L.; Hoda, N. Determination of Critical Micelle Concentration of Polybutadiene-Block-Poly(Ethyleneoxide) Diblock Copolymer by Fluorescence Spectroscopy and Dynamic Light Scattering. *J. Mol. Liq.* **2013**, *177*, 40–43.

(215) Nyrkova, I. A.; Semenov, A. N. On the Theory of Micellization Kinetics. *Macromol. Theory Simulations* **2005**, *14* (9), 569–585.

(216) Tuzar, Z.; Štěpánek, P.; Koňák, Č.; Kratochvíl, P. Block Copolymer Micelles near Critical Conditions. *J. Colloid Interface Sci.* **1985**, *105* (2), 372–377.

(217) Leibler, L.; Orland, H.; Wheeler, J. C. Theory of Critical Micelle Concentration for Solutions of Block Copolymers. *J. Chem. Phys.* **1983**, *79* (7), 3550–3557.

(218) Much, M.R.; Gast, A. P. Block Copolymers at Interfaces. 1. Micelle Formation. *Macromolecules* **1988**, *21* (18), 1360–1366.

(219) Lyubimov, I.; Wessels, M. G.; Jayaraman, A. Molecular Dynamics Simulation and PRISM Theory Study of Assembly in Solutions of Amphiphilic Bottlebrush Block Copolymers. *Macromolecules* **2018**, *51* (19), 7586–7599.

(220) Zhulina, E. B.; Borisov, O. V. Micelles Formed by an AB Copolymer with Bottlebrush Blocks: Scaling Theory . *J. Phys. Chem. B* **2021**.

(221) Grundler, J.; Shin, K.; Suh, H.-W.; Zhong, M.; Saltzman, W. M. Surface Topography of Polyethylene Glycol Shell Nanoparticles Formed from Bottlebrush Block Copolymers Controls Interactions with Proteins and Cells. *ACS Nano* **2021**, *15* (10), 16118–16129.

(222) Kratky, O; Porod, G. Rontgenuntersuchung Geloster Fadenmolekule. *Rec. Trav. Chim.* **1949**, *68*, 1106–1122.

(223) Sunday, D. F.; Chremos, A.; Martin, T. B.; Chang, A. B.; Burns, A. B.; Grubbs, R. H. Concentration Dependence of the Size and Symmetry of a Bottlebrush Polymer in a Good Solvent. *Macromolecules* **2020**, *53* (16), 7132–7140.

(224) Liu, C.; Kubo, K.; Wang, E.; Han, K. S.; Yang, F.; Chen, G.; Escobedo, F. A.; Coates, G. W.; Chen, P. Single Polymer Growth Dynamics. *Science (80-.).* **2017**, *358* (6361), 352–355.

(225) Jada, A.; Hurtrez, G.; Siffert, B.; Riess, G. Structure of Polystyrene-Block-Poly(Ethylene Oxide) Diblock Copolymer Micelles in Water. *Macromol. Chem. Phys.* **1996**, *197* (11), 3697–3710.

(226) Nicolai, T.; Colombani, O.; Chassenieux, C. Dynamic Polymeric Micelles versus Frozen Nanoparticles Formed by Block Copolymers. *Soft Matter* **2010**, *6* (14), 3111–3118.

(227) Inomata, K.; Nakanishi, E.; Sakane, Y.; Koike, M.; Nose, T. Side-Chain Crystallization

Behavior of Graft Copolymers Consisting of Amorphous Main Chain and Crystalline Side Chains: Poly(Methyl Methacrylate)-Graft-Poly(Ethylene Glycol) and Poly(Methyl Acrylate)-Graft- Poly(Ethylene Glycol). *J. Polym. Sci. Part B Polym. Phys.* **2005**, *43* (1), 79–86.

(228) Neugebauer, D.; Theis, M.; Pakula, T.; Wegner, G.; Matyjaszewski, K. Densely Heterografted Brush Macromolecules with Crystallizable Grafts. Synthesis and Bulk Properties. *Macromolecules* **2006**, *39* (2), 584–593.

(229) Inomata, K.; Sasaki, Y.; Nose, T. Packing Manner of Graft Copolymers with Rigid-Rod Main Chains and Amorphous-Crystalline Diblock Copolymers as Side Chains. *J. Polym. Sci. Part B Polym. Phys.* **2002**, *40* (17), 1904–1912.

(230) Kripotou, S.; Psylla, C.; Kyriakos, K.; Raftopoulos, K. N.; Zhao, J.; Zhang, G.; Pispas, S.; Papadakis, C. M.; Kyritsis, A. Structure and Crystallization Behavior of Poly(Ethylene Oxide) (PEO) Chains in Core-Shell Brush Copolymers with Poly(Propylene Oxide)-Block-Poly(Ethylene Oxide) Side Chains. *Macromolecules* **2016**, *49* (16), 5963–5977.

(231) Ndoni, S.; Papadakis, C. M.; Bates, F. S.; Almdal, K. Laboratory-Scale Setup for Anionic Polymerization under Inert Atmosphere. *Rev. Sci. Instrum.* **1995**, *66* (2), 1090–1095.

(232) Allgaier, J.; Willbold, S.; Taihyun, C. Synthesis of Hydrophobic Poly(Alkylene Oxide)s and Amphiphilic Poly(Alkylene Oxide) Block Copolymers. *Macromolecules* **2007**, *40* (3), 518–525.

(233) Love, J. A.; Morgan, J. P.; Trnka, T. M.; Grubbs, R. H. A Practical and Highly Active Ruthenium-Based Catalyst That Effects the Cross Metathesis of Acrylonitrile. *Angew. Chemie - Int. Ed.* **2002**, *41* (21), 4035–4037.

(234) Medrano, R.; Laguna, M. T. R.; Saiz, E.; Tarazona, M. P. Analysis of Copolymers of Styrene and Methyl Methacrylate Using Size Exclusion Chromatography with Multiple Detection. *Phys. Chem. Chem. Phys.* **2003**, *5* (1), 151–157.

(235) Lee, C. A. A.; Seo, H. S.; Armien, A. G.; Bates, F. S.; Tolar, J.; Azarin, S. M. Modeling and Rescue of Defective Blood-Brain Barrier Function of Induced Brain Microvascular Endothelial Cells from Childhood Cerebral Adrenoleukodystrophy Patients. *Fluids Barriers CNS* **2018**, *15* (1), 1–15.

(236) Lee, B.; Firestone, M. A. Electron Density Mapping of Triblock Copolymers Associated with Model Biomembranes: Insights into Conformational States and Effect on Bilayer Structure. *Biomacromolecules* **2008**, *9* (6), 1541–1550.

(237) Nawaz, S.; Redhead, M.; Mantovani, G.; Alexander, C.; Bosquillon, C.; Carbone, P. Interactions of PEO-PPO-PEO Block Copolymers with Lipid Membranes: A Computational and Experimental Study Linking Membrane Lysis with Polymer Structure. *Soft Matter* **2012**, *8* (25), 6744–6754.

(238) Zografos, A.; Lynd, N. A.; Bates, F. S.; Hillmyer, M. A. Impact of Macromonomer Molar Mass and Feed Composition on Branch Distributions in Model Graft Copolymerizations. *ACS Macro Lett.* **2021**, *10* (12), 1622–1628.

(239) Jakobi, B.; Bichler, K. J.; Sokolova, A.; Schneider, G. J. Dynamics of PDMS- g-PDMS

Bottlebrush Polymers by Broadband Dielectric Spectroscopy. *Macromolecules* **2020**, *53* (19), 8450–8458.

(240) Bichler, K. J.; Jakobi, B.; Sakai, V. G.; Klapproth, A.; Mole, R. A.; Schneider, G. J. Universality of Time-Temperature Scaling Observed by Neutron Spectroscopy on Bottlebrush Polymers. *Nano Lett.* **2021**, *21* (10), 4494–4499.

(241) Casares, D.; Escribá, P. V.; Rosselló, C. A. Membrane Lipid Composition: Effect on Membrane and Organelle Structure, Function and Compartmentalization and Therapeutic Avenues. *Int. J. Mol. Sci.* **2019**, *20* (9), 2167.

(242) Momot, K. I.; Kuchel, P. W. Pulsed Field Gradient Nuclear Magnetic Resonance as a Tool for Studying Drug Delivery Systems. *Concepts Magn. Reson. Part A* **2006**, *19* (2), 51–64.

(243) Kim, S.; Lee, S.; Choi, S.-H.; Char, K. Chain Exchange Kinetics of Bottlebrush Block Copolymer Micelles. *Macromolecules* **2021**, *54* (10), 4739–4746.

(244) Ataman, M.; Boucher, E. A. Properties of Aqueous Salt Solutions of Poly(Ethylene Oxide). *J. Polym. Sci. Part A-2, Polym. Phys.* **1982**, *20* (9), 1585–1592.

(245) Wang, J. C.; Bindokas, V. P.; Skinner, M.; Emrick, T.; Marks, J. D. Mitochondrial Mechanisms of Neuronal Rescue by F-68, a Hydrophilic Pluronic Block Co-Polymer, Following Acute Substrate Deprivation. *Neurochem. Int.* **2017**, *109*, 126–140.

(246) Daniel, W. F. M.; Burdyńska, J.; Vatankhah-Varnoosfaderani, M.; Matyjaszewski, K.; Paturej, J.; Rubinstein, M.; Dobrynin, A. V.; Sheiko, S. S. Solvent-Free, Supersoft and Superelastic Bottlebrush Melts and Networks. *Nat. Mater.* **2016**, *15* (2), 183–189.

(247) Arturson, G.; Wallenius, G. The Renal Clearance of Dextran of Different Molecular Sizes in Normal Humans. *Scand. J. Clin. Lab. Invest.* **1964**, *16* (1), 81–86.

(248) Nele, V.; Holme, M. N.; Kauscher, U.; Thomas, M. R.; Doutch, J. J.; Stevens, M. M. Effect of Formulation Method, Lipid Composition, and PEGylation on Vesicle Lamellarity: A Small-Angle Neutron Scattering Study. *Langmuir* **2019**, *35* (18), 6064–6074.

(249) Dave, P. C.; Tiburu, E. K.; Damodaran, K.; Lorigan, G. A. Investigating Structural Changes in the Lipid Bilayer upon Insertion of the Transmembrane Domain of the Membrane-Bound Protein Phospholamban Utilizing 31 P and 2 H Solid-State NMR Spectroscopy. *Biophys. J.* **2004**, *86*, 1564–1573.

(250) Zhou, Y.; Tang, H.; Wu, P. Intra-Molecular Interactions Dominating the Dehydration of a Poly(2-Isopropyl-2-Oxazoline)-Based Densely Grafted Polymer Comb in Aqueous Solution and Hysteretic Liquid-Liquid Phase Separation. *Phys. Chem. Chem. Phys.* **2017**, *19* (9), 6626–6635.

(251) Kučerka, N.; Nieh, M. P.; Katsaras, J. Fluid Phase Lipid Areas and Bilayer Thicknesses of Commonly Used Phosphatidylcholines as a Function of Temperature. *Biochim. Biophys. Acta - Biomembr.* **2011**.

(252) Huber, T.; Rajamoorthi, K.; Kurze, V. F.; Beyer, K.; Brown, M. F. Structure of Docosahexaenoic Acid-Containing Phospholipid Bilayers as Studied by 2H NMR and

Molecular Dynamics Simulations. *J. Am. Chem. Soc.* **2002**, *124* (2), 298–309.

(253) Kapoor, M. S.; D'Souza, A.; Aibani, N.; Nair, S. S.; Sandbhor, P.; kumari, D.; Banerjee, R. Stable Liposome in Cosmetic Platforms for Transdermal Folic Acid Delivery for Fortification and Treatment of Micronutrient Deficiencies. *Sci. Rep.* **2018**, *8* (1), 1–12.

(254) Matsuzaki, M.; McCafferty, F.; Karel, M. The Effect of Cholesterol Content of Phospholipid Vesicles on the Encapsulation and Acid Resistance of B-galactosidase from E. Coli. *Int. J. Food Sci. Technol.* **1989**, *24* (4), 451–460.

(255) Oberholzer, T.; Albrizio, M.; Luisi, P. L. Polymerase Chain Reaction in Liposomes. *Chem. Biol.* **1995**, *2* (10), 677–682.

(256) Buyens, K.; De Smedt, S. C.; Braeckmans, K.; Demeester, J.; Peeters, L.; Van Grunsven, L. A.; De Mollerat Du Jeu, X.; Sawant, R.; Torchilin, V.; Farkasova, K.; Ogris, M.; Sanders, N. N. Liposome Based Systems for Systemic SiRNA Delivery: Stability in Blood Sets the Requirements for Optimal Carrier Design. *J. Control. Release* **2012**, *158* (3), 362–370.

(257) Wu, P.; Chen, H.; Jin, R.; Weng, T.; Ho, J. K.; You, C.; Zhang, L.; Wang, X.; Han, C. Non-Viral Gene Delivery Systems for Tissue Repair and Regeneration. *J. Transl. Med.* **2018**, *16* (1), 1–20.

(258) Li, Shyh-Dar; Huang, L. Stealth Nanoparticles: High Density but Sheddable PEG Is a Key for Tumor Targeting. *J. Control. Release* **2010**, *145* (3), 178–181.

(259) Anselmo, A. C.; Mitragotri, S. Nanoparticles in the Clinic: An Update Post COVID-19 Vaccines. *Bioeng. Transl. Med.* **2021**, *6* (3), 1–20.

(260) Kang, J. Y.; Choi, I.; Seo, M.; Lee, J. Y.; Hong, S.; Gong, G.; Shin, S. S.; Lee, Y.; Kim, J. W. Enhancing Membrane Modulus of Giant Unilamellar Lipid Vesicles by Lateral Co-Assembly of Amphiphilic Triblock Copolymers. *J. Colloid Interface Sci.* **2020**, *561*, 318–326.

(261) Perera, R. M.; Gupta, S.; Li, T.; Leeuwen, C. J. Van; Bleuel, M.; Hong, K.; Schneider, G. J. Nanoscale Lipid/Polymer Hybrid Vesicles: Effects of Triblock Copolymer Composition and Hydrophilic Weight Fraction. **2022**, *4* (12), 8858–8868.

(262) Ting, J. M.; Tale, S.; Purchel, A. A.; Jones, S. D.; Widanapathirana, L.; Tolstyka, Z. P.; Guo, L.; Guillaudeu, S. J.; Bates, F. S.; Reineke, T. M. High-Throughput Excipient Discovery Enables Oral Delivery of Poorly Soluble Pharmaceuticals. *ACS Cent. Sci.* **2016**, *2* (10), 748–755.

(263) Ohnsorg, M. L.; Ting, J. M.; Jones, S. D.; Jung, S.; Bates, F. S.; Reineke, T. M. Tuning PNIPAm Self-Assembly and Thermoresponse: Roles of Hydrophobic End-Groups and Hydrophilic Comonomer. *Polym. Chem.* **2019**, *10* (25), 3469–3479.

(264) Özdemir, C.; Güner, A. Solution Thermodynamics of Poly(Ethylene Glycol)Water Systems. *J. Appl. Polym. Sci.* **2006**, *101* (1), 203–216.

(265) Hammouda, B.; Ho, D.; Kline, S. SANS from Poly (Ethylene Oxide)/ Water Systems. **2002**, 8578–8585.

(266) De Mel, J.; Hossain, M.; Shofolawe-Bakare, O.; Mohammad, S. A.; Rasmussen, E.; Milloy, K.; Shields, M.; Roth, E. W.; Arora, K.; Cueto, R.; Tang, S. C.; Wilson, J. T.; Smith, A. E.; Werfel, T. A. Dual-Responsive Glycopolymers for Intracellular Codelivery of Antigen and Lipophilic Adjuvants. *Mol. Pharm.* **2022**, *19* (12), 4705–4716.

(267) Kempe, K.; Neuwirth, T.; Czaplewska, J.; Gottschaldt, M.; Hoogenboom, R.; Schubert, U. S. Poly(2-Oxazoline) Glycopolymers with Tunable LCST Behavior. *Polym. Chem.* **2011**, *2* (8), 1737–1743.

(268) Paul, T. J.; Strzelczyk, A. K.; Feldhof, M. I.; Schmidt, S. Temperature-Switchable Glycopolymers and Their Conformation-Dependent Binding to Receptor Targets. *Biomacromolecules* **2020**, *21* (7), 2913–2921.

(269) Rodeheaver, G. T.; Kurtz, L.; Kircher, B. J.; Edlich, R. F. Pluronic F-68: A Promising New Skin Wound Cleanser. *Ann. Emerg. Med.* **1980**, *9* (11), 572–576.

(270) Ballas, S. K.; Files, B.; Luchtman-Jones, L.; Benjamin, L.; Swerdlow, P.; Hilliard, L.; Coates, T.; Abboud, M.; Wojtowicz-Praga, S.; Grindel, J. M. Safety of Purified Poloxamer 188 in Sickle Cell Disease: Phase I Study of a Non-Ionic Surfactant in the Management of Acute Chest Syndrome. *Hemoglobin* **2004**, *28* (2), 85–102.

(271) Sandez-macho, I.; Casas, M.; Lage, E. V; Rial-hermida, M. I.; Concheiro, A.; Alvarez-lorenzo, C. Colloids and Surfaces B : Biointerfaces Interaction of Poloxamine Block Copolymers with Lipid Membranes : Role of Copolymer Structure and Membrane Cholesterol Content. *Colloids Surfaces B Biointerfaces* **2015**, *133*, 270–277.

(272) Elsayed, M. M. A.; Ibrahim, M. M.; Cevc, G. The Effect of Membrane Softeners on Rigidity of Lipid Vesicle Bilayers: Derivation from Vesicle Size Changes. *Chem. Phys. Lipids* **2018**, *210* (September 2017), 98–108.

(273) Liu, G.; Fu, L.; Zhang, G. Role of Hydrophobic Interactions in the Adsorption of Poly(Ethylene Glycol) Chains on Phospholipid Membranes Investigated with a Quartz Crystal Microbalance. *J. Phys. Chem. B* **2009**, *113* (11), 3365–3369.

(274) Chandaroy, P.; Sen, A.; Alexandridis, P.; Hui, S. W. Utilizing Temperature-Sensitive Association of Pluronic F-127 with Lipid Bilayers to Control Liposome-Cell Adhesion. *Biochim. Biophys. Acta - Biomembr.* **2002**, *1559* (1), 32–42.

(275) Harris, F. M.; Best, K. B.; Bell, J. D. Use of Laurdan Fluorescence Intensity and Polarization to Distinguish between Changes in Membrane Fluidity and Phospholipid Order. *Biochim. Biophys. Acta - Biomembr.* **2002**, *1565* (1), 123–128.

(276) Ma, Y.; Benda, A.; Kwiatek, J.; Owen, D. M.; Gaus, K. Time-Resolved Laurdan Fluorescence Reveals Insights into Membrane Viscosity and Hydration Levels. *Biophys. J.* **2018**, *115* (8), 1498–1508.

(277) Rharbi, Y. Fusion and Fragmentation Dynamics at Equilibrium in Triblock Copolymer Micelles. *Macromolecules* **2012**, *45* (24), 9823–9826.

(278) Sampaio, J. L.; Gerl, M. J.; Klose, C.; Ejsing, C. S.; Beug, H.; Simons, K.; Shevchenko, A. Membrane Lipidome of an Epithelial Cell Line. *Proc. Natl. Acad. Sci. U. S. A.* **2011**, *108* (5), 1903–1907.

(279) Nicolau, D. V.; Burrage, K.; Parton, R. G.; Hancock, J. F. Identifying Optimal Lipid Raft Characteristics Required To Promote Nanoscale Protein-Protein Interactions on the Plasma Membrane. *Mol. Cell. Biol.* **2006**, *26* (1), 313–323.

(280) Dutta, D.; Donaldson, J. G. Search for Inhibitors of Endocytosis. *Cell. Logist.* **2012**, *2* (4), 203–208.

(281) García-Sáez, A. J.; Chiantia, S.; Schwille, P. Effect of Line Tension on the Lateral Organization of Lipid Membranes. *J. Biol. Chem.* **2007**, *282* (46), 33537–33544.

(282) Filippov, A.; Orädd, G.; Lindblom, G. Domain Formation in Model Membranes Studied by Pulsed-Field Gradient-NMR: The Role of Lipid Polyunsaturation. *Biophys. J.* **2007**, *93* (9), 3182–3190.

(283) Levental, K. R.; Malmberg, E.; Symons, J. L.; Fan, Y. Y.; Chapkin, R. S.; Ernst, R.; Levental, I. Lipidomic and Biophysical Homeostasis of Mammalian Membranes Counteracts Dietary Lipid Perturbations to Maintain Cellular Fitness. *Nat. Commun.* **2020**, *11* (1), 1–13.

(284) Lata, K.; Singh, M.; Chatterjee, S.; Chattopadhyay, K. Membrane Dynamics and Remodelling in Response to the Action of the Membrane-Damaging Pore-Forming Toxins. *J. Membr. Biol.* **2022**, *255* (2–3), 161–173.

(285) Pokorny, A.; Almeida, P. F. F. Permeabilization of Raft-Containing Lipid Vesicles by δ-Lysin: A Mechanism for Cell Sensitivity to Cytotoxic Peptides. *Biochemistry* **2005**, *44* (27), 9538–9544.

(286) Oglęcka, K.; Rangamani, P.; Liedberg, B.; Kraut, R. S.; Parikh, A. N. Oscillatory Phase Separation in Giant Lipid Vesicles Induced by Transmembrane Osmotic Differentials. *Elife* **2014**, *3*, 1–18.

(287) De Almeida, R. F. M.; Fedorov, A.; Prieto, M. Sphingomyelin/Phosphatidylcholine/Cholesterol Phase Diagram: Boundaries and Composition of Lipid Rafts. *Biophys. J.* **2003**, *85* (4), 2406–2416.

(288) Pokorny, A.; Yandek, L. E.; Elegbede, A. I.; Hinderliter, A.; Almeida, P. F. F. Temperature and Composition Dependence of the Interaction of δ-Lysin with Ternary Mixtures of Sphingomyelin/Cholesterol/POPC. *Biophys. J.* **2006**, *91* (6), 2184–2197.

(289) Kikas, P.; Chalikias, G.; Tziakas, D. Cardiovascular Implications of Sphingomyelin Presence in Biological Membranes. *Eur. Cardiol. Rev.* **2018**, *13* (1), 42–45.

(290) Tafesse, F. G.; Huitema, K.; Hermansson, M.; Van Der Poel, S.; Van Den Dikkenberg, J.; Uphoff, A.; Somerharju, P.; Holthuis, J. C. M. Both Sphingomyelin Synthases SMS1 and SMS2 Are Required for Sphingomyelin Homeostasis and Growth in Human HeLa Cells. *J. Biol. Chem.* **2007**, *282* (24), 17537–17547.

(291) Veatch, S. L.; Keller, S. L. A Closer Look at the Canonical "raft Mixture" in Model Membrane Studies. *Biophys. J.* **2003**, *84* (1), 725–726.

(292) Cornell, C. E.; Mileant, A.; Thakkar, N.; Lee, K. K.; Keller, S. L. Direct Imaging of Liquid Domains in Membranes by Cryo-Electron Tomography. *Proc. Natl. Acad. Sci. U.*

S. A. **2020**, *117* (33), 19713–19719.

(293) Korlach, J.; Schwille, P.; Webb, W. W.; Feigenson, G. W. Characterization of Lipid Bilayer Phases by Confocal Microscopy and Fluorescence Correlation Spectroscopy. *Proc. Natl. Acad. Sci. U. S. A.* **1999**, *96* (15), 8461–8466.

(294) Hughes, L. D.; Rawle, R. J.; Boxer, S. G. Choose Your Label Wisely: Water-Soluble Fluorophores Often Interact with Lipid Bilayers. *PLoS One* **2014**, *9* (2).

(295) Silbaugh, A.; Vallin, J.; Pelaez, F.; Kim, M.; Shao, Q.; Lee, H. S.; Bischof, J. C.; Azarin, S. M. Enhancing Electroporation-Induced Liposomal Drug Release in Suspension and Solid Phases. *Int. J. Pharm.* **2023**, *635* (November 2022), 122744.

(296) Hardy, R. C.; Cottington, R. L. Viscosity of Deuterium Oxide and Water in the Range 5 to 125 C. *J. Res. Natl. Bur. Stand. (1934).* **1949**, *42* (6), 573.

(297) Miyamoto, Y.; Fujiki, M.; Nomura, K. Synthesis of Homopolymers and Multiblock Copolymers by the Living Ring-Opening Metathesis Polymerization of Norbornenes Containing Acetyl-Protected Carbohydrates with Well-Defined Ruthenium and Molybdenum Initiators. *J. Polym. Sci. Part A Polym. Chem.* **2004**, *42* (17), 4248–4265.

(298) Rahman, M. A.; Lokupitiya, H. N.; Ganewatta, M. S.; Yuan, L.; Stefik, M.; Tang, C. Designing Block Copolymer Architectures toward Tough Bioplastics from Natural Rosin. *Macromolecules* **2017**, *50* (5), 2069–2077.

(299) Nickels, J. D.; Cheng, X.; Mostofian, B.; Stanley, C.; Lindner, B.; Heberle, F. A.; Perticaroli, S.; Feygenson, M.; Egami, T.; Standaert, R. F.; Smith, J. C.; Myles, D. A. A.; Ohl, M.; Katsaras, J. Mechanical Properties of Nanoscopic Lipid Domains. *J. Am. Chem. Soc.* **2015**, *137* (50), 15772–15780.

(300) Fredrickson, G. H. Surfactant-Induced Lyotropic Behavior of Flexible Polymer Solutions. *Macromolecules* **1993**, *26* (11), 2825–2831.

(301) Lin, T. P.; Chang, A. B.; Chen, H. Y.; Liberman-Martin, A. L.; Bates, C. M.; Voegtle, M. J.; Bauer, C. A.; Grubbs, R. H. Control of Grafting Density and Distribution in Graft Polymers by Living Ring-Opening Metathesis Copolymerization. *J. Am. Chem. Soc.* **2017**, *139* (10), 3896–3903.

(302) Radzinski, S. C.; Foster, J. C.; Chapleski, R. C.; Troya, D.; Matson, J. B. Bottlebrush Polymer Synthesis by Ring-Opening Metathesis Polymerization: The Significance of the Anchor Group. *J. Am. Chem. Soc.* **2016**, *138* (22), 6998–7004.

(303) Walsh, D. J.; Lau, S. H.; Hyatt, M. G.; Guironnet, D. Kinetic Study of Living Ring-Opening Metathesis Polymerization with Third-Generation Grubbs Catalysts. *J. Am. Chem. Soc.* **2017**, *139* (39), 13644–13647.

(304) Idiart, M. A.; Levin, Y. Rupture of a Liposomal Vesicle. **2004**, *061922* (October 2003), 1–8.

(305) Alam Shibly, S. U.; Ghatak, C.; Sayem Karal, M. A.; Moniruzzaman, M.; Yamazaki, M. Experimental Estimation of Membrane Tension Induced by Osmotic Pressure. *Biophys. J.* **2016**, *111* (10), 2190–2201.

(306) Chabanon, M.; Ho, J. C. S.; Liedberg, B.; Parikh, A. N.; Rangamani, P. Pulsatile Lipid Vesicles under Osmotic Stress. *Biophys. J.* **2017**, *112* (8), 1682–1691.